

Dissertation  
submitted to the  
Combined Faculty of Natural Sciences and Mathematics  
of Heidelberg University, Germany  
for the degree of  
Doctor of Natural Sciences

Put forward by

Rima Xenia Schüßler

born in: Heppenheim an der Bergstraße

Oral examination: 19.12.2019



**First High-Precision Mass Measurements at PENTATRAP on  
highly charged Xe and Re ions**

**Referees:**

**Prof. Dr. Klaus Blaum**

**Prof. Dr. Thomas Pfeifer**



## Die ersten Hochpräzisions-Massenmessungen mit hochgeladenen Xe- und Re-Ionen an PENTATRAP

Das Hochpräzisions-Massenspektrometer PENTATRAP wurde entwickelt, um Massenverhältnisse hochgeladener Ionen mit einer relativen Genauigkeit von  $10^{-11}$  zu bestimmen. Der einzigartige Aufbau des PENTATRAP-Experiments umfasst die externen Ionenquellen für die Produktion hochgeladener Ionen, die Detektionssysteme, welche einzelne Ionen nachweisen können, und insbesondere den Fallenturm aus fünf Penningfallen, welcher simultane Messungen einzelner Ionen ermöglicht. Im Rahmen dieser Arbeit wurden die ersten Hochpräzisions-Massenmessungen mit einer relativen Genauigkeit von teilweise besser als  $\delta m/m \approx 10^{-11}$  durchgeführt. Als erste Vergleichsmessung wurde die Massendifferenz von fünf Paaren von Xenonisotopen bestimmt. Im Vergleich mit den Literaturwerten wurde eine Übereinstimmung erzielt, wobei die Unsicherheiten der Massendifferenzen um einen Faktor 4 bis 1700 verbessert werden konnten. Um die Genauigkeit von PENTATRAP zu zeigen, wurde zusätzlich die Bindungsenergie des 37. Elektrons in Xenon durch eine Massendifferenzmessung von  $^{132}\text{Xe}^{17+}$  und  $^{132}\text{Xe}^{18+}$  bestimmt. Die Übereinstimmung von Theorie und Experiment erlaubt es in Zukunft empfindliche Tests der Quantenelektrodynamik mit Bindungsenergien höher geladener Ionen durchzuführen. Zuletzt ebnet die Entdeckung von metastabilen elektronischen Zuständen in Rhenium- und Osmiumionen durch Massendifferenzmessungen, bestätigt durch theoretische Berechnungen, den Weg für Penningfallen-Massenspektrometrie zu Tests von Atomstrukturtheorien oder der Suche nach geeigneten Uhrenübergängen in hochgeladenen Ionen beizutragen.

## First High-Precision Mass Measurements at PENTATRAP on highly charged Xe and Re ions

The high-precision Penning-trap mass spectrometer PENTATRAP was designed to perform mass-ratio measurements of highly charged ions with relative uncertainties of  $10^{-11}$ . The unique features of the PENTATRAP experiment are the external ion sources providing highly charged ions, the detection systems with single-ion sensitivity and especially the stack of five Penning traps, which allows simultaneous measurements of single ions in the traps. In the scope of this thesis, the first high-precision mass measurements with a relative precision partially below  $\delta m/m \approx 10^{-11}$  were performed. As a first benchmark test, the mass differences of five xenon isotope pairs were determined. Comparison to the literature values led to an improvement of the uncertainty of the mass differences of a factor between 4 and 1700, in agreement with literature. In order to demonstrate the accuracy of PENTATRAP, the binding energy of the 37<sup>th</sup> electron in  $^{132}\text{Xe}$  was determined as a proof-of-principle measurement by determining the mass difference of  $^{132}\text{Xe}^{17+}$  and  $^{132}\text{Xe}^{18+}$ . The agreement of the result with theory allows performing stringent tests of quantum electrodynamics using binding energies in ions with an even higher charge state in the future. Lastly, the discovery of metastable electronic states in highly charged rhenium and osmium ions by mass difference measurements, confirmed by theory, extends the applicability of Penning-trap mass spectrometry to tests of atomic structure theories and to the identification of long-lived excited states for a possible new generation of clocks using highly charged ions.



---

# Contents

---

<b>List of Figures</b>	<b>i</b>
<b>List of Tables</b>	<b>iii</b>
<b>1 Introduction</b>	<b>1</b>
1.1 Motivation for high-precision mass-ratio measurements . . . . .	3
1.1.1 Tests of the energy-mass equivalence principle . . . . .	3
1.1.2 Testing quantum electrodynamics (QED) . . . . .	3
1.1.3 Applications in neutrino physics . . . . .	4
1.1.4 Investigating the electronic structure in highly charged ions . . . . .	7
1.2 Structure of this thesis . . . . .	8
<b>2 Penning Trap Physics</b>	<b>11</b>
2.1 The ideal Penning trap . . . . .	12
2.2 The real Penning trap . . . . .	15
2.2.1 Shifts due to electric field imperfections . . . . .	15
2.2.2 Shifts arising from magnetic field imperfections . . . . .	17
2.2.3 Further shifts . . . . .	19
2.3 Mass measurements in a Penning trap . . . . .	21
2.4 Manipulation of the eigenmotions . . . . .	24
2.5 Ion motion detection . . . . .	25
2.5.1 Induced image current . . . . .	26
2.5.2 Ion signal - Dip spectrum . . . . .	28
2.5.3 Detection of the radial modes . . . . .	30
2.5.4 PnP-method . . . . .	33
<b>3 The High-Precision Mass Spectrometer PENTATRAP</b>	<b>37</b>
3.1 Production of ions in electron beam ion traps . . . . .	38
3.1.1 The Heidelberg Compact EBIT . . . . .	40
3.1.2 The DreEBIT . . . . .	46
3.2 Ion transportation . . . . .	46
3.3 Cryogenic setup of PENTATRAP . . . . .	49
3.3.1 Magnet laboratory . . . . .	49

3.3.2	Realisation of the detection system . . . . .	50
3.3.3	The trap tower . . . . .	53
3.3.4	Trap electronics . . . . .	55
<b>4</b>	<b>Measurement Procedure</b>	<b>57</b>
4.1	Experiment control . . . . .	58
4.2	Preparatory steps before a measurement . . . . .	59
4.3	Measurement structure . . . . .	63
4.3.1	Dip-measurement . . . . .	64
4.3.2	PnP-measurement . . . . .	65
4.3.3	$N$ -determination measurement . . . . .	66
4.4	Measuring the magnetic field gradient . . . . .	67
<b>5</b>	<b>Data Analysis Procedure</b>	<b>69</b>
5.1	Analysis steps . . . . .	70
5.2	Axial eigenfrequency determination . . . . .	73
5.3	Magnetron eigenfrequency determination . . . . .	76
5.4	Modified cyclotron eigenfrequency determination . . . . .	78
5.4.1	Reading out the phase . . . . .	79
5.4.2	Determination of the phase difference . . . . .	81
5.4.3	Determination of number of full revolutions $N$ . . . . .	82
5.4.4	Error assignment . . . . .	83
5.4.5	Calculation of the modified cyclotron frequency . . . . .	84
5.5	Comparison between joint and grouped analysis . . . . .	84
5.6	Free-space cyclotron frequency . . . . .	85
5.6.1	1. Filter - large uncertainty . . . . .	85
5.6.2	2. Filter - deviation . . . . .	86
5.6.3	Calculation of the free-space cyclotron frequency . . . . .	88
5.7	Frequency ratio determination . . . . .	88
5.7.1	Polynomial method . . . . .	89
5.7.2	Cancellation method . . . . .	92
5.8	Mass difference calculation . . . . .	92
<b>6</b>	<b>Xenon: Mass Measurements and Binding Energy Determination</b>	<b>95</b>
6.1	Mass measurements . . . . .	96
6.1.1	Ion order measurements . . . . .	102
6.1.2	Mass difference . . . . .	102
6.1.3	Systematic effects . . . . .	104
6.1.4	Comparison to AME2017 . . . . .	108
6.2	Binding energy of the 37 <sup>th</sup> electron in Xe . . . . .	109
6.2.1	Systematic shifts . . . . .	109
6.2.2	Calculation of the binding energy . . . . .	111

<b>7</b>	<b>Rhenium: Discovery of Metastable States</b>	<b>113</b>
7.1	Electronic structure of HCIs . . . . .	114
7.1.1	Electronic configuration of $^{187}\text{Re}^{29+}$ . . . . .	114
7.1.2	Excited states in an EBIT . . . . .	116
7.2	Performed measurements . . . . .	116
7.3	Data analysis . . . . .	118
7.4	Systematic effects . . . . .	122
7.5	Energy of the metastable state . . . . .	123
7.5.1	Experimental result . . . . .	123
7.5.2	Comparison with theory . . . . .	124
<b>8</b>	<b>Summary and Outlook</b>	<b>127</b>
	<b>Publications by Rima Schüssler</b>	<b>133</b>
	<b>Bibliography</b>	<b>135</b>



---

# List of Figures

---

1.1	Holmium de-excitation spectrum . . . . .	6
2.1	Eigenmotions of a cooled ion in a Penning trap . . . . .	14
2.2	Energy levels in a Penning trap . . . . .	15
2.3	Electrodes for a hyperbolic and cylindrical Penning trap . . . . .	17
2.4	Possible measurement schemes at PENTATRAP . . . . .	23
2.5	Basic principle of the image current detection method. . . . .	26
2.6	Ion equivalent circuit . . . . .	29
2.7	Dip spectra for different axial frequencies . . . . .	30
2.8	Double-dip spectrum around a single dip . . . . .	31
2.9	Schematic of the phases during a PnP-measurement . . . . .	33
2.10	Overview of the changes in radii during a PnP-measurement . . . . .	34
3.1	Overview of the PENTATRAP experiment . . . . .	38
3.2	Working principle of an EBIT . . . . .	39
3.3	CAD model of the Heidelberg compact EBIT . . . . .	40
3.4	Voltages applied to the HC-EBIT . . . . .	41
3.5	Laser ablation in the trapping region . . . . .	44
3.6	Laser pulse and trap opening sequence and the first Ho-spectrum . . . . .	45
3.7	Isotopically resolved charge-to-mass spectrum for Cl-ions produced in the DreEBIT . . . . .	47
3.8	CAD model of the vertical beamline and cryogenic setup . . . . .	48
3.9	Amplifier layout and picture . . . . .	52
3.10	Complete detection system of ion, resonator, and cryogenic amplifier . . . . .	53
3.11	Trap tower with detection system . . . . .	54
4.1	Preparation steps of ions in the traps before measurements . . . . .	60
4.2	FFT spectrum of a hot ion cooling in . . . . .	61
4.3	Loading of an ion into trap 1 . . . . .	62
4.4	Measurement structure of a typical mass measurement . . . . .	64
4.5	$F(N_i, \nu_+)$ for different evolution times . . . . .	67
5.1	Analysis procedure for the determination of the mass difference . . . . .	72

5.2	Resonator fit to a single-dip spectrum . . . . .	73
5.3	Fit of an axial dip . . . . .	76
5.4	Double-dip fit for the determination of the magnetron frequency. . . . .	77
5.5	Phase spectra of the axial mode after the coupling pulse . . . . .	79
5.6	Principle of unwrapping the phases of one measurement . . . . .	80
5.7	Measured averaged reference $\varphi_{\text{ref}}$ and accumulated $\varphi_{\text{acc}}$ phase and the phase difference $\Delta\varphi = \varphi_{\text{acc}} - \varphi_{\text{ref}}$ . . . . .	82
5.8	Comparison between joint and grouped analysis . . . . .	85
5.9	Filtering of the modified cyclotron frequencies with the first filter . . . . .	86
5.10	Display of the second filter for the axial frequencies . . . . .	87
5.11	Partition of the measured data points into parts for the polynomial fit . . . . .	90
5.12	Example of a polynomial ratio fit . . . . .	91
6.1	Measured Xe pairs and the natural abundance of Xe isotopes . . . . .	97
6.2	Ratios for $^{131}\text{Xe}/^{132}\text{Xe}$ mass measurements in two traps featuring different magnetic field changes . . . . .	99
6.3	Stability of the frequency ratio over several measurements . . . . .	101
6.4	Cyclotron frequency ratios for $^{134}\text{Xe}/^{132}\text{Xe}$ mass measurements to inves- tigate the influence of the ion order . . . . .	103
6.5	Measurement to determine the magnetic field gradient . . . . .	106
6.6	Xe mass differences of PENTATRAP compared to AME2017 . . . . .	108
6.7	Frequency ratios for Xe binding energy determination . . . . .	110
7.1	Level crossings in HCIs . . . . .	115
7.2	Identification of the electronic state of the Re ions . . . . .	119
7.3	Free-space cyclotron frequencies in both measurement traps for $^{187}\text{Re}^{29+}$ ions over one measurement . . . . .	120
7.4	Comparison of the cancellation and polynomial method . . . . .	121
7.5	All free-space cyclotron frequency ratios of metastable to ground state in $^{187}\text{Re}^{29+}$ . . . . .	123
7.6	Comparison of the experimental result to the values obtained by theory for the metastable state in $^{187}\text{Re}^{29+}$ . . . . .	125

---

## List of Tables

---

3.1	Characteristic values for the two axial detection systems . . . . .	51
4.1	Measurement types for the three eigenfrequencies . . . . .	58
5.1	Starting parameters for the dip fit routine . . . . .	75
5.2	Results of the $N$ -determination measurement . . . . .	83
6.1	Overview of performed measurements for the five Xe ion pairs and their statistical uncertainty . . . . .	98
6.2	Masses of the Xe isotopes taken from the Atomic-Mass Evaluation 2017 .	102
6.3	Frequency ratios and mass differences of the measured Xe pairs . . . . .	104
6.4	Summary of systematic uncertainties of the Xe mass measurements . . . .	107
7.1	Summary of all measurements performed using only $^{187}\text{Re}^{29+}$ ions . . . .	118



# 1

---

## Introduction

---

The mass of a particle is a fundamental property and its precise knowledge allows shedding light on the underlying physics. In the case of an atom or ion, the mass is given by the sum of its constituents and their interactions. Those interactions can be quantified using Einstein's relation  $E = mc^2$ . Measuring the mass of the atom or ion gives access to the binding energy, either in the nucleus or of the electrons in the shell.

The relative precision to which the mass needs to be determined depends on the physics to be investigated and ranges from  $\delta m/m \approx 10^{-7}$  for tests of nuclear mass models to  $\delta m/m \approx 10^{-12}$  which is required for investigations of quantum electrodynamics [Bla06]. Historically, improvements in the mass resolution have led to several discoveries in fundamental physics. For instance, one of the first mass spectrometers, using a combination of electric and magnetic fields to force ions with identical charge-to-mass ratio on the same trajectory towards a photographic plate, led to the discovery of Ne isotopes with mass numbers  $A = 20$  and  $A = 22$  in 1912 [Tho12]. An improvement of this spectrometer to a mass resolution of  $10^{-4}$  showed a discrepancy of the sum of the individual nucleon masses to their combined mass [Ast22]. This mass defect originates from the nuclear binding energy. For heavier atoms, a mass resolution of  $\delta m/m < 10^{-6}$  is needed to determine its effect with a relative uncertainty below  $10^{-2}$ . Investigations of the mass defect allowed to establish the nuclear shell model [May48; HJS49].

Compared to the nuclear binding energy, the effect of the atomic binding energy on the total mass of a particle is on the order of  $10^{-11}$  for outer shell electrons in mid-heavy atoms and increases to  $\approx 10^{-7}$  for the inner shell electrons. Measurements with the required precision to resolve these effects were made possible with the invention of the

Penning trap by Dehmelt [Deh90]. The advantage of Penning traps for high-precision mass measurements arises from the conversion of the mass to a frequency measurement, as the ion's cyclotron frequency is determined in a magnetic field.

The first high-precision mass measurements in a Penning trap determined the electron-to-proton mass ratio with a relative uncertainty of  $\delta m/m = 6 \cdot 10^{-8}$  [GKT80]. Hereby, the time of flight to a detector outside the Penning trap of both particles was determined, which allowed measuring mass differences with an uncertainty of  $\delta m/m = 10^{-8}$  [Bla06] and even  $10^{-9}$  when the Ramsey ion-cyclotron resonance detection technique is used [Geo+07]. This precision could recently be improved to  $\delta m/m \approx 10^{-10}$  by detecting the phase of the ions' motions instead of their arrival time on the detector [Eli+13]. The hereby examined physics include investigations of the shell structure of the nucleus [Ros+15], double-electron capture in  $^{164}\text{Er}$  [Eli+11], and contributions to nuclear astrophysics [Van+12], to name a few.

An even better precision can be reached by determining the ions' frequency with the image current detection technique. This non-destructive method allows to use only single ions in the trap, further increasing the accuracy due to the elimination of ion-ion interaction. The achievable uncertainty on the order of  $\delta m/m \lesssim 10^{-11}$  allowed, for example, determining the mass of the proton [Hei+17], comparing it to the anti-proton mass to test CPT symmetry [Ulm+15], and contributing to neutrino physics by investigating the  $\beta$ -decay of  $^3\text{T}$  [Mye+15].

So far, the highest precisions have been achieved for relatively light particles, e.g. proton, deuterium,  $^3\text{T}$  and  $^4\text{He}$ . The new Penning-trap experiment PENTATRAP was therefore designed to perform high-precision mass measurements on ions in the mid-heavy regime of the nuclear chart to a relative uncertainty below  $\delta m/m = 10^{-11}$ . The use of highly charged ions (HCIs) results in higher motional frequencies compared to singly charged ions, which, at the same absolute uncertainty, leads to a smaller relative uncertainty of the mass. So far, HCIs were only used at the Penning-trap experiments SMILETRAP, using stable nuclides [Ber+02], and TITAN, employing radioactive nuclides [Dil+06], both using the time-of-flight technique. At PENTATRAP, a cryogenic environment of the Penning traps ensures an as good as possible vacuum and, therefore, a long lifetime of the ions in the trap. This results in higher statistics on the frequency determination. However, the heart of PENTATRAP is the stack of five Penning traps. These allow simultaneously measuring the frequencies in two traps, while using the others as storage for an exchange of ions inbetween measurements, enabling alternating measurements of different ion species with just one ion in the trap. Thereby, the ion-ion interaction present in other simultaneous measurement methods [RTP04] is eliminated. Additionally, the ion species can be exchanged from one measurement to the next on the time scale of a few minutes.

## 1.1 Motivation for high-precision mass-ratio measurements

With the precision aimed at, PENTATRAP is able to contribute to fundamental physics investigations. In the following, direct applications for PENTATRAP will be discussed in more detail. The results of several of these are described in this thesis.

### 1.1.1 Tests of the energy-mass equivalence principle

A direct test of Einstein's energy-mass equivalence principle,  $E = mc^2$ , can be performed by comparing an energy change in a particle, i.e. during a radioactive decay, to its mass before and after. In [Rai+05] a neutron capture process in  $^{29}\text{Si}$  and  $^{33}\text{S}$  is investigated. Thereby, the mass of the atom  $m(^A X)$  before the capture process is changed to

$$m(^A X) \cdot c^2 + m(n) \cdot c^2 \rightarrow m(^{A+1} X) \cdot c^2 + E_\gamma \quad , \quad (1.1)$$

where  $E_\gamma$  is the energy of the emitted radiation in the form of  $\gamma$ -rays. These were measured with the GAMS4 crystal-diffraction facility at the Laue-Langevin Institute in Grenoble [Kes+01], while the mass differences of the mother and daughter nuclide were determined with Penning-trap mass spectrometry. In the case of the measurements involving S and Si, the result  $1 - \Delta mc^2/E = -1.4(4.4) \cdot 10^{-7}$  is so far the most stringent test of the energy-mass equivalence principle.

The uncertainty of this test was limited by the resolution of the  $\gamma$ -ray energy determination. A potentially more stringent test could be performed using  $^{35}\text{Cl}$ , as the  $\gamma$ -ray spectrum was already determined with a relative uncertainty of  $5 \cdot 10^{-8}$  [Jen+08]. Additionally, with the new GAMS6 a further improvement of this value is expected [Kre+08]. The mass ratio of  $^{35}\text{Cl}$  and  $^{36}\text{Cl}$  can thereby be determined by PENTATRAP. As both masses are already known to a level of  $\delta m = 4 \cdot 10^{-8} \text{ u}$ , a relative precision of the mass ratio of  $\approx 10^{-11}$  is sufficient for the calculation of the mass difference from the mass ratio, see Sec. 5.8. In this case the limiting factor would be the neutron mass uncertainty,  $\delta m_n/m_n = 5 \cdot 10^{-9}$  [Wan+17].

### 1.1.2 Testing quantum electrodynamics (QED)

QED describes the relativistic interaction of light and matter. Fundamental particle properties such as the  $g$ -factor of a bound electron [Ara+19] or binding energies in atoms [Vol+13] can be used to test QED. Especially in heavy, highly charged ions, where the QED contributions are the strongest, a comparison between experiment and theory becomes feasible.

With PENTATRAP it is possible to compare experimental to theoretical values for atomic binding energies by measuring the mass difference of ions with a different charge. While an interesting case would be bare U [MPS98], a first proof-of-principle measurement of the binding energy of the  $37^{\text{th}}$  electron in Xe was performed with PENTATRAP, see Chapter 6. Although this low charge state is not sensitive to QED contributions, it is still important to have a confirmation between theory and experiment.

For many applications of high-precision mass (difference) determination, the masses of the neutral atoms are of interest. From a measured mass difference of ions with charge  $q_1$  and  $q_2$ , the neutral mass difference  $\Delta m$  can be extracted using:

$$\Delta m = m_1 - m_2 = (m(A_1^{q_1+}) + q_1 \cdot m_e - E_{B,1}) - (m(A_2^{q_2+}) + q_2 \cdot m_e - E_{B,2}) \quad (1.2)$$

$$= m(A_1^{q_1+}) - m(A_2^{q_2+}) + (q_1 - q_2)m_e - \Delta E_B \quad . \quad (1.3)$$

The total binding energy difference  $\Delta E_B$  of the two ions needs to be calculated using QED. Measuring the masses of ions in different charge states but with the same nucleus leads to zero mass difference of the neutral atoms. In this case, the binding-energy difference  $\Delta E_B$  calculated by theory can be compared to experimental values:

$$\Delta E_B = m(A_1^{q_1+}) - m(A_2^{q_2+}) + (q_1 - q_2)m_e \quad . \quad (1.4)$$

### 1.1.3 Applications in neutrino physics

Neutrinos are electrically neutral elementary particles. They only interact via the weak interaction and can therefore only be detected indirectly. Their existence was initially proposed to explain the continuous  $\beta^-$ -decay spectrum (for the open letter from Pauli, see e.g. [JRR]). They were for the first time indirectly identified by the decay products in an inverse  $\beta^-$ -decay reaction [Cow+56].

According to the Standard Model of particle physics three generations of neutrinos and their anti-neutrinos exist for all three leptons ( $e^-$ ,  $\mu^-$  and  $\tau^-$ ). Furthermore, the neutrino is included as a massless particle. With the discovery, however, of the solar neutrino problem, where less neutrinos were observed to be emitted from the sun than expected, and its explanation using neutrino oscillations, at least one neutrino is not massless. Neutrino oscillations, where one neutrino is changed to another one, requires the mass eigenstates ( $\nu_i = \nu_1, \nu_2$  or  $\nu_3$ ) to be different than the flavour eigenstates ( $\nu_\alpha = \nu_e, \nu_\tau$  or  $\nu_\mu$ ) [Eid+04]:

$$|\nu_\alpha\rangle = \sum_i U_{\alpha i}^* |\nu_i\rangle \quad . \quad (1.5)$$

The matrix  $U_{\alpha i}^*$  is the Pontecorvo–Maki–Nakagawa–Sakata matrix (PMNS) and can be parametrized by three mixing angles,  $\theta_{12}$ ,  $\theta_{23}$ , and  $\theta_{13}$ , and one phase  $\delta_{CP}$  describing charge-parity violations [Val06]. The mixing angles depend on the squared mass differences  $\Delta m_{ij}^2 = m_i^2 - m_j^2$  and the travelled distance  $L$  from the point of creation to observation:

$$\theta_{ij} = \frac{\Delta m_{ij}^2 L}{4E} \quad , \quad (1.6)$$

where  $E$  is the particle's total energy. Therefore, from the observations of neutrino oscillations, only the mass differences of the mass eigenstates can be obtained. The currently known mass differences are  $\Delta m_{12}^2 = 7.35(18) \cdot 10^{-5} \text{ eV}$  from solar neutrino observations and  $|\Delta m_{31}^2| \approx |\Delta m_{32}^2| = 2.44(6) \cdot 10^{-3} \text{ eV}$  from the detection of neutrinos produced in the atmosphere [Oli+14].

One possibility to determine an upper limit for the (anti-)electron neutrino mass is to investigate decay processes, especially the  $\beta$ -decay and the electron-capture (EC) process. In both cases the energy released during the decay is distributed between the kinetic energy of the neutrino and the energy of the produced electrons ( $\beta$ ) or X-rays (EC). The maximum energy available for the decay is hereby equal to the mass difference of the mother and daughter nuclide, the so-called  $Q$ -value of the decay. Measuring the released energy, the high-energy endpoint corresponds to processes where nearly all of the energy is taken away by the electrons or X-rays and the neutrino is only left with its rest mass. If the neutrino would be massless, the high-energy endpoint would correspond to the  $Q$ -value and small deviations between the two values can be taken to arise from a non-zero neutrino mass.

Important for both processes are high statistics at the endpoint of the spectrum, as here the influence of the neutrino mass is at its largest. With a small  $Q$ -value the effect of the neutrino mass on the complete spectrum is higher, as the relative amount of data points at the endpoint is larger.

With mass spectrometry, the  $Q$ -value can be determined as the mass difference of the mother and the daughter nuclide. In the following, two examples of planned contributions with PENTATRAP will be given.

### $\beta$ -decay processes

The two  $\beta$ -decay processes with the smallest energy difference between the ground state of the mother and daughter nuclide are in  $^{187}\text{Re}$  (2.5 keV) and in  $^3\text{H}$  (18.6 keV) [EEN13]. One of the first measurements to be performed with PENTATRAP is, therefore, a determination of the mass difference of  $^{187}\text{Re}$  and its daughter nuclide  $^{187}\text{Os}$ .

During a  $\beta^-$ -decay process, a neutron in the nucleus is changed to a proton, while emitting an electron and anti-electron neutrino, to conserve the lepton number. In the case of  $^{187}\text{Re}$ , the process can be described by:



Due to the long lifetime of  $^{187}\text{Re}$  of  $\tau_{1/2} \approx 4 \cdot 10^7$  a [Nes+14], a large amount of Re is needed to determine the energy of the emitted electrons with high-enough statistics. The energy is therefore measured with cryogenic microcalorimeters, for example in [Arn+03]. The  $Q$ -value obtained here is  $Q = 2466.1(0.8)_{\text{stat}}(1.5)_{\text{sys}}$  eV.

In order to determine an upper limit of the anti-electron neutrino mass, a  $Q$ -value needs to be determined with, e.g., Penning-trap mass measurements. The currently most precise value,  $Q_{\text{SHIPTRAP}} = 2492(30)_{\text{stat}}(15)_{\text{sys}}$  eV, was determined with the Penning-trap experiment SHIPTRAP [Nes+14]. For the determination of an upper limit of the anti-electron neutrino mass from  $\beta^-$ -decay in  $^{187}\text{Re}$ , an independent measurement of the  $Q$ -value with an uncertainty on the order of a few eV will be needed as a consistency check of the  $Q$ -value obtained from fitting the spectrum with the theoretical description.

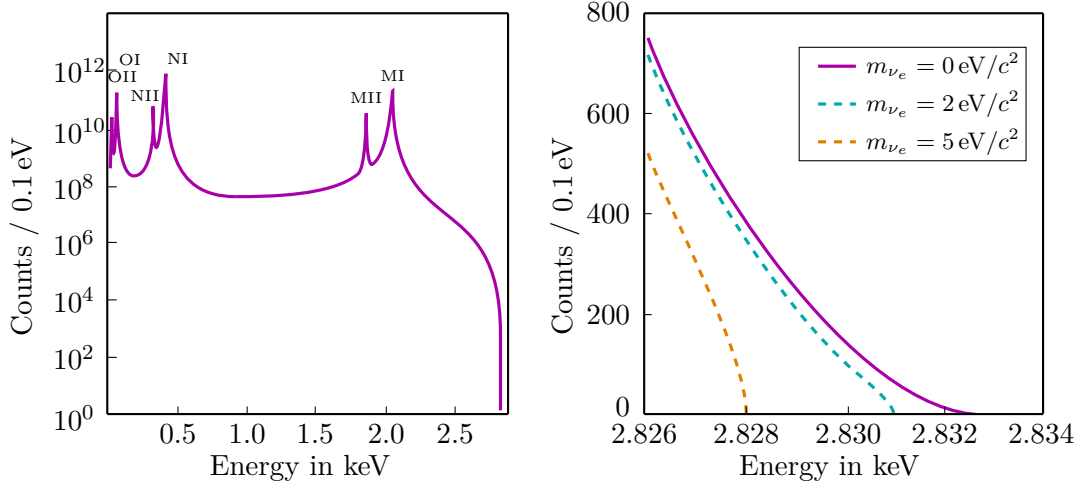
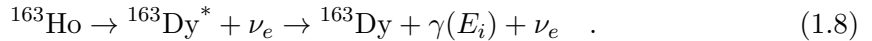


**Figure 1.1:** **Left:** A schematic of the complete Dy de-excitation spectrum following an electron-capture process in Ho. The peaks, Breit-Wigner resonances, correspond to the energy of the captured inner-shell electron. **Right:** Close up of the endpoint of the spectrum. Depending on the neutrino mass, shown here for the cases of  $m_{\nu_e} = 2 \text{ eV}/c^2$  (blue) and  $m_{\nu_e} = 5 \text{ eV}/c^2$  (orange), it is shifted to lower energy values than in the case of  $m_{\nu_e} = 0 \text{ eV}/c^2$  (magenta). Modified from [Gas+17].

### Electron capture in holmium (ECHO)

Another approach to determine an upper limit for the electron neutrino mass is the investigation of an electron-capture process. As a small  $Q$ -value is preferred, an optimal candidate is  $^{163}\text{Ho}$ , which decays to  $^{163}\text{Dy}$ . The inner-shell electrons have a finite possibility to be in the nucleus and can be captured, thereby changing a proton into a neutron. The electron capture process in Ho is described by:



In the first step, the daughter nuclide is produced in an excited state, as the decay left a hole in the electron shell. Subsequent de-excitation leads to a Dy atom in the ground state, while emitting energy in the form of  $\gamma$ -rays. This energy corresponds to the difference in the binding energy of the de-excited electron.

In Fig. 1.1 a schematic of a de-excitation spectrum is shown (left), with a close up of the endpoint region (right), [Gas+17]. Such a spectrum is measured with cryogenic microcalorimeters, where the released energy during the de-excitation is fully absorbed by the detector material. The peaks, Breit-Wigner resonances, in the full spectrum correspond to the energy of different inner-shell electrons in Ho, minus the nuclear recoil. As only atomic levels with a binding energy below the  $Q$ -value can be captured during the electron-capture process, the peaks correspond to electrons in a shell between 3s (M I) and 5p (O II). While the complete spectrum is shifted to smaller values by the

neutrino mass, the effect is most visible at the end of the spectrum, where the neutrino is only left with its rest mass, see right side of Fig. 1.1. The endpoint is then shifted, compared to a massless neutrino (magenta), to smaller values, shown for the cases of  $m_{\nu_e} = 2 \text{ eV}/c^2$  (blue) and  $m_{\nu_e} = 5 \text{ eV}/c^2$  (orange).

The theoretical description of the spectrum includes, besides the energy levels of the captured electrons, the  $Q$ -value of the transition. By fitting it to the experimental data, a result for  $Q$  is obtained. As an independent cross-check, the mass difference of Ho and its daughter Dy is determined using a Penning trap. Again, as in the case of Re, a rough estimation of the  $Q$ -value was performed with SHIPTRAP to be  $Q = 2833(30)_{\text{stat}}(15)_{\text{sys}} \text{ eV}$  [Eli+15]. For future measurements within the ECHo collaboration, a  $Q$ -value with an uncertainty of a few eV is needed, which will be determined with PENTATRAN.

$^{163}\text{Ho}$  needs to be produced by neutron irradiation of enriched  $^{162}\text{Er}$  targets in research reactors and the sample size for the mass measurements of the  $Q$ -value is expected to be on the order of  $10^{14}$  atoms (corresponding to 27 ng) [Sch17]. Conventional production of HCIs in an electron beam ion trap from bulk material is therefore not possible. For an efficient ionisation, a new ion source with a laser-ablation system was set up during this thesis, see Sec. 3.1.1, and [Sch17].

### 1.1.4 Investigating the electronic structure in highly charged ions

Optical clocks are based on the excitation of an electronic transition in an atom or singly charged ion and the precise determination of the transition frequency. Hereby, fractional uncertainties of  $\delta\nu/\nu \lesssim 10^{-18}$  have been obtained using ensembles of atoms in optical lattices [Kat11] or with individual ions in quantum-logic clocks [Bre+19]. At this level of precision, applications of clocks include new frequency standards, dark matter detection [DP14], and test of physics beyond the Standard Model of particle physics [San+19; Meh+18].

Such high-precision experiments require exceptional control of systematic shifts on the investigated transition. Promising candidates for a new generation of clocks are forbidden transitions in highly charged ions [DDF12a; DDF12b] or nuclear excitations, as is the case for  $^{229\text{m}}\text{Th}$  [Wen+16]. Due to their reduced size, highly charged ions feature a suppressed susceptibility to external perturbations, possibly enabling fractional inaccuracies below  $10^{-19}$ . Additionally, several highly forbidden electronic transitions have been proposed that feature highest sensitivities to a possible variation of the fine-structure constant [BDF10].

Identification of possible clock transitions in highly charged ions is challenging. The electronic structure of HCIs features multiple vacancies in semi-filled shells. Theoretical predictions, therefore, have to include also strong relativistic and sizeable QED contributions. This limits the accuracy of even the most advanced and time-consuming atomic structure calculations. Experimentally, the long lifetime and the corresponding sub-Hz linewidth restricts the application of narrow-linewidth spectroscopy lasers to identify the transitions.

A different approach to laser spectroscopy for the identification of metastable excited electronic states in a HCI are measurements of the mass difference of the corresponding

ion in the ground and excited state. Hereby, the mass of an ion is increased by the difference in binding energy of the two electronic states. While the binding energies of the electrons in HCIs can be several keV, transitions even down to the optical range can be found, e.g. near level crossings of electronic shells [BDF10; BDF11].

The required precision to identify such a transition with a mass measurement depends on the mass of the ion and the energy of the transition. Assuming a transition energy of 1 keV and a mass of the ion of 200 u, the relative change in mass after the excitation of the ion is on the level of  $\Delta m/m \approx 5 \cdot 10^{-9}$ . In order to acquire any knowledge of the transition energy, the relative uncertainty to which the mass ratio is determined should be several orders of magnitude smaller than the effect of the excitation on the mass. Such high-precision mass measurements are possible with PENTATRAP.

Mass measurements in a Penning trap to this precision require several hours of interrogation, which sets a lower limit on the ion's excited state lifetime. The corresponding linewidth of the investigated electronic transition is then  $< 10^{-5}$  Hz. The direct identification of transitions is possible with Penning-trap mass spectrometry, but challenging for laser spectroscopy. Therefore, the use of mass spectrometry opens up the possibility to identify very narrow transitions for possible applications in new HCI-based clocks, and to test the accuracy of many-electron atomic structure calculations.

## 1.2 Structure of this thesis

In the scope of this thesis some of the first high-precision mass measurements with PENTATRAP were performed, reaching uncertainties partially below  $\delta m/m \lesssim 10^{-11}$ . In order to reach such low uncertainties, a sophisticated experimental setup is required, providing long storage times of highly charged ions and dedicated detection systems for the motion of the ion in the trap.

In the next chapter, [Chapter 2](#), the motion of an ion in a Penning trap is explained. Due to the use of an electric and magnetic field the ion's motion can be separated into three independent motions with different eigenfrequencies, all of which need to be determined to obtain the free-space cyclotron frequency. They are detected by a non-destructive image current technique. Furthermore, the chapter includes the description of the manipulation of the ion's motion as well as systematic shifts due to non-perfect trapping conditions.

The experimental setup of PENTATRAP is shown in [Chapter 3](#). The highly charged ions used for the measurements at PENTATRAP, are produced with an electron beam ion trap (EBIT). The transfer beamline connecting the EBIT to the Penning traps allows selecting the ion species and is used to decelerate the HCIs leaving the EBIT with high kinetic energies in order to efficiently trap them in the Penning traps. The Penning traps and the detection system for the motion of the ion are situated in the cold bore of a superconducting magnet.

[Chapter 4](#) deals with the experimental procedure of the simultaneous high-precision mass measurements. Hereby, three single ions are loaded into three traps, while in two of them the measurements are performed. Exchanging the ion species after each measure-

ment leads to alternating frequency determinations of two ions. The three eigenmotions of an ion in a trap are thereby either determined by reading out the ions signal on a frequency spectrum or with a phase-sensitive technique. The latter also requires additional measurements to calculate the frequency from the detected phase of the ion's motion.

The data analysis procedure is presented in [Chapter 5](#). For two eigenfrequencies the ion's signal can be determined by fitting different functions to the recorded spectrum. The phase of the third is extracted from a phase spectrum. Care is taken to ensure an optimal fitting routine for unambiguous identification of the ion's frequency and to remove jumps in the phase determination. At the end, the determination of the mass difference from the frequency ratio is explained.

Two different ion species were used for the measurements performed during this thesis. In the first, [Chapter 6](#), the mass differences of different Xe isotope pairs were determined, as these were among the previously most precise known mass differences in the mid-heavy regime of the nuclear chart. With the measurements presented here, these could be further improved, partly by a factor of 1700. Additionally, a proof-of-principle measurement of the binding energy of the 37<sup>th</sup> electron in Xe was performed in order to test many-electron atomic structure theories. The result shows an agreement with calculations and demonstrates the accuracy of PENTATRAP.

In the second measurement case presented in [Chapter 7](#), a long-lived metastable state in Re ions was discovered. With a (preliminary) theoretical lifetime of around 200 d [[Ind19](#)] and a corresponding linewidth of  $\sim 6 \cdot 10^{-8}$  Hz such a transition would be challenging to identify with narrow-linewidth spectroscopy lasers. This measurement opens up the possibility to identify very narrow transitions for possible applications in new HCI-based clocks.

The thesis closes with a summary and outlook in [Chapter 8](#), where future measurement plans at PENTATRAP are discussed.



# 2

---

## Penning Trap Physics

---

In order to determine the mass of an atom, its trajectory needs to be perfectly defined for the duration of a measurement. One possibility to accomplish this is to charge the atom by removing one to several bound electrons, thereby allowing it to be influenced by electric and magnetic fields. After the determination of the ion's mass, the mass of the atom can be calculated by adding the masses of the removed electrons minus their binding energy.

The simplest imaginable control of the ions motion is to hold it fixed in position in space. It was proven by Samuel Earnshaw [Ear42] that an electrostatic potential minimum cannot be simultaneously realised in all three spatial directions. This limitation can be overcome by either combining electrostatic and radio frequency (*rf*) electric fields, resulting in the Paul trap [PS53], or combining electrostatic fields with a homogeneous magnetic field. The latter one is termed Penning trap, after Frans Michel Penning, who proposed the idea when he was studying vacuum gauges [Pen36]. The advantage of a Penning trap compared to a Paul trap is the use of static fields, which do not heat the particles by micromotion. Additionally, the stable magnetic field produced by a superconducting magnet allows for high-precision measurements of the ions properties, such as its mass.

The following sections will give an overview of the motion of a charged particle in an ideal Penning trap in Sec. 2.1, followed by how imperfect trapping potentials affect the ion in Sec. 2.2. Sec. 2.3 will cover the realisation of mass measurements in a Penning trap, which requires the manipulation of the ion's motion, see Sec. 2.4. This chapter

closes with the description of the detection of the motion of the ion inside the Penning trap, see Sec. 2.5.

## 2.1 The ideal Penning trap

The mass  $m$  of an ion with charge  $q$  can be determined by measuring the free-space cyclotron frequency

$$\nu_c = \frac{1}{2\pi} \frac{q}{m} B_0 \quad (2.1)$$

in a strong magnetic field  $\vec{B} = B_0 \hat{e}_z$ . The ion is confined on a circular orbit due to the Lorentz force perpendicular to but is free to move in the direction of the magnetic field. In a Penning trap, additional confinement in the axial direction is achieved by superimposing a weak quadrupolar electrostatic potential,

$$\Phi(\vec{r}) = C_2 V_0 \left( z^2 - \frac{x^2 + y^2}{2} \right) \quad , \quad (2.2)$$

where  $C_2$  is a coefficient reflecting the electrode structure to which the potential  $V_0$  is applied. Such a harmonic potential leads to a motion whose frequency is independent of the energy of the ion. The electric potential is confining in axial direction, but defocusing in the radial direction. The overall Lorentz force acting on the ion,

$$\vec{F}_L = q \left( \vec{E} + \vec{v} \times \vec{B} \right) = q \left( -\vec{\nabla} \Phi + \vec{v} \times \vec{B} \right) \quad , \quad (2.3)$$

where  $\vec{v}$  is the velocity, results in three equations of motion, of which the two in the radial ( $x$ - and  $y$ -) direction are coupled:

$$\begin{pmatrix} \ddot{x} \\ \ddot{y} \\ \ddot{z} \end{pmatrix} = \frac{qC_2V_0}{m} \begin{pmatrix} x \\ y \\ -2z \end{pmatrix} + \frac{q}{m} B_0 \begin{pmatrix} \dot{y} \\ -\dot{x} \\ 0 \end{pmatrix} \quad . \quad (2.4)$$

The equation for motion in  $z$ -direction is readily solved and leads to an oscillatory motion with the axial eigenfrequency:

$$\nu_z = \frac{1}{2\pi} \sqrt{\frac{2qC_2V_0}{m}} \quad . \quad (2.5)$$

The axial frequency only depends on the applied voltage, but not on the magnetic field strength, a fact which can be used to change  $\nu_z$  to be in resonance with the detection system, see Sec. 2.5.

In the radial direction, the interplay of the defocusing electric and confining magnetic field changes the simple circular motion in a purely magnetic field to one consisting of

two independent motions. The coupled equations of motion can be solved by introducing the coordinate  $u(t) = x(t) + iy(t)$ , which finally results in the two radial eigenfrequencies:

$$\nu_- = \frac{\nu_c}{2} - \sqrt{\frac{\nu_c^2}{4} - \frac{\nu_z^2}{2}} \approx \frac{1}{2\pi} \frac{2C_2V_0}{B_0} \quad , \quad (2.6)$$

$$\nu_+ = \frac{\nu_c}{2} + \sqrt{\frac{\nu_c^2}{4} - \frac{\nu_z^2}{2}} \approx \nu_c - \frac{1}{2\pi} \frac{2C_2V_0}{B_0} \quad , \quad (2.7)$$

the magnetron and modified cyclotron eigenfrequency, respectively. In first approximation, the magnetron frequency does not directly depend on the ion's charge or mass, but rather through the potential depth  $V_0$ , which is chosen such that the axial frequency is the same for all ion species in one trap. The modified cyclotron frequency is slightly smaller than the free-space cyclotron eigenfrequency ( $\frac{1}{2\pi} \frac{2C_2V_0}{B_0} \approx 10$  kHz for the settings at PENTATRAP), hence the name.

In order to end up with real, not complex, frequencies, the eigenfrequencies require positive expressions inside the square root. This leads to the stability criteria

$$\begin{aligned} qC_2V_0 &> 0 \quad , \\ \nu_c &> \sqrt{2}\nu_z \quad . \end{aligned} \quad (2.8)$$

With  $C_2$  being negative, the first condition reflects the need for a potential minimum (negative  $V_0$ ) for positively charged ions. The second condition holds if the radial confinement due to the magnetic field is stronger than the defocusing by the electric potential. Penning traps, therefore, employ a strong magnetic field of  $\sim 7$  T (for PENTATRAP) and a weak electric potential of up to  $-100$  V. In such a confinement the following hierarchy of the eigenfrequencies in the trap is observed

$$\nu_c > \nu_+ \gg \nu_z \gg \nu_- \quad . \quad (2.9)$$

Although it is not a trap eigenfrequency, two relations can be used to calculate the free-space cyclotron frequency. Looking at the two radial eigenfrequencies, the relation

$$\nu_c = \nu_+ + \nu_- \quad , \quad (2.10)$$

is easily derived. It holds in an ideal Penning trap as described above and allows reliable mass measurements to a relative uncertainty of  $10^{-8}$  [Bla06]. The second relation is the robust Brown-Gabrielse-Invariance Theorem [BG86]:

$$\nu_c = \sqrt{\nu_+^2 + \nu_z^2 + \nu_-^2} \quad . \quad (2.11)$$

As it also holds in a non-perfect Penning trap, see next section, it allows performing relative mass measurements to an uncertainty of below  $10^{-11}$  [Gab09], as will also be shown in Chapter 7.

A schematic motion of the ion in a Penning trap is shown in Fig. 2.1 together with the magnetic field orientation and the electric field in radial  $\rho = \sqrt{x^2 + y^2}$  and axial

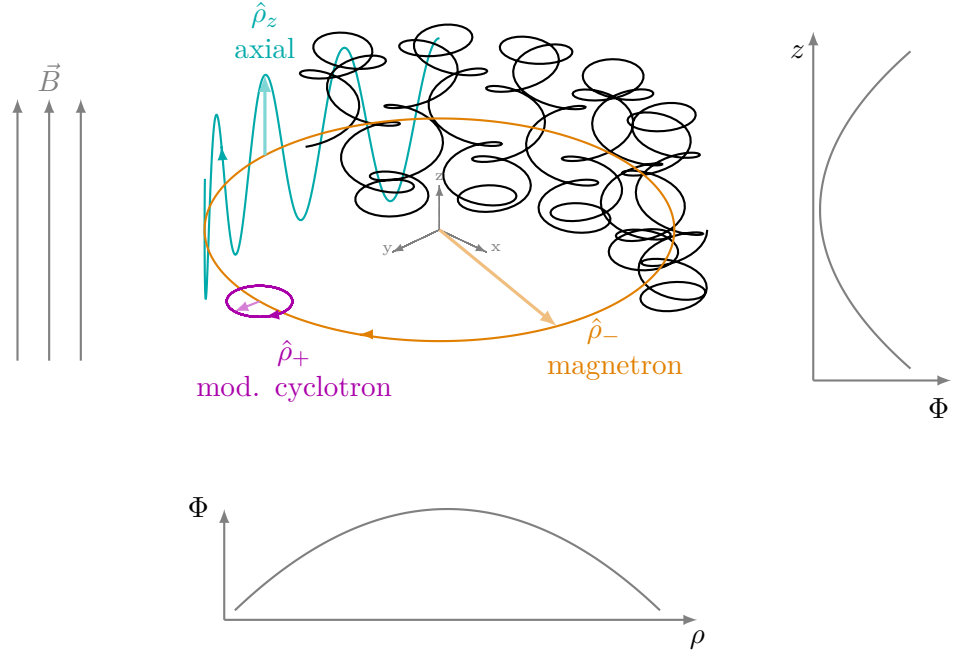


**Figure 2.1:** The three eigenmotions of a cooled ion in a Penning trap, for each motion separately in a different colour and combined in black, are shown together with the magnetic and electric fields. For graphic purposes, the frequency ratios of  $\nu_+/\nu_z \approx 2.8$  and  $\nu_z/\nu_- \approx 2.6$  were chosen. Typical amplitudes are  $\rho_+ \approx 2 \mu\text{m}$ ,  $\rho_z \approx 11 \mu\text{m}$ , and  $\rho_- \approx 2 \mu\text{m}$ , with the latter shown enlarged for graphic purposes.

$z$  direction. The amplitudes of the motions,  $\rho_+$ ,  $\rho_z$ , and  $\rho_-$ , depend on the motional energy. Since the three eigenmotions are independent harmonic oscillators, the total energy of an ion in a Penning trap in the quantum mechanical picture is given by

$$E = \underbrace{\left(n_+ + \frac{1}{2}\right) h\nu_+}_{E_+} + \underbrace{\left(n_z + \frac{1}{2}\right) h\nu_z}_{E_z} - \underbrace{\left(n_- + \frac{1}{2}\right) h\nu_-}_{E_-} \quad , \quad (2.12)$$

where  $n_i$  is the quantum number of the corresponding motion. The energy levels are schematically shown in Fig. 2.2. The magnetron energy  $E_-$  is dominated by potential energy and in the case of a reduction of motional quanta, e.g. through a cooling mechanism as described in Sec. 2.5.3, the magnetron radius increases. The magnetron motion is, therefore, metastable, shown by the decreasing energy for increasing  $n_-$  in Fig. 2.2.

At PENTATRAN, the ions axial motion can be cooled to the ambient temperature of the magnet bore, which is at 4 K. The radial motions are only cooled indirectly by coupling to the axial motion, which leads to temperatures on the order of 50 mK and 80 K (see Sec. 2.5.3) for the magnetron and the modified cyclotron motion, respectively.

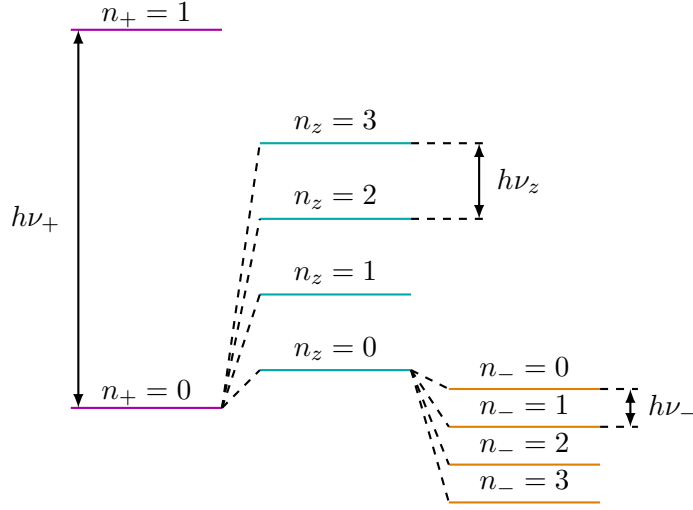


**Figure 2.2:** The energy levels of the ion motion in a Penning trap are shown. Due to the metastable character of the magnetron motion, the total energy decreases if motional quanta are added to this mode.

At these temperatures, the quantum numbers are still on the order of  $10^5$  and allow a classical treatment of the ion motion as described above.

## 2.2 The real Penning trap

Deviations from the ideal Penning trap are mainly caused by electric and magnetic field imperfections. Depending on the size and the nature of these imperfections, the trap eigenfrequencies are shifted compared to those in an ideal Penning trap.

### 2.2.1 Shifts due to electric field imperfections

As the electric field is produced by a set of electrodes, manufacturing tolerances and misalignment lead to deviations from the ideal electric field as described above. The real trap potential can be expressed by a series of Legendre polynomials  $P_k$  in cylindrical coordinates  $[\rho, z]$  [BG86] (due to rotational symmetry of the trap  $\phi$  does not play a role):

$$\Phi(z, \rho) = V_0 \sum_{k=1}^{\infty} C_k (z^2 + \rho^2)^{k/2} P_k \left( \frac{z}{\sqrt{z^2 + \rho^2}} \right) , \quad (2.13)$$

where  $k$  is a positive integer number larger than 1, as a term with  $k = 0$  would lead to an offset in the potential, but to no effect in the electric field. All coefficients  $C_k$  are functions of the geometry of the trap and the applied potentials. Due to the symmetry  $z \rightarrow -z$ , only even terms contribute to the potential. The first three terms are then

given by

$$\begin{aligned}
 \frac{\Phi(\rho, z)}{V_0} &= C_2 \left( z^2 + \frac{1}{2} \rho^2 \right) \\
 &+ C_4 \left( z^4 - 3\rho^2 z^2 + \frac{3}{8} \rho^4 \right) \\
 &+ C_6 \left( z^6 - \frac{15}{2} \rho^2 z^4 + \frac{45}{8} \rho^4 z^2 - \frac{5}{16} \rho^6 \right) \\
 &+ \dots \quad .
 \end{aligned} \tag{2.14}$$

If only the  $C_2$  term is taken into account, the potential of Eq. (2.2) is recovered. Including the first higher-order term changes the simple harmonic equation of motion for the axial motion to a Duffing type differential equation (see discussion in [Ulm11]):

$$\ddot{z} = -\frac{q}{m} 2V_0 \left( C_2 z + 2C_4 z^3 \right) \quad . \tag{2.15}$$

The nonlinear term leads to a dependency of the axial frequency on the axial amplitude  $\rho_z$  and consequently the axial energy,  $E_z = 2\pi^2 m \nu_z^2 \rho_z^2$ . This results in a shift in the axial frequency of:

$$\frac{\Delta\nu_z}{\nu_z} = \frac{3 C_4 E_z}{4 C_2^2 q V_0} \quad . \tag{2.16}$$

Using a perturbation theory approach [BG86; Kre92] a full correction matrix can be calculated. For the leading anharmonic contribution, this results in:

$$\begin{pmatrix} \Delta\nu_+/\nu_+ \\ \Delta\nu_z/\nu_z \\ \Delta\nu_-/\nu_- \end{pmatrix} = \frac{3}{qV_0} \frac{C_4}{C_2^2} \begin{pmatrix} \frac{1}{4}(\nu_z/\nu_+)^4 & -\frac{1}{2}(\nu_z/\nu_+)^2 & -(\nu_z/\nu_+)^2 \\ -\frac{1}{2}(\nu_z/\nu_+)^2 & \frac{1}{4} & 1 \\ -(\nu_z/\nu_+)^2 & 1 & 1 \end{pmatrix} \begin{pmatrix} E_+ \\ E_z \\ E_- \end{pmatrix} \quad . \tag{2.17}$$

In order to minimise this shift, the electrode structure producing the trapping potential needs to be chosen such that the effect of higher-order potential anharmonicities is reduced. An obvious choice for the shape of the electrodes producing a purely quadrupolar electric field are hyperbolically shaped electrodes, consisting of a ring and two end cap electrodes, see left side of Fig. 2.3, where the electrode surfaces follow the equipotential lines. The largest drawback from this choice is the need for holes in the end cap electrodes for injection of the ions into the trap, which leads to deviations from the perfect electric field. On the other hand, for certain ratios of length and radius, a stack of cylindrical electrodes also produces a near-perfect quadrupolar field in their center [GHR89]. This geometry has the advantage to be open for ions to access the trap center and allow adiabatic transport between several traps. Additionally, cylindrical electrodes can be manufactured to a precision of 5  $\mu\text{m}$  [Dör15], leading to well-defined trap electrode geometries.

A typical cylindrical electrode stack consists of five electrodes, the central ring and the two endcaps with correction electrodes in between, see right side of Fig. 2.3. The end cap electrodes, named historically after the hyperbolic trap design, are put on ground

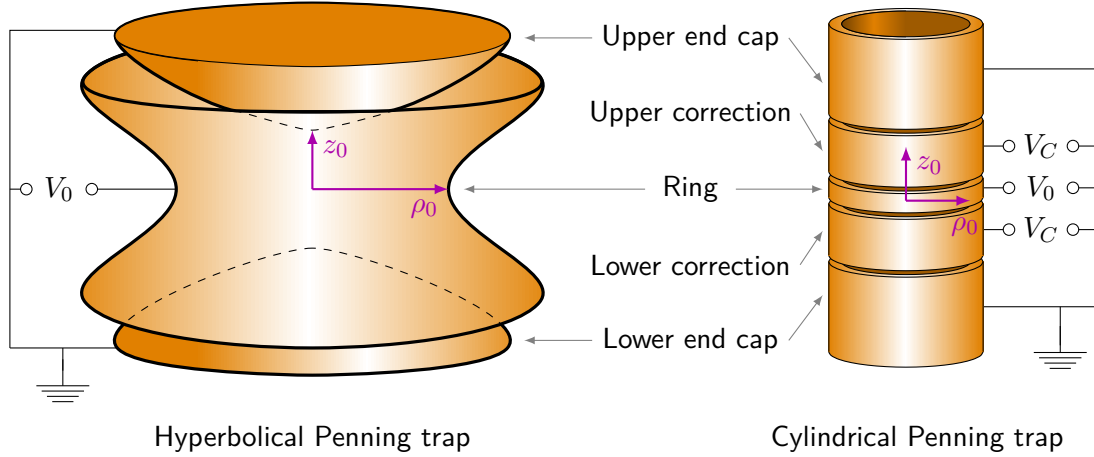


**Figure 2.3:** A schematic drawing of hyperbolic electrodes (**left**) of a Penning trap consisting of a ring electrode with radius  $\rho_0$  and two end caps placed  $2z_0$  apart. A quadrupolar electric field is realised by applying a voltage  $V_0$  between the ring electrode and the end caps. The same field can be generated by cylindrical electrodes (**right**) with additional correction electrodes and correction voltage  $V_C$ .

potential, while the trap depth is defined by the potential applied to the ring electrode  $V_{\text{ring}} = V_0$ . The correction electrodes help to mimic the quadrupolar potential with the applied voltage

$$V_C = V_0/\text{TR} \quad , \quad (2.18)$$

where the tuning ratio **TR** was introduced. For any trap, a tuning ratio can always be found such that  $C_4 = 0$ . While designing the trap tower, the trap dimensions, e.g. the inner radius of all electrodes and the different electrode lengths, can be chosen such that the trap is

**compensated:** By applying the right potentials to the trap electrodes the coefficients  $C_4$  and  $C_6$  can simultaneously be tuned to zero [Stu11] and

**orthogonal:** The ions axial frequency is independent of the voltage applied to the correction electrodes,  $\partial\nu_z/\partial\text{TR} = 0$ .

The design of the trap stack at PENTATRAP fulfilling these requirements within the manufacturing uncertainties is described in [Rou+12].

### 2.2.2 Shifts arising from magnetic field imperfections

Magnetic field imperfections arise mainly from the nature of superconducting magnets, as it is difficult to produce a homogeneous magnetic field over the length of the traps (for the magnetic field inside the Penning traps at PENTATRAP, see [Rep+12]). In order to

quantify the effect of higher-order terms, similar to the electric potential, the magnetic field can be expanded into a power series, where the first terms are given by:

$$B(z) = B_0 + B_1 z + B_2 z^2 + \dots \quad (2.19)$$

As in the center of the traps the radial contributions are usually negligible, only the axial contributions are considered here.

The effects of these additional terms on the ion's eigenfrequencies can be understood by looking at the magnetic moment arising due to the radial motions. The modified cyclotron eigenfrequency produces the magnetic moment [Moo13]:

$$\vec{\mu}_+ = -q \frac{2\pi\nu_+ \rho_+^2}{2} \hat{z} = -\frac{1}{2\pi} \frac{qE_+}{m\nu_+} \hat{e}_z \quad , \quad (2.20)$$

in the axial direction. The magnetic potential  $\Phi_{\text{mag}} = -|\vec{\mu}_+|B$  leads to an additional term in the Lorentz force, see Eq. (2.3), for the axial direction:

$$F_z = \partial_z(\vec{\mu}_+ \cdot \vec{B}(z)) = -q\pi\nu_+ \rho_+^2 (B_1 + 2B_2 z) \quad , \quad (2.21)$$

where only the two lowest order terms,  $B_1$  and  $B_2$ , were included.

The first contribution,  $B_1$ , leads to a constant, additional term in the equation of motion of the axial eigenfrequency. This shifts the central position of the axial motion by:

$$\Delta z = \frac{B_1}{2\pi m C_2 V_0} \frac{E_+}{\nu_+} \quad . \quad (2.22)$$

The magnetic field at the new central position is given by  $B_{\text{first}} = B_0 + B_1 \Delta z$ , which leads to a shift in the free-space cyclotron frequency:

$$\Delta\nu_c = \frac{1}{2\pi} \frac{q}{m} B_1 \Delta z = \frac{1}{4\pi^2} \frac{q}{m^2} \frac{B_1^2}{C_2 V_0} \frac{E_+}{\nu_+} \quad . \quad (2.23)$$

The second part,  $B_2$ , and the corresponding force  $F_2 = -2q\pi\nu_+ \rho_+^2 B_2 z$  adds another term depending on the axial position to the equation of motion

$$\ddot{z} = \left( 4\pi^2 \nu_z^2 - \frac{qB_2 E_+}{2\pi m^2 \nu_+} \right) z \quad , \quad (2.24)$$

which leads to the axial eigenfrequency shift

$$\frac{\Delta\nu_z}{\nu_z} \approx \frac{qB_2 E_+}{8\pi^3 m^2 \nu_+ \nu_z^2} \quad . \quad (2.25)$$

The calculation can be performed identically for a magnetic moment produced by the magnetron motion and for higher-order magnetic field terms in the radial direction. The total frequency shifts resulting from an inhomogeneous magnetic field  $B_2$  using a quantum mechanical treatment are given by [BG86]:

$$\begin{pmatrix} \Delta\nu_+/\nu_+ \\ \Delta\nu_z/\nu_z \\ \Delta\nu_-/\nu_- \end{pmatrix} = \frac{1}{4\pi^2 m \nu_z^2} \frac{B_2}{B_0} \begin{pmatrix} -(\nu_z/\nu_+)^4 & 1 & 2 \\ 1 & 0 & -1 \\ 2 & -1 & -2 \end{pmatrix} \begin{pmatrix} E_+ \\ E_z \\ E_- \end{pmatrix} \quad , \quad (2.26)$$

where Eq. (2.25) can be recovered by using the valid approximation  $\nu_+ \approx \nu_c$ . Therefore, in order to minimise this shift for a given  $B_2$ , the energy of the eigenmotions needs to be reduced. A measurement procedure to quantify the effect of  $B_1$ , one of the main sources of systematic uncertainties, is described in Sec. 4.4.

### 2.2.3 Further shifts

#### Field drifts

Additional to the spatial deviation from the ideal trapping potentials, also a drift in time is possible for both the electric and magnetic fields. A decrease of the magnetic field over time is expected due to the nature of superconducting magnets, e.g. the flux creep effect [And62]. In general, this drift is manageable as long as it is slow compared to the measurement time, e.g. for a determination of the modified cyclotron frequency with the PnP-method (see Sec. 2.5.4), the magnetic field drift needs to be below  $8 \cdot 10^{-10}$  T/h to unambiguously identify the frequency at PENTATRAP, see Sec. 5.4.2.

A drift or fluctuation of the voltage source directly translates to a change in the axial frequency:

$$\frac{\Delta\nu_z}{\nu_z} = \frac{1}{2} \frac{\Delta V_0}{V_0} . \quad (2.27)$$

Due to the nature of the axial frequency measurement, explained in Sec. 4.3.1, a drift or fluctuation of the voltage source is averaged over, leading to a larger uncertainty of the axial frequency. For a determination of the free-space cyclotron frequency on a low  $10^{-10}$  level (the precision achieved with PENTATRAP for one single frequency determination), the axial frequency needs to be known to a relative uncertainty of  $5 \cdot 10^{-8}$  and the voltage source stable to half this level,  $\Delta V/V \leq 2.5 \cdot 10^{-8}$ , over the time of the measurement, see Sec. 3.3.3.

#### Mixed effects of electric and magnetic field

Systematic shifts of the eigenfrequencies can arise due to a misalignment between the trap electrodes, and therefore the electric field, and the magnetic field. This effect can be described by two angles,  $\theta$  and  $\phi$ , and changes the magnetic field to:

$$B_{\text{tilted}}(\theta, \phi) = B_0 \begin{pmatrix} \sin(\theta) \cos(\phi) \\ \sin(\theta) \sin(\phi) \\ \cos(\theta) \end{pmatrix} . \quad (2.28)$$

Additionally, due to manufacturing tolerances or charge patches on the electrodes, the shape of the harmonic electric field can exhibit an elliptic part:

$$\Phi_{\text{ell}}(\vec{r}) = C_2 V_0 \left( z^2 - \frac{x^2 + y^2}{2} - \epsilon \frac{x^2 - y^2}{2} \right) , \quad (2.29)$$

where  $\epsilon$  is the ellipticity parameter. While the eigenfrequencies are shifted by the tilt and the ellipticity,  $\nu_i \rightarrow \bar{\nu}_i(\epsilon, \theta, \phi)$ , it was shown in [BG82] that the invariance theorem

still holds:

$$\nu_c^2 = \bar{\nu}_+^2(\epsilon, \theta, \phi) + \bar{\nu}_z^2(\epsilon, \theta, \phi) + \bar{\nu}_-^2(\epsilon, \theta, \phi) \quad . \quad (2.30)$$

In order to quantify the tilt and ellipticity, this invariant calculation of  $\nu_c$  is compared to the free-space cyclotron frequency  $\bar{\nu}_c$  resulting from the sideband relation given in Eq. (2.10). The difference results in the expression [Gab09]:

$$\bar{\nu}_c - \nu_c = \nu_- \left( \frac{9}{4}\theta^2 - \frac{1}{2}\epsilon^2 \right) \quad . \quad (2.31)$$

By assuming either the ellipticity or the tilt to be zero, an upper limit for the other quantity can be obtained.

### Image charge shift

An ion in the trap induces image charges and, since its moving, an image current in the trap electrodes. While the image current is used to detect the ion's motion and determine the frequency, see Sec. 2.5, the electric field produced by the image charges changes the total electric potential the ion experiences.

The shift can be calculated analytically by approximating the Penning trap with a hollow cylinder [Häf00]. While the axial frequency stays the same, the radial frequencies are shifted by

$$\Delta\nu_{\pm} = \mp \frac{q^2}{16\pi^3\epsilon_0\rho_0^3\nu_c} \quad , \quad (2.32)$$

with  $\epsilon_0$  the vacuum permittivity and  $\rho_0$  the trap radius as shown in Fig. 2.3. Using Eq. (2.11), the resulting shift of the cyclotron frequency can be calculated to:

$$\frac{\Delta\nu_c}{\nu_c} = \left( \frac{\nu_-}{\nu_c} - \frac{\nu_+}{\nu_c} \right) \frac{m}{4\pi\epsilon_0 B_0^2 \rho_0^3} \approx \frac{m}{4\pi\epsilon_0 B_0^2 \rho_0^3} \quad . \quad (2.33)$$

The image charge shift scales with  $1/\rho_0^3$  and, therefore, decreases with a larger trap radius.

In a real Penning trap, the image charge shift cannot be calculated analytically but can be determined with the help of simulations [Sch+19a]. As shown in Sec. 2.3, for the determination of a free-space cyclotron frequency ratio of two ions only the difference in the shift of the cyclotron frequencies is important. The image charge shift only depends on the mass of the ion and, therefore, for the frequency ratio only the mass difference  $\Delta m$  of the two ions is important. With the largest mass difference of  $\Delta m = 2 \text{ u}$  used in any measurement at PENTATRAP so far, this relative shift results in  $\approx 5 \cdot 10^{-12}$  and is below the statistical uncertainty of the respective measurement.

### Relativistic Shifts

The rest mass  $m_0$  of every moving object is increased due to relativistic effects by  $m = m_0/\sqrt{1-(v/c)^2}$ , where  $v$  is the velocity of the object and  $c$  the speed of light. For the fastest motion in the Penning trap, the modified cyclotron motion, the velocity

is  $v_+ \approx \sqrt{2m_0 E_+}$ . The resulting mass increase leads to a shift of the free-space cyclotron frequency:

$$\frac{\Delta\nu_c}{\nu_c} = 1 - \frac{m_0}{m} = 1 - \sqrt{1 - \left(\frac{v_+}{c}\right)^2} \approx \frac{E_+}{m_0 c^2} . \quad (2.34)$$

Usually, as the ion is cooled to a temperature of  $\nu_+/\nu_z \cdot 4$  K (see [Sec. 2.5.3](#)), the energy of the modified cyclotron frequency is only  $\sim 10$  meV. Since the shift is proportional to  $1/m_0$ , it is only larger than  $1 \cdot 10^{-12}$  for ions lighter than  $^{12}\text{C}$ . For all planned measurements at PENTATRAP, and especially the measurements presented here, it is therefore negligible.

### Ion-Ion Interaction

Due to the cylindrical electrodes of the Penning-trap stack, the electric field of an ion leads to Coulomb repulsion between itself and an ion in a neighbouring trap, resulting in a shift of the equilibrium position of the ion of interest. This ion-ion interaction is calculated in [\[Rou12\]](#). Generally, as the electric field and thus the Coulomb repulsion decreases with  $1/r$ , the distance between the ions should be maximised. For the trap center distances of two neighbouring traps of 24 mm at PENTATRAP, even for the case of a single proton being influenced by a charge  $q = 81+$  in the neighbouring trap, this shift is negligible.

## 2.3 Mass measurements in a Penning trap

In a Penning trap all three eigenfrequencies need to be measured to calculate the free-space cyclotron frequency with a relative precision better than  $\delta\nu_c/\nu_c \approx 10^{-10}$ . The uncertainty to which the eigenfrequencies need to be determined depends on the ratio of the eigenfrequency to the free-space cyclotron frequency. Using [Eq. \(2.11\)](#) the uncertainty of the cyclotron frequency can be written as

$$\delta\nu_c = \left[ \underbrace{\left(\frac{\nu_+}{\nu_c} \delta\nu_+\right)^2}_{\approx 1} + \underbrace{\left(\frac{\nu_z}{\nu_c} \delta\nu_z\right)^2}_{\approx 10^{-2}} + \underbrace{\left(\frac{\nu_-}{\nu_c} \delta\nu_-\right)^2}_{\approx 10^{-3}} \right]^{\frac{1}{2}} . \quad (2.35)$$

From here it becomes clear, that in order to determine the cyclotron frequency to a specific uncertainty, the axial eigenfrequency needs to be measured only by a factor of roughly 100 less precise (a factor of 1000 for the magnetron eigenfrequency), while the modified cyclotron frequency needs to be measured to the same uncertainty.

In order to calculate the mass from the cyclotron frequency, additionally the magnetic field and the charge state need to be known. While the elementary charge is fixed in the new SI system to  $1.602176634 \cdot 10^{-19}$  C [\[SI19\]](#), the absolute magnetic field, on the other hand, cannot be determined to the same precision of the free-space cyclotron frequency at the position of the ion in the trap. It can be calibrated, however, with the use of a

second, reference ion, whose cyclotron frequency leads to the magnetic field:

$$B = 2\pi \frac{m_{\text{ref}}}{q_{\text{ref}}} \nu_{c,\text{ref}} \quad . \quad (2.36)$$

The mass of the ion of interest is then:

$$m_{\text{ioi}} = \frac{q_{\text{ioi}}}{2\pi\nu_{c,\text{ioi}}} B = \frac{q_{\text{ioi}} \nu_{c,\text{ref}}}{q_{\text{ref}} \nu_{c,\text{ioi}}} \cdot m_{\text{ref}} = \frac{q_{\text{ioi}}}{q_{\text{ref}}} \frac{1}{R} \cdot m_{\text{ref}} \quad . \quad (2.37)$$

where in the last step the ratio of the two frequencies,  $R = \frac{\nu_{c,\text{ioi}}}{\nu_{c,\text{ref}}}$ , was introduced.

The calculation above assumes a constant magnetic field in time and identical trap settings or simultaneous measurements of the two cyclotron frequencies. Both cases do not reflect the experimental reality, as the fields drift over time and the ion-ion interaction prevents measurements with highly charged ions from reaching the highest precision for simultaneous measurements in the same trap. Instead, at PENTATRAP the two free-space cyclotron frequencies are determined one after the other with a single ion in one trap. Since this requires storage traps, the trap stack consists of five Penning traps, four of which are currently used for measurements.

The left side of Fig. 2.4 shows a measurement procedure with two ions and one measurement trap. First, the cyclotron frequency of ion A is determined at time  $t_1$ , corresponding to position 1 of the ions in the trap stack. Afterwards, the ions are adiabatically transported one trap up. After the measurement of ion B at time  $t_2$ , the ratio of the two frequencies is given by:

$$R_{\text{one trap}} = \frac{\nu_{c,A}}{\nu_{c,B}} = \frac{\frac{q_A}{m_A} B(t_1)}{\frac{q_B}{m_B} B(t_2)} = \frac{q_A m_B}{q_B m_A} \frac{B(t_1)}{B(t_2)} \quad . \quad (2.38)$$

For a precise determination of the ratio  $R$ , the magnetic field change over time should be known. Repeating the measurement process above, e.g. continuously measuring the two cyclotron frequencies alternately, both frequencies exhibit the same time dependence as the magnetic field. During the analysis of the data, the ratio can be determined by fitting the same polynomial function to both sets of frequencies for the two ions to account for the drifting magnetic field. Hereby, one of the two polynomial functions is scaled with a factor  $R$ , which then corresponds to the ratio of the two frequencies. This ratio and a reference ion with a well-known mass  $m_B$  can then be used to determine the mass difference of the ion of interest and the reference ion, see Sec. 5.8. More details about the polynomial method are given in Sec. 5.7.1.

Unique for PENTATRAP are the five traps as shown in Fig. 2.4. These allow for simultaneous measurements in several traps, as the measurement scheme on the right side shows. Instead of two ions, three are loaded into the traps, with the first and the last being the reference ion. Using the same analysis as described above, this measurement scheme would simply lead to a factor of two in the number of data points during the same time interval as compared to using just one measurement trap. Another possibility

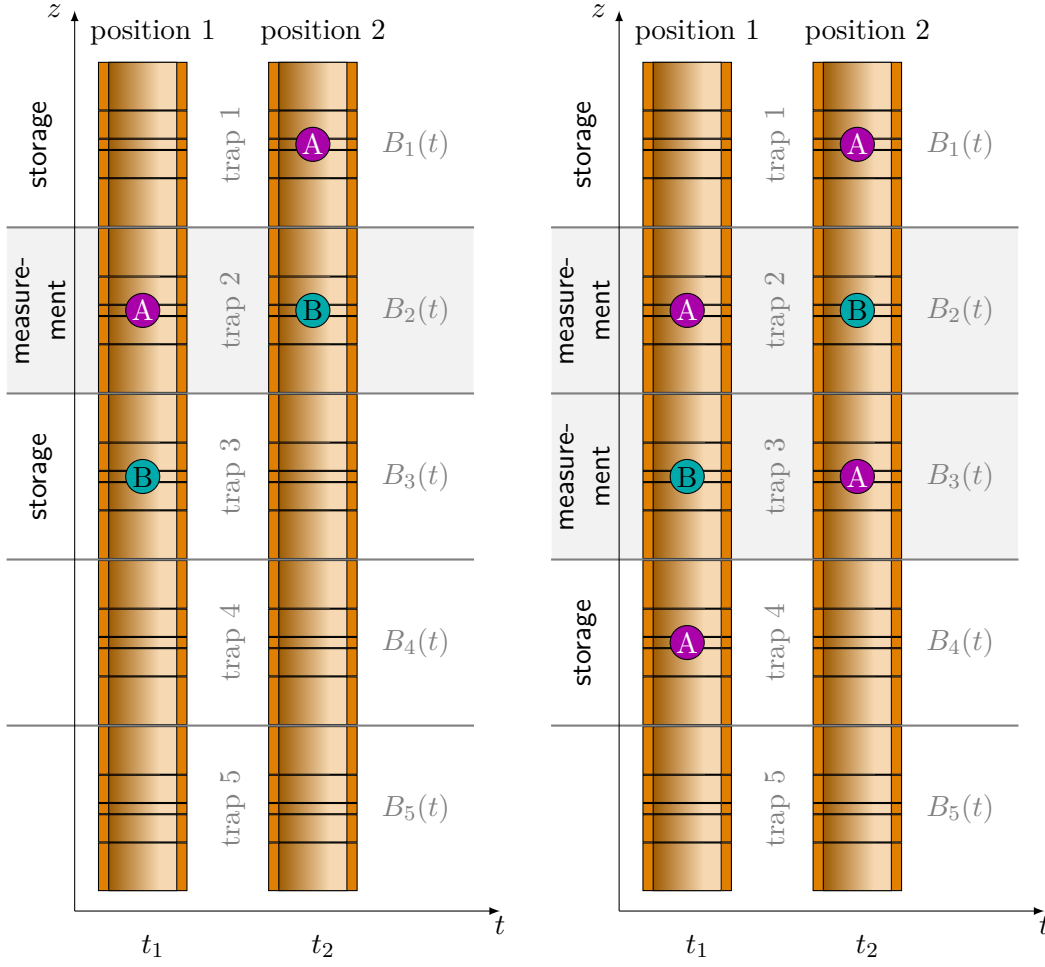


**Figure 2.4:** Two possible measurement schemes at PENTATRAP. **Left:** Using one trap for measuring the free-space cyclotron frequency and the two neighbouring traps for storage. The cyclotron frequency ratio is determined by shifting ions one trap up or down after one measurement. This defines the position of the ions in the traps. **Right:** Three ions in the traps allow simultaneous determinations of cyclotron frequency ratios in two traps, here trap 2 and 3. Again, the adjacent traps are used for storage inbetween measurements.

is to combine the measurements at the same time, in this case  $t_1$ , to a ratio of the two cyclotron frequencies:

$$R(t_1) = \frac{\nu_2^A(t_1)}{\nu_3^B(t_1)} = \frac{q^A m^B B_2(t_1)}{q^B m^A B_3(t_1)}, \quad (2.39)$$

where the index 2 and 3 refer to the trap in which the cyclotron frequency was measured (for legibility the index  $c$  of  $\nu_c$  was dropped). After shifting the ions one trap up, the

ratio at time  $t_2$  reads:

$$R(t_2) = \frac{\nu_2^B(t_2)}{\nu_3^A(t_2)} = \frac{q^B m^A B_2(t_2)}{q^A m^B B_3(t_2)} . \quad (2.40)$$

Assuming the magnetic fields in the two traps to drift over time, but exhibiting constant ratios,  $B_2/B_3 = \text{const.}$ , the two ratios can be combined to:

$$R_{\text{cancel}} = \sqrt{\frac{R(t_1)}{R(t_2)}} = \frac{q^A m^B}{q^B m^A} \sqrt{\frac{B_2(t_1) B_3(t_2)}{B_3(t_1) B_2(t_2)}} = \frac{q^A m^B}{q^B m^A} , \quad (2.41)$$

leading to a cancellation of the magnetic field influence. A comparison of the two methods, the polynomial and the cancellation, is performed in [Sec. 7.3](#).

Systematic shifts of the free-space cyclotron frequency also affect the ratio of the two frequencies. Assuming the shifts  $\Delta\nu_1$  and  $\Delta\nu_2$  for two cyclotron frequencies  $\nu_1$  and  $\nu_2$ , respectively, results in a shift of the ratio:

$$\begin{aligned} \Delta R &= \frac{\nu_1 + \Delta\nu_1}{\nu_2 + \Delta\nu_2} - \frac{\nu_1}{\nu_2} \\ &\approx \frac{\nu_1}{\nu_2} \left( \frac{\Delta\nu_1}{\nu_1} - \frac{\Delta\nu_2}{\nu_2} \right) , \end{aligned} \quad (2.42)$$

where second order terms were dropped. Already for a shift on the order of  $\Delta\nu_c/\nu_c \approx 10^{-6}$ , higher-order terms do not influence the frequency ratio above  $10^{-12}$  any more. Only the difference of the shift for both cyclotron frequencies needs to be known in order to correct the ratio. The effect of the shifts discussed in [Sec. 2.2](#) on the frequency ratio will be shown in [Sec. 6.1.3](#).

## 2.4 Manipulation of the eigenmotions

The ion's motion can be manipulated by irradiating a radiofrequency field (*rf*-field) using one of the trap electrodes. Depending on which trap electrode and frequency is used, the eigenmotions can either be excited by applying a dipolar field at the eigenfrequency of the motion or energy can be transferred between two modes with a quadrupolar field if the frequency of the drive is equal to the sum or difference frequency of the two coupled modes.

### Excitation of the modes

The three eigenmotions can be excited by applying a resonant *rf*-drive to one of the trap electrodes such that the electric field points in the direction of the specific motion. In the case of the axial motion, the drive can be written as:

$$\vec{E}_{\text{exc}} = e_0 \sin(2\pi\nu_{rf}t) \begin{pmatrix} 0 \\ 0 \\ z \end{pmatrix} , \quad (2.43)$$

where  $e_0$  is the amplitude of the excitation. If the drive is resonant,  $\nu_{rf} = \nu_z$ , the amplitude of the axial motion is increased during the time the *rf*-drive is applied to the trap. This can be used to clean the trap of unwanted ion species, see [Sec. 4.2](#), by exciting their motion until they escape the trapping potential. In general, it can also be used to imprint a phase to one of the motions when applying the *rf*-pulse for a certain time.

### Coupling of the modes

Applying a quadrupolar field to the trap allows coupling and exchanging energy between two eigenmotions. As the quadrupolar field needs to point in both directions of the motions, for a coupling including the axial motion it is applied to a split trap electrode. The coupling between, for example, modified cyclotron and axial mode can be expressed by:

$$\vec{E}_{\text{couple}} = c_0 \cos(2\pi\nu_{\text{couple}}t) \begin{pmatrix} z \\ 0 \\ x \end{pmatrix}, \quad (2.44)$$

with  $\nu_{\text{couple}} = \nu_+ - \nu_z$  the resonant coupling frequency of the two modes and  $c_0$  the amplitude.

In order to describe the two processes mathematically, the Green's function treatment of a harmonic oscillator and coupled modes, as well as the rotating wave approximation can be used. Following such a calculation in [[Höc16](#)], the general solutions to the equations of motion for both the axial  $z(t)$  and the modified cyclotron motion  $x_+(t)$  for near-resonant coupling are given by:

$$\begin{aligned} x_+(t) &= A_0 e^{i\Omega t} + A_1 e^{-i\Omega t} \quad \text{and} \\ z(t) &= c_0^* (-A_0 e^{i\Omega t} + A_1 e^{-i\Omega t}) \quad , \end{aligned} \quad (2.45)$$

where the prefactors  $A_0$  and  $A_1$  are defined by the conditions before the coupling pulse. The factor  $c_0^*$  is hereby proportional to the strength of the coupling pulse,  $c$ , and the eigenfrequencies of the motions to be coupled. The frequency  $\Omega$  is defined by

$$\Omega = \frac{c_0 q}{4 m} \frac{1}{\sqrt{\omega_z(\omega_+ - \omega_-)}} \quad . \quad (2.46)$$

The energy in the modified cyclotron mode, which is proportional to

$$|X_+(t)|^2 = |A_0|^2 + |A_1|^2 + 2\Re(A_0 A_1^* e^{i2\Omega t}) \quad , \quad (2.47)$$

oscillates with the Rabi frequency  $2\Omega$ . When a coupling drive is on, the energy in both modes is thereby transferred from one mode to the other and back. This fact is used in the determination of the modified cyclotron frequency, see [Sec. 2.5.4](#).

## 2.5 Ion motion detection

At PENTATRAP, the ion's eigenfrequencies are determined by a non-destructive image current detection technique, where the current induced in the trap electrodes by the

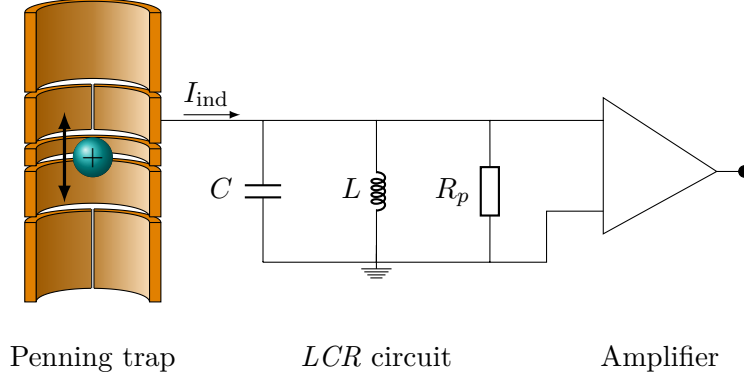


**Figure 2.5:** Basic principle of the image current detection method. The ion in the trap induces the image current  $I_{\text{ind}}$  into the trap electrodes. A resonant  $LCR$  circuit picks up the current and transfers it to a measurable voltage, which is amplified.

ion's motion is determined. At the same time, this technique cools the ion's motions to the temperature of the detection system. Usually, only the axial frequency is directly measured, while the radial motions are coupled to the axial to be determined.

### 2.5.1 Induced image current

In order to quantify the induced current in the trap electrodes and the effect on the ion, the trap can be modelled as an infinitely extended parallel plate capacitor. The current induced in the plates by an ion oscillating with velocity  $\dot{\rho}_i$  is given by [Sho38; Ram39]:

$$I_{\text{ind}}(t) = \frac{q}{D_i} \dot{\rho}(t) = 2\pi\nu_i \frac{q}{D_i} \rho_i(t) \quad . \quad (2.48)$$

$D_i$  is the distance between the plates. For a cylindrical Penning trap, the distance can be considered as an effective electrode distance  $D_{\text{eff}}$ . The index  $i \in (+, z, -)$  refers to any of the three eigenmotions. In the following only the axial motion,  $i = z$ , will be investigated.

The main parts of the detection system are shown in Fig. 2.5. The induced current in the trap electrodes is transferred to a measurable voltage by an effective resistance with impedance  $Z_{\text{det}}$ ,

$$U_{\text{ind}} = Z_{\text{det}} I_{\text{ind}} \quad , \quad (2.49)$$

and afterwards amplified. Usually, this impedance consists of a parallel  $LCR$  circuit realised by a superconducting coil with inductance  $L$  in a housing, therefore also called a resonator. The total capacitance  $C$  of the system consists of the trap capacitance, the parasitic capacitance of the coil and that of the wiring. The resonance frequency of the tank circuit is

$$\nu_R = \frac{1}{2\pi\sqrt{LC}} \quad , \quad (2.50)$$

while possible resistive contributions are taken into account by the resistance

$$R_p = 2\pi\nu_R L Q \quad . \quad (2.51)$$

The quality factor  $Q$  of a tank circuit is defined by the ratio of stored electromagnetic energy to energy loss per cycle. Experimentally more accessible is the definition by:

$$Q = \frac{\nu_R}{\Delta\nu_R} \quad , \quad (2.52)$$

where  $\Delta\nu_R$  is the width of the resonance curve 3 dB below the maximum. The impedance  $Z_{\text{det}}$  of a parallel  $LCR$  circuit is then easily calculated:

$$\begin{aligned} Z_{\text{det}}(\nu) &= \left( \frac{1}{Z_L} + \frac{1}{Z_C} + \frac{1}{Z_R} \right)^{-1} \\ &= \left( \frac{1}{i2\pi\nu L} + i2\pi\nu C + \frac{1}{R_P} \right)^{-1} \\ &= R_P \left( 1 + iQ \left( \frac{\nu}{\nu_R} - \frac{\nu_R}{\nu} \right) \right)^{-1} \quad . \end{aligned} \quad (2.53)$$

On resonance,  $\nu = \nu_R$ , the imaginary part evaluates to zero and the impedance is equal to the resistance.

The measurable electronic signal of the tank circuit is the thermal Johnson-Nyquist noise [Joh28; Nyq28]. For any electric conductor with resistance  $R$  it is given by the root-mean-squared voltage at the frequency bandwidth  $\Delta\nu$

$$u_{th} = \sqrt{4k_B T R \Delta\nu} \quad , \quad (2.54)$$

with the Boltzmann constant  $k_B$  and the temperature  $T$  of the tuned circuit. For the resonator,  $R = \Re(Z_{\text{det}})$ , the measurable signal is

$$u_{res} = \sqrt{\frac{4k_B T R_P \Delta\nu}{1 + Q^2 \left( \frac{\nu}{\nu_R} - \frac{\nu_R}{\nu} \right)^2}} \quad . \quad (2.55)$$

A resonance curve is then obtained by performing a fast Fourier transformation (FFT) of  $u_{res}$  recorded for a certain time.

The connection of the parallel tank circuit to the trap electrode leads to a damping term in the equation of motion for the axial mode, which results from the voltage drop over trap electrodes. The additional field creates the force

$$F_{\text{ind}} = \frac{q}{D_{\text{eff}}} U_{\text{ind}} = Z_{\text{det}} \frac{q^2}{D_{\text{eff}}^2} \dot{z} \quad (2.56)$$

at the position of the ion. The equation of motion of the axial mode is, therefore, changed to:

$$\ddot{z}(t) + \underbrace{\frac{q^2 Z_{\text{det}}}{m D_{\text{eff}}^2}}_{\gamma} \dot{z}(t) + (2\pi\nu_z)^2 z(t) = 0 \quad , \quad (2.57)$$

where the complex damping constant  $\gamma$  was introduced. Both, the real and the imaginary part of  $\gamma$  influence the motion of the ion:

**Resistive cooling:** The real part leads to a resistive cooling of the ion's motion until it is in thermal equilibrium with the  $LCR$  circuit. The cooling time constant

$$\tau(\nu) = \frac{1}{\Re(\gamma)} = \frac{m}{\Re(Z_{\det}(\nu))} \frac{D_{\text{eff}}^2}{q^2} \quad (2.58)$$

is smallest for the highest impedance, i.e. at resonance  $\nu = \nu_R$ .

**Image current shift:** Due to the imaginary part of the impedance the eigenfrequency is shifted by [Nat93]:

$$\begin{aligned} \Delta\nu_z^{IC} &= \frac{\delta_R \delta_z}{4} \frac{\nu_z - \nu_R}{(\nu_z - \nu_R)^2 + \delta_R^2/4} \\ &\approx \frac{\delta_z}{\delta_R} (\nu_z - \nu_R) = \frac{2Q^2 L q^2}{m D_{\text{eff}}^2} (\nu_z - \nu_R) \quad , \end{aligned} \quad (2.59)$$

where a small detuning  $\nu_z \approx \nu_R$  was assumed.  $\delta_R = \nu_R/2Q$  and  $\delta_z = 1/\tau(\nu_R)$  are the resonators and ions damping constants for a small detuning, respectively. The shift depends on the detuning of the ion's frequency from the resonator frequency,  $\nu_z - \nu_R$ . For a  $^{187}\text{Re}^{29+}$  ion this shift evaluates to  $1.3\%(\nu_z - \nu_R)$  and is for typical frequencies and settings at PENTATRAP negligible.

## 2.5.2 Ion signal - Dip spectrum

The equation of motion given in Eq. (2.57) for an ion cooled to thermal equilibrium with the resonator can be rewritten in terms of the induced current  $I_{\text{ind}}$ :

$$\frac{m D_{\text{eff}}^2}{q^2} \ddot{I}_{\text{ind}} + Z_{\det} \dot{I}_{\text{ind}} + (2\pi\nu_z)^2 \frac{m D_{\text{eff}}^2}{q^2} I_{\text{ind}} = 0 \quad . \quad (2.60)$$

Comparing Eq. (2.60) with a differential equation of a series  $LCR$  circuit:

$$L\ddot{I} + R\dot{I} + \frac{1}{C}I = 0 \quad (2.61)$$

allows identifying an effective capacitance,  $C_{\text{ion}}$ , and inductance,  $L_{\text{ion}}$ , of the ion:

$$C_{\text{ion}} = \frac{q^2}{(2\pi\nu_z)^2 m D_{\text{eff}}^2} \quad \text{and} \quad L_{\text{ion}} = \frac{m D_{\text{eff}}^2}{q^2} \quad , \quad (2.62)$$

while the resistance is equal to the impedance of the tank circuit,  $R = Z_{\det}(\nu)$ . The ion equivalent circuit is shown in Fig. 2.6.

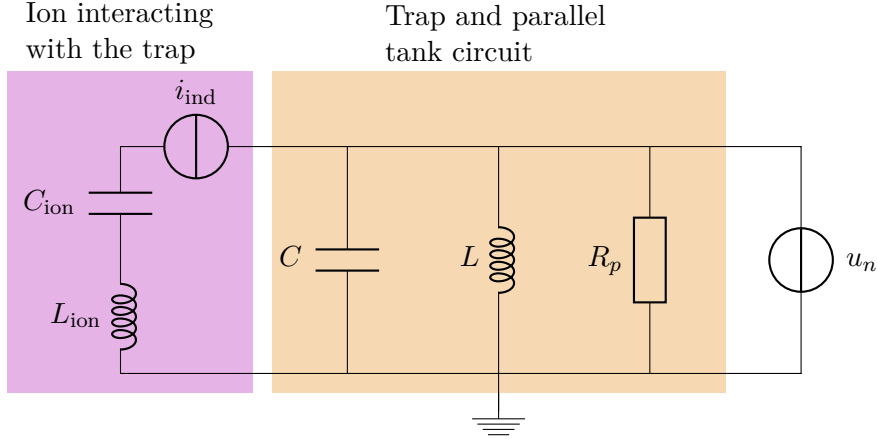


**Figure 2.6:** Ion equivalent circuit. In the trap the ion can be modelled by a series  $LC$ -circuit with inductance  $L_{\text{ion}}$  and capacitance  $C_{\text{ion}}$ . The trap and the connected resonator behave as an  $LCR$  circuit. Adapted from [Köh15].

The resonance frequency of the series  $LC$  circuit of the ion is the axial eigenfrequency,  $\nu_z = 1/2\pi\sqrt{L_{\text{ion}}C_{\text{ion}}}$ . The combined effective resistance of the ion in the trap and the tank circuit results in:

$$\begin{aligned} Z_{\text{dip}} &= \left[ \frac{1}{R} + \left( i2\pi\nu L_{\text{ion}} + \frac{1}{i2\pi\nu C_{\text{ion}}} \right)^{-1} \right]^{-1} \\ &= \underbrace{\left[ \frac{1}{R_p} + \frac{iQ}{R_p} \left( \frac{\nu}{\nu_R} - \frac{\nu_R}{\nu} \right) \right]^{-1}}_{1/Z_{\text{det}}} + \underbrace{\frac{i}{2\pi\nu\tau R_p} \left( \frac{\nu_z^2}{\nu^2} - 1 \right)^{-1}}_{1/Z_{\text{ion}}} \end{aligned}, \quad (2.63)$$

where the cooling time constant at the resonator frequency  $\tau = \tau(\nu_R) = L_{\text{ion}}/R_p$  was used. In contrast to the parallel  $LCR$  circuit, the impedance of a series  $LC$  circuit has a minimum at the resonance frequency. The total impedance of the tank circuit and the ion, therefore, consists of the resonance curve of the tank circuit produced by the thermal noise of the real part of the resonator impedance with a sharp dip at the frequency of the ion.

Similar to Eq. (2.55), the measurable signal of the ion in the trap is given by the thermal noise of the combined impedance

$$u_{\text{dip}} = \sqrt{4k_B T \Re(Z_{\text{dip}}) \Delta\nu}, \quad (2.64)$$

where the real part of the combined effective impedance of the ion in the trap and the parallel tank circuit is given by

$$\Re(Z_{\text{dip}}) = \frac{R_p}{1 + \left[ \frac{\nu}{2\pi\tau(\nu^2 - \nu_z^2)} - Q \left( \frac{\nu}{\nu_R} - \frac{\nu_R}{\nu} \right) \right]^2}. \quad (2.65)$$

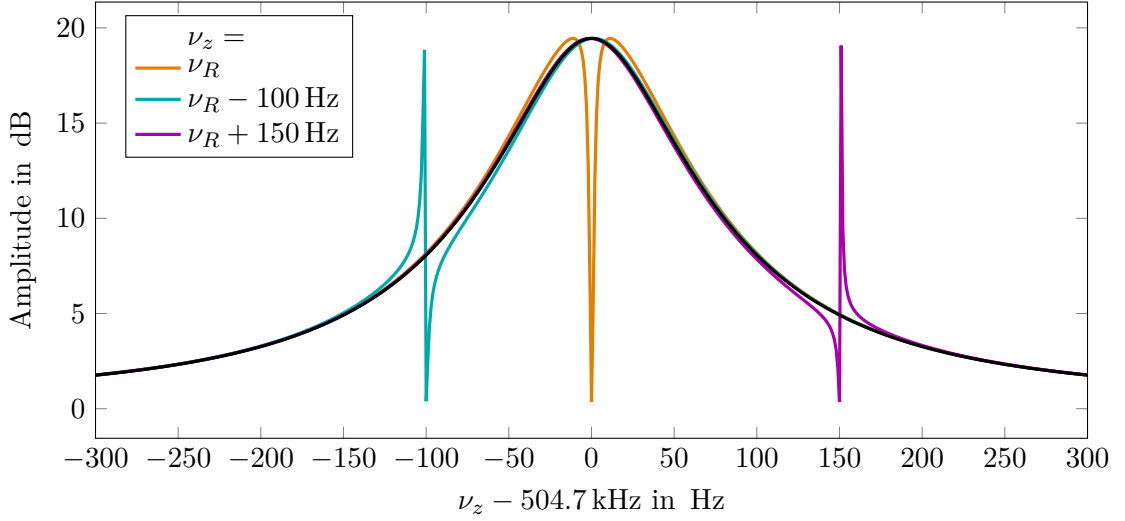


**Figure 2.7:** For three different values of the axial eigenfrequency  $\nu_z$  a simulated dip spectrum is shown. The further the ion's axial frequency deviates from the resonator frequency, the more its dispersive manner is noticeable. The black curve shows the resonance curve of the resonator without an ion in the trap for a quality factor of  $Q = 5000$ . The frequency of  $\approx 504.7$  kHz corresponds to the resonance frequency of the detection system in trap 3.

By recording such a resonator spectrum with an axial dip and fitting the theoretical curve given by Eq. (2.64), the axial frequency can be obtained. In Fig. 2.7 a simulated spectrum for three different axial frequencies, one on resonance with the  $LCR$  circuit, one shifted by 100 Hz to lower frequencies and one shifted to higher by 150 Hz, is shown. The black curve corresponds to the resonator without an ion as described by Eq. (2.55). If the axial frequency deviates from the resonance frequency of the resonator, a dispersive manner of the dip is observed as it also exhibits a peak structure. If it is even further off, the dip will completely turn into a peak. Even though the dip form changes, the axial frequency can still be recovered by a fit of Eq. (2.64) to the spectrum. Hereby, the axial dip width

$$\delta\nu_z = \frac{N_{\text{ion}}}{2\pi} \frac{1}{\tau} = \frac{N_{\text{ion}}}{2\pi} \frac{R_p q^2}{m D_{\text{eff}}^2} \quad (2.66)$$

helps in determining the number of ions  $N_{\text{ion}}$  in the trap. This method to determine the axial frequency has the advantage that the ion is cooled to small oscillation amplitudes and is, therefore, less prone to systematic shifts.

### 2.5.3 Detection of the radial modes

As shown in Sec. 2.4 the application of a quadrupolar  $rf$ -field can be used to couple two motional modes, which leads to a periodic transfer of energy from one mode to the

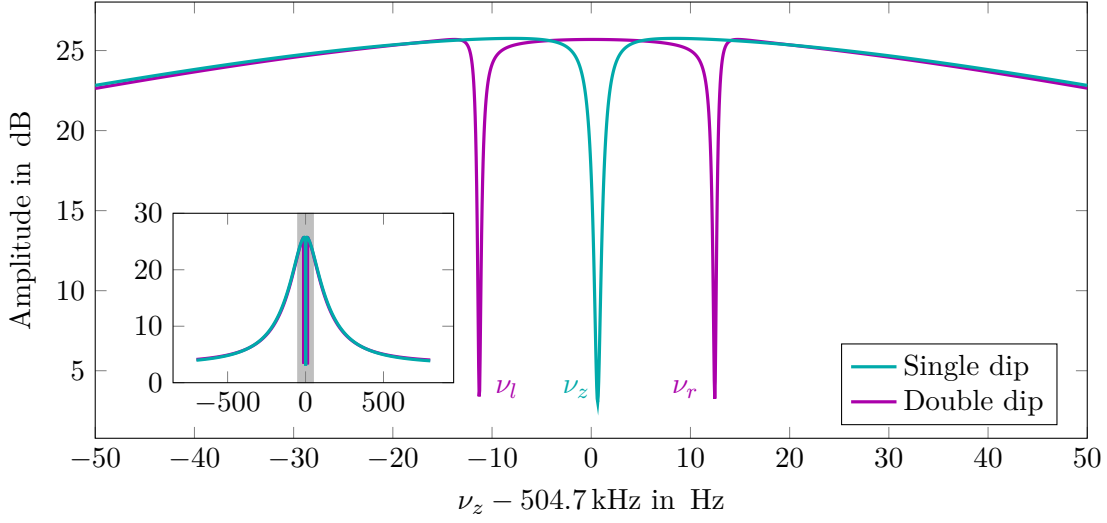


**Figure 2.8:** Due to a coupling pulse, the single axial dip at  $\nu_z$  (blue) splits into two dips (magenta) at  $\nu_{l,r}$ . Here, the frequency of the coupling pulse is not detuned and the double dips are symmetric around the single dip. The inset shows the full resonator spectrum with the gray area marking the region of the double dips. The same resonator settings as in Fig. 2.7 were chosen.

other. Here, the coupling of the radial modes to the axial modes has two effects, first, the cooling of the radial modes and, second, the detection of their frequencies.

### Sideband cooling

The energy transferred to the axial mode is directly dissipated by the tank circuit until the average number of motional quanta in both coupled modes is the same:  $\langle n_{\pm} \rangle = \langle n_z \rangle$  [BG86]. The final achievable temperature is therefore

$$T_{\pm} = \frac{\nu_{\pm}}{\nu_z} T_z \quad . \quad (2.67)$$

While the axial mode is in direct contact with the liquid helium at 4.2 K via the tank circuit, temperatures of 53 mK and 80 K are achievable for the magnetron and modified cyclotron motion, respectively. An additional resonator at the modified cyclotron frequency would allow cooling the motions further down, as the achievable temperatures are then scaled with  $\nu_{-,z}/\nu_+$ .

### Double dip

The coupling to the axial frequency leads to a splitting of the detected axial signal, e.g. the dip in the resonator spectrum, into two signals. The two dips appear at the

frequencies  $\nu_{l,r} = \nu_z + \epsilon_{l,r}$ , see Fig. 2.8, with [Ulm11]:

$$\epsilon_{l,r} = -\frac{1}{2} \left( \delta \pm \sqrt{(2\Omega)^2 + \delta^2} \right) . \quad (2.68)$$

Here,  $\delta$  is the detuning of the couple pulse frequency to the true coupling frequency:

$$\nu_{rf,\pm} = \nu_{\pm} \mp \nu_z + \delta . \quad (2.69)$$

The difference in sign for the coupling of the magnetron and modified cyclotron motion to the axial arises from the metastable nature of the magnetron motion. The distance of the two dips can be increased by a larger amplitude of the coupling field, as the Rabi frequency  $2\Omega$ , see Eq. (2.46), is proportional to the amplitude.

The Rabi splitting of the dips can mathematically be described by two ions in the trap with the axial frequencies  $\nu_{l,r}$ . Thus, following Eq. (2.63), the overall effective impedance of the system is given by:

$$\begin{aligned} Z_{\text{double}} &= \left[ \frac{1}{Z_{\text{det}}} + \frac{1}{Z_{\text{ion1}}} + \frac{1}{Z_{\text{ion2}}} \right]^{-1} \\ &= R_p \left[ 1 + iQ \left( \frac{\nu}{\nu_R} - \frac{\nu_R}{\nu} \right) + \frac{i}{2\pi\nu\tau_l} \left( \frac{\nu_l^2}{\nu^2} - 1 \right)^{-1} + \frac{i}{2\pi\nu\tau_r} \left( \frac{\nu_r^2}{\nu^2} - 1 \right)^{-1} \right]^{-1} . \end{aligned} \quad (2.70)$$

The dip widths, proportional to the cooling time constants  $1/\tau_l$  and  $1/\tau_r$  of the left and the right dip, respectively, are a factor of two smaller than that of the single axial dip. Again, the measured spectrum can be described by the noise

$$u_{\text{double}} = \sqrt{4k_B T \Re(Z_{\text{double}}) \Delta\nu} . \quad (2.71)$$

In Fig. 2.8 such a double dip spectrum is shown together with the single dip spectrum. The coupling pulse was chosen to be on resonance, leading to symmetric dips (magenta) around the single dip (blue).

From the position of the two dips the magnetron or the modified cyclotron frequency can be calculated by:

$$\nu_l + \nu_r = 2\nu_z - \delta = \nu_z \mp \nu_{rf} \pm \nu_{\pm} . \quad (2.72)$$

Assuming the frequencies of all dips,  $\nu_z$  and  $\nu_{l,r}$ , can be measured to the same uncertainty, the radial frequencies are determined to the uncertainty of  $\sqrt{3}\delta\nu_z$ . While this uncertainty is sufficient for the magnetron eigenfrequency, the modified cyclotron frequency could thereby only be determined to a relative precision of  $\delta\nu_+/\nu_+ \approx 2 \cdot 10^{-9}$ . In order to improve this limitation in precision, the modified cyclotron eigenfrequency is measured with the PnP-method explained in the next section.

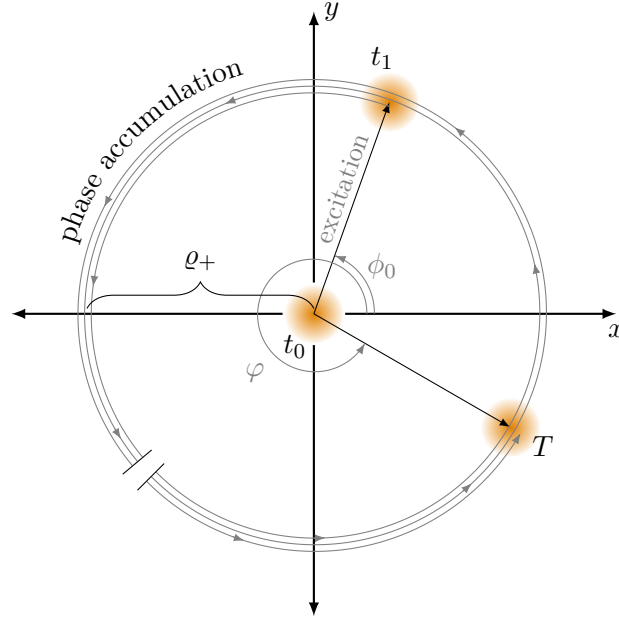


**Figure 2.9:** Evolution of the modified cyclotron motion after an excitation pulse, setting the starting phase  $\phi_0$  at time  $t_1$ . After an accumulation time, here shown exemplary with three rotations, the motion has acquired the phase  $2\pi N + \varphi$  at time  $T$ .

#### 2.5.4 PnP-method

For a more precise measurement of an eigenfrequency, its phase can be determined, as the frequency corresponds to a phase evolution in a given time interval. Even if the phase can only be obtained with a 10% uncertainty, this leads to an increased precision of the frequency determination by a factor of 10. As the modified cyclotron frequency needs to be determined most precisely, the so-called PnP-method (PnP  $\hat{=}$  Pulse and Phase) [Cor+89] is employed for its determination.

After an excitation pulse at time  $t_0$ , increasing the radius of the modified cyclotron motion to  $\varrho_+$ , its amplitude can be expressed by

$$\vec{\rho}_+(t) = \varrho_+ \begin{pmatrix} \cos(2\pi\nu_+t + \phi_0) \\ \sin(2\pi\nu_+t + \phi_0) \\ 0 \end{pmatrix}, \quad (2.73)$$

with the starting phase  $\phi_0$ . The phase evolution after excitation is shown in Fig. 2.9.

After certain time  $T$  the amplitude of the motion in  $x$ -direction is given by:

$$x_+(T) = \varrho_+ \cos(2\pi\nu_+T + \phi_0) = \varrho_+ \cos(\phi(T)) \quad (2.74)$$

where  $\phi(T)$  is the total phase. While the expression  $\nu_+T$  usually evaluates to values larger than  $2\pi$ , the measurable quantity,  $\varphi$ , lies in the interval of 0 and  $2\pi$ . The phase

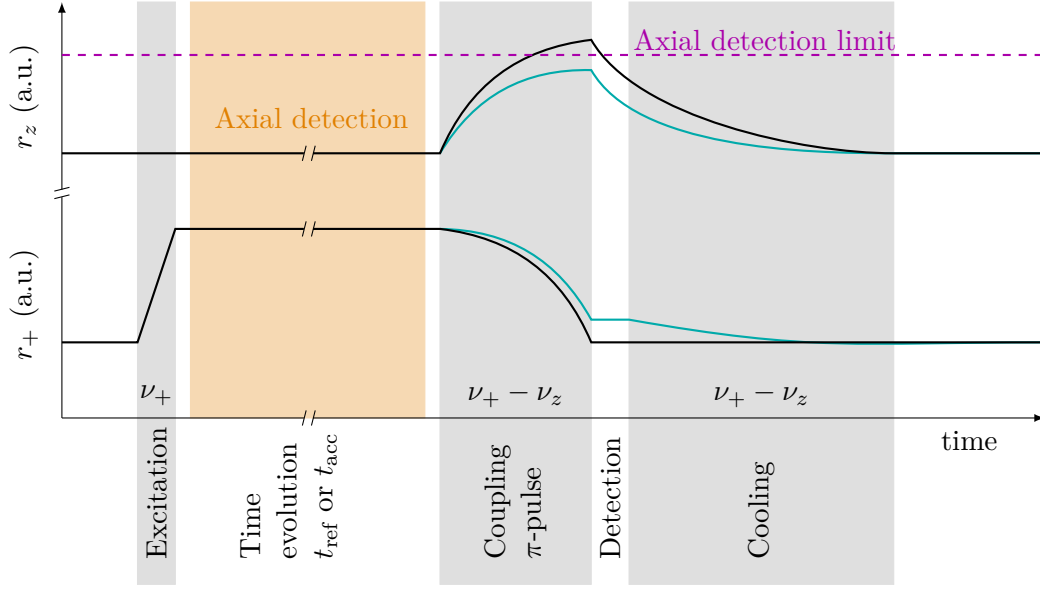


**Figure 2.10:** An overview of the changes in radii during a PnP-measurement. In the first step, the modified cyclotron radius is excited to a larger orbit (excitation) and the phase is evolving during the following time evolution period. A  $\pi$ -pulse afterwards couples the modified cyclotron to the axial mode, which then makes it possible to readout the phase (detection). Lastly, the two modes are cooled. The blue lines correspond to a coupling pulse deviating from a  $\pi$ -pulse. During the long phase evaluation time  $t_{\text{acc}}$  an axial spectrum is recorded (axial detection).

at time  $T$  can, therefore, be divided into:

$$\phi(T) = 2\pi\nu_+T + \phi_0 = 2\pi N_T + \varphi \quad . \quad (2.75)$$

$N_T$  is the number of full revolutions performed during time  $T$ . The starting phase  $\phi_0$  is unknown but cancels out as only the measurable phase difference between two times  $T_a$  and  $T_b$  is of interest:

$$\begin{aligned} \Delta\varphi = \varphi_a - \varphi_b &= 2\pi\nu_+T_a + \phi_0 - 2\pi N_a - (2\pi\nu_+T_b + \phi_0 - 2\pi N_b) \\ &= 2\pi\nu_+\Delta t - 2\pi N \quad , \end{aligned} \quad (2.76)$$

with  $N = N_a - N_b$  and  $\Delta t = T_a - T_b$ . By measuring two phases, the modified cyclotron frequency can be calculated using:

$$\nu_+ = \frac{1}{2\pi} \frac{\Delta\varphi + 2\pi N}{\Delta t} \quad . \quad (2.77)$$

The main steps of such a measurement are shown in Fig. 2.10. They are performed for both a short, reference time  $T_a = t_{\text{ref}}$ , and a long accumulated time  $T_b = t_{\text{acc}}$ :

1. **Excitation:** The cooled modified cyclotron motion is excited by a dipole excitation, as described by Sec. 2.4. Thereby, the radius is increased to  $\varrho_+$  and the starting phase  $\phi_0$  is defined by the applied  $rf$ -pulse and its length. For both times,  $T_a$  and  $T_b$ , the settings for the excitation pulse need to be identical.
2. **Phase accumulation:** The excited motion evolves for a time  $T_b = t_{acc} = 40.05$  s. New to this scheme is the simultaneous axial frequency determination during the long phase accumulation time. A spectrum exhibiting a single dip is recorded, such that a later fit to the data allows determining the axial frequency. Due to this simultaneous measurement, possible drifts in the fields affect both motions alike, leading to a smaller systematic uncertainty. During the reference time  $t_{ref} = 0.1$  s no spectrum is recorded.
3. **Coupling:** A quadrupolar electric field applied for the time  $t_\pi = \pi/2\Omega$  couples the modified cyclotron motion to the axial motion. This  $\pi$ -pulse transfers the phase and the amplitude of the modified cyclotron motion to the initially cooled axial mode, whose phase is not defined.
4. **Detection:** The phase is measured as the phase of the axial mode by determining the phase of the FFT signal at the position of the axial dip (for details, see Sec. 5.4.1). If the coupling pulse is too far detuned, as shown by the blue line in Fig. 2.10, the signal in the axial mode is too small, i.e. below the noise level, and the phase cannot be readout.
5. **Cooling:** Both modes are cooled, the axial by direct contact to the detection system, the modified cyclotron by again coupling both modes for a longer time (longer than the cooling time constant).

The effect of the coupling  $\pi$ -pulse on the modes can be understood by looking at the result of a coupling pulse on the modes as described in Eq. (2.45). Setting  $t = 0$  before the coupling pulse is applied, the cyclotron mode is at its excited radius,  $\varrho_+$ , and has accumulated the phase  $\varphi$ , whereas the axial mode can be seen as having 0 radius, as it is cooled down. The solutions to the equations of motions thus become:

$$\begin{aligned} x_+(0) &= A_0 + A_1 &= \varrho_+ e^{i\varphi} \\ z(0) &= c_0^*(-A_0 + A_1) = 0 \quad . \end{aligned} \quad (2.78)$$

From the second equation follows  $A_0 = A_1$  and, therefore,  $A_0 = 1/2\varrho_+ e^{i\varphi}$ . After the coupling pulse has been applied for the time  $t_\pi = \frac{\pi}{2}\frac{1}{\Omega}$  the amplitudes have changed to

$$\begin{aligned} x_+(t_\pi) &= i(A_0 - A_1) &= 0 \\ z(t_\pi) &= -ic_0^*(A_0 + A_1) = -ic_0^*\varrho_+ e^{i\varphi} \\ &= c_0^*\varrho_+ e^{i\varphi} e^{i\frac{3}{2}\pi} \quad . \end{aligned} \quad (2.79)$$

For an ideal  $\pi$ -pulse the energy of the cyclotron mode is now completely transferred to the axial mode. The phase is also transferred from one to the other mode, but the

prefactor  $-i$  gives a phase shift of  $\frac{3}{2}\pi$  when comparing the cyclotron phase before the pulse to the axial phase afterwards. As shown in Eq. (2.76), this constant offset will cancel out. The same argument holds for the phase of the coupling pulse, which drops out in rotating-wave approximation, but is kept constant in the function generator.

Experimentally, the  $\pi$ -pulse depends on the strength of the quadrupolar field, i.e. the voltage applied to the Penning trap electrodes, and the duration it is applied. For a non-perfect coupling pulse,  $t_{\pi+x} = \frac{\pi}{2} \frac{1}{\Omega} + x$ , arising from either a shifted frequency or a wrong pulse length, the amplitude of the axial mode after coupling is modulated with the offset  $x$ :

$$\begin{aligned} z(t_{\pi+x}) &= c_0^* \varrho_+ e^{i\varphi} (-e^{i\Omega(\frac{\pi}{2} \frac{1}{\Omega} + x)} + e^{-i\Omega(\frac{\pi}{2} \frac{1}{\Omega} + x)}) \\ &= c_0^* \varrho_+ e^{i\varphi} e^{i\frac{3}{2}\pi} \cos(\Omega x) \quad . \end{aligned} \quad (2.80)$$

The phase is not affected, but the amplitude of the axial mode decreases if  $x \neq 0$ . For example, for the blue line in Fig. 2.10, not the complete energy is transferred and the axial amplitude stays below the detection limit.

# 3

---

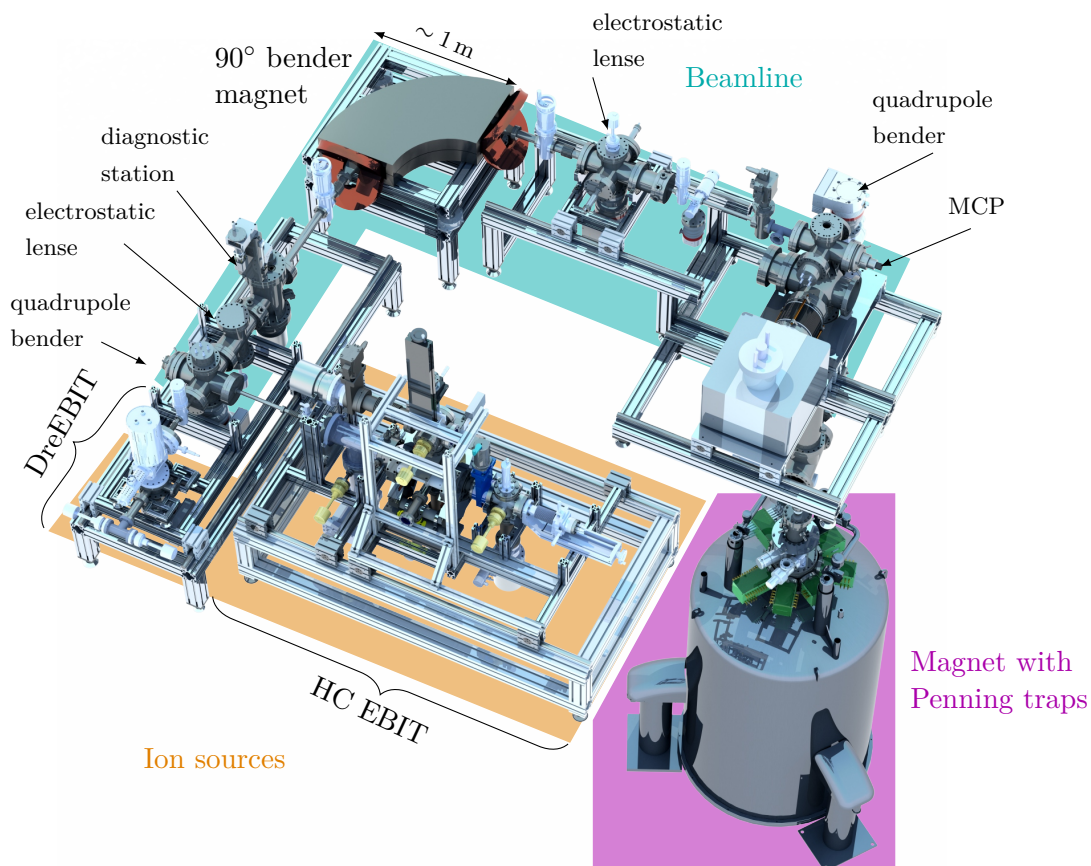
## The High-Precision Mass Spectrometer PENTATRAP

---

High-precision mass measurements of highly charged ions (HCIs) require an experimental setup for the production and selection of the ions, as well as to provide sufficiently long storage times in an as good as possible vacuum in the Penning traps. The PENTATRAP vacuum setup can be separated into three parts: 1) the production of HCIs inside an electron beam ion trap (EBIT), 2) the beamline components to select, decelerate, and efficiently transport the ions to 3) the Penning traps inside the cold bore of a superconducting magnet. The complete setup of the PENTATRAP experiment is shown Fig. 3.1.

While some experiments (e.g. [Stu+11]) use an internal ion source in their Penning-trap stack, the production of HCIs using electron-impact ionisation requires a high-energy, high-current electron beam, which can only be produced by a heated ( $\sim 1450$  K) cathode. Therefore, at PENTATRAP external ion sources in the form of EBITs are used, see Sec. 3.1. With an electron beam energy of up to 10 kV, the two EBITs used for the measurements presented in this thesis, the Heidelberg compact (HC) EBIT (Sec. 3.1.1) and the DreEBIT (Sec. 3.1.2), are sufficient for the production of the required charge states.

The ions extracted from the EBITs are selected according to the desired charge-to-mass ratio  $q/m$  using a  $90^\circ$  bender magnet with a mass resolution of  $m/\Delta m \approx 400$  and transported inside the vacuum of the beamline to the Penning traps (Sec. 3.2). Several ion beam steering elements such as quadrupole benders and einzel lenses guide the beam into the Penning traps inside the magnet, while diagnostic stations with micro-channel



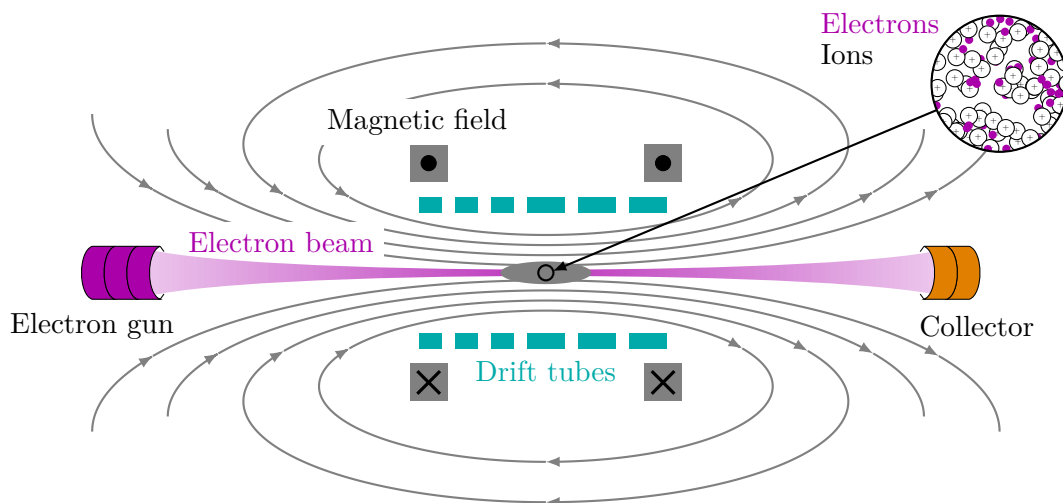
**Figure 3.1:** The PENTATRAP experiment consists of two ion sources (orange), the Penning-trap stack inside the superconducting magnet (magenta) and the beamline (blue) connecting both parts. For more details see text. Modified from [Sch17].

plate (MCP) detectors allow monitoring the ion beam. In the vertical beamline, see Sec. 3.2, two pulsed drift tubes are used to decelerate the ions down to energies which allow trapping in the Penning traps.

All parts except the magnet housing the Penning traps are situated on the ground floor of the experimental hall at the Max-Planck-Institut für Kernphysik. In order to provide long storage times for the ions in the trap, the complete experimental setup in the magnet, situated one floor below, is cooled down to liquid helium temperatures.

### 3.1 Production of ions in electron beam ion traps

HCIs are efficiently produced inside EBITs using the process of electron-impact ionisation. Hereby, the bound electrons of a neutral target are subsequently removed from the



**Figure 3.2:** Working principle of an electron beam ion trap. The electrons emitted by a heated cathode inside the electron gun are accelerated into the middle of the drift tubes by a potential difference. The radius of the electron beam is compressed by an inhomogeneous magnetic field, leading to high electron current densities in the trap center. There, atoms are ionised and trapped by applying suitable potentials to the drift tube electrodes. The electrons are stopped inside the collector.

Coulomb potential until the kinetic energy of the electrons in the beam is smaller than the ionisation energy of the outermost bound electrons of the target. The charge state of the trapped ions is reduced by recombination of electrons impacting on the ions in the trap into a bound state and charge exchange with ions in lower charge states as well as neutral background gas. Therefore, an equilibrium of the charge state distribution of the ion cloud will be reached after a certain time  $t_{eq}$ .

The basic working principle of an EBIT is shown in Fig. 3.2. Electrons are emitted from a heated cathode inside an electron gun and accelerated towards the center of a drift tube stack, consisting of cylindrical electrodes, by a potential difference applied between the two. An additional inhomogeneous magnetic field compresses the radius of the electron beam and increases the electron current density in the trap center, both leading to a confinement of the ions in radial direction. Atoms crossing the electron beam are ionised by electron-impact ionisation and subsequently trapped in center of the drift tubes when a potential minimum is applied. While the electrons move out of the trapping region, the radius of the electron beam again increases, until the electrons impact on the collector surface.

At PENTATRAN, a commercial DreEBIT [DRE10; Zsc+09] was used to produce the ions for the measurements presented here. Additionally, a second EBIT was setup in the scope of this thesis and the Master thesis of Christoph Schweiger [Sch17]. This EBIT is a Heidelberg compact EBIT (HC-EBIT) [Mic+18] and was modified for efficient

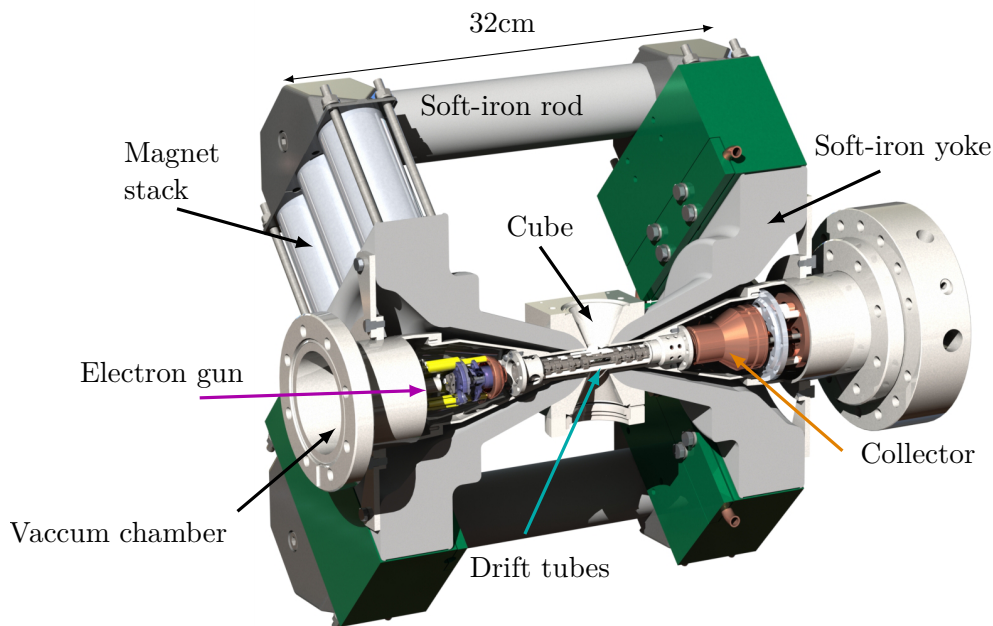


**Figure 3.3:** A cut view of the CAD model of the Heidelberg compact EBIT is shown with the main parts labelled. The wire probe setup is not included. For more details see text

production of Ho ions. More details of the working principle of an EBIT will be given in the following using the example of the HC-EBIT.

### 3.1.1 The Heidelberg Compact EBIT

The  $^{163}\text{Ho}$  samples expected for a measurement of the  $Q$ -value of the electron capture process (see Sec. 1.1.3 for more information) are on the order of  $10^{14}$  atoms. Therefore, an efficient ionization procedure needs to be employed. The idea is based on [EM95], where the so-called wire probe technique was proposed. Thereby, a wire with the sample to be ionized at the tip was guided close to the electron beam. Lower energetic electrons on large radii should then impact on the tip and sputter off material. First tests performed with an HC-EBIT using such a setup either did not lead to ions being produced or the production rate was too low to identify them. In the scope of the PhD thesis of Christoph Schweiger [Sch20], a pulsed laser is therefore included in the current setup to ablate material from the tip of the wire.

In order to set up such a wire probe system, a HC-EBIT was built up. The use of a second EBIT allowed performing mass measurements at PENTATRAP with ions from the DreEBIT during the commissioning of the HC-EBIT. It was tested in a separate laboratory with a beamline consisting of a bender magnet (the same model as the one in the PENTATRAP beamline, see Sec. 3.2) and an MCP behind to record the intensity of the

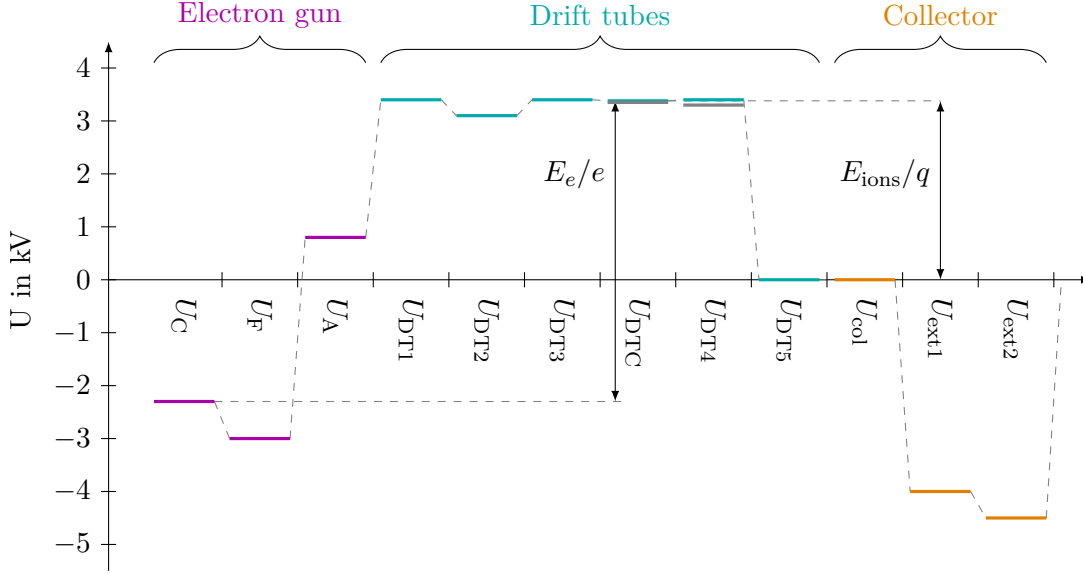


**Figure 3.4:** The voltages applied to all electrodes inside the HC-EBIT for the measured data shown here. The electrons energy at the position of the ionisation is given by the potential difference between cathode and central drift tube,  $E_e = (|U_C| + U_{DTC}) \cdot e$ . The energy of the extracted ion per charge is given by the potential of the central drift tube. For the explanation of the names, see text.

ions depending on the magnetic field in the bender magnet. Using two separate setups has the advantage that the high-precision mass measurements performed at PENTATRAP are not influenced by the changing magnetic field in the bender magnet during the commissioning of the HC-EBIT. In Fig. 3.1 the HC-EBIT is shown at its future position at the PENTATRAP beamline.

The main parts of the HC-EBIT are shown in Fig. 3.3, as a cut through of the CAD model, with a close up of the target at the tip and the laser shown in Fig. 3.5 later in this chapter. The electron gun, the drift tubes, the collector, and the magnetic field will be described in more detail in the following. Typical settings for the electric potentials applied to each of the electrodes are shown in Fig. 3.4 and will be used to describe the effect on the ions and electrons.

The vacuum chamber consists of two cones attached to a cube in the center. Four CF40 ports on the cube allow optical and mechanical access to the trapping region. To one of the ports a feedthrough flange is attached in order to provide the potentials to the drift tubes, which are centered in the cube. The others are used for the wire probe protruding into the trapping region, an X-ray detector and a vacuum pump at the same port which is also used for the laser access.

The inhomogeneous magnetic field is produced by 72 NdFeB permanent magnets, 36 on both sides of the drift tubes in four groups of 3x3 magnets (magnet stack in Fig. 3.3). The magnetic flux is guided around the vacuum chamber by a soft-iron yoke reaching

close to the trapping region in the cube. A high magnetic field of 0.8 T is thereby produced in the trap center.

The electrons are produced, focused and accelerated within the electron gun. The barium-impregnated tungsten cathode [Mic+18] is heated to 1450 K by applying a heating current of  $\approx 1.25$  A. The thereby emitted electrons are accelerated away from the cathode by a potential difference between the cathode (usually  $U_C \sim -2$  kV) and anode at  $U_A \approx 1$  kV, see Fig. 3.4. In between, an additional electrode at a more negative potential than the cathode ( $U_F \approx -3$  kV) allows focussing the electron beam through the anode and into the drift tubes. After leaving the electron gun, it is further accelerated to the center of the drift tubes at  $U_{DTC} \sim 3.5$  kV. Additionally, the inhomogeneous magnetic field increases from the electron gun, which is positioned at  $B_C \approx 0$  T, to  $B_{DTC} \approx 0.8$  T in the center of the drift tubes.

The increasing Lorentz force acting on the electrons forces them on a circular orbit with radius  $r_e$ , which, due to the conservation of magnetic flux,  $\Phi_{mag} = \pi r_e^2 B$ , is compressed as the magnetic field increases:

$$r_e^{\text{DTC}} \sim r_C \sqrt{\frac{B_C}{B_{\text{DTC}}}} \quad , \quad (3.1)$$

where  $r_C$  is the radius of the electron beam at the cathode. While more exhaustive models exist to describe the compression of the electron beam [Bri45; Her58], this simple approach shows that the electron current density is highest and the electron beam radius smallest at the highest magnetic field  $B_{DTC}$  at the central drift tube. At this position, an axial potential minimum is applied to the drift tubes. Thereby, the ions are trapped axially and can be most efficiently ionised to higher charge states. Radially, the ions are trapped by the magnetic field and the negative space charge of the electrons.

The drift tube stack of the HC-EBIT consists of six electrodes, where the first three can be used as an electrostatic lens to further focus the electrons into the trap center by applying suitable voltages to  $U_{DT1}$  to  $U_{DT3}$ . The potential of the central electrode,  $U_{DTC}$ , is  $\approx 20$  V below the neighbouring electrodes,  $U_{DT3}$  and  $U_{DT4}$ . This potential also defines the electrons' kinetic energy,  $E_e = (|U_C| + U_{DTC}) \cdot e$ , and the energy of the ions when they are ejected from the trap,  $E_{\text{ions}} = U_{DTC} \cdot q$ , as the following beamline is at ground potential.

Inside the trapping region several processes influence the charge state distribution of the trapped ions:

**Electron impact ionisation:** For an efficient ionisation by electron impact ionisation the kinetic energy of the electrons in the electron beam should be larger than the electrons' binding energy  $E_{\text{bin}}$  by  $E_e \approx 3E_{\text{bin}}$  [Lot67]. The voltages supplied to the drift tubes are limited to below 8 kV, while the power supply of the cathode (*iseq HPn 20*) allows for a maximum of  $-2$  kV. Therefore, for the ions used in the measurements presented in this thesis and future measurements, especially those including Ho ions, the maximum charge states which can be efficiently bred are around  $\text{Xe}^{43+}$  ( $E_{\text{bind}} \approx 3.3$  kV),  $\text{Re}^{46+}$  ( $E_{\text{bind}} \approx 2.5$  kV), and  $\text{Ho}^{39+}$  ( $E_{\text{bind}} \approx$

3.0 kV) [TC88]. These are well above the desired charge states for the experiments at PENTATRAP.

**Electron impact excitation:** Instead of further increasing the charge state, elastic electron impact can also lead to an excitation of the ion. This is discussed in more detail in Sec. 7.1.2.

**Radiative recombination:** Electrons from the electron beam can also recombine with the ion, thereby decreasing the charge state of the ion. The released energy during this process, usually in the X-ray regime, can be detected and used to investigate the ions in the trap.

**Charge exchange:** Collisions with ions in lower charge states or background gas atoms lead to recombination of electrons in the HCIs. This is a limiting factor for the charge breeding process, especially at room-temperature.

After a certain time  $t_{eq}$  of the ions in the trap center, an equilibrium will be established between the electron ionisation and recombination processes. At this time the charge state distribution in the trap will not change any more. Both processes depend on the energy of the electrons, which can be used to influence the production rate of a certain charge state. For example, for the production of lower charge states, the time of the ions in the EBIT, the so-called breeding time  $t_{breed}$ , or the electron beam energy need to be decreased.

The central drift tube of the HC-EBIT has four openings to allow optical access to the trap center, which are covered by a stainless steel mesh with a 2 mm x 2 mm grid size to still approximate a homogeneous trapping potential. For the wire probe setup, one side of the mesh is completely left open to be able to guide the target on the wire tip close to the electron beam. A homogeneous trapping potential is ensured by applying a slightly lower voltage to the target compared to the central drift tube electrode to mimic the desired electric potential at the tip position (see the grey line in Fig. 3.4 at  $U_{DTC}$ ). The potential of drift tube four,  $U_{DT4}$ , can be switched using a high-voltage switch (*BEHLKE GHTS 60*) to a potential lower than the central drift tube (grey line) in order to extract the ions from the trap.

After leaving the drift tubes, the electrons are stopped inside the water-cooled collector by an electrode at ground potential,  $U_{col} = 0$  V. In order to prevent the electrons from escaping further, two additional electrodes at a potential of  $U_{ext1} = -4$  kV and  $U_{ext2} = -4.5$  kV repel the electrons and extract the positively charged ions through the collector into the adjacent beamline.

At the HC-EBIT two diagnostic tools are used to determine the trap content, e.g. the charge state distribution of the ions. First, the ions can be ejected from the trap center by lowering  $U_{DT4}$  and guiding the ions through the collector. A 90° bender magnet allows separating the extracted ions by their charge-to-mass ratio  $q/m$  and the recording of a  $q/m$  spectrum by changing its magnetic field and measuring the ions signal on an MCP. As the ions are all accelerated with the same potential difference, their velocity

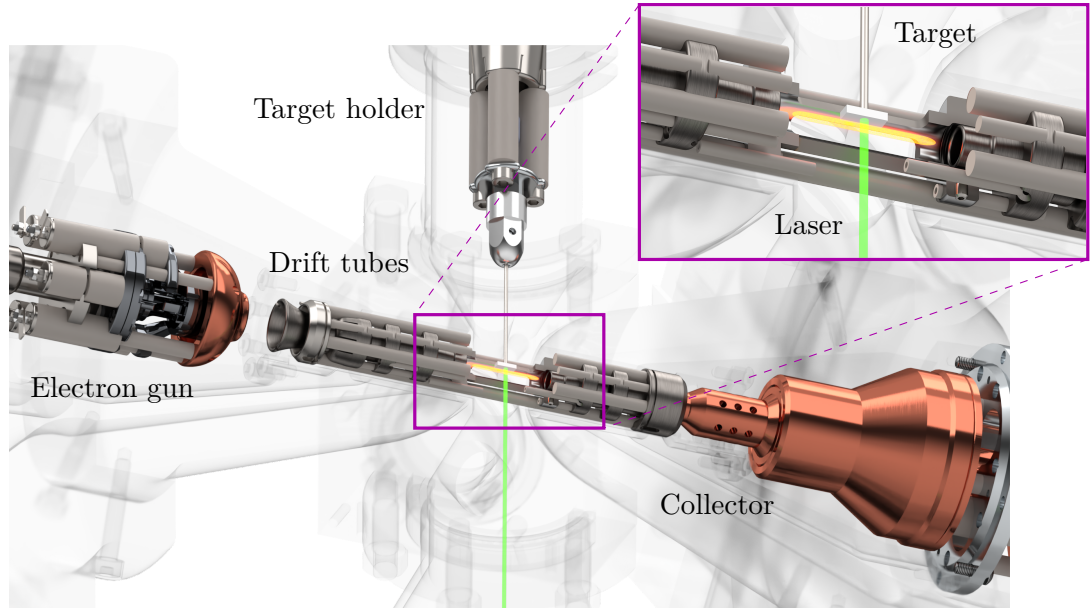


**Figure 3.5:** CAD Model of interior parts of the HC-EBIT with the drift tubes (cut open in the middle around the trapping region), electron gun, and collector. The vacuum chambers are only shown faded out. In the inset, the target is shown close to the ion cloud (yellow), with the laser (green) hitting the target from the opposite side of the drift tubes. Modified from [Sch+19b].

when exiting the EBIT depends on the mass,  $v = \sqrt{2E_{\text{ions}}/m}$ . The radius of the ions moving in a magnetic field  $B$ ,

$$r = \frac{mv}{qB} = \sqrt{\frac{2mE_{\text{ions}}}{q^2B^2}} \quad , \quad (3.2)$$

can, therefore, be changed by varying the magnetic field and allowing only ions with a certain charge-to-mass ratio to exit the magnet. Second, an X-ray detector records the radiation resulting from excitation and relaxation processes in the trap region, which is discussed in [Sch17].

The position of the target inside the trapping region can be controlled by a three-axis step-motor controlled manipulator. In order to position it next to the electron beam, see Fig. 3.5, the target is moved into the drift tubes while the X-ray spectrum is observed for Bremsstrahlung from electrons impacting on the target, as the course of the electrons through the EBIT is changed by the position of the target. Similarly, the right potential applied to the tip is determined.

The laser used for the ablation is a frequency-doubled 532 nm Nd:YAG laser system with a few mJ pulse energy. The timing sequence for the ejection of the ions and the laser pulse is shown in Fig. 3.6. After a waiting period of 50  $\mu\text{s}$  after ejecting the ions from the EBIT center to one side by lowering the potential  $U_{\text{DT4}}$  at time  $t = 0$ , the

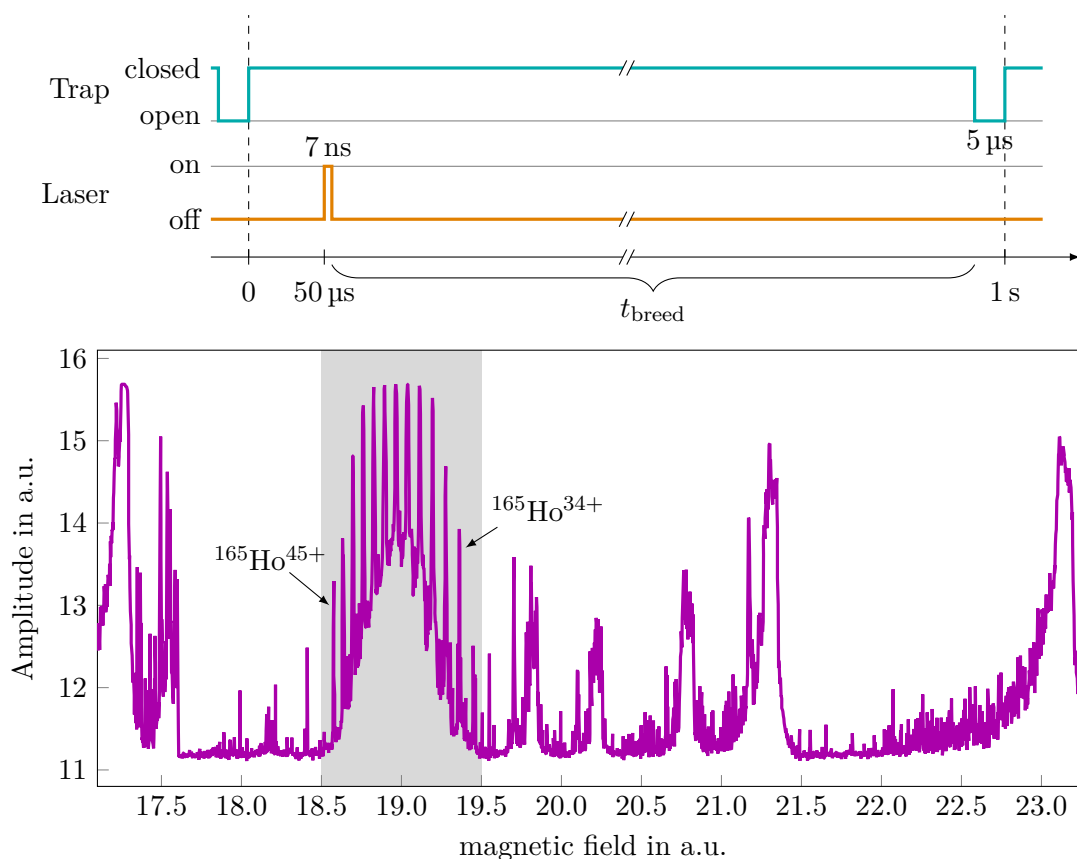


**Figure 3.6:** **Top:** Sequence for the production and extraction of ions using laser ablation from the wire-probe target. The open trap describes the time where drift tube 4 was switched to a lower potential and the ions were extracted from the trap. **Bottom:** The first Ho spectrum recorded behind the bender magnet (uncalibrated) with an MCP. The gray area corresponds to the Ho ions, the rest of the peaks are either from rest gas ions or Bremsstrahlung in the beamline.

laser pulse is on the target for 7 ns. The ions are left inside the trap for  $t_{\text{breed}}$ , before being extracted and the sequence starts again after 1 s in total. The plot below shows the first recorded Ho spectrum with the HC-EBIT produced using a Ho-foil target with a natural isotopic abundance. The grey area marks the region where the evenly spaced peaks correspond to HCIs of  $^{165}\text{Ho}$  in the charge states between  $q = 34+$  and  $q = 45+$ . Rest gas ions are responsible for the rest of the peaks. A calibration of the x-axis of such a spectrum is explained in [Sec. 3.2](#).

In order to produce ions in different charge states, the breeding time  $t_{\text{breed}}$ , the potential applied to the target or the electron energy can be varied. These effects are investigated in [\[Sch20\]](#). Additionally, the lower limit on the sample size for an efficient

production with a usable yield, i.e. the target can be used for some thousand laser shots, is described in [Sch+19b].

### 3.1.2 The DreEBIT

The EBIT used for the production of the ions for the mass measurements presented in this thesis is a commercially available, tabletop Dresden-EBIT3 (DreEBIT) [Zsc+09]. It was set up and commissioned in [Rep12], where also a MIVOC (Metal Ions from Volatile Components) system was built. The MIVOC system, extended in [Doo15], allows introducing gases and volatile compounds into the EBIT. The main feature is controllable valves, which make switching between different atom samples possible.

Similar to the HC-EBIT, the DreEBIT is also a room-temperature EBIT with permanent magnets, reaching a magnetic field strength in the center of 0.25 T. The cathode consists of a metal alloy containing cerium and iridium. With a maximum electron beam energy of 9.5 keV in the trap center, similar charge states can be reached as with the HC-EBIT. The trapping region consists of three drift tubes, where the inner one is used to provide the axial potential minimum of the trap and defines the energy of the ions after extraction of  $E_{\text{ions}} = 6.48 \text{ keV} \cdot q$ . The collector is at ground and water-cooled as well, while three extractor electrodes can be used as an einzel lens during the extraction of the ions.

While the MIVOC system allows using different samples quickly after one another, remains of previous samples inside the vacuum of the EBIT may contaminate the extracted ion beam. For the mass measurements presented here, this was not a problem. The Xe ions were produced from one single gas bottle, either with the natural or, in the case of measurements involving  $^{126}\text{Xe}$ , enriched isotope abundance, while for the Re measurements a single isotope volatile compound was sufficient. For future measurements requiring different atomic samples, both the DreEBIT and the HC-EBIT employed at PENTATRAP will be used for the production of the different ion species for mass-ratio measurements.

## 3.2 Ion transportation

The ions are transported from the ion source into the Penning-trap stack inside the high-vacuum beamline. Along the way, the ions' energy needs to be reduced to be able to capture them in the Penning traps. Additionally, the ion species is preselected and the ion beam can be monitored with several diagnostic tools.

The beamline consists of a horizontal and a vertical part, see Fig. 3.1 and Fig. 3.8 later in this chapter, respectively. The horizontal part includes the EBITs and the 90° bender magnet up to the quadrupole bender guiding the ions into the vertical beamline. Before and after the bender magnet einzel lenses allow to steer and focus the ion beam. A fixed MCP behind a quadrupole bender is used to monitor the ion beam. Additionally, a diagnostic station equipped with an MCP and a Faraday cup (see [Dör15]) below the

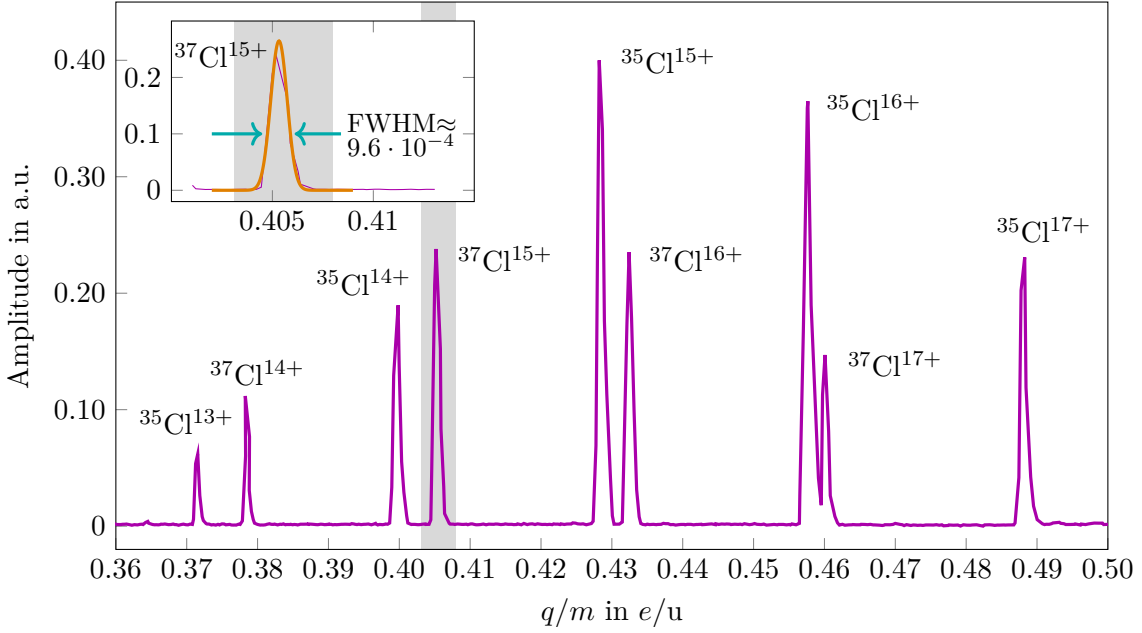


**Figure 3.7:** Isotopically resolved charge-to-mass  $q/m$  spectrum for Cl-ions produced in the DreEBIT from a  $\text{CH}_2\text{Cl}_2$  compound. It was measured with the MCP at the end of the horizontal beamline. As an example, the Gaussian fit to the peak of  $^{37}\text{Cl}^{15+}$  is shown in the inset. This yields a mass resolution of  $(q/m)/\Delta(q/m)_{\text{FWHM}} \approx 420$ . Modified from [Sch+16].

quadrupole bender can be moved into the ion beam for detection of the ions. Several valves can be used to maintain an excellent vacuum if some parts need to be exchanged.

In order to calibrate the magnetic field strength or the applied current of the  $90^\circ$  bender magnet to the ions' charge-to-mass ratio of the transmitted ions, an ion ensemble containing several isotopes is used. In Fig. 3.7 a spectrum recorded with the MCP at the end of the horizontal beamline is shown for ions from two Cl isotopes,  $^{35}\text{Cl}$  and  $^{37}\text{Cl}$ .

Hereby interesting are crossings, where two isotopes in different charge states have the same charge-to-mass ratio  $q/m$ :

$$\frac{q}{m_1} = \frac{q+1}{m_2} . \quad (3.3)$$

For the two Cl isotopes,  $^{35}\text{Cl}$  and  $^{37}\text{Cl}$ , this would happen at the purely mathematical charge state of  $q = 17.5+$  for  $^{35}\text{Cl}$ , which corresponds to  $q/m = 0.5$ . However, also the peaks of  $^{35}\text{Cl}^{17+}$  and  $^{37}\text{Cl}^{18+}$  at  $q/m \approx 0.49$  cannot be distinguished. This is used to assign the charge states of the whole spectrum. In order to calibrate the x-axis, several peaks are then fitted, as shown in the inset, with a Gaussian function to determine their position and to assign their  $q/m$ . Both bender magnets, in the test setup of the HC-EBIT and the PENTATRAP beamline have a similar mass resolution of  $m/\Delta m \sim 400$  [Sch+16].

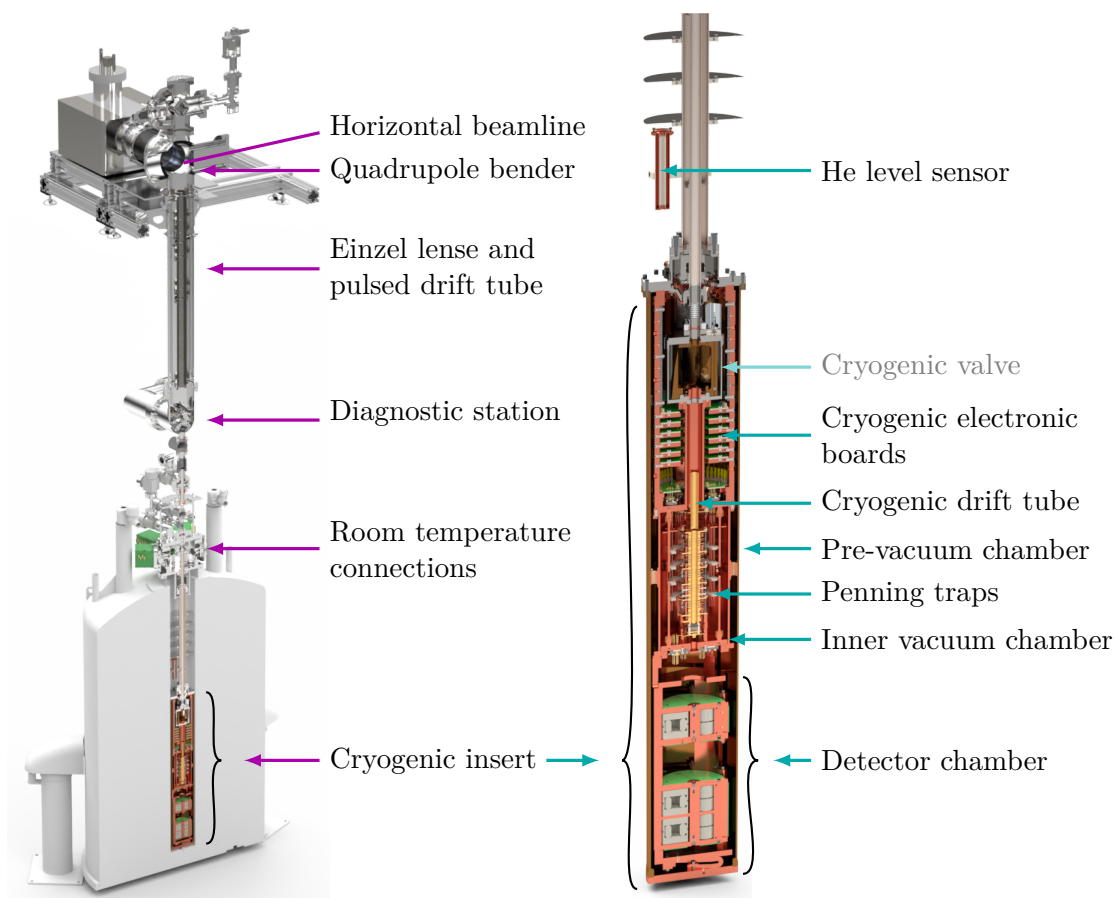


**Figure 3.8:** **Left:** A cut view of the CAD model of the vertical beamline is shown including the cryogenic insert in the magnet's bore. **Right:** Close up of the cryogenic setup featuring the Penning traps, detectors, and cryogenic drift tube. The cryogenic valve will be installed in the future.

For a wider range of  $q/m$  an ensemble consisting of several isotopes, for example Xe, can be used. Here, not only crossings of  $1 \cdot e$  but also larger differences  $n \cdot e$  can be included.

In the vertical beamline below the electrostatic quadrupole bender, shown in Fig. 3.8, a einzel lens allows refocusing the ion beam. The ions are produced in the DreEBIT at a potential  $E_{\text{DreEBIT}}/q = 6480 \text{ V}$ . Their energy is reduced by the first pulsed drift tube, whose potential at  $6270 \text{ V}$  is pulsed to ground potential at the moment the ions are in its field-free region. Thereby, the ions' kinetic energy is reduced to  $\approx 210 \text{ eV}$  per charge. The second, cryogenic drift tube at a potential of  $\approx 200 \text{ V}$  is pulsed down to  $-10 \text{ V}$  potential. The kinetic energy per charge of the ions is thereby reduced by the difference in the two potentials applied to the drift tube and the ions are left with a few  $10 \text{ eV}$  per charge. The timing of the pulses for the drift tubes is crucial for the efficient loading of HCIs into the Penning traps. Therefore, an FPGA card is used to set up the

triggers for the EBIT, e.g. the ion ejection, the pulsed drift tubes in the vertical beamline and the cryogenic region, see [Sec. 3.3](#), and the loading of the ions into the Penning traps, which is described in [Sec. 4.2](#).

Below the first pulsed drift tube, a movable diagnostic station equipped with an MCP and a Faraday cup. Similar to the electron beam, the ion beam entering the magnetic field of the superconducting magnet is compressed according to [Eq. \(3.1\)](#). In order to provide a good vacuum in the trapping region, a thin tube with a diameter of 3 mm can be used as a pumping barrier between the beamline vacuum at room temperature and the cryogenic region. A cryogenic valve to close off the trap vacuum from the beamline and further improve the vacuum in the Penning traps will be implemented in the future. Its design is described in [[Ris18](#)].

### 3.3 Cryogenic setup of PENTATRAP

The heart of PENTATRAP is the stack of five Penning traps inside the superconducting magnet. As the magnet has a cold bore, the experiment comes into direct contact with liquid He. In order to prevent vacuum connections from breaking due to the rapid cool down, the trap stack is mounted inside an additional inner vacuum chamber, see [Fig. 3.8](#). The boards for the signals to the trap electrodes and the detection system are situated in an outer, pre-vacuum chamber and connected to the traps via vacuum feedthroughs.

#### 3.3.1 Magnet laboratory

The superconducting magnet housing the Penning traps is situated one floor below the beamline in a separate temperature-stabilised laboratory, which also houses the vertical beamline, voltage source for the Penning traps and further voltage and function generators. Critical for high-precision mass measurements is the effect of ambient pressure, the temperature in the room, and external magnetic field fluctuations. Their effect and stabilisation for a successful performance of PENTATRAP were investigated in [[Kro19](#)]:

**Voltage stabilisation:** A change in temperature in the magnet room influences the stability of the voltage source, see [Sec. 3.3.3](#), for the Penning traps. As this directly leads to a change in the axial frequency of the ion, the room is air-conditioned with a temperature stability of below 20 mK/h.

**Magnetic field stabilisation:** Critical for the performance of the Penning traps is also the level of liquid He inside the magnet bore. If the level changes, different parts of the cryogenic setup are immersed in helium, which leads to changes in the expansion of the cryogenic setup and thereby of the position of the traps in the magnetic field. The boil-off pressure of the helium and thus also the He level inside the bore is, therefore, stabilised.

With this stabilisation in a closed room, the magnetic field inside the Penning traps only changes by  $\Delta B/\Delta t = -2 \cdot 10^{-10}$  T/h. This corresponds to a change of  $\Delta B/\Delta t = -7 \cdot 10^{-11}$  T/40s over the time of one frequency determination.

Magnetic field sensors inside the magnet laboratory measure the changes in the external magnetic fields. The PENTATRAP experiment is close to two superconducting EBITs ([Gon+07; Cre+04] and [Epp07]), whose magnets are not continuously operating and are, therefore, charged up and down regularly. As these influence the high-precision measurements at PENTATRAP, it is important to determine changes in the external magnetic fields and stop measurements, as the thereby caused changes in the eigenfrequencies lead to non-resonant *rf*-fields during the PnP-measurement, see Sec. 4.3.2.

### 3.3.2 Realisation of the detection system

At PENTATRAP, the ion's eigenfrequencies are detected with an axial detection system consisting of a high- $Q$   $LCR$ -circuit connected to one trap electrode, a cryogenic amplifier and room-temperature electronics including further amplifiers and a downmixer. The detection principle is described in Sec. 2.5, with the connection to the Penning traps shown in Fig. 3.11 later in this chapter. The used  $LCR$  circuit features a high parallel resistance  $R_p = 2\pi\nu_R QL = Q/2\pi\nu_R C$ . For a given resonance frequency  $\nu_R$ ,  $R_p$  can be maximised by increasing the inductance  $L$  or the quality factor  $Q$  and minimising the parasitic capacitance  $C$ . The tank circuit is, therefore, realised by a toroidal coil made out of superconducting wire inside a normal conducting shielding and will in the following be referred to as called resonator.

#### Resonator

In order to maximise the  $Q$ -value, energy losses in the resonator arising from the wire resistance and losses induced in the surrounding materials as well as the coil body material need to be minimised. The wire resistance is reduced by choosing a superconducting material, in this case the type-II superconductor NbTi, which has a critical temperature of  $T_c \approx 9.5$  K and features a high critical magnetic field of  $B_{c2} \approx 10$  T [Sch02]. While external magnetic fields degrade the surface resistance of superconductors, it was shown in [Ulm+09] that NbTi still has lower surface resistances than copper at the axial frequencies used at PENTATRAP.

Dielectric losses arising due to the material of the coil body are characterised by the dielectric loss tangent  $\tan(\delta)$ , which is inversely proportional to the parallel resistance,  $R_p \propto 1/\tan(\delta)$ . Therefore, PTFE (polytetrafluoroethylene), which has a low loss tangent of  $\tan(\delta) \sim 10^{-4}$  is chosen for the coil body as well as the rings holding the coil in place.

The shield around the coil, the housing of the resonator, defines the surroundings of the coil and fixes the parasitic capacitances. Due to the use of a toroidal coil, the fields extending outside of the coil body are minimised compared to a helical coil. Still, losses could be further reduced by using a superconducting shield. As superconductors expel and distort external magnetic fields and the resonators are mounted close to the traps, the housing is made out of oxygen-free high thermal conductivity copper (OFHC) to keep the magnetic field in the Penning traps as homogeneous as possible.

Several designs for the coil body were tested and finally, two different designs at the two measurement traps are used with the design described in [Sch15] for trap 2 and the

**Table 3.1:** Characteristic values for the two axial detection systems at trap 2 and 3. The effective electrode distance was taken from [Rou12]. The  $Q$ -value is given for the case of the resonator already connected to the trap and  $R_p$  is calculated according to Eq. (2.51). The capacitance  $C$  and inductance  $L$  were measured.

trap	$\nu_R$	$N$	$L$	$C$	$D_{\text{eff}}$	$R_p$	$Q$	tap
2	740 kHz	500	1.4 mH	10 pF	11.1 mm	19.5 M $\Omega$	3000	1/3
3	504 kHz	1100	3.3 mH	6.9 pF	11.1 mm	71.1 M $\Omega$	6800	1/3

one described in [Moo13] for trap 3. In Tab. 3.1 the main parameters for the two coils are given. In order to reach resonance frequencies between 500 kHz to 700 kHz, 500 – 1000 windings of 75  $\mu\text{m}$  NbTi are needed. Both coil bodies feature spacers on their outside, such that the wire can be wound in layers in between. The wire is insulated with PTFE, leading to a total diameter of 120  $\mu\text{m}$  and is thermally connected and spatially kept in place by a thin PTFE tape. The ends of the wire are welded to a copper wire for further, easier handling, i.e. for soldering to the trap electrodes or capacitively to ground. The tap, see below, is made after around one-third of the windings.

### Cryogenic amplifier

The second important part of the cryogenic axial detection system is the amplifier for the resonator signal. It features a low voltage and current noise density around the axial frequency, a high input resistance and negligible parasitic feedback. The design is described in detail in [Rou12; Stu11], here only the main design ideas are presented.

The amplifier is based on Gallium-Arsenide (GaAs) field-effect transistors (FETs), which work even at cryogenic temperatures. The circuit layout is shown on the left in Fig. 3.9. Parallel dual-gate FETs (NE25139, magenta) form the input stage in common-source arrangement topology, which offers a high input resistance and a voltage amplification of the signals applied to the gate voltage. Therefore, the signal from the resonator is mixed with a constant offset voltage,  $U_{g1}$ . By shortening the two gates and using two FETs in parallel incoherent noise at the amplifier input is reduced by a factor of four. Feedback on the input arises from the parasitic gate-to-drain Miller capacitance [Mil20] and is suppressed by forming a cascode stage with a third transistor, 3SK124 (NEC), shown in orange. Keeping its gate on a constant voltage,  $U_{g2}$ , the transistor is a low impedance load to the first stage. The third stage (blue) is formed by another 3SK124 in source follower configuration, such that the amplifier output matches the 50  $\Omega$  impedance of the following transmission lines.

Similar to the resonator, the dielectric losses of the board material leads to higher losses in the complete system and increases the gate-to-drain capacitance. The board material is, therefore, also made out of PTFE with a copper layer, in which the board layout is milled. All components used are surface-mount devices (SMDs), with high- $Q$  capacitors and thin-film resistors. The ground potential around the board components is ensured by several tens of small ( $\sim 0.5$  mm) holes, through which electrical contact to

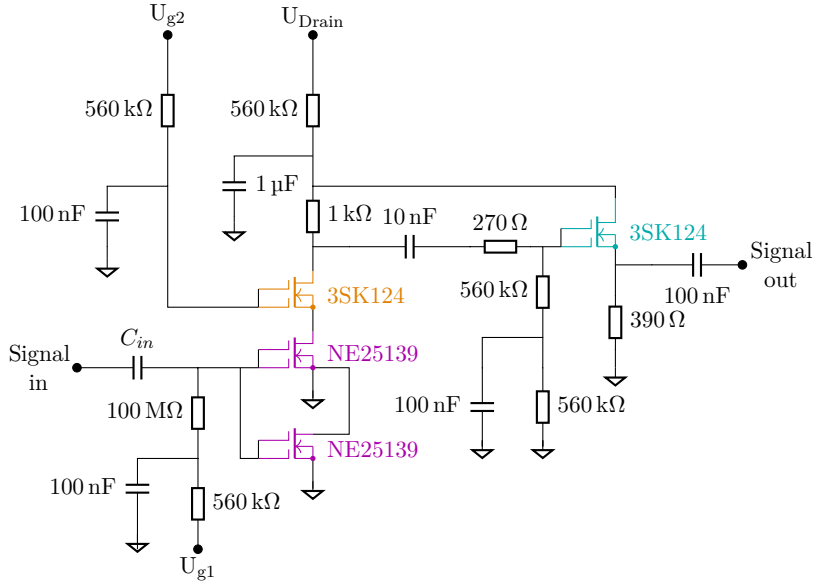


**Figure 3.9:** **Left:** Amplifier layout with the colours of the transistors corresponding to different stages, as described in the text. **Right:** Picture of a board with two amplifiers.

the backside of the board is provided, see the picture of an amplifier on the right side of Fig. 3.9.

### Combination of resonator and amplifier

The complete losses of the resonator and the amplifier combined are reduced by placing the amplifier as close as possible to the resonator. This also reduces the capacitance of the wiring and, therefore, the resonators capacitance. A figure of merit is the signal-to-noise ratio ( $SNR$ ) of the complete detection system together with the ion. In Fig. 3.10 the cryogenic amplifier is modelled by an ideal amplifier with input-related current and voltage noise sources,  $i_{en}$  and  $u_{en}$ , respectively, and the input capacitance  $C_{in}$  and resistance  $R_{in}$ . The resonator is coupled to the amplifier by a couple capacitance  $C_c$  and the tap, a connection cable attached to the resonator coil, dividing the coil with inductance  $L$  into two parts with  $L_1$  and  $L_2$ . The coupling parameter  $\kappa$  is then given by [Dör15]:

$$\kappa \equiv \frac{U_{in}}{U_{LCR}} \approx \frac{L_2}{L} \frac{C_c}{C_{in} + C_c} \quad , \quad (3.4)$$

where  $U_{in}$  is the voltage at the amplifier input and  $U_{LCR}$  the voltage across the  $LCR$ -circuit. For the dip detection, the  $SNR$  is given by the amplitude of the noise resonance

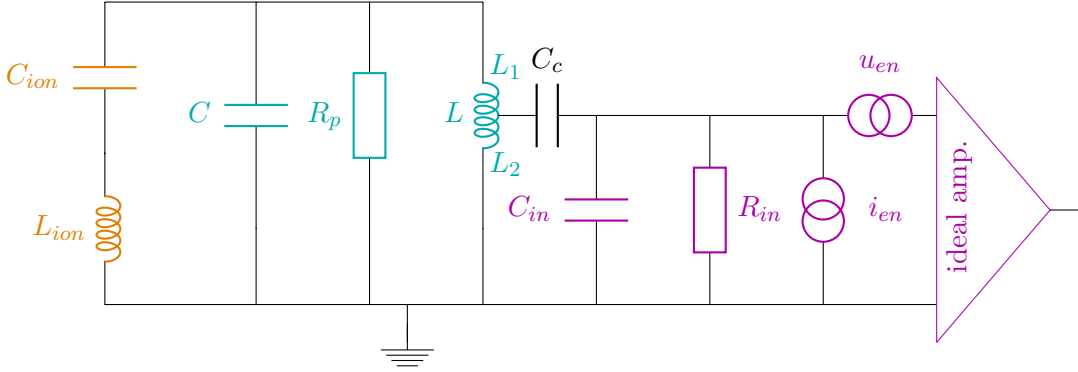


**Figure 3.10:** Complete detection system consisting of the ion (orange), the resonator (blue) and the cryogenic amplifier (magenta). The resonator is coupled to the amplifier with a tap, dividing the inductance into  $L_1$  and  $L_2$ , and the couple capacitance  $C_c$ . The real amplifier is modelled by an ideal amplifier with input resistance  $R_{in}$  and capacitance  $C_{in}$ . The noise contributions of the input are taken into account by noise current  $i_{en}$  and voltage  $u_{en}$  sources.

divided by the voltage noise floor:

$$SNR = \frac{\sqrt{\kappa^2 4k_B T R_p + \kappa^4 R_p^2 i_{en}^2}}{u_{en}}. \quad (3.5)$$

For a high  $SNR$  the noise contributions need to be kept small, whereas the parallel resistance of the resonator  $R_p$  should be increased by maximising the  $Q$ -value. Furthermore, for a large  $\kappa$  the noise contribution  $\kappa^4 R_p^2 i_{en}^2$  is also increased. As the coupling  $\kappa$  also affects the parallel resistance  $R_p$  acting on the ion, it should be chosen such that the dip widths are on the order of a few Hz. For the resonators at PENTATRAP, the position of the tap was put at 1/3 of the windings, i.e.  $L_1 = 2/3L$  [Rou12].

### 3.3.3 The trap tower

For the measurements performed in this thesis, the trap tower designed in [Rou12] was used. It consists of five orthogonal and compensated (see Sec. 2.2.1) traps, each consisting of five electrodes. In Fig. 3.11 the electrode stack of the five Penning traps is shown together with the connected detection system and excitation lines for the two measurement traps, trap 2 and 3. For graphical purposes, the slits in the halved electrodes are all shown at the same position. In the experiment, the split electrodes from one trap are oriented perpendicular to each other.

The trap electrodes are made out of OFHC copper (purity > 99.999%) in order to minimise the magnetic permeability, which can be caused by impurities. The electrodes are additionally plated with 20  $\mu\text{m}$  of gold to avoid oxidation of the copper and disturbances of the electrostatic trapping potentials. The tolerances for the copper are  $\pm 5 \mu\text{m}$  and  $\pm 1 \mu\text{m}$  for the gold layer. Sapphire rings are used to isolate the trap electrodes from

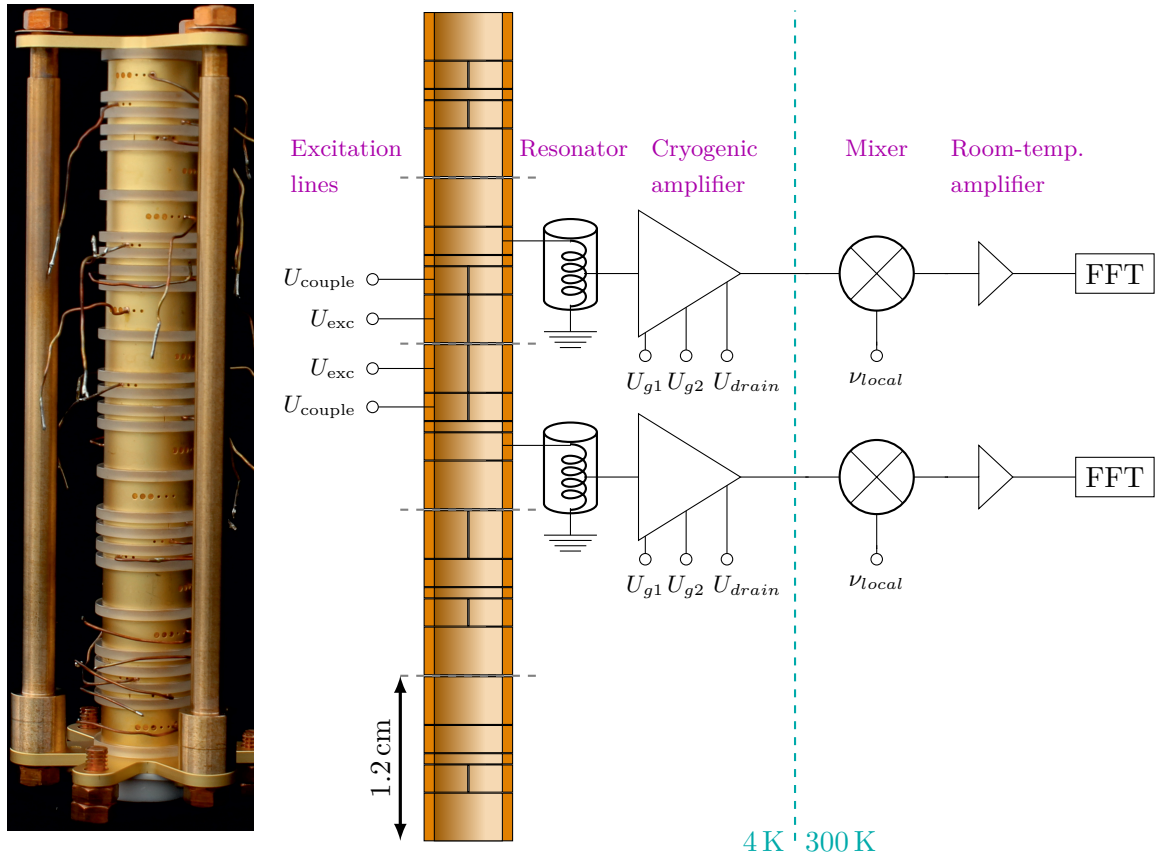


**Figure 3.11:** **Left:** Picture of the trap tower. **Right:** Schematic of the trap tower showing the split electrodes, the excitation lines and the detection system. The blue line separates the room-temperature parts and those in the cryogenic region. At room temperature, the signals are downmixed to frequencies around  $\approx 10$  kHz and further amplified, before the FFT is performed.

each other. The manufacturing process of the trap electrodes and the sapphire rings is described in [Rep12].

In order to apply a dipole excitation or a quadrupolar coupling field as described in Sec. 2.4, the orientation of the applied field must include the directions of involved modes. Therefore, some of the trap electrodes are split, such that the field extends both in the radial and the axial direction. For the measurement traps, one end cap electrode and one correction electrode are split. For the coupling of the modes, denoted by  $U_{\text{couple}}$  in Fig. 3.11, one half of a correction electrode is used. While the axial mode could be excited with a signal applied to a full electrode, connecting the excitation line also to a split electrode,  $U_{\text{exc}}$ , allows exciting the radial modes as well.

Care needs to be taken to ensure that excitation or coupling fields are not applied to an electrode next to a detection system, as then the picked up *rf*-signal is stronger

than the signal measured from the detector. The two detection systems used here are, therefore, connected to a full correction electrode on the other side of the central ring electrode as the excitation lines. In principle, trap 4 is also equipped with a detection system, but not used for the measurements here, as the narrow dip width requires long averaging times for an axial dip detection.

The measurement scheme described in Sec. 2.3 uses three ions to measure the free-space cyclotron frequency in two traps. Due to the transportation of the ions one trap up or down in between measurements, leading to an exchange of the ions in the measurement traps, in total four traps are needed. In the future, the fifth trap can be used to monitor the magnetic field changes by continuously determining the free-space cyclotron frequency of an ion with well known mass [Rou+12]. Another possibility is to determine the axial frequency and use it as a reference for the voltage source (StaRep, see next section).

### 3.3.4 Trap electronics

In Fig. 3.11 the main signals, without the trapping potentials, needed for acquiring the ion's signal are shown. As described in Sec. 2.2.3, the stability of the potentials applied to the trap electrodes needs to be on the level of  $10^{-8}$  over the time of the axial frequency determination. To that end the ultra-stable voltage source StaRep (Stable Reference for Penning-Trap Experiments) [Böh+16] was designed. It consists of 25 channels, five for each trap, and features a stability of  $\Delta V/V \leq 4 \cdot 10^{-8}$  on a 10 min time scale. The maximum voltage it provides is 100 V, allowing the trapping of ions with a charge-to-mass ratio of  $q/m > 0.0749 e/u$ , for an axial detection system at 740 kHz. For Xe, this corresponds to a minimal charge state of  $q = 10+$ . The resolution of StaRep of  $\leq 1.5 \mu\text{V}$  allows setting the axial frequency with a precision of  $10^{-5}$  Hz.

For the excitation and coupling of the ion's motions, a function generator (*Keysight Trueform Waveform Generator 33600A*) is used to apply sine functions with the right frequency. With a 1  $\mu\text{Hz}$  resolution, the frequency can be set precisely enough for the applications at PENTATRAP. In order to have well-defined pulses, e.g. for the PnP-measurement, see Sec. 2.5.4, the trigger for the start and end of the pulses is externally applied by a delay pulse generator (*SRS DG645*).

For the amplification of the ion's signal with the cryogenic amplifier, it is mixed with a constant voltage, the gate voltage  $U_{g1}$ , at the input of the amplifier. This constant voltage is provided by a precision voltage source with a stability of  $\approx 1 \text{ mV}$  (*Stahl BS 1-10*). Additionally, it also supplies the voltages  $U_{g2}$  and the drain voltage  $U_{\text{drain}}$  of the amplifier.

The ion's signal at room-temperature needs to be digitalised and, in order to recover the frequencies, a fast Fourier transform (FFT) needs to be performed. Readily available FFT analysers usually do not provide a frequency resolution below 1 Hz. Therefore, in [Ris18] a professional sound card (*Fireface UC RME*) was set up. It features a clock input, which allows synchronisation with a 96 kHz signal from a function generator, which itself is synchronized with a 10 MHz standard (*SRS FS725*). Before performing the FFT, the frequencies are downmixed with a local oscillator frequency,  $\nu_{\text{local}} \approx \nu_z - 10 \text{ kHz}$ , to

reduce the axial frequency to frequencies around 10 kHz in the audio frequency range, see Fig. 3.11. During the analysis, the local oscillator frequency is then added again to recover the true frequencies of the ions in the trap.

The FFT of the signal is finally performed with a custom PYTHON program on a PC. For more detail see [Doo18].

# 4

---

## Measurement Procedure

---

In the course of this thesis, different measurement series were performed with PENTATRAP. The first were proof-of-principle measurements of the mass difference of several xenon isotopes, as some xenon masses are among the up-to-now most precise determined masses in the mid-heavy regime of the nuclear chart. Another measurement series covered determinations of the energies of metastable excited states in highly charged rhenium and osmium ions.

For both cases the measurement setup is similar regarding the determination of the three eigenfrequencies, see [Tab. 4.1](#). The modified cyclotron frequency ( $\nu_+ \approx \nu_c \approx 13$  MHz to 16 MHz), needs to be determined to nearly the same precision as the desired precision of the free-space cyclotron frequency, as the two frequencies are approximately the same. It is determined with the phase-sensitive PnP technique (see [Sec. 2.5.4](#) and [\[Cor+89\]](#)). The other two frequencies are determined with a single dip (axial) and double dip (magnetron) measurement. Therefore, one measurement consists of several sub measurements to determine the three eigenfrequencies, namely a Dip-measurement (described in [Sec. 4.3.1](#)), an  $N$ -determination measurement (see [Sec. 4.3.3](#)) to determine the number of full revolutions of the phase of the modified cyclotron motion, and the PnP-measurement ([Sec. 4.3.2](#)) for the determination of this modified cyclotron phase and the axial frequency.

In order to perform a relative mass measurement as described in [Sec. 2.3](#), three ions (where the first and third ion are of the same species) need to be loaded into three traps. They are cooled by coupling all eigenfrequencies to the axial motion and thereby dissipating their energy into the detection system. The high-precision measurement

**Table 4.1:** Measurement types for the three eigenfrequencies. The stated precision is achieved by one single measurement of the frequency and the repetitions show how often the eigenfrequency was measured in one measurement cycle for one ion in one trap.

mode	measurement	precision	repetitions
magnetron	double dip	0.1 Hz	1
axial	single dip	0.02 Hz	250
modified cyclotron	PnP	0.002 Hz	250

requires the eigenfrequencies to be known to a  $\sim 100$  mHz level before the start of the measurement such that the *rf*-signals for the coupling and excitation of the modes can be set accordingly. These are determined during the preparation of the ions for the measurement.

The complete experiment is remote controlled with a self-written control system (Sec. 4.1), which is used to prepare the ions (see Sec. 4.2) and to set up the measurement (Sec. 4.3). As an example of how a systematic shift to the eigenfrequencies of the ions can be measured, the determination of higher order magnetic field terms (see Sec. 2.2.2) will be explained in Sec. 4.4.

## 4.1 Experiment control

The control system for PENTATRAP is written in PYTHON and was set up in the scope of Alexander Rischka’s PhD thesis [Ris18] and Menno Door’s Master’s thesis [Doo18]. It is designed to be as flexible as possible to allow for the introduction of new measurement schemes or adapting already existing ones to new measurement ideas. It covers the complete remote control of all experimental settings and devices and can be divided into three parts: the ion production and beamline, the preparation of ions in the trap and the high-precision measurement.

Control of the ion source and beamline is required for the production and transport of the ions to the Penning traps. Here, all settings, e.g. the voltages applied to the DreEBIT, the lenses and pulsed drift tubes, were optimised during the first capturing of ions in the trap. As this will only change with the addition of the HC-EBIT to the beamline, the processes, timings, and nearly all voltages do not need to be changed when switching from one ion species to the next. A graphical interface of the beamline settings allows to view all settings and apply small adjustments to improve ion loading. The breeding time in the DreEBIT and the current applied to the  $90^\circ$  bender magnet need to be changed regularly in order to select the desired charge-to-mass ratio  $q/m$  of the ions.

Contrary, the control for the preparation of the ions inside the Penning traps needs to be fast and flexible, for the experimenter to be responsive to the ion behaviour in the trap. The basis is a trap control class in PYTHON, which is imported into several different

scripts, e.g. for ion transport or cleaning of excess ions from the trap. The experimenter can influence the ions by a command-line interface using predefined commands, while adjusting their parameters, including, for example, the frequency of a coupling pulse or the potentials applied to the trap electrodes.

The script for the mass measurement procedure is based on the same commands used for the control of the ions. It consists of subscripts for the individual steps of one measurement, for example, a Dip- or PnP-measurement. A configuration file needs to be adapted to every measurement, where the trap voltages, coupling and excitation frequencies, and position of the ions, to name a few, are defined.

## 4.2 Preparatory steps before a measurement

The main steps before the start of the measurement are the loading of three single ions into three traps and the simultaneous eigenfrequency determination of two ions in the two measurement traps to a 100 mHz level. The schematic of such a preparation is shown in Fig. 4.1.

Important for the preparation of the ions is the FFT spectrum of the induced image current. For fast ion work, a running window FFT is used, where always the last 1 s of streamed data is Fourier transformed and the spectrum updates every 50  $\mu$ s. The frequency span is  $\pm 5$  kHz around the resonance of the axial detection system and allows seeing, in the case of Xe, ions with different  $q/m$  ratios. The signal of the ion after loading is a peak above the noise level of the resonator at its axial frequency due to its high axial energy. This signal is used to fine tune the ring electrode voltage to bring the ion into resonance with the detector for cooling. With only a resolution of 1 Hz, the signal of a cooled ion, i.e. the dip in the noise spectrum, is not visible, as in trap 2 it is smaller than the resolution of the spectrum. It requires several spectra to be averaged and recorded for a longer time to be observable. For a determination of the three eigenfrequencies by the dip method, the FFT is changed to include several seconds (up to 20 s) of data, leading to a sub-Hz resolution.

As an example of the FFT spectrum during ion preparation, the signal of an excited ion is shown in Fig. 4.2. Here, the axial motion of the ion was excited to higher motional energy at  $t = -1.5$  s by an axial burst, an  $rf$ -dipole pulse at the axial frequency, and the ion's signal is visible as a peak. As the ion is still in resonance with the resonator, its energy is dissipated and it cools in again. After a total of 5.5 s, the ion is completely cooled down and not visible any more in the spectra. In order to see the dip, the acquisition time of the FFT would then need to be increased and possibly several spectra averaged to resolve the dip.

In the following, the individual steps for ion preparation will be explained in more detail based on Fig. 4.1.

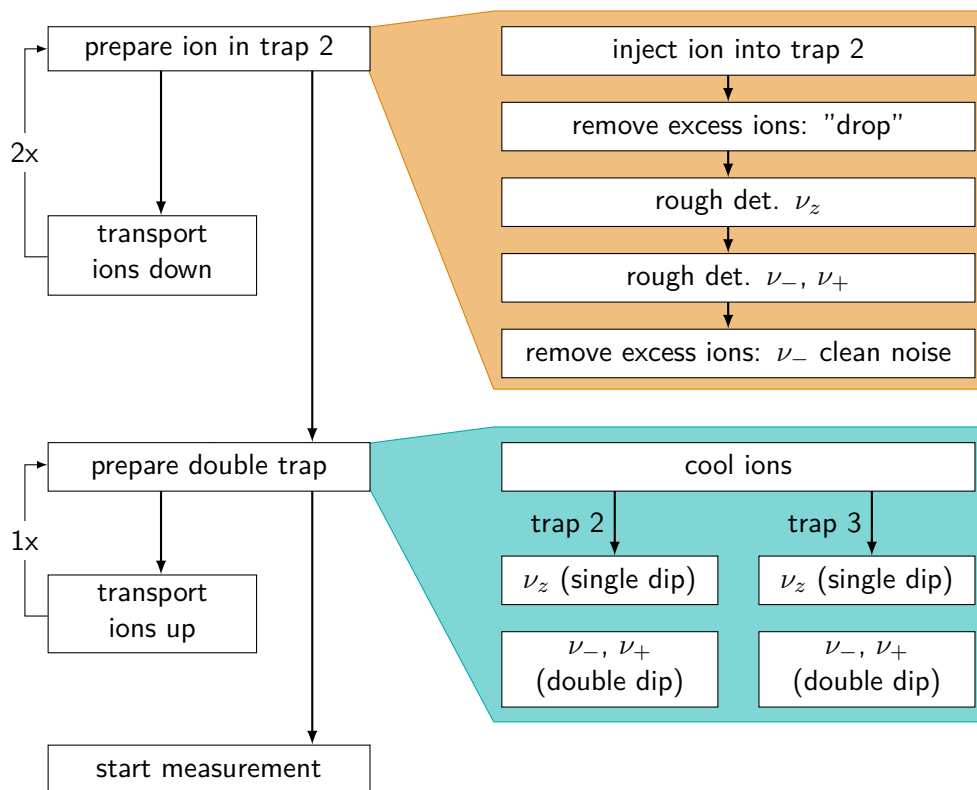


**Figure 4.1:** Preparation steps of ions in the trap before measurements. The ion is loaded into trap 2 and cooled after all excess ions are removed by dropping the trap potential. Its eigenfrequencies are roughly determined before a magnetron clean noise is used to ensure that only a single ion remains in the trap. The ion is then transported one trap down. This process is repeated three times, such that three single ions are available (orange). Afterwards, the eigenfrequencies of two ions in trap 2 and trap 3 are simultaneously determined (blue) for both positions of the three ions in the traps.

### Prepare ion in trap 2

The ions produced in the DreEBIT are preselected by the  $90^\circ$  bender magnet before being guided to the traps. The resolution of the magnet is sufficient to identify the different charge states and isotopes with the MCP at the end of the horizontal beamline, but the transmittance of the beamline allows several charge states and isotopes to reach the traps. The following steps, shown in orange in Fig. 4.1, are needed for the preparation of one single ion.

**Inject ion into trap 2:** An ion bunch is loaded by pulsing down the drift tube on the collector side in the EBIT and transporting the ions through the beamline. In Fig. 4.3 the process of loading into trap 1 is shown. The cryogenic pulsed drift tube

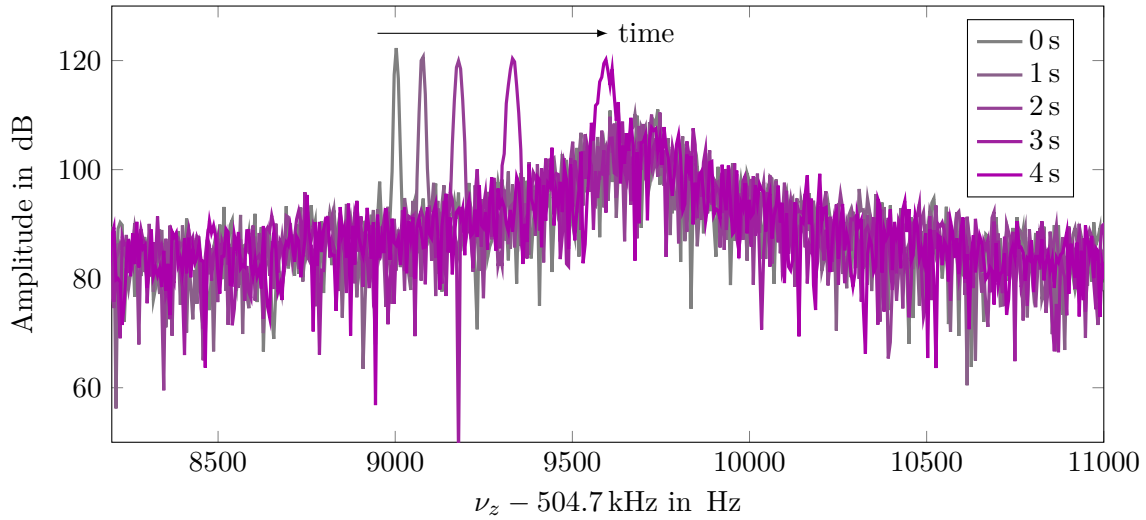


**Figure 4.2:** FFT spectrum of hot a ion cooling in. At time  $t = -1.5$  s the axial motion is excited. As the ion is still in resonance with the resonator, it loses its energy and cools in, see Sec. 2.5.1. After 5.5 s it is cooled down again and the peak disappears.

above the traps is pulsed to a negative potential of  $-10$  V while the ions are in the field-free region (top). Their kinetic energy is hereby decreased to only a few 10 eV per charge. The holder structure of the Penning-trap stack is at ground potential and produces a slightly higher potential on the trap axis. The ions can overcome this potential barrier (as shown in the middle) and move into trap 1, where the upper end cap, correction, and ring electrodes are also at  $-10$  V. The cryogenic drift tube is then pulsed up again to 200 V and a harmonic trap is formed in trap 1 confining the ions (bottom). Afterwards, the ions are adiabatically transported into trap 2, where, as it is equipped with a detection system, the ions can be monitored and prepared.

**Remove excess ions, “drop”:** Usually, more than one ion is loaded into trap 2. As they are not cooled but have high kinetic energies, their signal appears as a peak on the resonator spectrum, similar to the ones shown in Fig. 4.2. Additionally, ions with a large magnetron radius probe anharmonic trap potentials and their axial frequencies can be shifted out of the FFT window. To remove unwanted ions, the trap can be switched to a low trapping potential (“dropping the potential”) for a short time (up to 10 s) allowing ions with a higher axial or magnetron energy to leave the trap. Before, the ion of interest should have, at least very shortly, been in resonance with the resonator to slightly cool the axial motion. Additionally, if unwanted ions persist, a broadband magnetron excitation pulse can be applied to increase the magnetron energy of the ions. If ions remain after several tries, the

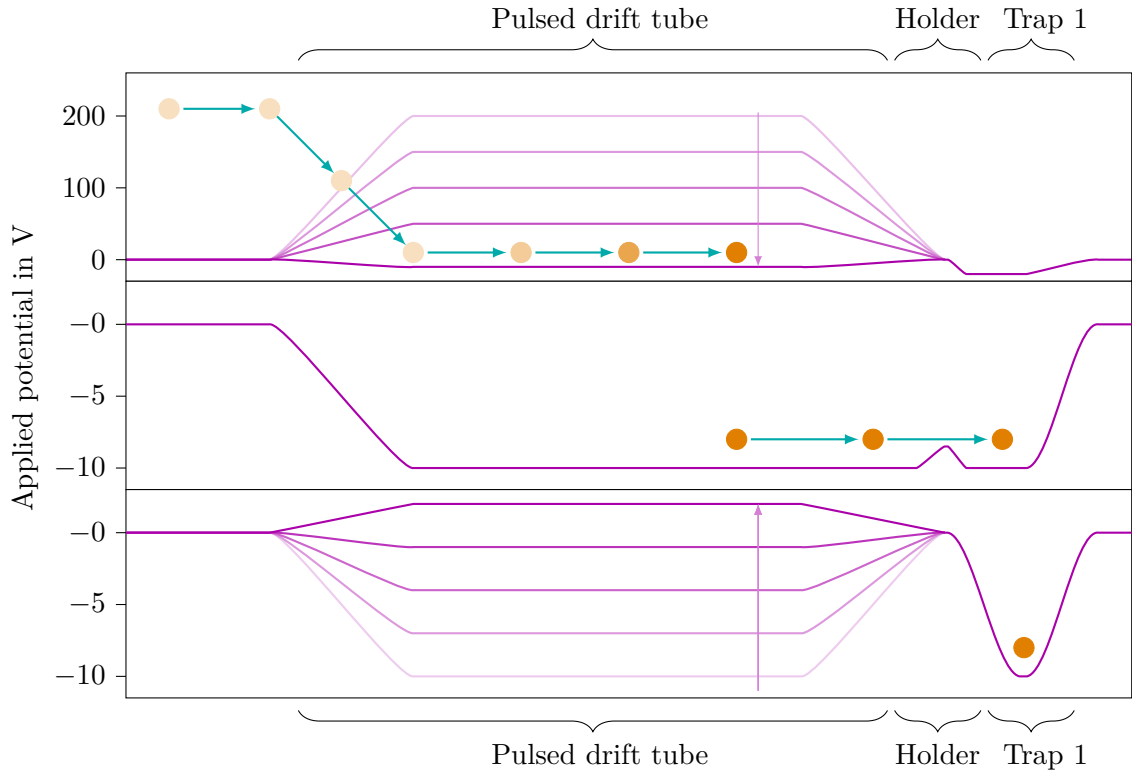


**Figure 4.3:** Loading of ions into trap 1. **Top:** The kinetic energy of the ions (orange, energy not to scale) arriving from the beamline is reduced when they move into the high potential of the pulsed drift tube. This is then pulsed down to a lower potential, effectively decreasing the ions' kinetic energy when they leave the region again. **Middle:** The holder structure of the Penning traps is at ground potential. Since the upper end cap and the correction electrode are set to  $-10\text{ V}$ , the ions can continue into trap 1. **Bottom:** The pulsed drift tube is pulsed up again and a harmonic potential is formed in trap 1.

trap can be emptied by moving the ions to trap 5 (if no ions are in the other traps) or trap 1 (they escape during the next loading process), and load anew.

**Rough determination of  $\nu_z$ ,  $\nu_+$ , and  $\nu_-$ :** If only one ion is left in the trap, the axial frequency can be determined by changing the trap voltage such that the ion is at the center frequency of the resonator. In order to cool the magnetron motion, its frequency is inferred from previous measurements and a quadrupolar coupling is applied to the trap. As the magnetron energy is transferred to the axial motion, a peak appears again until the magnetron energy is dissipated into the resonator. The same steps are repeated for the modified cyclotron frequency. All three eigenfrequencies are then roughly determined by a quick fit to a spectrum exhibiting either a single or double dip.

**Remove excess ions, magnetron clean noise:** In order to ensure that only one ion is left in the trap, a wide range magnetron excitation is turned on, which increases the magnetron energy of all ions in the trap. Simultaneously, the magnetron motion of the ion of interest, which was tuned to resonance with the resonator before, is cooled by applying an *rf*-signal, coupling its magnetron and axial frequency. Both signals are turned on for several minutes.

Finally, the ion is adiabatically transported one trap down by subsequently lowering the potential applied to the electrodes between the two ring electrodes of both traps. The ion loading process is repeated twice for the measurement scheme described in Sec. 2.3 to be possible. This leads to three ions in trap 2, 3, and 4, i.e. position 1 of the ions in the trap stack. Hereby, the second ion should be a different species than the first and third.

### Prepare double trap

As the voltages applied to the neighbouring traps change the axial eigenfrequency of the ion, the three trap frequencies need to be determined simultaneously, shown in blue in Fig. 4.1, for both measurement traps such that both axial eigenfrequencies coincide with the resonance frequencies of their respective detection system. Thereby, the ions are first cooled again after the excess ions are removed. The voltages are then iteratively changed in both traps such that a single dip at the center frequency of the resonator is achieved for both ions. In order to keep the applied voltages symmetric, the trapping potential of trap 3 is also applied in trap 1 and the potential of trap 2 in trap 4.

This process will have slightly changed ( $< 1$  Hz) the axial frequency and therefore also the radial frequencies. For both ions, a symmetric double dip around the axial frequency needs to be restored by changing the frequency of the applied *rf* coupling field. Finally, all three eigenfrequencies are saved in the configuration file for the measurement. The procedure is then repeated after the ions were transported one trap up, i.e. they are in position 2, see Fig. 2.4, in trap 1, 2, and 3, such that for both positions of the ions in the trap stack the frequencies are determined.

## 4.3 Measurement structure

A high-precision mass measurement at PENTATRAP consists of several cycles divided into sub measurements, which are then repeated until the script is stopped, usually when ions in the trap were lost. The structure of one cycle for the Xe measurements is shown in Fig. 4.4. It takes about 12 h, with nearly all of the time taken up by the PnP-measurement. The longest run of the measurements presented in this thesis was over four cycles, i.e. roughly 2 days.

Before the start of the cycle, the ions in the traps are motionally cooled again. The order of the sub measurements, which are explained in the following, starts with a Dip-measurement (shown in blue in Fig. 4.4), where all three eigenfrequencies are determined by a single or a double dip, followed by the PnP-measurement (magenta),

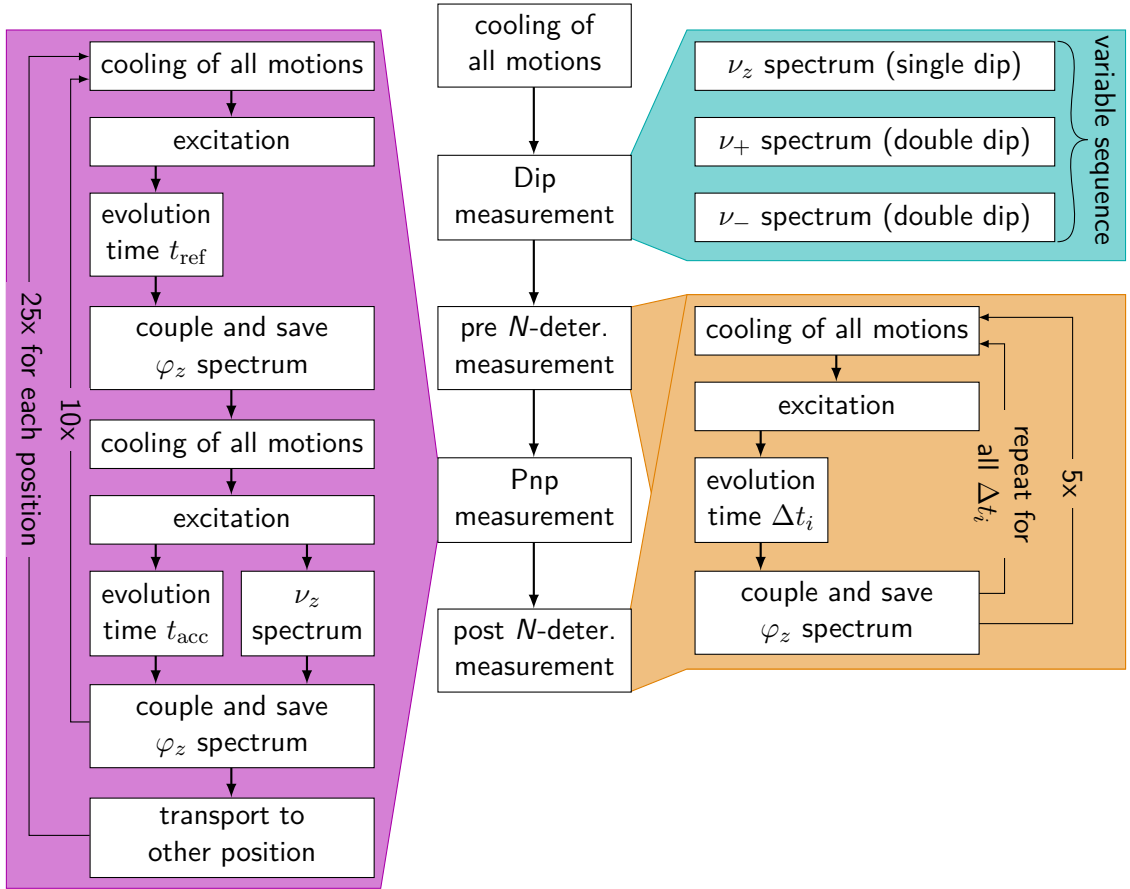


**Figure 4.4:** Measurement structure of a typical cycle. After the cooling of the ions, the three sub measurements, Dip- (blue),  $N$ -determination (orange) and PnP-measurement (magenta) are performed. For more detail on the sub measurements, refer to text.

during which the axial and modified cyclotron frequencies are determined. Before and after (pre and post) the total number of full revolutions of the phase is measured with an  $N$ -determination measurement (orange).

### 4.3.1 Dip-measurement

Spectra for all three eigenfrequencies are, in a variable sequence, saved, either with a single or a double dip for both positions of the ions and in both traps. For most of the measurements in Xe, a single dip spectrum for the axial frequency would be saved before and after a double dip for both magnetron and modified cyclotron frequency. The axial frequency is then interpolated to the time of the double dip spectra and used to calculate the radial frequencies from the position of the double dips, using Eq. (2.72). While the double-dip result for the modified cyclotron frequency can be used as a cross-

check for the frequency obtained in the PnP-measurement and for the  $N$ -determination, only the magnetron frequency is determined from the double dip for the calculation of the free-space cyclotron frequency.

As explained in Sec. 2.3, the magnetron frequency needs to be known to the lowest precision, with a 1 Hz resolution being adequate. The drift of the magnetron frequency over one cycle due to a drift in the magnetic field is only around  $\delta\nu_- = 0.1$  Hz. It is, therefore, sufficient to perform this double dip measurement only once before the start of one measurement cycle. If the ions lived for more than one cycle, the magnetron frequency from the next cycle can be used to interpolate to the time of the axial and modified cyclotron frequency determination in the PnP-measurement.

The difference in the magnetron frequencies of the two ion species, e.g.  $^{131}\text{Xe}^{17+}$  and  $^{132}\text{Xe}^{17+}$ , is  $\approx 1\%$ , which corresponds to a frequency difference of 150 Hz and 70 Hz for trap 2 and trap 3, respectively. The relative mass difference of Re in the ground to the metastable state is only on the order of  $\Delta m/m \approx 10^{-9}$ , see Chapter 7, and, therefore, the frequencies determined by the dip method are the same for both ions in one trap. It is sufficient for the magnetron eigenfrequency to be determined only during the preparation of the ion and the dip measurement is not performed for the Re measurements.

### 4.3.2 PnP-measurement

The calculation of the modified cyclotron frequency from a phase measurement,

$$\nu_+ = \frac{1}{2\pi} \frac{\Delta\varphi + 2\pi N}{\Delta t} \quad , \quad (4.1)$$

was derived in Sec. 2.5.4. There, also the main steps of a PnP-measurement were discussed. They are shown in magenta in Fig. 4.4 and will only be explained very shortly here.

The modified cyclotron motion is excited by an excitation pulse to a certain radius, thereby defining an unknown starting phase of the motion in the radial plane. After an evolution time,  $t_{\text{ref}} = 0.1$  s or  $t_{\text{acc}} = 40.05$  s, the modified cyclotron mode is coupled to the axial mode and the transferred phase  $\varphi_+$  is read out as the phase of the axial frequency  $\varphi_z$ . Since the excitation and the coupling pulses are the same for both evolution times, taking the difference of the phases,  $\Delta\varphi$ , and of the time,  $\Delta t$ , removes unknown but constant, additional phases, making the calculation of  $\nu_+$  possible. Afterwards, all motions are cooled again by coupling to the axial frequency.

New to this scheme is the simultaneous axial frequency determination during the evolution time  $t_{\text{acc}}$ . For a time  $t_z = 36$  s, which is slightly smaller than the evolution time of the modified cyclotron frequency such as not to be affected by the  $rf$ -pulses of the excitation and coupling of the modes, an axial frequency spectrum is recorded. Therefore, both frequencies were determined at nearly the same electric and magnetic field, minimising the uncertainty in the free-space cyclotron frequency determination.

The measurement of the two evolution times is repeated 10 times for higher statistics. The ions are afterwards transported to the other position, e.g. one trap up or down, see Fig. 2.4. The above-described measurements correspond to one so-called pnp-cycle of

the PnP-measurement. In total, 25 pnp-cycles are performed before the end of the PnP-measurement in both traps and positions.

The precision of the phase determination scales with duration of the long phase accumulation time  $t_{\text{acc}}$ , while a long phase accumulation time requires the setup to be stable during this time. Additionally, as a spectrum of the axial frequency is recorded simultaneously, the maximal recording time here is also given by the phase accumulation time. At a longer averaging time the axial dip can smear out as drifts in the frequency are averaged over, while for a short time on the order of just a few seconds the dip might not be resolvable due to higher noise contributions. Therefore, as a trade off, the time  $t_{\text{acc}} = 40.05$  s is chosen.

The coupling strength of the  $\pi$ -pulse transferring the energy of the modified cyclotron to the axial motion is found beforehand by optimising the signal in the frequency spectrum after the coupling, i.e. the height of the peak of the axial ion should be maximised. In order to prevent systematic shifts due to different excitation strengths and different modified cyclotron radii, the amplitude of the pulses, both for excitation and coupling, are kept the same for the two ions in one trap. Instead, to still apply a complete  $\pi$ -pulse, the length of the pulses is adapted to the ion.

### 4.3.3 $N$ -determination measurement

In order to calculate  $\nu_+$ , the full number of revolutions  $N$  needs to be known. To that end, the steps of a PnP-measurement are performed for several times  $\Delta t_i$  and  $N_i$  is calculated:

$$N_i(\nu_+) = \nu_+ \cdot \Delta t_i - \frac{\Delta \varphi_i}{2\pi} \quad . \quad (4.2)$$

First, the right  $\nu_+$  needs to be found, such that  $N_i$  is an integer for all times  $\Delta t_i$ . Second, the full number of revolutions can then be calculated for the time interval of the reference and the accumulated time.

The idea behind the determination of  $N$  can be understood by looking at the absolute difference of  $N_i$  to the closest integer  $[N_i]$  for different  $\nu_+$ ,

$$F(N_i, \nu_+) = |N_i - [N_i]| \quad . \quad (4.3)$$

On the left side of Fig. 4.5 this is shown for a correct modified cyclotron frequency of  $\nu_+ = 100$  Hz for different phase accumulation times (coloured plots).  $F(N_i, \nu_+)$  is zero for  $N_i$  being an integer, which happens at  $\nu_+$ , but also at  $\nu_+ \pm s/\Delta t_i$ , with  $s$  being an integer. The sum of  $F(N_i, \nu_+)$  for all time intervals  $\Delta t_i$  is shown on the right side in black and demonstrates the need for several evolution times to determine  $N$ . Only the frequencies, where the sum is zero, can be considered to be the right frequency. There, the determination of  $\nu_+$  by the dip method comes into play as a starting parameter.

Fig. 4.5 also demonstrates the need for accumulation intervals which fulfill the relation  $\Delta t_i/\Delta t_j \neq s_i/s_j$ . If this is not the case, as shown in the top panel, the two frequencies 100 Hz and 101 Hz could be considered to be the right frequency. In the bottom panel, the accumulation times were slightly off, such that the sum of  $F(N_i, \nu_+)$  only shows one minimum at the right frequency of 100 Hz.

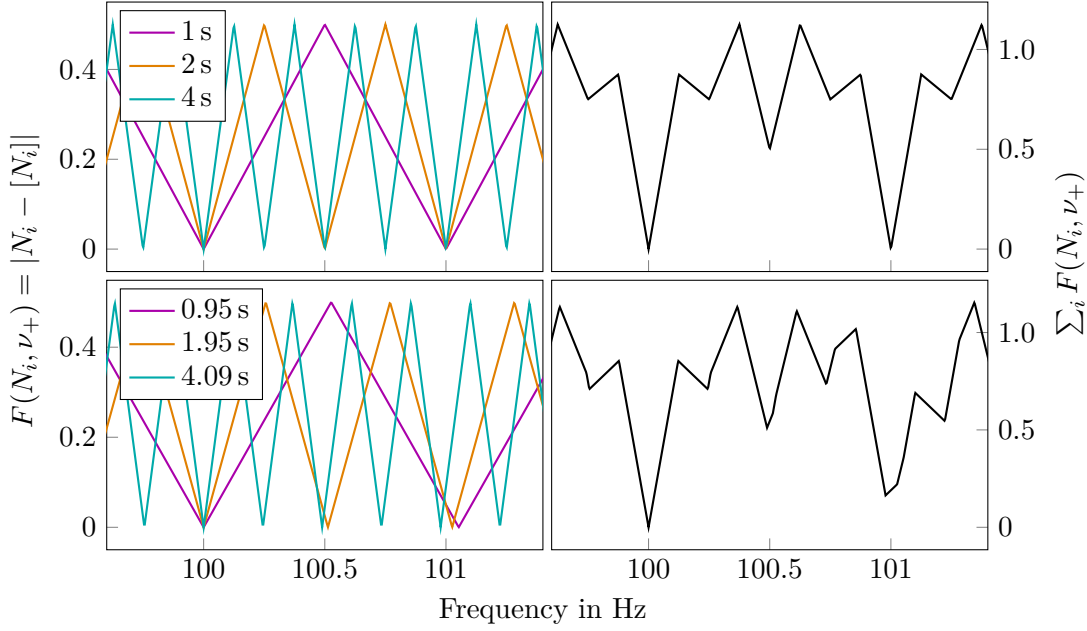


**Figure 4.5:**  $F(N_i, \nu_+)$  for different evolution times. **Top:** The time intervals  $\Delta t_i$  are multiples of each other (left, coloured), leading to two possible right frequencies, at 100 Hz and 101 Hz, as shown by the sum of fractional parts being zero (right, black). **Bottom:** The time intervals  $\Delta t_i$  are slightly off and only one frequency represents the correct modified cyclotron frequency.

In reality, as the phases exhibit an uncertainty of 0.2 rad, more than three phase-evolution times are used to unambiguously identify  $\nu_+$  and  $N$ . Therefore, eight times between  $t_{\text{ref}} = 0.1$  s and  $t_{\text{acc}} = 40.05$  s are chosen, see Tab. 5.2. For higher statistics, the measurement is repeated 5 times for all accumulation times.

This measurement is performed before and after the PnP-measurement. During the  $\sim 11$  h measurement the phase difference can change by more than  $2\pi$  due to the decreasing magnetic field, see Fig. 5.7. The post  $N$ -determination measurement can be used as a cross check by comparing it to the last phase determination during the PnP-measurement. This way, a possibly wrong phase unwrapping, see Sec. 5.4.2, is prevented. During the analysis of the Xe data, it was noted that the phase was stable enough to skip the second  $N$ -determination measurement. It was, therefore, not performed for the Re measurements.

## 4.4 Measuring the magnetic field gradient

Most of the systematic shifts discussed in Sec. 2.2 need to be estimated as they cannot be measured with the current trap setup. For example, the image charge shift measured in [Sch+19a] requires two resonators precisely tuned to the axial eigenfrequency of a

proton and  $^{12}\text{C}^{6+}$  ion. As only one resonator is currently used at PENTATRAP for each measurement trap, such a measurement is not possible.

One of the main sources of systematic shifts is higher-order magnetic field terms, especially a gradient, and is one of the few systematic effects which can be measured. An example of such a measurement will be explained in the following. The estimation of the other systematic shifts is given in [Sec. 6.1.3](#) for the mass measurements of Xe ions.

In the presence of a lower order term  $C_1$ , e.g. arising from patch potentials on the trap electrodes, the trapping potential in axial direction is changed to

$$\hat{\Phi}_z = C_2 V_0 z^2 + C_1 V_1 z \quad , \quad (4.4)$$

where  $V_1$  is the strength of the gradient field and  $C_1$  reflects the dependency on the trap geometry. The resulting axial equation of motion exhibits an additional, constant driving term

$$\ddot{z} = -\frac{2qC_2V_0}{m}z - \frac{qC_1V_1}{m} \quad . \quad (4.5)$$

Solving the driven harmonic oscillator equation leads to a shift of the equilibrium position of the axial motion of:

$$\Delta z = \frac{C_1 V_1}{2C_2 V_0} \quad , \quad (4.6)$$

but does not change the axial frequency.

In the presence of higher-order terms, the magnetic field at the position of the ion is changed to:

$$B_{\Delta z} = B_0 + B_1 \Delta z \quad . \quad (4.7)$$

This leads to a relative shift of the free-space cyclotron frequency of:

$$\frac{\Delta \nu_c}{\nu_c} = \frac{C_1 V_1}{2C_2 V_0} \frac{B_1}{B_0} \quad . \quad (4.8)$$

Experimentally, an artificial  $C_1$ -term can be produced by applying an offset voltage to one, or with opposite sign to both, correction electrodes [[Doo18](#)]. By varying this voltage and measuring the free-space cyclotron frequency, higher-order magnetic field terms can be investigated. Such a measurement is analysed in [Sec. 6.1.3](#).

# 5

---

## Data Analysis Procedure

---

For the determination of the mass ratio of two ions, their free-space cyclotron frequencies need to be calculated. Therefore, all sub measurements described in the previous chapter need to be analysed to determine the three eigenfrequencies. As during one measurement cycle already more than 3000 spectra are saved, the analysis is performed with several self-written scripts for each of the sub measurements. These include fitting of the single or double dip spectra, determining the phase and calculating the modified cyclotron frequency, and finally calculating the free-space cyclotron frequency and the frequency ratio.

Automated scripts, which only require the basic measurement setting as input, e.g. the rough frequencies determined during the preparation of the ions, are used to perform the analysis. In the scope of this thesis the analysis was performed with MATHEMATICA 11.3, which is a computer-algebra program written in the WOLFRAM language. A vast variety of functions is predefined, making quick mathematical calculations and graphical presentations of data possible. With the help of the NOTEBOOK, the interface between the Kernel and the programmer, more sophisticated scripts, called Modules, can be written, along with the possibility to handle data by importing and exporting. In general, the analysis of the data is performed independently by a second person using a PYTHON-based data analysis package and the final result comprises both analyses.

In the following chapter, the steps needed to determine all three eigenfrequencies and the free-space cyclotron frequency required for the calculation of the frequency ratio are explained in detail. The example data shown is taken from different measurements and the frequencies given thus do not have to match from one example to the next.

## 5.1 Analysis steps

As explained in the previous chapter, a measurement consists of several sub measurements, namely the Dip-, PnP-, and pre/post  $N$ -determination measurements, which are needed to calculate the frequencies:

**Dip-measurement:** For the determination of the radial eigenfrequencies ( $\nu_+$  and  $\nu_-$ ) one spectrum during coupling to the axial motion, as well as at least one axial spectrum with no coupling is recorded. Depending on the measurement, the cyclotron double-dip spectrum was left out. If it is performed, it can be taken as a starting value for the  $N$ -determination. Fitting of the spectrum with the respective function yields the three eigenfrequencies, from which only the value of the **magnetron** frequency is taken for the determination of the free-space cyclotron frequency. The other two eigenfrequencies need to be determined to higher precision and are therefore measured more often (axial) or with a phase-sensitive technique (modified cyclotron).

**PnP-measurement:** The **modified cyclotron** frequency is determined with the PnP-technique, see Sec. 2.5.4, by measuring the phase difference between the reference phase ( $\varphi_{\text{ref}}$ ) and the phase after a long accumulation time ( $\varphi_{\text{acc}}$ ). While the phase accumulation is ongoing, a spectrum featuring an **axial** dip is saved. This is repeated ten times for higher statistics.

**Pre/Post  $N$ -determination:** In order to calculate the **modified cyclotron** frequency from the phase measurements, the number of full revolutions  $N$  is needed. This is done before (pre), and, as a consistency check for the Xe measurements, also after (post) the PnP-measurement.

The measurement is performed in several cycles and for different positions of the ions in the traps, see Fig. 2.4, as the ions are shifted inbetween measurements, leading to an alternating  $\nu_c$  determination for two different ion species in one trap. During the analysis, it is interesting to compare the frequencies of one certain ion in one trap over the whole measurement, for example, to see a drift in the modified cyclotron frequency due to the changing magnetic field. As there are two positions and two traps, these trends can be investigated in four different cases during one measurement.

The ten spectra for both the axial frequency and the modified cyclotron phase can be analysed in two ways:

**Jointly:** In order to estimate the quality of the acquired data and to get a clue on the behaviour of the various parameters of the system, a course analysis which is based on averaging all 10 spectra or phases is performed.

**In groups of 2:** The averaging of all ten phases or spectra leads to a loss of information about the temporal behaviour of the measured quantities. Thus, an averaging must

be avoided. Presently, the axial dip width in trap 2 and the resulting signal-to-noise ratio requires averaging at least two spectra to be able to determine the axial frequency reliably. Additionally, only determining the phase of one spectrum does not allow assigning a realistic uncertainty. Using instead groups of two spectra gives the possibility to see short term fluctuations, e.g. in the external magnetic field, and to identify data with an unusual behaviour which require a closer look afterwards.

Combining all three eigenfrequencies to the free-space cyclotron frequency is done for both the joint and the grouped analysis. This allows a last consistency check if the analysis for both cases was successful.

The analysis of the data is divided into several steps, see Fig. 5.1. In the following, a short description of these steps is given. The eigenfrequencies are marked bold at the step where they are calculated:

1. **Axial averaging:** The ten axial spectra are averaged together for the joint analysis and in groups of two for the grouped analysis.
2. **Axial fitting:** The **axial frequency** of the dip is determined by fitting the averaged spectra.
3. **Dip-measurement:** The results from the Dip-measurement are analysed by fitting the spectra with the respective functions to determine all three eigenfrequencies, especially the **magnetron eigenfrequency**. Here, the averaging of the spectra is already done during the measurement and just one spectrum is saved for each frequency determination.
4.  **$N$ -determination:** The number of full revolutions  $N$  of the phase is calculated by reading out the axial phase for multiple accumulations times.
5. **Phase determination:** The phase is readout of the axial phase spectra and averaged, both for the grouped and the joint analysis. With  $N$  known from the previous step, the **modified cyclotron frequency** is then calculated.
6. **Comparison:** As a cross-check, a comparison of joint and grouped analysis is performed to discover fit problems or a wrong unwrapping of the phase in the grouped analysis.
7. **Free-space cyclotron frequency:** The **free-space cyclotron frequency** is calculated with the invariance theorem given in Eq. (2.11).
8. **Ratio determination:** Finally, the ratio of the two frequencies in both traps is determined by either the polynomial or the cancellation method.

The analysis described in the following is divided into the calculation of the eigenfrequencies. This includes **step 1** and **2** for the axial (Sec. 5.2), **step 3** for the magnetron (Sec. 5.3) and **step 4** and **5** for the modified cyclotron frequency (Sec. 5.4), followed by

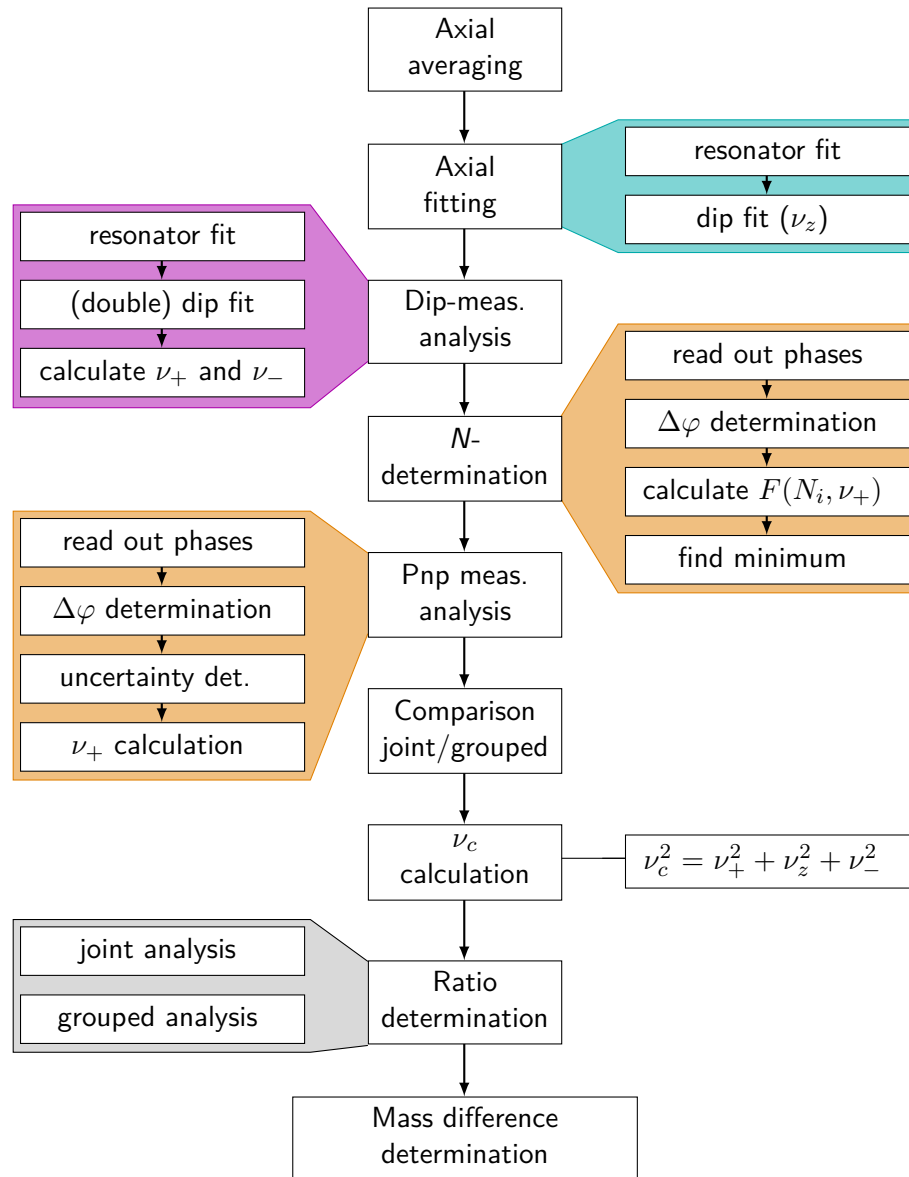


**Figure 5.1:** Analysis procedure for the determination of the mass difference. The colours separate the steps needed to determine the axial frequency (blue), magnetron frequency (magenta), and modified cyclotron frequency (orange). The steps are described in detail in the text.

a comparison of the grouped and joint analyses (**step 6**, [Sec. 5.5](#)) and the determination of the free-space cyclotron frequency (**step 7**, [Sec. 5.6](#)). In [Sec. 5.7](#), the calculation of the frequency ratio will be explained (**step 8**).

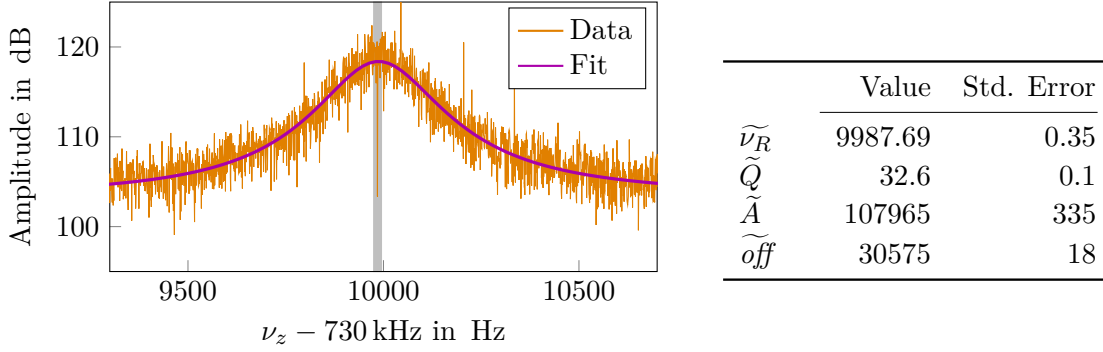


**Figure 5.2:** Resonator fit to a single-dip spectrum. The data (orange) is plotted with the local oscillator frequency,  $\nu_{\text{local}} = 730$  kHz, subtracted. Even though the spectrum features several noise peaks, the resonator fit (magenta) describes it well. The grey area marks the region around the dip shown in Fig. 5.3. In the table on the right the fit parameters and their uncertainties are stated. The small  $\tilde{Q}$  is explained in the text.

## 5.2 Axial eigenfrequency determination

Before the axial frequency is determined by fitting the spectra with the theoretical description, the spectra are averaged (**step 1**). The amplitude of the recorded spectra is given in dB. For the determination of the axial frequency, the averaging of the logarithmic scale or first converting it to a linear scale, then averaging and converting back, does not change the result of the axial frequency.

The signal of the axial detection system as given by Eq. (2.54) is further amplified at room temperature, with an amplification factor  $A$ , before the FFT is performed, see Fig. 3.11. The cryogenic amplifier also adds an additional thermal noise term  $u_{en}$ :

$$u_{th}^{\text{det}} = A \cdot \sqrt{u_{sig}^2 + u_{en}^2} \quad , \quad (5.1)$$

where  $u_{sig}$  is the thermal noise of the signal, for example the resonator. A thermal dependence  $\kappa_{\text{det}}$  of the transfer function of the signal on the frequency is possible, which would add an additional factor  $(1 + \kappa_{\text{det}}(\nu - \nu_R))$  in Eq. (5.1) [Köh15]. During the analysis of the axial spectra no effect on the axial frequency of this term in the fitting function was observed. In order to make the fit routine more efficient, this term, and hence the additional fitting parameter  $\kappa_{\text{det}}$ , was not included.

For the axial fit (**step 2**) to work reliably, starting values for the fit parameters are required. These are obtained from first only fitting the resonator spectrum with the function

$$F_{\text{res}}(\nu) = 10 \log \left[ \frac{\tilde{A}}{1 + \tilde{Q}^2 \left( \frac{\nu}{\tilde{\nu}_R} - \frac{\tilde{\nu}_R}{\nu} \right)^2} + \tilde{off} \right] \quad (5.2)$$

to the spectrum with the amplitude in dB. Here,  $u_{res}$  (Eq. (2.55)) was inserted into Eq. (5.1) for  $u_{sig}$ . The parameters of the fit are the resonance frequency  $\tilde{\nu}_R$  and  $Q$ -value  $\tilde{Q}$  of the resonator, as well as the amplitude  $\tilde{A}$ . The offset  $\tilde{off}$  represents the noise floor of the spectrum. The result of such a resonator fit to a spectrum featuring an axial dip from trap 2 is shown in magenta in Fig. 5.2, with the values obtained for the parameters of  $F_{res}(\nu)$  in the table next to it. The fit is performed with the function `NONLINEARMODELFIT` in `MATHEMATICA` and the uncertainties are taken from the `PARAMETER TABLE`.

The result of the  $Q$ -value is not in agreement with the values stated in Sec. 3.3.2. This is due to its definition

$$Q = \frac{\nu}{\Delta\nu} \quad . \quad (5.3)$$

While the width of the resonance curve  $\Delta\nu$  is not changed by subtracting the local oscillator frequency, the  $Q$ -value scales with the frequency at which the spectrum is recorded. In order to compare to the experimental value, it can be scaled up to the real frequency  $\nu_{real}$

$$Q_{real} = \frac{\nu_{real}}{\nu_{down}} Q_{down} \quad . \quad (5.4)$$

Here,  $\nu_{down}$  is the downmixed frequency around 10 kHz as shown in the Fig. 5.2 and  $Q_{down}$  is the resulting value at this frequency, again either from a fit to the resonator or dip fit. This leads to a more realistic  $Q_{real} \approx 2300$ , which is closer to the value given in Tab. 3.1 ( $Q = 3000$ ) for trap 2.

The fit function for the single dip can be expressed by

$$F_{dip}(\nu) = 10 \log \left[ \frac{A}{1 + \left[ \frac{\nu}{2\pi\tau(\nu^2 - \nu_z^2)} - Q \left( \frac{\nu}{\nu_R} - \frac{\nu_R}{\nu} \right) \right]^2 + off} \right] \quad , \quad (5.5)$$

where the  $u_{dip} = \sqrt{4k_B T \Re(Z_{dip}) \Delta\nu}$  (Eq. (2.64)) was inserted into Eq. (5.1) for  $u_{sig}$ . Compared to the resonator fit, the function is described by the additional parameters for the axial frequency  $\nu_z$  and the cooling time constant  $\tau$ .

Tab. 5.1 shows the starting values for the dip fit routine. The values with a tilde are taken from the resonator fit. There are two possibilities for the starting value of the axial frequency: (1) it can be taken from the configuration file of the measurement setup, i.e. from the preparation of the ion or (2) the fitted resonator curve, see Fig. 5.2, is subtracted from the spectra and the minimum is taken around the resonator frequency. The second method has the advantage that if jumps in the axial frequency occur, its starting value is already close to the real frequency. Both starting values lead to the same frequency determination, while the first possibility is more reliable. This could be related to the implementation of the fitting algorithm in `MATHEMATICA`, `NONLINEARMODELFIT`, which could be more robust with less precise starting values, e.g. the precision of the axial frequency specified in the configuration file is on a 100 mHz level, whereas the spectrum is recorded with frequency steps of  $\Delta\nu_{spectrum} = 1/t_z = 0.027$  Hz.

**Table 5.1:** Starting parameters for the dip fit routine. The values with a tilde are results from the resonator fit. The restrictions originate from several test runs of the fit routine and are not all simultaneously necessary for all spectra, but also do not disrupt the routine if all are applied.

	starting value	restriction
$\nu_R$	$\widetilde{\nu}_R$	$ \nu_R - \widetilde{\nu}_R  \leq 1000 \text{ Hz}$
$\nu_z$	$\nu_{z,\text{config}}$	$ \nu_z - \nu_{z,\text{config}}  \leq 2 \text{ Hz}$
$\tau$	0.3	$\tau > 0$
A	$\widetilde{A}$	$A > 0$
Q	$\widetilde{Q}$	$Q > 0$
off	$\widetilde{\text{off}}$	$\text{off} > 0$

As jumps in the axial frequency only happened before the stabilisation system in the magnet laboratory was optimised (see Sec. 3.3.1), the axial frequency taken from the preparation of the ion is a good enough guess as a starting parameter.

The last column of Tab. 5.1 shows the restrictions for the individual fit parameters. The starting value of the axial frequency for the grouped spectra needs to be known better than for the joint spectra, where the starting value can be several Hz off. This is due to the fact that averaging more spectra also averages out the noise, while noise peaks close to the axial dip can be more pronounced in the grouped spectra. Therefore, the starting value for the grouped fit is taken from the fit to the joint spectra.

If any of the last four parameters in Tab. 5.1 becomes negative during the `NONLINEARMODELFIT`, the logarithm cannot be applied and the fit routine results in an error. In order to prevent this, these values are restricted to be positive.

The result of an axial dip fit is shown Fig. 5.3 with the values for the parameters shown in the table on the right side. The fit function describes the fit reasonably well, as no artefact is visible in the residuals in the lower plot. An obviously failed fit would result in an offset of the dip frequency by at least 1 Hz, such that the fitting curve and the data points obviously do not match any more. Effects on a smaller scale cannot be noticed by looking at such a spectrum and the fitting function needs to be trusted. A comparison between different scripts and programming languages is, therefore, useful.

The fitting routine for the axial frequency was optimised for the downmixed spectra, i.e. the local oscillator frequency was subtracted, as shown in the plots. While fitting of the spectra results in the same value for both the downmixed spectrum and the spectrum at the true frequencies, it is less robust in the latter case. At the higher frequencies, a negative noise dip close to the axial dip was more often mistaken for the axial signal. Therefore, the fitting is performed at the downmixed frequency of  $\sim 10 \text{ kHz}$  and the local oscillator frequency is added afterwards.

As shown in Fig. 5.2 the full spectrum exhibits several positive noise peaks and also negative noise dips extending to values smaller than the resonator curve. They disappear from spectrum to spectrum and are usually only a fraction of the dip width wide, and

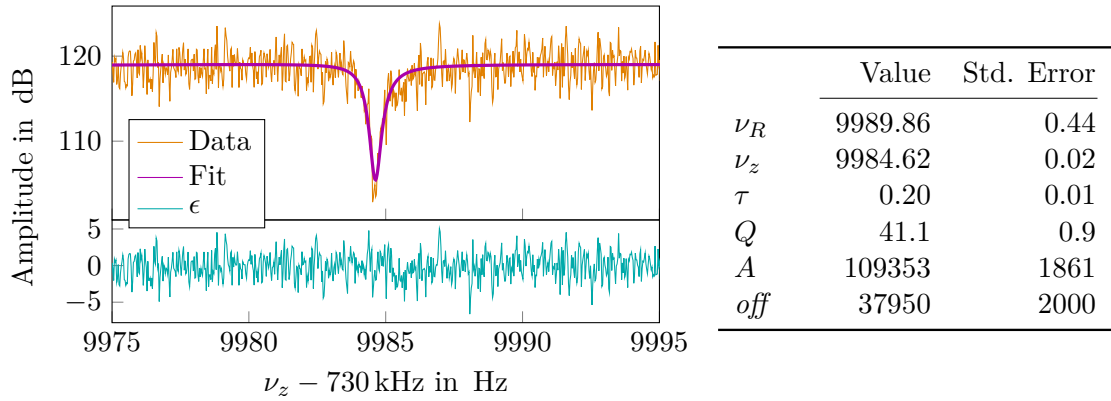


**Figure 5.3:** Detailed view of the axial dip from the spectrum shown in fig Fig. 5.2 (grey area). The fit describes the flanks of the resonator around the dip and the dip itself well, see the residuals  $\epsilon$  in the lower plot. The table on the right gives the results of the `NONLINEARMODELFIT` with the uncertainties from the covariance matrix.

hence cannot be ions. In order to prevent the fit algorithm from identifying one of these as the ion’s signal, only the spectrum around the center of the resonator ( $\nu_R \pm 30$  Hz) is taken into account to fit the axial dip. While the dip is then fitted well, see the residuals in Fig. 5.3, the left out noise floor of the resonator is usually not met quite so well and offset to higher values (compare the two results for *off* and their uncertainties). As the possible values for the axial frequency are already quite restricted, see Tab. 5.1, the whole spectrum could be taken into account if no negative noise dips fall into the region around the dip. Thereby, the computing time is increased quite drastically. While the noise floor, in this case, is reproduced well by the fit, the resonator shape around the dip suffers. As the effect of the data range on the axial frequency is well below its uncertainty, the dip fit is performed using the small frequency range around the dip. In the future, more investigations of the included frequency range are of interest, see [Lan19].

As already mentioned above, the fit works more reliably at the down-mixed frequency. This can be understood as an artefact of the fit algorithm. In a least-square algorithm, the optimal fitting curve is found by minimising the sum of the distances of all data points to the curve squared. The precision to which this is evaluated depends on the computing power and the algorithm used. If the axial frequency is at 730 kHz and the fit evaluates to a certain relative precision, then the absolute uncertainty is larger than compared to a downmixed frequency.

### 5.3 Magnetron eigenfrequency determination

In order to determine the magnetron frequency, the Dip-measurement is analysed (**step 3**). For the Xe measurements, the sequence of the saved spectra was: axial (single dip)

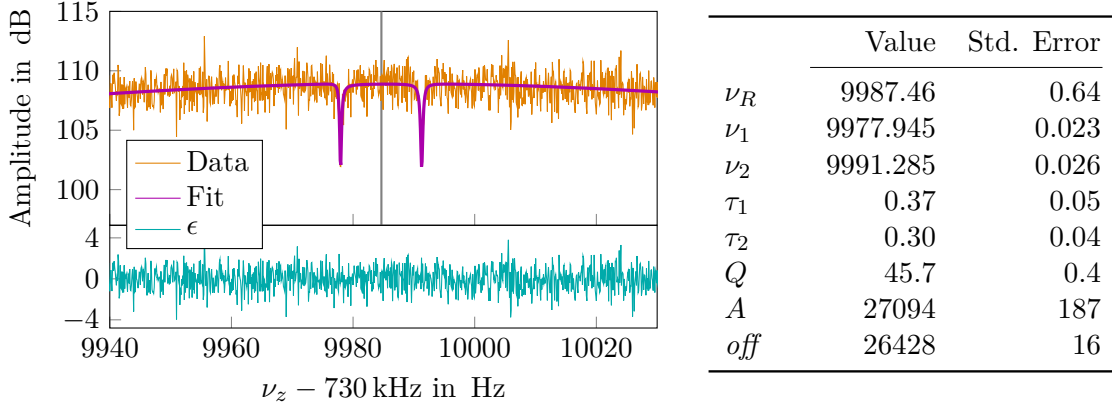


**Figure 5.4:** **Left:** Double dip fit for the determination of the magnetron frequency, with the residuals of the fit shown below. The grey line corresponds to the axial frequency, interpolated from the axial measurement before and after recording this double dip spectrum. **Right:** The results for the fit parameters and their uncertainties are stated in the table.

– magnetron (double dip) – modified cyclotron (double dip) – axial (single dip). The axial frequency can, therefore, be interpolated to the time when the magnetron double dip spectrum was saved.

The magnetron eigenfrequency is determined by applying an *rf*-field at the frequency

$$\nu_{rf} = \nu_-^{rf} + \nu_z^{rf} \quad (5.6)$$

to one of the correction or end cap electrodes, which results in a double dip in the spectrum, see Sec. 2.5.3. Similarly to the single dip, the fit function for a double dip can be found by inserting  $u_{double}$  (given in Eq. (2.71)) for  $u_{sig}$  in Eq. (5.1):

$$F_{double}(\nu) = 10 \cdot \log \left[ \frac{A}{1 + \left[ \frac{\nu}{2\pi\tau_1(\nu^2 - \nu_1^2)} + \frac{\nu}{2\pi\tau_2(\nu^2 - \nu_2^2)} - Q \left( \frac{\nu}{\nu_R} - \frac{\nu_R}{\nu} \right) \right]^2 + off} \right]. \quad (5.7)$$

The steps for the double dip fit are similar to the ones for the single dip. First, the resonator is fitted with Eq. (5.2) and the parameters are used as the starting parameters for the double dip fit. The positions of the two dips are found by subtracting the resonator fit from the spectrum and taking the two minima around the resonator frequency while ensuring one is lower and one higher such as not to accidentally mistake a noise peak for the ion's signal. The starting parameters for the dip widths  $1/2\pi\tau_1$  and  $1/2\pi\tau_2$  are chosen to be 1.

In Fig. 5.4 a double dip spectrum and the corresponding fit are shown together with the results for the parameters. The axial frequency used in the *rf*-field for this double

dip was  $\nu_z^{rf} = 9984.6 \text{ Hz} + 730 \text{ kHz}$  (grey line). The frequencies of the two dips lie, nearly perfectly, symmetric around the axial frequency. As expected from the Rabi splitting, the dip widths  $1/2\pi\tau_1$  and  $1/2\pi\tau_2$  agree within  $1\sigma$  and are roughly half the width of the single dip, which is given in Fig. 5.3. In the lower plot the residuals of the data and the fit is shown. The double dip structure is not visible there and the fit describes the data well.

From the double dip fit, the magnetron frequency can be calculated by [Ulm11]:

$$\nu_- = \nu_{rf} + \nu_z^* - \nu_1 - \nu_2 \quad . \quad (5.8)$$

Here, the axial frequency  $\nu_z^*$  is the interpolated value from the fitted single dip spectra saved before and after the magnetron double dip measurement. With the uncertainty of the axial frequency from the single spectrum,  $\approx 0.02 \text{ Hz}$ , see Fig. 5.3, the total uncertainty of the magnetron frequency is

$$\Delta\nu_- = \sqrt{(\delta\nu_z^*)^2 + (\delta\nu_l)^2 + (\delta\nu_r)^2} \approx 0.035 \text{ Hz} \quad , \quad (5.9)$$

which is below the required precision, see Sec. 2.3.

For the Re measurements the Dip-measurement was not performed. As the voltages applied to the traps are identical for the metastable and the ground state, also the magnetron (and axial) frequency are the same for both ions on the level to which they can be determined with a double dip. It is sufficient, therefore, to take the value from the ion preparation with an uncertainty of  $0.1 \text{ Hz}$ , which is larger than the uncertainty of the double-dip method but still below the required uncertainty.

## 5.4 Modified cyclotron eigenfrequency determination

The modified cyclotron frequency is determined with a PnP-measurement consisting of 20 phase measurements per pnp-cycle for each ion in each trap, ten for the reference time  $t_{\text{ref}}$  and ten for the long accumulation time  $t_{\text{acc}}$ . The phase difference  $\Delta\varphi_i = \varphi_{\text{acc},i} - \varphi_{\text{ref},i}$  of each run  $i$  is needed to calculate the modified cyclotron frequency according to Eq. (2.77) for the time interval  $\Delta t = t_{\text{acc}} - t_{\text{ref}}$ . This results in ten modified cyclotron frequency values for each pnp-cycle of one ion in one trap.

The individual steps for the calculation of the modified cyclotron frequency, which will be explained in the following in more detail, are:

1. **Reading out the phase:** For each phase determination, a spectrum around the axial frequency is recorded. The phase needs to be readout from this spectrum at the position of the axial frequency.
2. **Determining the phase difference:** For each of the ten long and short phases the phase difference is determined. This requires to remove sudden jumps in successive measurements of  $\pm 2\pi$ , see Sec. 5.4.1.
3.  **$N$ -determination:** A separate measurement of phase differences for several different accumulation times allows inferring the total number of full revolutions  $N$ .

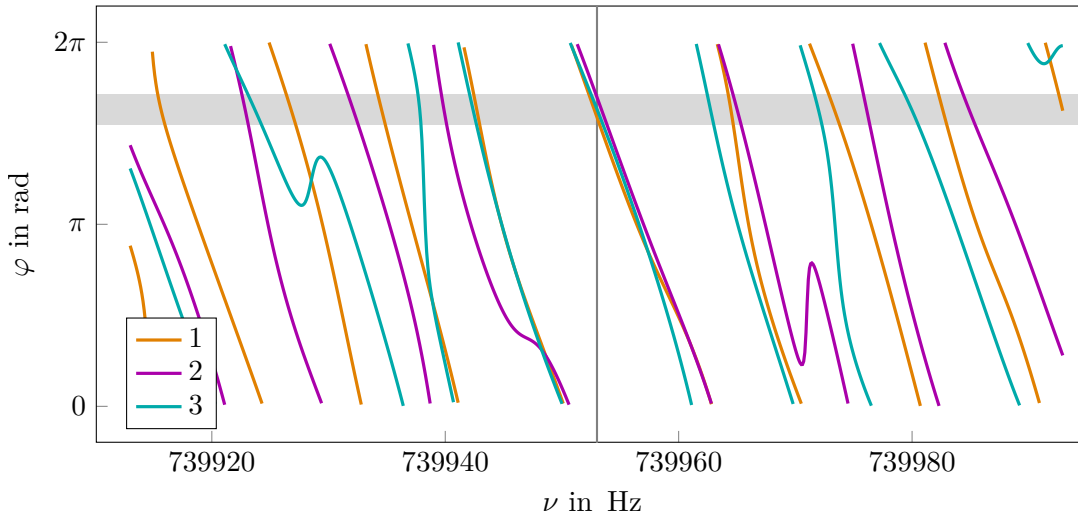


**Figure 5.5:** Three subsequent phase spectra of the axial mode after the coupling pulse. The phase is random, except around the axial frequency (vertical grey line), where the three curves coincide. At the position of the axial frequency the phase for the modified cyclotron frequency is read out (horizontal grey bar).

4. **Error assignment:** For the joint and the grouped analysis the phases are averaged. The uncertainty is then the error of the mean value.
5. **Modified cyclotron frequency calculation:** Following Eq. (2.77), the modified cyclotron frequency is determined.

#### 5.4.1 Reading out the phase

For all 20 (ten reference and ten accumulated) phase measurements for one ion during one pnp-cycle a phase spectra of the axial resonator around the axial frequency is saved. In Fig. 5.5 three consecutive spectra for the accumulated phase are shown. The axial frequency used in the coupling of the two modes is marked by the vertical grey line, the readout phases at this frequency lie in the horizontal grey area. The phase is only defined around the axial frequency, which can be seen as only there the three phases overlap. For higher or lower frequencies they quickly run out of tune.

A single readout phase is not assigned an error. The main reason for that is the fluctuation of the phase from one spectrum to the next. Averaging of the ten phases for the joint analysis leads to an error of the mean value of around 0.2 rad. An error could be assigned by taking the axial frequency uncertainty and reading out an upper and lower limit for each phase, which results in an uncertainty well below the scattering of the individual values and is thus negligible compared to the averaging uncertainty.

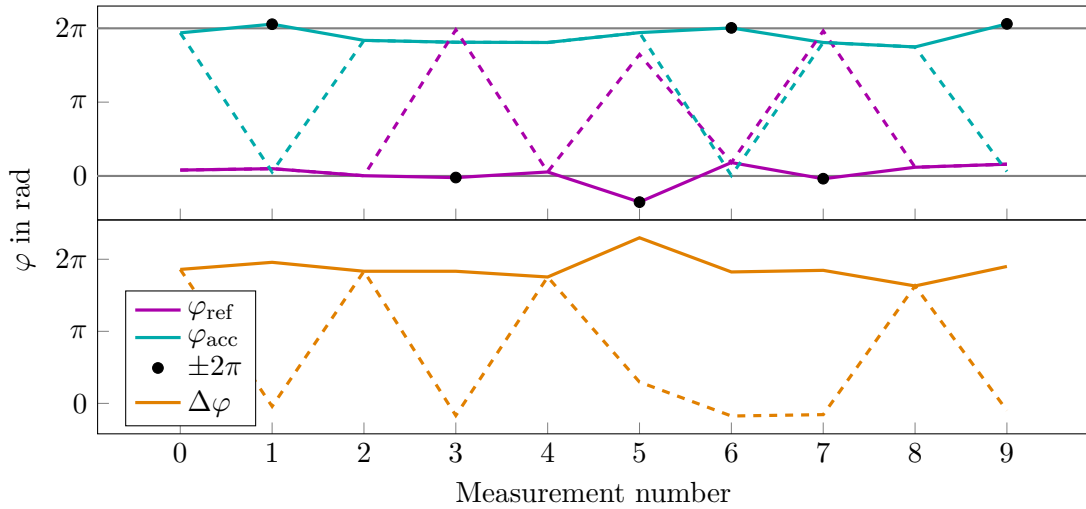


**Figure 5.6:** Principle of unwrapping the phases. **Top:** The measured phases for the reference and accumulated time (dashed lines) and their unwrapped results (solid lines) are shown. The black dots indicate where  $\pm 2\pi$  was added. **Bottom:** The difference of the two phases is shown, again the dotted line corresponds to the difference of the measured phases and the full line to the difference of the unwrapped phases.

### Phase unwrapping

When dealing with phases, the phase is always wrapped, meaning it is bound between 0 and  $2\pi$ . A trend during the phase measurement, e.g. a changing magnetic field, will lead to a gradually changing phase. For a long enough measurement time, such a trend will always lead to jumps of  $\pm 2\pi$ . For example, if the phase is close to the boundary of 0 for one phase spectra, a small drift will result in the following phase being slightly below  $2\pi$ , while it would actually extend to smaller values than 0. Removing these jumps is called unwrapping the phase and leads to phase values outside of  $\{0, 2\pi\}$ , see Fig. 5.6.

In general, the phase accumulation time is chosen such that the changes in phase from one measurement to the next are  $\ll \pi$ . The process of phase unwrapping can be described by:

$$\Delta\varphi = \varphi_1 - \varphi_2 = \begin{cases} < -\pi : & \varphi_2 \rightarrow \varphi_2 + 2\pi \\ \in (-\pi, \pi) : & \varphi_2 \rightarrow \varphi_2 \\ > \pi : & \varphi_2 \rightarrow \varphi_2 - 2\pi \end{cases} . \quad (5.10)$$

Only in the case where the  $\Delta\varphi \in (-\pi, \pi)$  a phase jump is seen as unrealistic. With an expected uncertainty of the phase of 0.2rad in the joint analysis, a random phase jump of  $\approx \pi$  seems to be unrealistic and the phase justifiable. If the determined phase uncertainty is larger than that, it is an indication that one or several phases are wrongly unwrapped and  $\pm 2\pi$  is missing.

### 5.4.2 Determination of the phase difference

For both the reference and accumulated time, the phase needs to be unwrapped before calculating the difference. In Fig. 5.6 the principle of unwrapping is shown for both phases of one ion in one pnp-cycle separately (top) and their difference (bottom). The dashed lines correspond to the wrapped phases, constrained by 0 and  $2\pi$  and the black dots indicate where  $\pm 2\pi$  was added on the unwrapped phase (solid line). After the unwrapping, the phases are stable around one value with a scattering of  $\approx 3\%$ . In an ideal measurement, the unwrapped phase difference should be constant or show a trend, e.g. a decreasing magnetic field leads to a decrease in phase over time.

When calculating the phase difference between the two evaluation times  $t_{\text{ref}}$  and  $t_{\text{acc}}$ , it is also possible to first calculate the difference and then unwrap the phase. This can require additional factors of  $\pm 2\pi$  or  $\pm 4\pi$  instead of only  $\pm 2\pi$  when for both phases at one time a shift by  $\pm 2\pi$  is needed.

#### Phases over time

In principle, it should also not make a difference if the unwrapping of the phase is started at the first value going forward or the last value going backwards. In the case of the accumulated phase in Fig. 5.6 (blue), starting with the last value would lead to a shift of the complete accumulated phase down by  $2\pi$  and with it also the phase difference  $\Delta\varphi$ . Here, both results are justifiable. In order to find out which one is correct, or, in general, if the first phase should have already been changed by  $\pm 2\pi$ , the change of phases over time needs to be looked at. This is done in two steps:

1. **Comparing to  $N$ -determination:** If the phase of the first pnp-cycle differs from that in the  $N$ -determination measurement performed before the start of the PnP-measurement, that phase can be adapted accordingly. As the  $N$ -determination takes more time intervals  $\Delta t$  into account, it is more reliable in the determination of the phase and of  $N$ . This works only if  $|\varphi_{N\text{-det.}} - \varphi_{1.\text{ cycle}}| < \pi$  of the “true phases”.
2. **Comparing to other cycles:** The phase distribution over time follows mainly a linear trend to smaller phases due to the decreasing magnetic field. A sudden jump of  $\pm 2\pi$  from one pnp-cycle to the next is easily visible, see Fig. 5.7. There, both the averaged reference and averaged accumulated phases over one measurement are shown. While the reference phase  $\varphi_{\text{ref}}$  is nearly constant (orange), the accumulated phase  $\varphi_{\text{acc}}$  (magenta) decreases over time and performs two jumps in this measurement. In the lower plot, the unwrapped phase difference is shown. Hereby, all phases of one ion in one trap over the whole measurement are unwrapped by comparing the result of one pnp-cycle to that before.

If the second  $N$ -determination measurement is performed after the PnP-measurement or if the measurement runs for more than one cycle, the phase of the last pnp-cycle can be compared to the following  $N$ -determination measurement. For a full cycle, the

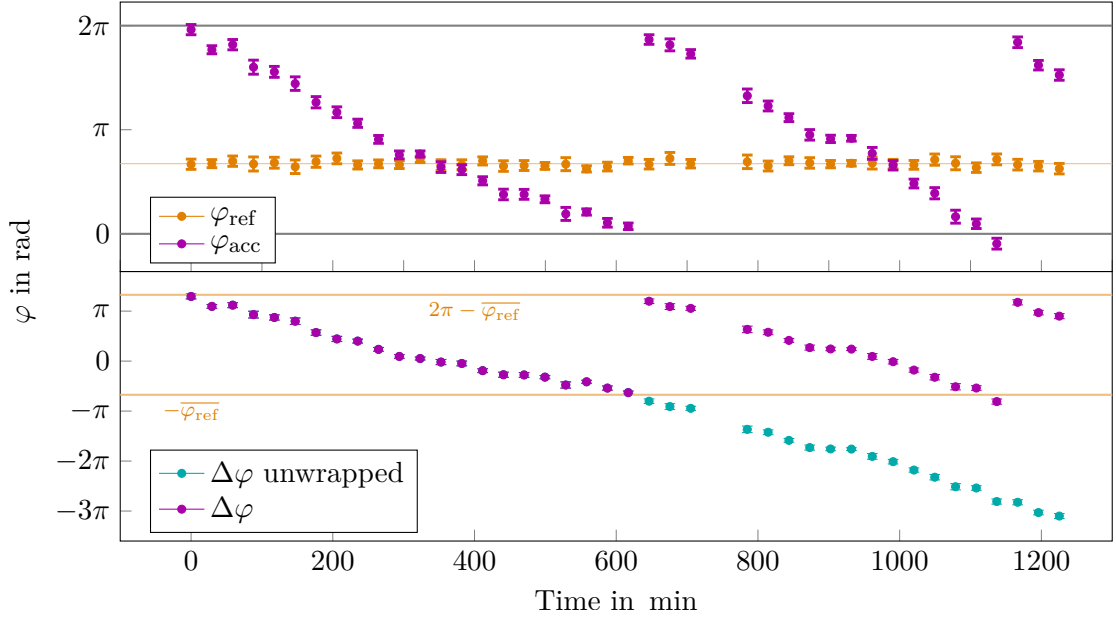


**Figure 5.7:** Measured averaged reference phase  $\varphi_{\text{ref}}$  and accumulated phase  $\varphi_{\text{acc}}$  (top) and their phase difference  $\Delta\varphi = \varphi_{\text{acc}} - \varphi_{\text{ref}}$  (bottom). **Top:** The reference phase (orange) stays nearly constant and its mean is shown by the horizontal line. The accumulated phase (magenta) decreases over time and jumps twice by  $2\pi$ . The unwrap before averaging can lead to phases not bound between 0 and  $2\pi$ , see 4<sup>th</sup> last point of  $\varphi_{\text{acc}}$ . **Bottom:** The blue points show the unwrapped phases of the phase difference (magenta). The orange lines indicate the bounds for  $\Delta\varphi$ , with the upper bound for  $\varphi_{\text{acc}} = 2\pi$  and the lower  $\varphi_{\text{acc}} = 0$ .

phase can decrease by up to  $2 \cdot 2\pi$ , as shown in Fig. 5.7, and the  $N$  from the second determination should then be smaller by 2 compared to the pre  $N$ -determination.

### 5.4.3 Determination of number of full revolutions $N$

The measurement for the determination of the number of full revolutions is described in Sec. 4.3.3. For the analysis the same steps are performed as for the PnP-measurement, with the difference that now there are several accumulated phases, but still only one reference phase. All phase differences  $\Delta\varphi_i$  are measured five times. In order to determine  $N$  one can look at the difference between  $N_i$  and the nearest integer  $[N_i]$ :

$$F(N_i, \nu_+) = |N_i - [N_i]| \quad . \quad (5.11)$$

In Tab. 5.2  $N_i$  is calculated for all time and phase differences with  $t_{\text{ref}} = 0.1$  s and  $\varphi_{\text{ref}} = 2.78$  rad for three different frequencies  $\nu_+$  resulting in a difference of  $\pm 1$  in  $N$  for the longest interval  $\Delta t = t_{\text{acc}} - t_{\text{ref}} = 39.95$  s, i.e. the interval used in the PnP-measurement. In the last row, the sum of  $\sum F(N_i, \nu_+)$  for all time intervals is given.

**Table 5.2:** Results of the  $N$ -determination measurement. The full number of revolutions is calculated from the time intervals  $\Delta t_i$  and phase differences  $\Delta\varphi_i$  determined with  $t_{\text{ref}} = 0.1$  s and phase  $\varphi_{\text{ref}} = 2.78$  rad for three different frequencies  $\nu_+$ , resulting in the correct  $N$  and  $N \pm 1$  for the longest time interval of 39.95 s. In the last row the sum of all differences of  $N_i$  to the nearest integer,  $\sum F(N_i, \nu_+)$ , is shown, with the minimal value for the correct  $\nu_+$  shown in black.

Measurement:		$N_i = \nu_+ \Delta t_i - \frac{\Delta\varphi_i}{2\pi}$ for $\nu_+ =$		
$\Delta t_i$ /s	$\Delta\varphi_i$ /rad	16672959.68 Hz	16672959.71 Hz	16672959.73 Hz
0.15	0.08	2500943.88	2500943.89	2500943.89
0.5	-1.09	8336479.94	8336479.95	8336479.96
0.95	-1.14	15839311.79	15839311.82	15839311.84
4.95	-2.85	82531150.93	82531151.05	82531151.18
10.95	-1.53	182568908.68	182568908.95	182568909.23
22.95	2.12	382644424.47	382644425.04	382644425.62
31.95	-2.43	532701062.23	532701063.03	532701063.82
39.95	1.98	666084738.96	666084739.96	666084740.96
		$\sum F(N_i, \nu_+) = 1.52$	0.53	1.32

In this case, the modified cyclotron frequency obtained during the preparation of the ion was  $\nu_+ = 16672959.61$  Hz. While varying the frequency in an interval of  $\pm 0.5$  Hz, the minimum of  $\sum F(N_i, \nu_+)$  is found (here for  $\nu_+ = 16672959.71$  Hz in the middle column) at the frequency where the sum results in the smallest value. In order to show that this frequency and the corresponding number of full revolutions are correct, the columns left and right are evaluated for the frequency  $\nu_+$  resulting in the next lower and higher  $N$ . Interesting to note is that for all three frequencies the first few  $N_i$  barely change, while for the following time intervals it is obvious that  $N_i$  cannot be an integer (for example for  $\Delta t = 10.95$  s).

#### 5.4.4 Error assignment

For both the joint and the grouped analysis the phases are finally averaged before calculating the modified cyclotron frequency:

$$\overline{\Delta\varphi}_{\text{final}} = \frac{\sum_i^n (\Delta\varphi_i)}{n} \quad , \quad (5.12)$$

with  $n = 2$  (grouped) or  $n = 10$  (joint).

The phases are determined without uncertainty and are statistically distributed around their mean value for one pnp-cycle. The averaging of either two or 10 phases allows then to assign an uncertainty to the mean value. This results in random uncertainties as shown in Fig. 5.8.

While the phase measurements during one pnp-cycle are expected to be normally distributed, the mean of the small samples with either two or ten data points does not reflect the mean of the true underlying statistical distribution as, for example, in one group only values from the tail of the distribution could be included. The distance of the mean of the small samples to the true mean of the statistical distributions follows a Student  $t_{n-1}$  distribution, where  $n$  is the sample size [Stu08]. In order to account for the random distribution of the phases, the uncertainties of the mean values are increased by an additional factor arising from the Student distribution  $s_{\text{Student}}$  [Hel75]. The final uncertainty is then given by:

$$\delta\overline{\Delta\varphi}_{\text{final}} = \sigma(\Delta\varphi) \cdot s_{\text{Student}} \quad . \quad (5.13)$$

The two Student factors to increase the uncertainties of the grouped ( $s_2$ ) and the joint ( $s_{10}$ ) analysis are:

$$s_2 = 1.89 \quad (5.14)$$

$$s_{10} = 1.06 \quad . \quad (5.15)$$

#### 5.4.5 Calculation of the modified cyclotron frequency

The modified cyclotron frequency is then calculated by

$$\nu_+ = \frac{1}{2\pi} \frac{2\pi N + \overline{\Delta\varphi}_{\text{final}}}{\Delta t} \quad . \quad (5.16)$$

Only the phase has an uncertainty, which leads to:

$$\delta\nu_+ = \frac{\delta\overline{\Delta\varphi}_{\text{final}}}{2\pi\Delta t} \quad . \quad (5.17)$$

This calculation is identically performed for the grouped, as well as the joint analysis.

### 5.5 Comparison between joint and grouped analysis

Before the free-space cyclotron frequency is calculated, the joint and grouped analyses are compared. This allows identifying a failed fit or a wrong unwrap of one of the phases. The comparison between the joint and the grouped analysis is done graphically for the axial and the modified cyclotron frequencies.

Ideally, the frequencies obtained from the grouped analysis should scatter around that of the joint analysis, see Fig. 5.8. There, the joint analysis is set as zero (black and grey area). The axial (left, magenta) and modified cyclotron (right, orange) frequencies of the grouped analysis are distributed equally around the joint analysis. The coloured bars show the mean value of the grouped results, which for the axial frequency only deviates by 2 mHz from the joint analysis, while both uncertainties are roughly the same. This small shift of the mean value can be explained by noise peaks or dips,

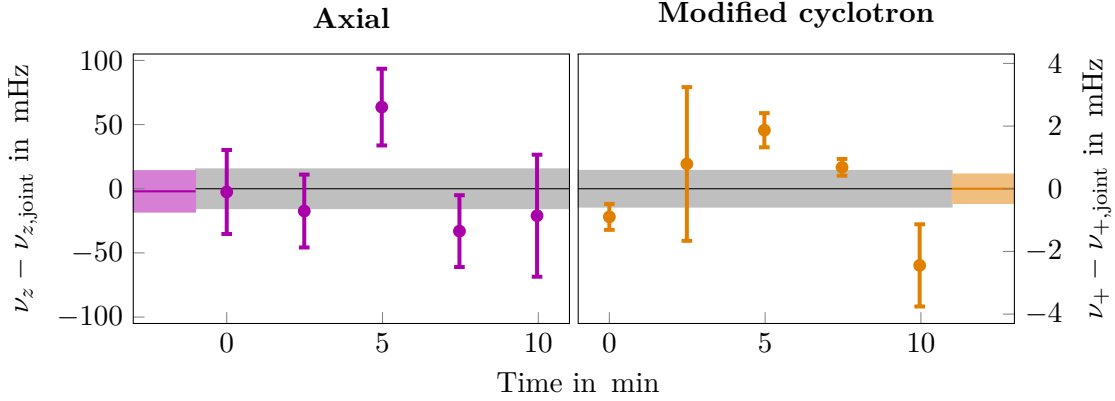


**Figure 5.8:** Comparison between joint (black) and grouped (coloured) analysis. For graphical purposes the joint analysis is set to zero, the grey bar shows its uncertainty. The comparison for the axial frequencies is shown **left**, the one for the modified cyclotron frequencies on the **right**. The coloured bar shows the mean of the grouped analysis.

which average out in the joint analysis but are still present in the grouped analysis. The calculation of the modified cyclotron motion from the phases is purely statistical and the mean values of the grouped analysis and the result from the joint analysis are identical. The uncertainties vary due to the small sample size and the different averaging. After the optimisation of the analysis scripts to the description above, no discrepancy between the grouped and the joint analysis was found.

## 5.6 Free-space cyclotron frequency

No matter how carefully the phases are unwrapped or the axial spectra fitted, in rare cases it can fail, resulting in an erroneous determination of modified cyclotron phase or the axial eigenfrequency. These values must be excluded from further data analysis. To that end, two filters are set on both the phases and the axial frequencies. First, those points with an unreasonable large error are taken out. These can arise from e.g. random phase fluctuations which could not be unwrapped. The second filter removes data points which deviate too much from the average values and arise as the axial fit fails to find the dip due to e.g. through random noise in the axial spectra before fitting.

### 5.6.1 1. Filter - large uncertainty

This filter compares the uncertainty of each data point of the grouped analysis with the mean value of the uncertainty of all frequencies of this ion in one trap over the measurement run. The mean value of the uncertainty is given by:

$$\overline{\delta\nu_i} = \frac{\sum_{n=1}^{n_{\max}} \delta\nu_{i,n}}{n_{\max}}, \quad (5.18)$$

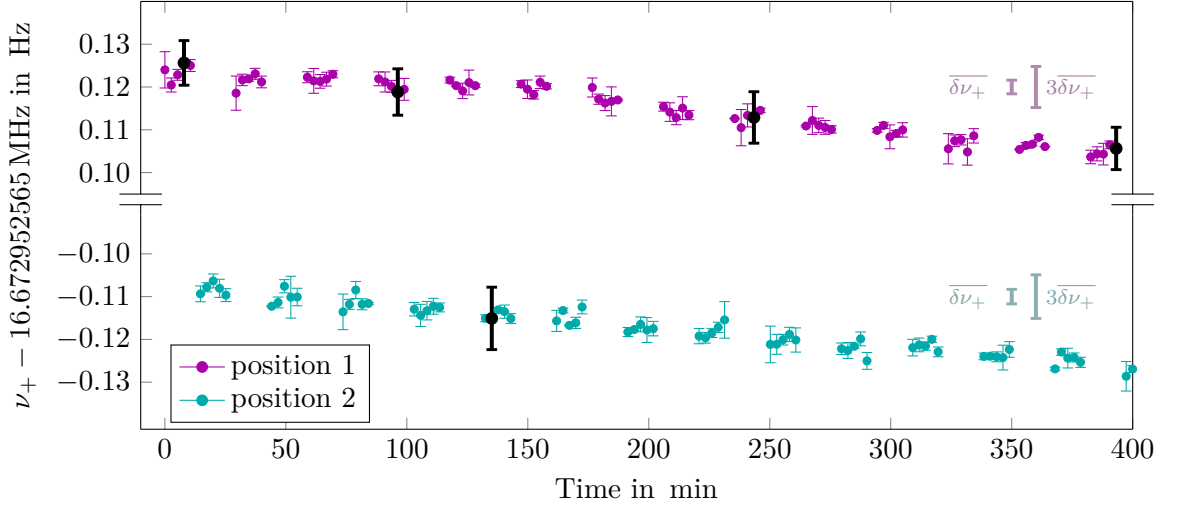


**Figure 5.9:** Filtering of the modified cyclotron frequencies with the first filter. The black data points feature a too large uncertainty. For comparison, the average error  $\overline{\delta\nu_+}$  is shown on the right together with the filter threshold  $3\overline{\delta\nu_+}$ .

where  $i = +, z$  and  $n_{\max}$  the number of data points, maximal 25 per cycle. The outliers are defined by a  $3\sigma$  exclusion criterion. Those data points, for which the relation

$$\delta\nu_{i,n} > 3\overline{\delta\nu_i} \quad (5.19)$$

holds are removed.

The application of this filter is shown in Fig. 5.9 for the modified cyclotron frequency of two positions, 1 and 2, in trap 2. The mean uncertainty  $\overline{\delta\nu_+}$  and the filter threshold  $3\overline{\delta\nu_+}$  are shown above the measured frequencies. The black data points have an uncertainty larger than the filter threshold and are removed in further calculations. The large errors can originate from phase jumps around  $\pm\pi$ , which are just on the edge of being unwrapped.

For graphical purposes, this extreme example was chosen, as position 1 exhibits quite a few removed data points. In a full cycle of 25 pnp-cycles, usually, only one or two data points are removed as is the case for position 2.

### 5.6.2 2. Filter - deviation

The aim of the second filter is to remove results from the grouped analysis which deviate too much (see below) either from their mean value or from the joint analysis. To that end, the uncertainties of all frequencies for one ion in one trap (it) are averaged:

$$\overline{\delta\nu_{it}} = \frac{\sum_{n=1}^{n_{\max}} \delta\nu_n}{n_{\max}} \quad (5.20)$$

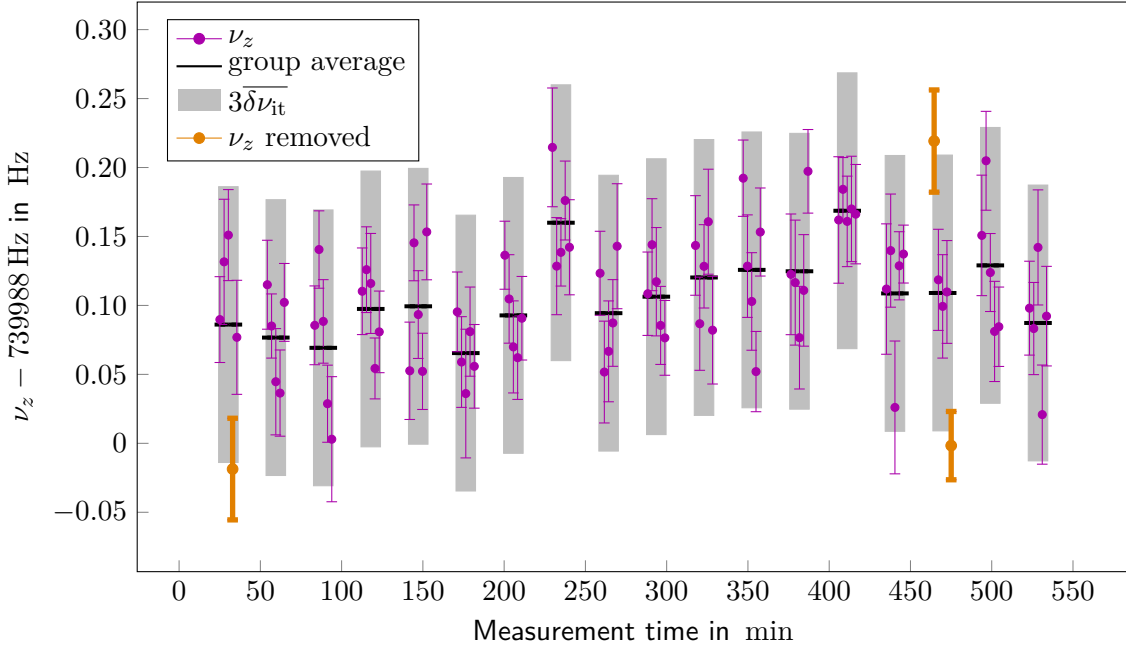


**Figure 5.10:** Display of the second filter for the axial frequencies. The magenta data points are the results of the grouped analysis. For each group the average (black line) and the filter condition (grey box) is shown. The orange data points deviate more than  $3\overline{\delta\nu_{it}}$  from the mean value and are therefore discarded in the further calculation.

In order to also take into account short term drifts on the time scale of one pnp-cycle, the individual frequencies from the grouped analysis for one pnp-cycle are compared to their mean value (mv):

$$\overline{\nu_{mv}} = \frac{\sum_{n=1}^5 \nu_n}{5} \quad . \quad (5.21)$$

Alternatively, the frequency resulting from the joint analysis could be taken here, as the two are nearly the same, see Fig. 5.8.

The filter threshold is then a  $3\sigma$  criterion and given by

$$\left| \nu_n - \overline{\nu_{mv}} \right| > 3\overline{\delta\nu_{it}} \quad . \quad (5.22)$$

The second filter is visualised in Fig. 5.10, where the black line is the average frequency  $\overline{\nu_{mv}}$  for that pnp-cycle and the grey area the filter threshold  $3\overline{\delta\nu_{it}}$ . The orange data points are removed from the data set. Here, again a more extreme example was chosen.

It is worth noting, that the analysis of the filtered and unfiltered data yields statistically the same results due to the small number of outliers present in the data. Choosing a  $4\sigma$  criterion leads to no data points being excluded anymore.

### 5.6.3 Calculation of the free-space cyclotron frequency

As the last step, the uncertainty for the modified cyclotron frequencies is addressed before the free-space cyclotron frequency is calculated. In Fig. 5.9 it can be seen that the uncertainties of the individual data points can be quite different. For example, all data points in the second to last group in position 1 have error bars around the size of the marker, while others are close to the filter threshold. As these uncertainties are relatively arbitrary due to the statistically fluctuating phases, for the calculation of  $\nu_c$  the uncertainty of the individual data points  $\delta\nu_{+,n}$  are averaged and set for all results:

$$\delta\nu_{+,n} \rightarrow \overline{\delta\nu_+} \quad . \quad (5.23)$$

As the ratio between the two ion species can be determined by a fitting routine (see Sec. 5.7.1), this has the advantage that all data points are weighted the same and do not unnecessarily distort the result of the fitting.

The free-space cyclotron frequency is then calculated by the invariance theorem (see Eq. (2.11)):

$$\begin{aligned} \nu_c &= \sqrt{\nu_+^2 + \nu_z^2 + \nu_-^2} \quad \text{with} \\ \delta\nu_c &= \sqrt{\left(\frac{\nu_+}{\nu_c} \delta\nu_+\right)^2 + \left(\frac{\nu_z}{\nu_c} \delta\nu_z\right)^2 + \left(\frac{\nu_-}{\nu_c} \delta\nu_-\right)^2} \quad . \end{aligned} \quad (5.24)$$

In order to determine the influence of the three eigenfrequencies on the uncertainty of the free-space cyclotron frequency, the individual contributions need to be calculated. For example, the eigenfrequencies from the grouped analysis of one of the Re measurements are:

$$\begin{aligned} \nu_+ &= 16664151.550(2) \text{ Hz} \\ \nu_z &= 739945.04(5) \text{ Hz} \\ \nu_- &= 16429.5(1) \text{ Hz} \end{aligned}$$

This leads to the uncertainty of the free-space cyclotron frequency of :

$$\delta\nu_c = \sqrt{(1.998 \text{ mHz})^2 + (2.22 \text{ mHz})^2 + (0.1 \text{ mHz})^2} = 3 \text{ mHz} \quad . \quad (5.25)$$

The largest uncertainty, therefore, results from the axial dip determination, while the uncertainty contribution from the magnetron frequency is negligibly small. The dip determination might be improved by further studying of the fit function or routine, as is done, for example, in [Lan19], where the effect of noise peaks on the axial frequency is investigated. Alternatively, the axial frequency can be determined by a phase-sensitive technique.

## 5.7 Frequency ratio determination

There are two possibilities for the frequency ratio determination:

**Polynomial:** Both measurement traps are analysed individually. The measured free-space cyclotron frequencies of both ion species in one trap are divided into parts and each part is fitted with a polynomial to account for magnetic field drifts during the measurement. The ratio between the two polynomials is then the frequency ratio. This has the advantage that it can be applied for just one trap. Sudden jumps for both ions can be taken into account by choosing the partition of the data points accordingly.

**Cancellation:** Assuming the magnetic field ratio of the two measurement traps to be constant, the cyclotron frequency ratio can be calculated for both positions and traps together. Following the calculation in [Sec. 2.3](#), the magnetic field cancels out in the frequency ratio. It requires all three ions to live until the end of the measurement.

A comparison of the two methods is given in [Sec. 7.3](#), where the application was possible due to the sufficiently long storage time of all three ions.

### 5.7.1 Polynomial method

In each trap, the cyclotron frequency of two different ions is alternately measured. The magnetic field is a slowly varying function over time and as a result, the free-space cyclotron frequency follows the same trend for both ions in one measurement trap. On a time interval of a few hours, the varying magnetic field can be approximated by a polynomial of low order. In principle, this is the same idea as interpolating the value of one ion to the time of the other ion, with the advantage that trends are better described. The magnetic field is thereby described by a simultaneous fit to both free-space cyclotron frequencies of the two ions in one trap. Hereby, the parameters describing the polynomial are common to both ions, the difference is an additional factor to one of the fitting functions, which is the frequency ratio.

The data sets are divided into several parts, each consisting of about five data points for both positions, see [Fig. 5.11](#). Care is taken to ensure that no sudden frequency jumps are included in any part. The parts for the different ions can be different in length, see last division. During this measurement the stabilisation system of the magnet laboratory was not yet optimised, leading to an unexpected increase in the cyclotron frequency. Since it was optimised, no such jumps were measured anymore. The length of 5 point was chosen as then the polynomial still describes the trend well, and, at the same time, is not over-defined, while also taking short term trends in the magnetic field into account.

The cyclotron frequency is expected to decrease over time, as, due to the nature of superconducting magnets, the magnetic field decreases [[Str14](#)]. The polynomial degree of [Eq. \(5.28\)](#) is chosen to be three, as this also allows to account for short term changes and thereby yields a more reliable ratio from the fit.

The timestamp of the determined cyclotron frequencies is taken from the time of the first axial spectrum. As the time interval between the measurements of the frequencies

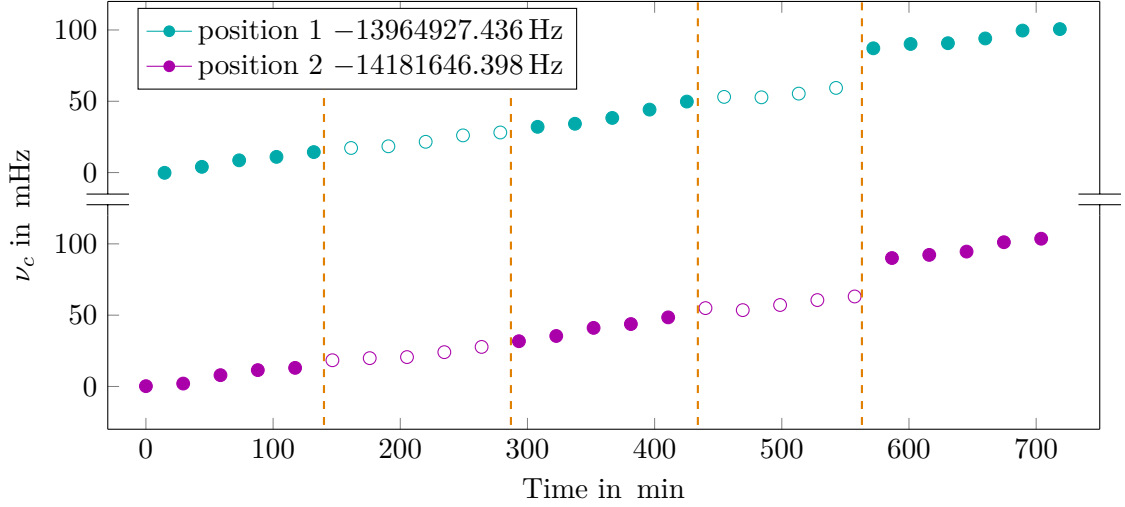


**Figure 5.11:** Partition of the measured data points in trap 2 into parts. The filled and empty circle correspond to different parts. Care is taken that a jump, as seen inbetween the last two parts, does not lie within one group.

is constant, it does not matter which of the timestamps is taken. Therefore, the first data point of the grouped analysis is at the same time than the joint analysis.

The simultaneous fit of two data sets with common parameters is achieved in MATHEMATICA by using a two-dimensional fit routine. Therefore, an additional parameter is added to the frequencies:

$$(t, \nu_c, \delta\nu_c) \rightarrow (y, t, \nu_c, \delta\nu_c) \quad , \quad (5.26)$$

with

$$y = \begin{cases} 1 : & \text{for position 1} \\ 2 : & \text{for position 2} \end{cases} \quad , \quad (5.27)$$

where the positions are defined by configuration of the ions in the trap stack as shown in Fig. 2.4.

The two fitting functions  $g_1(t)$  and  $g_2(t)$  for the frequencies in one trap of position 1 and position 2, respectively, can be expressed by:

$$\begin{aligned} g_1(t) &= at^3 + bt^2 + ct + d \\ g_2(t) &= R \cdot (at^3 + bt^2 + ct + d) \quad , \end{aligned} \quad (5.28)$$

where  $a$ ,  $b$ ,  $c$ , and  $d$  are the fitting parameters with appropriate dimensions, such that  $g_i(t)$  results in Hz. The parameter  $R$  gives the ratio of the charges and masses of the two ions, i.e.:

$$R = \frac{m_1 q_2}{m_2 q_1} \quad , \quad (5.29)$$

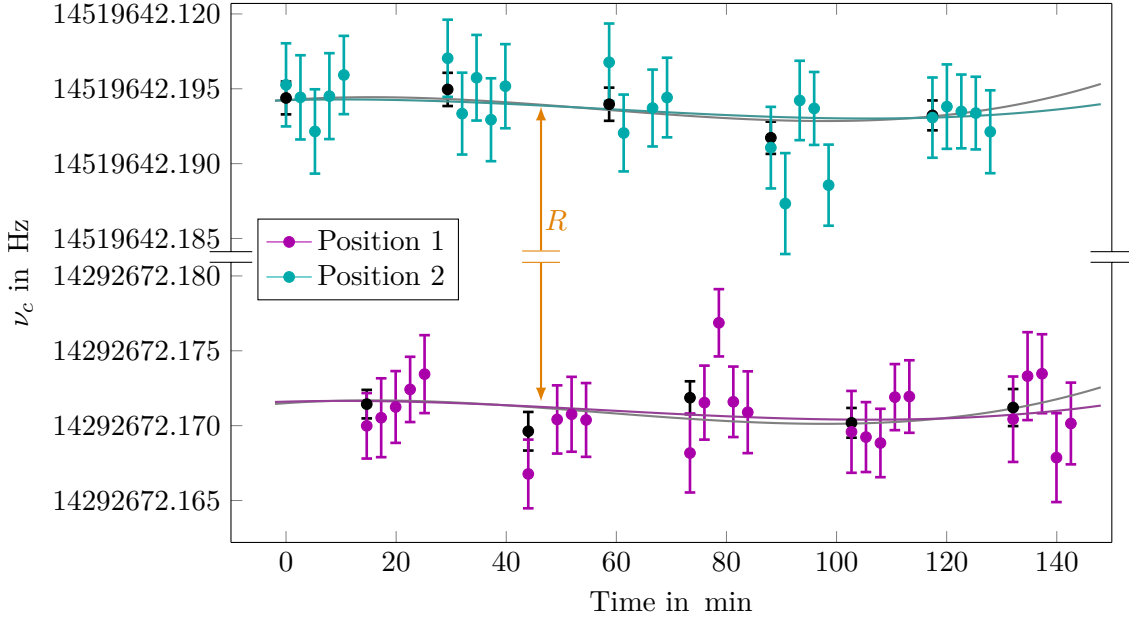


**Figure 5.12:** Polynomial fit to a group of free-space cyclotron frequencies in trap 2. The black dots are the joint analysis and the grey line is the corresponding fit, the coloured dots and lines corresponds to the grouped analysis.

as the magnetic field is described by the polynomial. With the help of the discrete Kronecker function,

$$\delta_K[x] = \begin{cases} 1 & \text{for } x = 0 \\ 0 & \text{for } x \neq 0 \end{cases}, \quad (5.30)$$

the two functions  $g_1(t)$  and  $g_2(t)$  can be combined to the two-dimensional fit function

$$F(y, t) = \delta_K[y - 1] \cdot g_1(t) + \delta_K[y - 2] \cdot g_2(t), \quad (5.31)$$

depending on the position  $y$  and the time  $t$ . In this way the first term evaluates to 0 for all data points from position 2 and vice versa.

In Fig. 5.12 a typical ratio fit from a measurement in trap 2 is shown. The black data points and the grey fit correspond to the joint analysis, the coloured ones to the grouped. The results for both analyses are given by:

$$R_{\text{joint}} = 1.015880167867(46) \quad (5.32)$$

$$R_{\text{grouped}} = 1.015880167862(46) \quad (5.33)$$

In the case shown here, the difference between the grouped and the joint analysis is only 10% of their uncertainty and while the uncertainties for both analyses are usually similar, they are by chance identical here. Depending on how many data points are discarded (see e.g. the missing second point in the second group for position 1) the joint

and the grouped analysis for other parts can have larger differences, but never deviate more than their uncertainty. For the final mass ratio determination, the filtered data is taken.

### 5.7.2 Cancellation method

Assuming the ions loaded to be A - B - A, with the ions in trap 1, 2, and 3 for position 1 at time  $t_1$  and in traps 2, 3, and 4 for position 2 at time  $t_2$ , the free-space cyclotron frequency ratios of the two positions can be written as:

$$R_{\text{pos1}} = \frac{\nu_{\text{B, pos1}}^{\text{trap2}}}{\nu_{\text{A, pos1}}^{\text{trap3}}} = \frac{q_{\text{B}} m_{\text{A}} B_{\text{trap2}}(t_1)}{q_{\text{A}} m_{\text{B}} B_{\text{trap3}}(t_1)} \quad \text{and} \quad R_{\text{pos2}} = \frac{\nu_{\text{A, pos2}}^{\text{trap2}}}{\nu_{\text{B, pos2}}^{\text{trap3}}} = \frac{q_{\text{A}} m_{\text{B}} B_{\text{trap2}}(t_2)}{q_{\text{B}} m_{\text{A}} B_{\text{trap3}}(t_2)} . \quad (5.34)$$

The frequency ratio  $R$ , assuming the magnetic field ratio  $B_{\text{trap2}}/B_{\text{trap3}}$  to be constant in time, results in a cancellation of the magnetic fields in the calculation:

$$R = \sqrt{\frac{R_{\text{pos1}}}{R_{\text{pos2}}}} = \sqrt{\frac{\nu_{\text{B, pos1}}^{\text{trap2}}}{\nu_{\text{A, pos1}}^{\text{trap3}}} \cdot \frac{\nu_{\text{A, pos2}}^{\text{trap3}}}{\nu_{\text{B, pos2}}^{\text{trap2}}}} = \frac{q_{\text{B}} m_{\text{A}}}{q_{\text{A}} m_{\text{B}}} . \quad (5.35)$$

The uncertainty is given by

$$\delta R = \frac{R}{2} \sqrt{\left(\frac{\delta \nu_{\text{B, pos1}}^{\text{trap2}}}{\nu_{\text{B, pos1}}^{\text{trap2}}}\right)^2 + \left(\frac{\delta \nu_{\text{A, pos1}}^{\text{trap3}}}{\nu_{\text{A, pos1}}^{\text{trap3}}}\right)^2 + \left(\frac{\delta \nu_{\text{B, pos2}}^{\text{trap2}}}{\nu_{\text{B, pos2}}^{\text{trap2}}}\right)^2 + \left(\frac{\delta \nu_{\text{A, pos2}}^{\text{trap3}}}{\nu_{\text{A, pos2}}^{\text{trap3}}}\right)^2} . \quad (5.36)$$

This results in a value for the frequency ratio for every pnp-cycle. It is only applicable if all three ions live long enough in the traps and that the first and last ion are of the same species, with the middle ion being a different one. Additionally, the magnetic field ratio needs to be constant on the level of the required uncertainty over the measurement time of one pnp-cycle. With these limitations, the polynomial method was chosen for the data presented in this thesis.

## 5.8 Mass difference calculation

The ratio  $R$  relates the two cyclotron frequencies,  $R = \frac{\nu_{c,1}}{\nu_{c,2}} = \frac{m_2 q_1}{m_1 q_2}$ , where the magnetic field either cancels out or is described by the polynomial. For an identical charge state the frequency ratio simplifies to:

$$R = \frac{m_2}{m_1} . \quad (5.37)$$

The mass difference can then be expressed by using the frequency ratio:

$$\Delta m = m_2 - m_1 = (R - 1) m_1 \quad (5.38)$$

with the uncertainty:

$$\delta(\Delta m) = \sqrt{(m_1 \cdot \delta R)^2 + ((R - 1) \cdot \delta m_1)^2} . \quad (5.39)$$

The precision of mass  $m_1$  needed for a certain precision in the determination of the other mass or the mass difference, depends on the ratio  $R$ . In the case of the measurement of the metastable state in Re, the frequency ratio leads to  $R - 1 \approx 1 \cdot 10^{-9}$ , while the uncertainty is determined to a level of  $\delta R \approx 9 \cdot 10^{-12}$ . Therefore, in the calculation of the mass difference, the mass uncertainty needs to be known only to  $\delta m_1/m_1 \approx 10^{-3}$ , for it to become negligible.

The mass of the highly charged  $^{187}\text{Re}^{29+}$  can be calculated in first approximation by

$$m\left(^{187}\text{Re}^{29+}\right) = 187 \cdot u - 29 \cdot m_e + E_{\text{binding}} \quad . \quad (5.40)$$

The mass of the removed electrons only change the mass of the Re atom at the  $10^{-6}$  level, the binding energy  $E_{\text{binding}}$  well below that level. Therefore, it is sufficient to take the neutral mass with the atomic mass unit  $u = 1.66053906660(50) \cdot 10^{-27}$  kg [CD18], while also ignoring its uncertainty. The uncertainty of the mass difference is then only given by  $\delta\Delta m = m_1 \cdot \delta R$ . For the Xe measurements, a mass difference of 1 u leads to  $R - 1 > 8 \cdot 10^{-3}$ . Here, also the mass of the electrons and the binding energies have to be taken into account.



# 6

---

## Xenon: Mass Measurements and Binding Energy Determination

---

The PENTATRAP experiment was set up to determine mass ratios to a relative uncertainty of  $10^{-11}$  and below for ions in the mid-heavy regime. In this mass region, only the mass differences of a few isotopes have been determined to a precision of  $10^{-10}$ , among them Kr and Xe [HRM13]. The first measurements at PENTATRAP, mass difference and binding energy measurements, were, therefore, performed on stable Xe isotopes to demonstrate the design specification and to reach a relative frequency ratio uncertainty on the level of a few  $10^{-11}$ .

Additionally, using Xe has the following advantages: Natural Xe gas consists of several stable isotopes, which allows easily switching the isotope of interest and not only perform one but several frequency ratio measurements without changing the ion production. Determining the mass differences of a chain of isotopes with high precision, as is demonstrated in this thesis by measuring the mass differences of five ion pairs, is important as an input parameter for isotope shift measurements for contributions to Dark Matter search [FGV18]. Furthermore, the Xe isotopes allow testing the production of HCIs with various abundances, see Fig. 6.1, and set a lower limit for the transport efficiency to the traps. Lastly, it serves as a back bone for the next version of the Atomic-Mass Evaluation 2017 (AME2017, [Wan+17]), by linking other measurements to the more precise mass measurements of Xe presented here.

In this chapter, two measurements with different physical background are presented. In the first section, high-precision mass measurements of Xe isotope pairs are described.

The free-space cyclotron frequency ratios of five pairs of Xe isotopes were thereby measured. Comparing the results thereby obtained for the mass differences of the ion pairs to the values in the AME2017, all results agree within  $1\sigma$ . The better-known mass differences could be improved by at least a factor of 4, with the mass difference of the two least known isotopes by even a factor of 1700.

In order to demonstrate the full potential of PENTATRAP, the binding energy of the 37<sup>th</sup> electron in Xe was determined. While the mass differences in the AME2017 are known to at least a factor of 4 less precise than the PENTATRAP result, the uncertainty of the theoretical calculations of the binding energy is on the same level as the uncertainty of the measurement. A comparison of the result to theoretical calculations of the binding energy, therefore, allows determining the accuracy achieved by PENTATRAP. Additionally, it is a proof-of-principle measurement of the electronic binding energy, for example, for future tests of QED.

The results presented in this chapter will be published in [Ris+19].

## 6.1 Mass measurements

Five mass ratios were measured on six stable isotopes between  $^{126}\text{Xe}$  and  $^{134}\text{Xe}$ , see Fig. 6.1, where arrows indicate the pairs. The frequency ratios  $R$  of the three pairs between  $^{129}\text{Xe}$  and  $^{134}\text{Xe}$  were already measured with another Penning trap to a precision  $\delta R \approx 8 \cdot 10^{-11}$  [HRM13], and serve as a test bench for the accuracy of PENTATRAP. The remaining two measurements were performed to improve the uncertainty of the mass of  $^{126}\text{Xe}$ , which so far is known to the lowest precision of all stable Xe isotopes [Wan+17].

The vast number of stable isotopes in Xe also allowed to test the efficiency of the ion production and loading of a certain ion species when several are present in the EBIT and the ejected ion bunch. With a gas bottle featuring the natural abundance, see Fig. 6.1, attached to the EBIT, it was possible to load  $^{128}\text{Xe}$  ions into the Penning traps. The lowest abundance limit for the efficient production and transport of the ions is therefore about  $\approx 2\%$ . For the measurement of the ratio including  $^{126}\text{Xe}$  an enriched sample of Xe was taken, where its abundance was increased to  $\approx 2\%$ .

The charge state of all ions in the measurement was  $q = 17+$ , which could easily be produced in the DreEBIT. All electronic shells up to 4d are completely filled at  $q = 17+$ , and no metastable states were detected, contrary to the measurements performed with Re, see Chapter 7.

The Xe measurements were started with the pair  $^{131}\text{Xe} / ^{132}\text{Xe}$ , since both have similar abundances of 21.2% and 26.9%, respectively. This allowed to easily transport and load them into the Penning traps without a change of voltages applied in the beamline, timings or even the current in the bender magnet. The complete beamline and the ion transport were optimised for this ion pair and, due to the good transmittance, the same settings could be used to also load all the other Xe isotopes. Finally, with the optimised scripts, only three full measurements of this ion pair were taken. Additionally, as the mass difference is only 1u, the systematic shifts are also smaller than e.g. of  $^{129}\text{Xe} / ^{131}\text{Xe}$ .

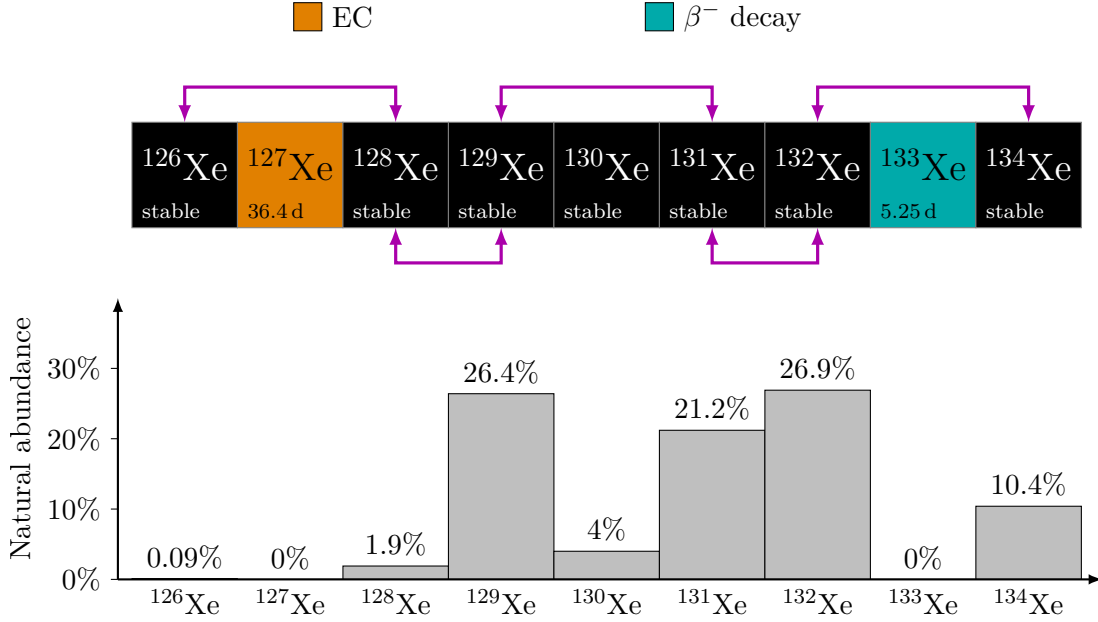


**Figure 6.1:** **Top:** Xe isotopes and their lifetime [MPG10] used in the measurements presented here. The magenta arrows indicate which mass ratios were determined. The colours distinguish the decay modes of the isotopes: the black ones are stable, the orange decays via an electron capture (EC) process and the blue with a  $\beta^-$ -decay. **Bottom:** Natural abundance of Xe isotopes [Lae+03].

For all measurements, the order of the sub measurements was: 1. Dip-measurement, 2. pre  $N$ -determination, 3. PnP-measurement and 4. post  $N$ -determination, as shown in Fig. 4.4. During the Dip-measurement, first, a spectrum featuring a single dip for the axial frequency was saved, followed by spectra with double dips for both radial frequencies. A second axial dip spectrum afterwards allows interpolating the axial frequency to the time of the radial frequency measurements. This leads to a more precise determination of the magnetron frequency.

For each determination of a mass ratio several measurements were performed, see the summary in Tab. 6.1. In between measurements, new ions had to be loaded, as the ions changed their charge state due to recombination during collisions with residual gas atoms in the trap volume. The typical lifetime and, therefore, the duration of a measurement was 14 h. The FFT window has a span of 5 kHz around the center of the resonator, which corresponds to a voltage range applied to the ring electrode of  $V_0 \pm 0.8$  V for a  $^{132}\text{Xe}^{17+}$  ion to have an axial frequency in this range. If the ion captures an electron, the potential needs to be lowered by  $\Delta V_0 \approx 3$  V to put the ion back into the same FFT range. Therefore, an ion at a lower charge state is not recorded anymore during the measurement. When checking the trap content after the measurement was stopped due to ion loss always revealed the ion in a lower charge state, making charge exchange the dominant loss mechanism in the traps.

**Table 6.1:** Overview of performed measurements for the five ion pairs and their statistical uncertainty. The number of measurements  $\#$  differs between the ion pairs, depending on the charge exchange of the ions in the traps. The number of determined frequency ratios is not correlated to the statistical uncertainty.

ions		#	pnp-cycles		# ratios			$\delta R_{\text{stat}}$
			trap 2	trap 3	trap 2	trap 3	sum	
$^{128}\text{Xe}^{17+}$	$^{126}\text{Xe}^{17+}$	2	122	8	24	2	26	$18 \cdot 10^{-12}$
$^{129}\text{Xe}^{17+}$	$^{128}\text{Xe}^{17+}$	2	97	97	19	19	38	$9 \cdot 10^{-12}$
$^{131}\text{Xe}^{17+}$	$^{129}\text{Xe}^{17+}$	5	79	101	16	18	34	$9 \cdot 10^{-12}$
$^{132}\text{Xe}^{17+}$	$^{131}\text{Xe}^{17+}$	3	63	47	11	8	19	$13 \cdot 10^{-12}$
$^{134}\text{Xe}^{17+}$	$^{132}\text{Xe}^{17+}$	2	49	49	10	10	20	$19 \cdot 10^{-12}$

As can be seen in Tab. 6.1 the number of performed pnp-cycles of the ions is randomly distributed. One pnp-cycle takes about half an hour to measure and thus also their lifetimes in the trap is arbitrary. While for  $^{131}\text{Xe} / ^{129}\text{Xe}$  five measurements were needed to end up with a total of 34 ratio values, for  $^{128}\text{Xe} / ^{129}\text{Xe}$  already two measurements were sufficient to determine a total of 38 ratios.

From the general measurement setup several effects could influence the ratio of two free-space cyclotron frequencies:

- 1. Magnetic field stability:** In order to employ the cancellation method (see Sec. 5.7.2), the magnetic field ratio of the two measurement traps as a function of time needs to be constant during the measurement of one pnp-cycle.
- 2. Reloading ions:** After ions are lost, a new measurement is set up with new ions and starting parameters, i.e. not noticed excess ions will be removed and the eigenfrequencies newly determined during the preparation of the ions.
- 3. Ion order:** The three ions can be loaded in two different orders: A - B - A or B - A - B. This changes the field the middle ion experiences and a comparison between the two orders can be used to investigate the ion-ion interaction.

In the following sections, these effects are investigated in more detail.

### Magnetic field stability

Important for the application of the cancellation method for the determination of the frequency ratio is a constant magnetic field ratio of both measurement traps. This requires an as stable environment in the magnet laboratory as possible. If this is not the case, the magnetic field changes shown in Fig. 6.2 for two measurement cycles, separated by the gap in the measurement data, are obtained. Here, the filled/empty dots indicate frequencies measured simultaneously, while the colours differentiate between the two ion species. The free-space cyclotron frequencies in trap 2 are rapidly changing to higher and

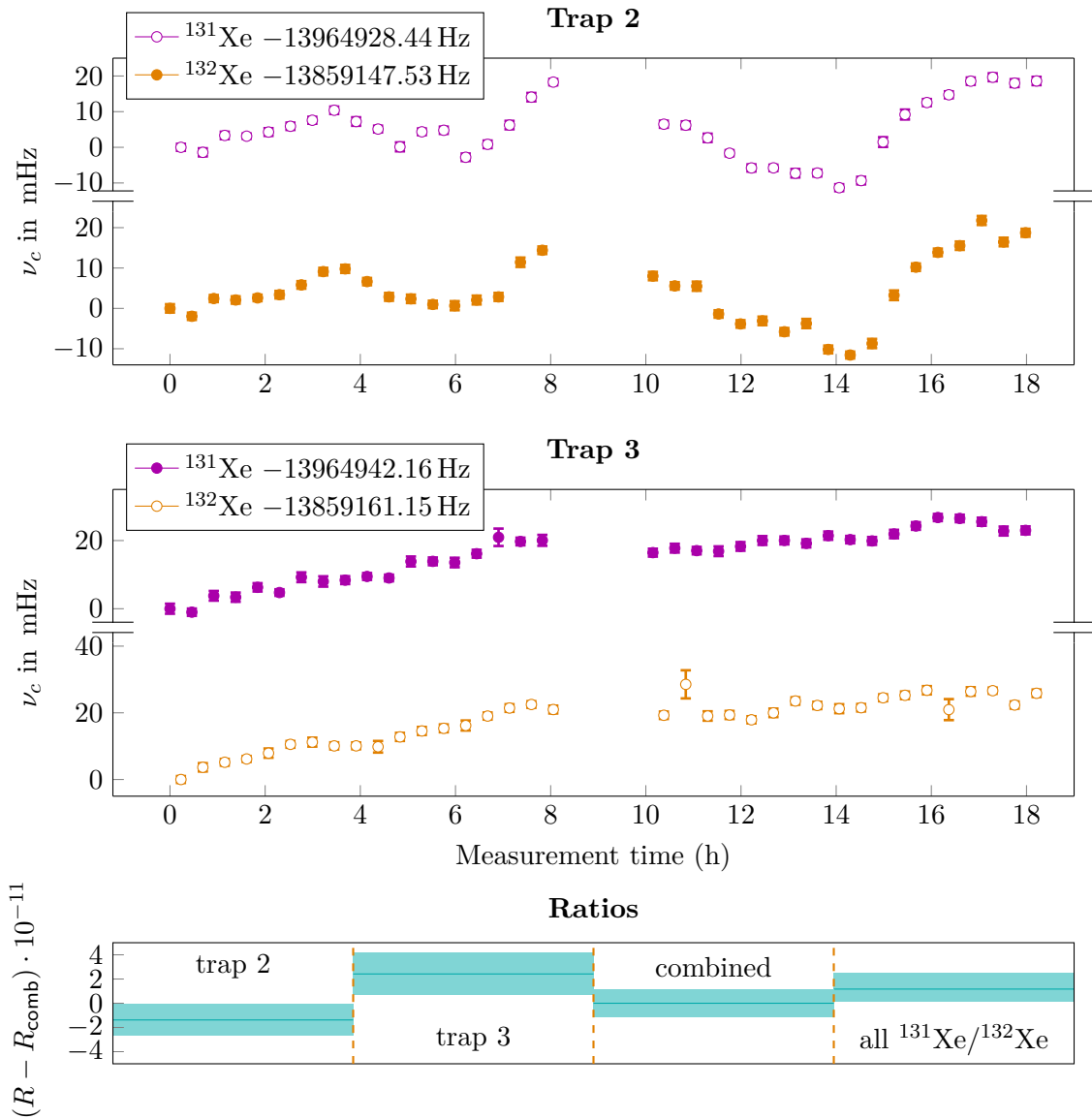


**Figure 6.2:** **Top:** The two plots for trap 2 and trap 3 show different free-space cyclotron frequencies behaviours for one measurement run of both  $^{131}\text{Xe}$  (magenta) and  $^{132}\text{Xe}$  (orange) ions due to a changing magnetic field. The empty/filled dots indicate measurements performed simultaneously. **Bottom:** Cyclotron frequency ratios obtained with the polynomial method for trap 2 and trap 3, the combined result of this measurement run and the result for all three measurement runs of this ion pair are compared. The combined result  $R_{\text{comb}} = 1.0076325692053$  is hereby set to zero. For details see text.

lower values compared to the slow trend upwards in trap 3 (the ordinates for both trap 2 and 3 show roughly the same frequency range). Especially during the fast decrease in trap 2 between 10 h-14 h, the magnetic field ratio of the two traps is expected to also change during one pnp-cycle.

The effect of the magnetic field on the frequency ratio is demonstrated in the lower plot. The ratios were determined with the polynomial method. Trap 2 and trap 3 lead to ratios which differ by more than  $1\sigma$ , but still agree within a  $2\sigma$  range. While the final frequency ratio obtained for both traps for this measurement lies in between (combined), the total ratio of all three measurement runs of  $^{131}\text{Xe}$  and  $^{132}\text{Xe}$  tends slightly more to the result from trap 3. This demonstrates the need for a stable environment in the magnet laboratory. Additionally, the uncertainties of the free-space cyclotron frequency in trap 3 of some points are larger by at least a factor of 2 compared to the rest, e.g. the second frequency in cycle 2 of  $^{132}\text{Xe}$ . Here, sudden jumps or shifts in the magnetic field can lead to a phase shift of up to  $\approx \pi$ , just below the unwrap principle. When averaging the phases, this leads to a larger uncertainty. In the grouped analysis, these points are removed by the first filter, see [Sec. 5.6.1](#).

For all the Xe measurements, the environmental stabilisation system [[Kro19](#)] was not yet optimised. Additionally, not many measurements were running for several cycles, further limiting the applicability of the cancellation method. Therefore, the frequency ratios were determined with the polynomial method, which allows to independently analyse both traps.

### Stability between measurements

Loading new ions for each measurement has the advantage that the starting conditions are renewed. While great care is taken to ensure that only one single ion remains in the trap by using the so-called magnetron clean noise (see [Sec. 4.2](#)), a finite possibility remains for excess ions to still be present on a higher magnetron radius. To ensure an empty trap for the next measurement, the traps can be cleaned by transporting all ions into trap 5, which is independent of the ions magnetron radius or eigenfrequencies. Thereby, the measurement traps are emptied of all remaining ions, while the ion content of trap 5 also does not influence the measurement. Additionally, lowering the potential on the bottom side of the trap also allows the ions to escape from trap 5 away from the trap stack.

For the pair  $^{129}\text{Xe} / ^{131}\text{Xe}$  in total five separate measurements were performed, each resulting in at least two results for the frequency ratio. All ratios are shown in [Fig. 6.3](#), with each measurement separated by the dashed lines. Additionally, the data points are sorted by traps per measurement, with filled data points corresponding to measurements performed in trap 2, the empty ones to those in trap 3.

The plot in the middle shows the result for the mean ratio of each of the five measurements. The result for the final ratio when including all five measurements is set to zero. With a final uncertainty of  $\delta R/R = 9 \cdot 10^{-12}$ , all measurements agree within  $1\sigma$ . As no large differences are observed between the single measurements, the cleaning of the traps of excess ions is working sufficiently well. Furthermore, the measurements

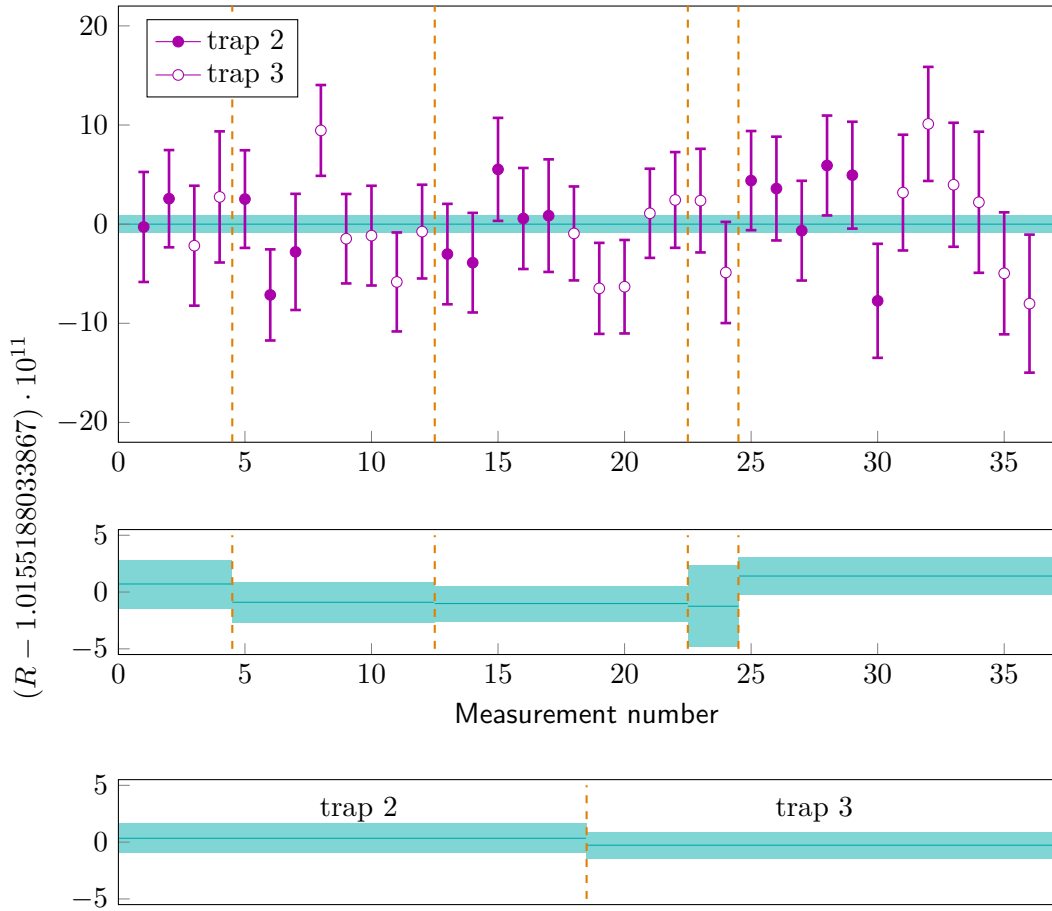


**Figure 6.3:** Cyclotron frequency ratios for  $^{129}\text{Xe}$  and  $^{131}\text{Xe}$  to investigate the stability over several measurements. **Top:** The orange lines divide the separate measurements, i.e. new ions were loaded. The blue bar shows the final result of all ratios combined. The filled dots correspond to measurements in trap 2, the empty ones to those in trap 3. **Middle:** Frequency ratios for the different measurements. **Bottom:** Frequency ratios in trap 2 and trap 3.

were performed over the course of one week, mostly during the night. To this level of precision, therefore, also external influences are not affecting the measurements.

The plot at the bottom compares the ratios obtained for the two measurement traps. As the axial frequencies and the detection systems are different, effects arising from these would also systematically shift the ratios. Again, no such obvious shift is visible, as the two ratios are overlapping.

**Table 6.2:** Masses of the Xe isotopes taken from the Atomic-Mass Evaluation 2017 [Wan+17]. The mass uncertainty for isotopes heavier than  $^{128}\text{Xe}$  is sufficient to calculate the mass difference from the frequency ratio, while for the other two isotopes the mass of  $m(^{129}\text{Xe})$  and the ratio  $R_{128-129}$  is used.

isotope	mass $\mu\text{u}$	uncertainty $\mu\text{u}$	rel. uncertainty
$^{126}\text{Xe}$	125 904 297	4	$3.2 \cdot 10^{-8}$
$^{128}\text{Xe}$	127 903 531.0	1.1	$8.6 \cdot 10^{-9}$
$^{129}\text{Xe}$	128 904 780.859	0.006	$4.7 \cdot 10^{-11}$
$^{131}\text{Xe}$	130 905 084.136	0.009	$6.9 \cdot 10^{-11}$
$^{132}\text{Xe}$	131 904 155.087	0.006	$4.6 \cdot 10^{-11}$
$^{134}\text{Xe}$	133 905 393.034	0.010	$7.5 \cdot 10^{-12}$

### 6.1.1 Ion order measurements

For each measurement, three ions are loaded, with the middle ion being a different species than the other two of the same species. As only the middle ion is surrounded by two ions, using the ion order A - B - A and B - A - B, allows investigating the effect of ions in adjacent traps. The two measurements of  $^{132}\text{Xe} / ^{134}\text{Xe}$  were, therefore, performed in the two different ion orders.

In Fig. 6.4 the two measurements are displayed, with the filled dots corresponding to the first measurement and the empty ones to the second. In the first measurement, running for one full cycle, i.e. 25 pnp-cycles and therefore five ratio values for each measurement trap, the ion order was  $^{134}\text{Xe} - ^{132}\text{Xe} - ^{134}\text{Xe}$ . The second measurement with the ion order  $^{132}\text{Xe} - ^{134}\text{Xe} - ^{132}\text{Xe}$  ran for one pnp-cycle less, but still resulted in five ratio values.

In the bottom plot, the two different results for the frequency ratios are shown. The difference between the two values is  $R_2 - R_1 \approx 4.1 \cdot 10^{-12}$  and therefore a factor of  $\sim 5$  smaller than the uncertainties of the two results,  $\delta R_1 \approx \delta R_2 \approx 2 \cdot 10^{-11}$ . As expected from Sec. 2.2.3, the effect of the ion-ion interaction can, therefore, be neglected.

### 6.1.2 Mass difference

The mass difference  $\Delta m$  can be calculated according to Eq. (5.38). The required uncertainty to which at least one of the two masses  $m_1$  or  $m_2$  needs to be known, depends on the value of  $R - 1$ . For the Xe masses  $R - 1 \leq 1.5 \cdot 10^{-2}$  (for  $^{126}\text{Xe} / ^{128}\text{Xe}$ ) and in order to not be limited by the mass uncertainty of the better known mass when calculating the mass difference,

$$\delta(\Delta m) = \sqrt{(m_1 \cdot \underbrace{\delta R}_{10^{-11}})^2 + (\underbrace{(R - 1)}_{\leq 10^{-2}} \cdot \delta m_1)^2} \quad , \quad (6.1)$$

the uncertainty needs to be below  $\delta m_1 / m_1 < 10^{-9}$ .

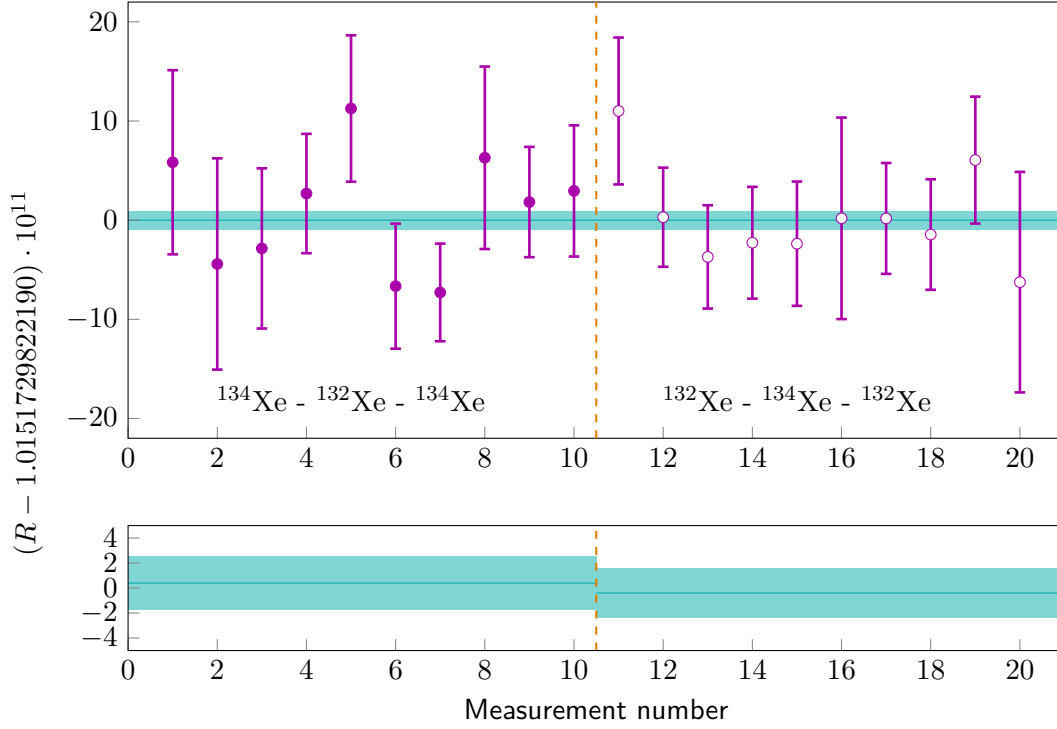


**Figure 6.4:** Cyclotron frequency ratios for  $^{134}\text{Xe}/^{132}\text{Xe}$  mass measurements to investigate the influence of the ion order. **Top:** The dashed orange line divides the separate measurements and indicate the different orders of the ions in the trap, where the first measurement had the ion order  $^{134}\text{Xe} - ^{132}\text{Xe} - ^{134}\text{Xe}$  and the second  $^{132}\text{Xe} - ^{134}\text{Xe} - ^{132}\text{Xe}$ . The blue bar shows the final result of all ratios combined. **Bottom:** Comparison of the frequency ratios for both measurements.

The currently most precise values for the Xe masses are taken from the AME2017 and shown in Tab. 6.2. The relative uncertainty of the isotopes  $^{129}\text{Xe}$  and heavier are all known precise enough for any mass difference to be calculated from the frequency ratio including any of these isotopes. For the pair  $^{126}\text{Xe} / ^{128}\text{Xe}$ , the uncertainty is insufficient for both isotopes. Therefore, the ratio  $^{128}\text{Xe} / ^{129}\text{Xe}$  is first used to determine the mass of  $^{128}\text{Xe}$  to a better precision, with which then the mass of  $^{126}\text{Xe}$  can be calculated:

$$\Delta m_{126-128} = m(^{126}\text{Xe}) - m(^{128}\text{Xe}) = \left( \frac{1}{R_{126-128}} - 1 \right) \cdot m(^{128}\text{Xe}) \quad (6.2)$$

$$= \frac{\left( \frac{1}{R_{126-128}} - 1 \right) \cdot m(^{129}\text{Xe})}{R_{128-129}}, \quad (6.3)$$

where the ratios  $R_{128-129} = m(^{129}\text{Xe})/m(^{128}\text{Xe})$  and  $R_{126-128} = m(^{128}\text{Xe})/m(^{126}\text{Xe})$  were used.

**Table 6.3:** Frequency ratios and mass differences for the Xe measurements determined with PENTATRAP. The last column states the improvement in precision compared to the literature value from the AME2017 given in Tab. 6.2. The systematic uncertainties are explained in Sec. 6.1.3.

ion pair	cyclotron frequency ratio	mass difference / u	impr.
$^{134}\text{Xe}^{17+}/^{132}\text{Xe}^{17+}$	$1.015172982205(19)_{\text{stat}}(8)_{\text{sys}}$	$2.0012379454(25)_{\text{stat}}(11)_{\text{sys}}$	4
$^{132}\text{Xe}^{17+}/^{131}\text{Xe}^{17+}$	$1.007632569193(13)_{\text{stat}}(6)_{\text{sys}}$	$0.9990709566(17)_{\text{stat}}(8)_{\text{sys}}$	6
$^{131}\text{Xe}^{17+}/^{129}\text{Xe}^{17+}$	$1.015518803388(9)_{\text{stat}}(8)_{\text{sys}}$	$2.0003032735(12)_{\text{stat}}(10)_{\text{sys}}$	7
$^{129}\text{Xe}^{17+}/^{128}\text{Xe}^{17+}$	$1.007828736895(10)_{\text{stat}}(6)_{\text{sys}}$	$1.0012501056(13)_{\text{stat}}(8)_{\text{sys}}$	740
$^{128}\text{Xe}^{17+}/^{126}\text{Xe}^{17+}$	$1.015880167834(18)_{\text{stat}}(8)_{\text{sys}}$	$1.9992333282(23)_{\text{stat}}(10)_{\text{sys}}$	1700

The mass differences thereby obtained are stated in Tab. 6.3. Here, the results from both the analysis performed with MATHEMATICA (this work) and PYTHON (Alexander Rischka) are combined.

### 6.1.3 Systematic effects

Most of the shifts and systematic uncertainties are easily estimated and their uncertainties are larger than the shift they produce in the ratio. Additionally, the systematic effects are well below the statistical uncertainty of the frequency ratios and only their uncertainties will be taken into account, while the ratio is not corrected.

The following list summarizes all systematic effects taken into account. Where numbers are given, the systematic effect was measured or could be calculated.

**Shifts associated with the resonator:** The position of the axial dip on the resonator can shift the ratio due to different depths of the axial dip signal and the coil pulling effect [Stu11]. The effect on the frequency ratio if one of the frequencies is detuned by 20 Hz is

$$\Delta R_{20\text{Hz}} = 3(3) \cdot 10^{-11} \quad . \quad (6.4)$$

During a measurement the difference in the axial frequency of the two ions is  $\Delta\nu_z \leq 0.1\text{Hz}$ . Assuming a linear behaviour, the corresponding shift and its uncertainty are, therefore,  $\ll 10^{-11}$  for the measurements performed here and, additionally, consistent with zero.

**Polynomial fit:** The length of the chosen groups as well as the degree of the polynomial used in the fit affect the frequency ratio. While the length of the groups is set to be around five and is adapted to the behaviour of the free-cyclotron frequency (see Fig. 6.2 and Fig. 5.11), the order of the polynomial was varied to estimate its effect. The difference in the ratio for a third and a second order polynomial fit resulted in

$$R_{3\text{rd}} - R_{2\text{nd}} = 3.7 \cdot 10^{-12} \quad , \quad (6.5)$$

while the uncertainty in both cases was around  $\delta R \approx 1.2 \cdot 10^{-11}$ .

**Image charge shift:** The image charge shift explained in Sec. 2.2.3 and discussed in [Sch19] can be roughly and conservatively estimated by  $\Delta R_{\text{ICS}}(\Delta m = 1\text{u}) \approx 2.4 \cdot 10^{-12}$  and  $\Delta R_{\text{ICS}}(\Delta m = 2\text{u}) \approx 4.8 \cdot 10^{-12}$  depending on the mass difference  $\Delta m$  of the two ions.

**Ion-ion interaction** Both the theoretical description (see Sec. 2.2.3) and the estimation from the ion order measurement showed no effect of an ion in an adjacent trap.

**Relativistic shift:** As described in Sec. 2.2.3, the relativistic mass increase leads to a shift of  $< 1 \cdot 10^{-12}$  for all ions heavier than carbon. For the frequency ratio, only the difference of the shifts to both ions is of importance. As this difference is also well below the shift of the free-space cyclotron frequency, this shift can be neglected.

**Higher-order electric field terms:** The uncertainty in the determination of the tuning ratio TR is  $\delta\text{TR}/\text{TR} \approx 10^{-3}$ , which leads to a higher order electric field term  $C_4$  being present in the trapping potential, with  $C_4/C_2 \approx 5 \cdot 10^{-3}$  [Rou12]. The effect on the free-space cyclotron frequency can be calculated by the formulas derived in [Ket+14] and is given by:

$$\Delta\nu_c = -\frac{C_4}{C_2} \frac{3}{2d^2} \frac{\nu_+\nu_-}{\nu_+ - \nu_-} \rho_+^2 \quad , \quad (6.6)$$

where all motions are assumed to be cooled, except the modified cyclotron motion. This is excited during the PnP-measurement to  $\rho_+ \approx 10 \mu\text{m}$ , where it then probes the  $C_4$  terms. The characteristic trap dimension  $d$  corresponds to  $d \approx 1/C_2$ .

For all the Xe measurements, this shift results in  $\Delta\nu_c/\nu_c \approx 8 \cdot 10^{-12}$ . As described in Sec. 2.3, only the difference in the shifts affects the ratio of the frequencies, which in this case is  $\ll 1 \cdot 10^{-12}$ .

**Higher-order magnetic field terms:** Higher-order magnetic field terms lead to a systematic uncertainty, which can be determined by a measurement. The effect on the eigenfrequencies is explained in Sec. 2.2.2, while a possible measurement procedure is given in Sec. 4.4.

In order to shift the ion's position along the axial direction, offset voltages  $\pm U_{\text{off}}$  are applied to the correction electrodes with opposite sign for the upper and lower electrode. This adds a  $C_1 z$ -term to the trapping potential  $\Phi$  and shifts the minimum position depending on the strength of the offset voltage. The cooled ion's position along the  $z$ -axis is then also shifted to a new minimum position  $z_{\text{new}}$  of the potential. At this position the probed magnetic field is

$$B = B_0 + B_1 z_{\text{new}} \quad , \quad (6.7)$$

and the free-space cyclotron frequency is determined in this magnetic field.

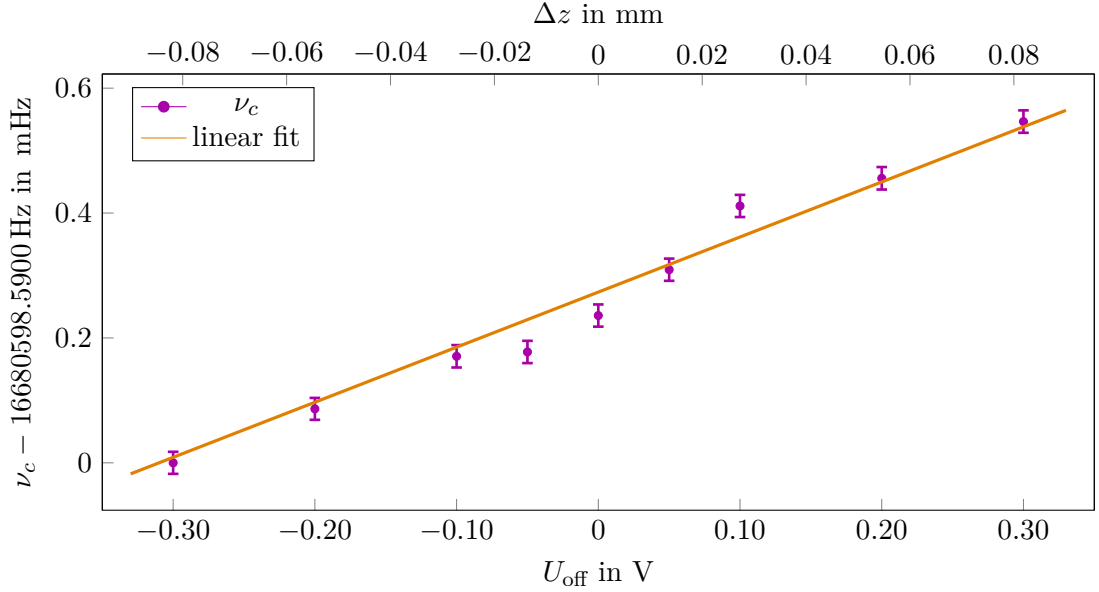


**Figure 6.5:** Measured shift in the cyclotron frequency (magenta) depending on the offset voltage  $U_{\text{off}}$  to the correction electrodes. The positional shift (top abscissa) can be determined by simulating the trap potential. The fit to determine the  $B_1$  term is given in orange.

For each applied shift to the correction electrodes, the three eigenfrequencies are determined with the dip or double-dip method. In order to calculate the magnetron and modified cyclotron frequency, the axial frequency, measured before and after the radial frequencies, is interpolated to the time of the radial frequency determination and also used for the calculation of the free-space cyclotron frequency.

The change of the free-space cyclotron frequency in trap 3 is shown in Fig. 6.5 depending on the applied offset voltage  $U_{\text{off}}$ . In order to convert the applied voltage gradient into a shift in position, the potentials created by the electrodes are simulated with COMSOL MULTIPHYSICS<sup>TM</sup>. For each electrode, the created potential in the trap center is simulated with 1 V applied, while the rest are at ground potential. This allows scaling the single contributions of each electrode with the applied potential in the measurement while adding them to receive the complete potential of the trap. The resulting calibration of the abscissa is shown with a second axis above the plot. A linear fit to the data points results in the magnetic field gradients in the two measurement traps of:

$$B_1^{\text{trap } 2} = 1.41(5) \frac{\mu\text{T}}{\text{mm}} \quad (6.8)$$

$$B_1^{\text{trap } 3} = -1.46(8) \frac{\mu\text{T}}{\text{mm}} \quad . \quad (6.9)$$

**Table 6.4:** Summary of systematic uncertainties of the ratio determination and the quadratic sum of all shifts for both mass differences,  $\Delta m = 1\text{u}$  and  $\Delta m = 2\text{u}$ .

shift	sys. uncertainty
resonator	$\ll 10^{-11}$
Polynomial fit	$4 \cdot 10^{-12}$
ion in adjacent trap	$\ll 10^{-12}$
image charge ( $\Delta m = 1\text{u}$ )	$\sim 3 \cdot 10^{-12}$
image charge ( $\Delta m = 2\text{u}$ )	$\sim 5 \cdot 10^{-12}$
relativistic shift	$< 1 \cdot 10^{-12}$
Higher order $\Phi$	$\ll 1 \cdot 10^{-12}$
$B_1$ ( $\Delta m = 1\text{u}$ )	$2 \cdot 10^{-12}$
$B_1$ ( $\Delta m = 2\text{u}$ )	$4 \cdot 10^{-12}$
$\sum(\Delta m = 1\text{u})$	$5.3 \cdot 10^{-12}$
$\sum(\Delta m = 2\text{u})$	$7.5 \cdot 10^{-12}$

When applying the offset voltages to the correction electrodes, not only a  $C_1$ -term appears in the trapping potential, but also higher-order terms, see calculation and explanation in [Doo18]. In the presence of a  $\Phi_3 = C_3 V_3$  the axial frequency scales quadratically with the applied  $U_{\text{off}}$ . Scanning this offset voltage and determining the axial frequency, already present  $C_1$  and  $C_3$  terms in the trapping potential can be cancelled out, at which offset the axial frequency is at its minimum value. As described above, the simulations can be used to convert this offset voltage of the minimum axial frequency to a positional shift along the  $z$ -axis. Repeating this measurement for ions with different charge-to-mass ratios, the shift of the position due to already present  $C_1$  and  $C_3$  terms depending on the applied ring electrode voltages can be determined.

With this measurement performed in [Doo18] for trap 2 and the strength of the  $B_1$  determined above, the following shifts are obtained:

$$\Delta R_{B_1}(\Delta m = 1\text{u}) = 2 \cdot 10^{-12} \quad (6.10)$$

$$\Delta R_{B_1}(\Delta m = 2\text{u}) = 4 \cdot 10^{-12} \quad (6.11)$$

While the measurements also probe magnetic field terms on the order of  $B_2$  and higher, their effect can be neglected as they scale at least with the positional shift squared. Additionally, such terms would also influence the fit in Fig. 6.5, where a linear fit describes the data reasonably well.

In Tab. 6.4 all systematic shifts are summarized. The final sum is given in the two lowest rows for a mass difference of  $\Delta m = 1\text{u}$  and  $\Delta m = 2\text{u}$ . The differences between the systematic uncertainties arise mainly due to higher-order magnetic field terms and the

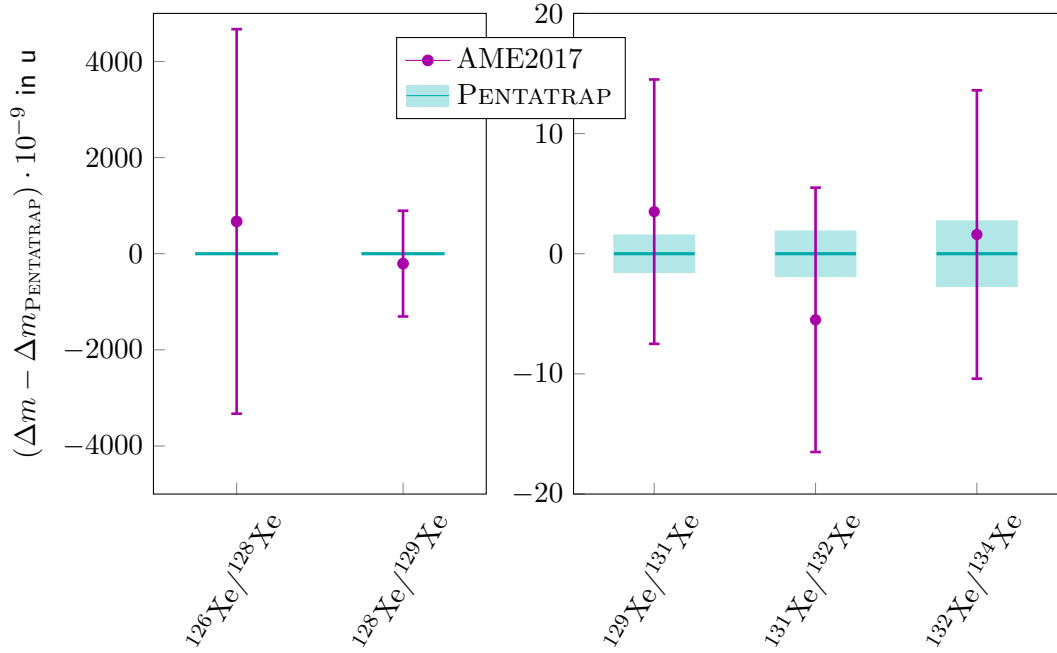


**Figure 6.6:** Xe mass differences obtained by PENTATRAP compared to AME2017. For the comparison, the mass difference measured with PENTATRAP  $\Delta m_{\text{PENTATRAP}}$  was set to zero. In the left plot the uncertainties of the PENTATRAP results are smaller than the marker.

image charge shift, while the rest does not depend on the mass difference. For the calculation of the mass differences the rounded values of the total systematic uncertainties  $\delta R_{\text{sys},1\text{u}} = 6 \cdot 10^{-12}$  and  $\delta R_{\text{sys},2\text{u}} = 8 \cdot 10^{-12}$  are taken.

#### 6.1.4 Comparison to AME2017

In Fig. 6.6 the mass differences obtained with PENTATRAP are compared to the AME2017 values. For the comparison, the PENTATRAP value was subtracted from both mass differences, such that the PENTATRAP results are shown at zero. Here, both the systematic and statistical uncertainty were quadratically added together. All mass differences of PENTATRAP agree within  $1\sigma$  with the AME2017 value. Due to the large differences of the uncertainty of the AME2017 values, the plot is divided into two parts.

In the left plot, the mass differences involving the less-known isotopes  $^{126}\text{Xe}$  and  $^{128}\text{Xe}$  are shown. Due to the large uncertainty of the AME2017 values, the uncertainty of the PENTATRAP result is smaller than the width of the marker. As can be seen in Tab. 6.3, the uncertainty of these two measurement cases is on the same order as the other mass differences shown in the right plot. The uncertainties of the two mass differences could be improved by a factor of 740 and 1700 for  $^{128}\text{Xe} / ^{129}\text{Xe}$  and  $^{126}\text{Xe} / ^{128}\text{Xe}$ , respectively.

The plot on the right side allows to better compare the results of the AME2017 and PENTATRAP. The uncertainty of the PENTATRAP result is at least a factor of 4 smaller. The agreement between the AME2017 and the PENTATRAP result demonstrates the good and reliable performance of PENTATRAP.

## 6.2 Binding energy of the 37<sup>th</sup> electron in Xe

The precision of the masses of the Xe isotopes is not high enough to perform a detailed test of the accuracy reached at PENTATRAP. Therefore, a measurement of the binding energy of the 37<sup>th</sup> electron in <sup>132</sup>Xe was performed by measuring the mass difference of the ion in the charge states  $q = 17+$  and  $q = 18+$ . The result is in agreement with theoretical calculations of the binding energy of similar or better precision and demonstrates the accuracy and precision of PENTATRAP. This serves as a proof-of-principle measurement for QED tests on HCs.

The measurements of the binding energy were one of the first measurements to be performed with PENTATRAP. As at this time only one resonator was working sufficiently well, all measurements were done in trap 2. In total, six measurement runs were performed over the course of one week, resulting in 49 frequency ratio determinations, which were analysed with the polynomial method. In comparison to the mass measurements, 15 instead of ten phases and axial spectra were saved during one pnp-cycle and the long phase evolution  $t_{\text{acc}}$  time was only 20 s instead of 40.05 s, see Sec. 4.3.2. The final result of two independent analyses,

$$R_{E_B} = \frac{\nu_c(^{132}\text{Xe}^{18+})}{\nu_c(^{132}\text{Xe}^{17+})} = \frac{18 m(^{132}\text{Xe}^{17+})}{17 m(^{132}\text{Xe}^{18+})} = 1.058827929543(17)_{\text{stat}} \quad , \quad (6.12)$$

shows that the same statistical uncertainty could be reached with this measurement setup as compared to the mass measurements. This is also visible in Fig. 6.7 where all measured ratios are shown. The scattering around their mean value extends to similar ranges as for the mass measurements.

### 6.2.1 Systematic shifts

The difference in their charge-to-mass ratio is larger for ions in a different charge state, but with the same mass, compared to ions in the same charge state, but with different masses as in the case of the mass measurements. Only the systematic shifts discussed in Sec. 6.1.3 for the mass difference measurements, which depend on the charge-to-mass ratio, evaluate to different values in the analysis of the binding energy measurement:

**Image charge shift:** The image charge shift only depends on  $\Delta m$  and is independent of the charge state, see Eq. (2.33). Therefore, this shift is not applicable to the binding energy measurement.

**Higher-order magnetic field terms:** The effect of the magnetic field term  $B_1$  depends on the difference in the voltages applied to the ring electrode for both ions.

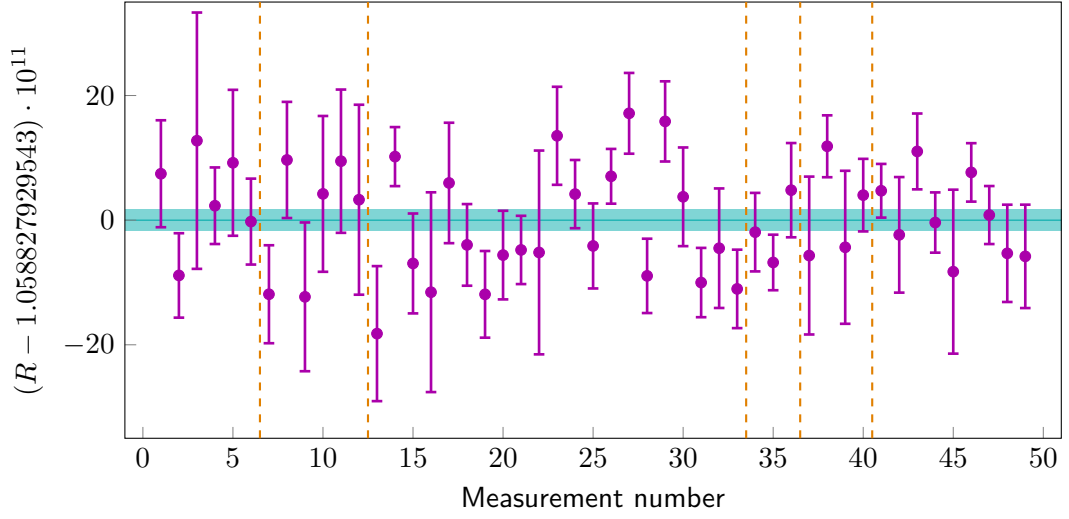


**Figure 6.7:** All measured cyclotron-frequency ratios of  $^{132}\text{Xe}^{18+} / ^{132}\text{Xe}^{17+}$ . The blue bar shows the final result of the mass difference. The dashed lines separate the different measurement runs.

As this depends on the charge-to-mass ratio, the difference is larger compared to the mass measurements, resulting also in a larger shift of the frequencies. The shift in axial position for  $q = 17+$  and  $q = 18+$  was measured in [Doo18] and results in a shift due to  $B_1$ :

$$\frac{\Delta\nu_c}{\nu_c}(q = 17+) = 4.30(19) \cdot 10^{-10} \quad , \quad (6.13)$$

$$\frac{\Delta\nu_c}{\nu_c}(q = 18+) = 3.89(20) \cdot 10^{-10} \quad . \quad (6.14)$$

As described in Sec. 2.3, the shift on the frequency ratio depends on the difference of the shifts to the free-space cyclotron frequencies. Therefore, the frequency ratio needs to be corrected by:

$$R_{\text{corr}} = R_{\text{meas}}(1 + 4.1(2.8) \cdot 10^{-11}) \quad . \quad (6.15)$$

The uncertainty of the ratio shift is quadratically added to the overall systematic uncertainty.

**Higher-order electric field terms:** While this shift depends on the charge-to-mass ratio of the ions through the eigenfrequencies, the effect on the frequency ratio is again negligible.

The final systematic uncertainty is then only given by the small uncertainty of the polynomial method ( $4 \cdot 10^{-12}$ ) and the uncertainty of the  $B_1$  shift. The corrected frequency ratio results in:

$$R_{E_B, \text{corr}} = 1.058827929585(17)_{\text{stat}}(30)_{\text{sys}} \quad . \quad (6.16)$$

### 6.2.2 Calculation of the binding energy

The calculation of the binding energy, given in Eq. (1.4), for the Xe ions can be expressed by:

$$\begin{aligned}\Delta E_B &= m(A_1^{q_1+}) - m(A_2^{q_2+}) + (q_1 - q_2)m_e \\ &= m(^{132}\text{Xe}^{17+}) - m(^{132}\text{Xe}^{18+}) - m_e \\ &= \left(\frac{17}{18}R - 1\right) m(^{132}\text{Xe}^{18+}) - m_e \quad .\end{aligned}\quad (6.17)$$

The uncertainty is given by

$$\delta(\Delta E_B) = \sqrt{\left(\frac{17}{18}m(^{132}\text{Xe}^{18+}) \cdot \delta R\right)^2 + \left(\left(\frac{17}{18}R - 1\right) \delta m(^{132}\text{Xe}^{18+})\right)^2 + (\delta m_e)^2} \quad .\quad (6.18)$$

Due to the weighting of the ratio with the two charge states,  $\frac{17}{18} \cdot R - 1 \approx 4.2 \cdot 10^{-6}$ , the mass  $m(^{132}\text{Xe}^{18+})$  needs to only be known better than  $\delta m/m < 10^{-5}$  for its uncertainty to be negligible. The mass of  $m(^{132}\text{Xe}^{18+})$  can be expressed as

$$m(^{132}\text{Xe}^{18+}) = m(^{132}\text{Xe}) - 18 \cdot m_e + E_{\text{bind}}(18e^-) \quad ,\quad (6.19)$$

where  $m(^{132}\text{Xe})$  is the mass of the neutral Xe isotope and  $E_{\text{bind}}(18e^-)$  the binding energy of the removed 18 electrons. The effect of the mass of 18 electrons in a Xe atom is on the order of  $18m_e/m(^{132}\text{Xe}^{18+}) \approx 8 \cdot 10^{-5}$  and, therefore, needs to be considered, while the binding energy ( $E_{\text{bind}}(18e^-) \approx 4 \text{ keV}$  [Kra+]) can be ignored, as it only affects the neutral mass on the level of  $\approx 3 \cdot 10^{-8}$ .

The frequency ratio of  $^{132}\text{Xe}^{17+}$  and  $^{132}\text{Xe}^{18+}$  leads to the binding energy of the 37<sup>th</sup> electron:

$$\Delta E_B = 432.4(1.3)_{\text{stat}}(3.4)_{\text{sys}} \text{ eV} \quad .\quad (6.20)$$

Presently, there is no experimental value of this binding energy known to which the result obtained with PENTATRAP could be compared. In order to demonstrate the accuracy of the measurement, the binding energy is calculated by theory. This is performed with the multi-configuration Dirac-Hartree-Fock (MCDHF) method [Gra79; DMO71] to account for relativistic corrections, such as the Breit correction, due to the high nuclear charge. At these low charge states, the QED corrections only amount to  $\approx 20 \text{ meV}$  [Har19] and cannot be resolved within the current experimental precision. Still, the two independently obtained theory values agree within the uncertainties with the result from PENTATRAP:

$$\begin{aligned}\Delta E_{\text{Theo1}}^{\text{prelim.}} &= 432.9 \text{ eV} && \text{[Ind19]} \\ \Delta E_{\text{Theo2}} &= 435.1(3) \text{ eV} && \text{[Har19]} \\ \Delta E_{\text{PENTATRAP}} &= 432.4(1.3)_{\text{stat}}(3.4)_{\text{sys}} \text{ eV} \quad .\end{aligned}\quad (6.21)$$

The first theory value and its uncertainty is still under investigations. The uncertainty is expected to be  $\delta \Delta E \approx 3 \text{ eV}$  [Ind19].

While the contributions of the QED corrections to the binding energy, in this case, are too small, it can still be seen as a proof-of-principle measurement for the test of many-electron atomic structure theories. As the QED contributions increase with increasing charge state of the ions, very highly charged ions, e.g. hydrogen-like systems, can be used in future measurements of electron binding energies. An uncertainty of the binding energies on the order of  $\approx$  eV allows then to perform stringent tests of bound-state QED in the strong electromagnetic fields of nuclei [Häf+00].

# 7

---

## Rhenium: Discovery of Metastable States

---

Measurements in Re were started in order to determine the  $Q$ -value of the  $\beta$ -decay in  $^{187}\text{Re}$  to its daughter nuclide  $^{187}\text{Os}$ . The chosen charge state was  $q = 29+$  as this corresponds to a closed electronic shell in Re and just one electron in the outer shell in Os. Such ions can be more selectively charge bred in an EBIT as opening up a closed shell corresponds to a large increase in ionization energy. Furthermore, the binding energy can be calculated more easily for a closed shell. First measurements resulted in two different values for the free-space cyclotron frequency ratio of these ions, which led to a more thorough investigation.

The measurements of  $^{187}\text{Re}^{29+} / ^{187}\text{Re}^{29+}$  resulted again in two values of the ratio. The first is unity, which is expected when weighing two ions of the same species against each other. The second differed on the level of  $10^{-9}$ , which corresponds to a mass difference of  $\approx 200 \text{ eV}/c^2$ . An identification as an excited electronic state in one of the Re ions leading to the larger mass, was possible with FLEXIBLE ATOMIC CODE (FAC) calculations [Gu08; Bek19]. As a consistency check, also  $^{187}\text{Os}^{30+}$  ions were investigated, which feature the same electronic configuration as  $^{187}\text{Re}^{29+}$ . Also here a metastable electronic state with an excitation energy of  $\approx 207 \text{ eV}$  was found.

More thorough calculations of this metastable, excited state confirmed the experimental result. Furthermore, with a (preliminary) theoretical lifetime of  $\sim 200 \text{ d}$  [Ind19] and a linewidth of  $5 \cdot 10^{-8} \text{ Hz}$ , it is challenging to characterize this transition by narrow-linewidth laser spectroscopy. Both states were the first long-lived metastable electronic

states to be directly identified with Penning-trap mass spectrometry. This opens up the possibility to use Penning-trap mass spectrometry to confirm and detect metastable states in HCIs, which could be used for a new generation of clocks. Furthermore, as only few transitions are known in HCIs, more measurements could lead to an advancement in theoretical models in this energy region.

## 7.1 Electronic structure of HCIs

When filling the shells of neutral atoms, the electrons always fill the shells with the lowest energy first. For hydrogen and hydrogen-like ions, the level structure follows the so-called Coulomb ordering. A non-relativistic calculation leads to the shells or orbitals with the lowest principle quantum number  $n$  to be occupied first, followed by the sub-shells ordered according to their azimuthal quantum number  $l$ . This leads to the ordering of

$$\text{Coulomb ordering: } 1s^2 2s^2 2p^6 3s^2 3p^6 3d^{10} 4s^2 4p^6 4d^{10} 4f^{14} \dots, \quad (7.1)$$

with s, p, d, f corresponding to  $l = 0, 1, 2, 3$ .

This ordering changes for atoms and especially for lowly charged ions. For example, following the explanation given in [QV14],  $K^+$  has all shells filled up to 3p. Following the Coulomb ordering, the final electron for neutral potassium would be in the 3d shell, while in reality the 4s shell is filled. This change arises from the interaction of multiple electrons in the shell. While electron  $e_1^-$  changes the electric field for electron  $e_2^-$  and vice versa, the inner shell electrons also screen the electric field of the nucleus for outer electrons. Thereby, orbitals with a smaller effective radius are energetically preferred. The ordering of the energy levels in the periodic table is, therefore, different from the Coulomb ordering and follows the  $n + l$  rule, leading to the Madelung ordering. First, the orbitals with the lowest  $n + l$  are filled, where, for the same  $n + l$ , the shell with the lowest  $n$  is favoured. This leads to the ordering:

$$\text{Madelung ordering: } 1s^2 2s^2 2p^6 3s^2 3p^6 4s^2 3d^{10} 4p^6 5s^2 4d^{10} 5p^6 \dots. \quad (7.2)$$

For heavy highly charged ions the screening effect of the inner shell electrons is minimised. Thereby, at a certain point in the isoelectronic sequence (same number of electrons, but different elements) the ordering is expected to return to the Coulomb ordering when increasing the charge state. For the isoelectronic sequence of K ( $Z = 19$ ), this is the case for  $Sc^{2+}$ , where the 3d shell is filled before the 4s. The change in the ordering leads to a level crossing at certain charge states for specific levels [Ber+12]. The level crossings up to the shell  $\sim 5f$  are shown in Fig. 7.1.

### 7.1.1 Electronic configuration of $^{187}\text{Re}^{29+}$

In  $^{187}\text{Re}^{29+}$  the shells are filled following the Coulomb ordering and all shells up to 4d are filled [Kra+], see magenta coloured levels in Fig. 7.1. The lowest-lying excited state can then be found in the next higher-energetic orbital which would be filled when going to

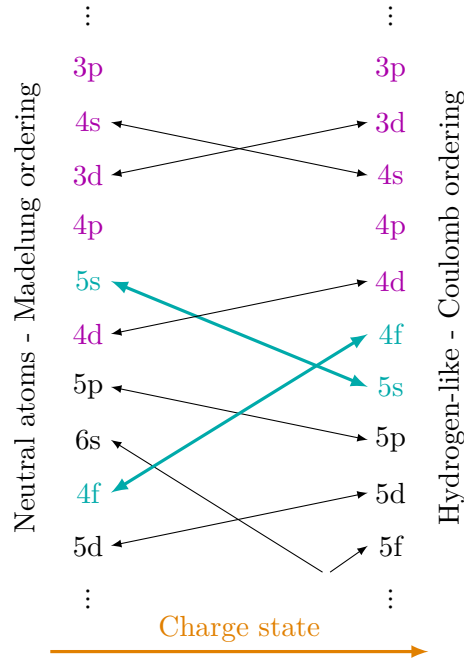


**Figure 7.1:** Level crossings in HCIs occur when the ordering of the electronic shells changes from the Madelung ordering in neutral atoms to the Coulomb ordering in hydrogen-like ions due to the screening effect of inner shell electrons. The magenta coloured levels indicate the shells filled, the blue arrows the level crossing of interest in  $\text{Re}^{29+}$ . Based on [Ber+12].

$q = 28+$ . Looking at the isoelectronic sequence of Ag ( $Z = 47$ , the number of remaining electrons as in  $^{187}\text{Re}^{28+}$ ), the level crossing is found between  $\text{Pm}^{14+}$ , whose outer shell is the 5s, and  $\text{Sm}^{15+}$ , where the valence electron occupies the 4f shell. Therefore, the lowest-lying excited state in  $^{187}\text{Re}^{29+}$  can be found in the 4f shell [Kra+]. The blue levels show this level crossing in Fig. 7.1.

As described above, the electronic configuration of  $^{187}\text{Re}^{29+}$  ends at  $4d^{10}$ :

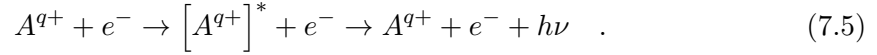
$$[^{187}\text{Re}^{29+}] = [\mathbf{Kr}] 4d^{10} = 1s^2 2s^2 2p^6 3s^2 3p^6 3d^{10} 4s^2 4p^6 4d^{10} \quad . \quad (7.3)$$

Prerequisite for a mass measurement of an ion in a metastable state is a sufficiently long lifetime of the excited state. In order to achieve high enough statistics, the excited state needs to be present for at least several hours. Calculations using FAC reveal a vast majority of high-energetic levels, of which most decay immediately back to a lower-lying state [Bek19]. The long-lived state was found in the electronic configuration

$$[^{187}\text{Re}^{29+}]^* = [\mathbf{Kr}] 4d^9 4f^1 \quad . \quad (7.4)$$

### 7.1.2 Excited states in an EBIT

Inelastic collisions between high-energetic electrons of the electron beam and the target atoms or ions can lead to the excitation of bound electrons into open shells close to the ground state [QV14]. This process, called electron-impact excitation, does not change the charge state of the ions:



The excited state  $[A^{q+}]^{*}$  decays back to the ground state while emitting energy in the form of radiation,  $h\nu$ . The type of transition between the excited state and ground state depends on the quantum numbers of the two states. For example, in an electric dipole (E1) transition, the difference in total angular momentum of the involved states needs to be  $\Delta j \leq 1$  to account for the angular momentum of the emitted or absorbed photon during the transition.

In general, electronic transitions in atoms can be characterized by the transition matrix, which reflects the parity of the involved states and defines the transition probability. If the transition matrix vanishes in dipole approximation, i.e. the electric dipole transition is forbidden by symmetry considerations, it can only be excited or de-excited via higher-order multipole transitions, e.g. magnetic dipole (M1), electric quadrupole (E2), and so on. Since the transition rate of such transitions is suppressed by many orders of magnitude compared to multipole transitions of lower order [CCS51], excited electronic states which can only de-excite via a higher-order multipole transition feature long lifetimes.

The excited state in  $^{187}\text{Re}^{29+}$  has a total angular momentum of  $j = 5$  and can, therefore, only decay back to the ground state ( $j = 0$ ) via an E5 transition with a long lifetime of around 200 d [Ind19]. This corresponds to a small linewidth of  $5 \cdot 10^{-8}$  Hz. The effects of hyperfine quenching [IPM89] and magnetic quenching [BSO03] lead to a mixing of the energy levels and a possible smaller lifetime. While these effects are currently being investigated [Ind19], the measurements performed with this metastable state still allows determining a lower limit of the lifetime.

## 7.2 Performed measurements

Compared to the Xe measurements in the previous chapter, a few changes to the experimental setup and the measurement scheme were made:

**Stabilization system:** The level of liquid helium, the pressure in the magnet bore, as well as the temperature in the lab, were stabilized. Thus, magnetic field drifts present during some of the Xe measurements, as shown in Fig. 6.2, were reduced for the measurements with Re and exhibit nearly the same trend for both measurement traps, see Fig. 7.3. The cancellation method (see Sec. 5.7.2) could, therefore, in principle be applied.

**Magnetron frequency determination:** The magnetron frequency was only determined during the preparation of the ions. The missing value for it can be treated as an unknown shift in the free-space cyclotron frequency ratio. As described in Sec. 2.3, only the difference in the shifts of both cyclotron frequencies is of importance to the ratio determination. As the mass difference between the metastable and the ground state is on the order of  $10^{-9}$ , and the magnetron frequency is identical for both ion species to the precision to which it could be determined, the effect on the ratio can be neglected.

**Loading specific ions:** The small mass difference is only detectable during the phase measurement of the modified cyclotron frequency. It cannot be determined which ion is loaded before the data is analysed. This led to several measurements performed with three identical ions and, thus, the desired order of ions (metastable - ground - metastable or vice versa) could not be met regularly. The number of measurements needed to reach a certain precision is therefore considerably larger than in the case where the ion order can be regulated.

**Systematic shifts:** On the other hand, all settings, i.e. voltages and *rf*-pulses, are the same for ions in the ground and the metastable state. Therefore, any systematics leading to an absolute shift in the ratio would need to be on the order of  $> 10^{-3}$  to be relevant for a relative mass difference of  $\Delta m/m \approx 10^{-9}$ . No such shift depending on the mass difference exists.

In Tab. 7.1 an overview over all measurements for which the ions' electronic state could be identified is shown together with the rough results (ratio is 1 or  $\neq 1$ ). G is used to denote the ground state and M the metastable state. The number of measurements corresponds to a continuous measurement campaign of either using only  $^{187}\text{Re}^{29+}$  or measuring  $^{187}\text{Re}^{29+}$  against  $^{187}\text{Os}^{29+}$ . In total, 18 measurements of the metastable state using only  $^{187}\text{Re}^{29+}$  were performed. The 9 measurements not listed in Tab. 7.1 were either performed with three identical ions or the ion lifetime in the trap was too short and no identification was possible.

For the production rate of the metastable and the ground state, the number of ions produced in the respective state can be investigated. Out of the 26 ions which could unambiguously be identified in the measurements as listed in Tab. 7.1, 14 are in the metastable state and 12 in the ground state. Even with this relatively low statistics, the production probability of the metastable state is about 50%.

The idea behind the identification of the excited state is shown in Fig. 7.2. Three ions are loaded into the three traps, trap 2, 3, and 4, and their free-space cyclotron frequency is alternately measured in the two measurement traps, trap 2 and trap 3. In trap 3, the fit to determine the frequency ratio with the polynomial method (see Sec. 5.7.1) shows that the magenta and orange ions are the same species. The polynomials for both ions are overlapping within the measurement uncertainty. For this example, the frequency ratio is determined to:

$$R_{\text{trap } 3} - 1 = 2.5(6.9) \cdot 10^{-11} \quad (7.6)$$

**Table 7.1:** Summary of all measurements performed using only  $^{187}\text{Re}^{29+}$  ions. The number of the measurement # corresponds to the number in a series of measurements, not exclusively using only  $^{187}\text{Re}^{29+}$ . Only the measurements are listed for which an identification of the ions' electronic state was possible. The rough results of the frequency ratio in the two traps is denoted by 1 or  $\neq 1$ . The state of the three ions is either G for the ground state and M for metastable. The number of pnp-cycles in both traps depend on the lifetime of the ions and is correlated with the number of frequency ratios which could be determined with the polynomial method.

#	ratio in		state of			pnp-cycles in		# ratios	
	trap 2	trap 3	ion 1	ion 2	ion 3	trap 2	trap 3	trap 2	trap 3
6	1	$\neq 1$	G	G	M	3	2	-	-
7	$\neq 1$	1	G	M	M	7	7	1	1
8	$\neq 1$	$\neq 1$	M	G	M	13	13	3	3
9	$\neq 1$	1	M	G	G	12	12	3	3
10	$\neq 1$	1	G	M	M	3	3	-	-
26	$\neq 1$	$\neq 1$	M	G	M	11	14	2	3
28	$\neq 1$	$\neq 1$	M	G	M	72	100	14	20
29	$\neq 1$	$\neq 1$	G	M	G	15	4	3	1
30	?	$\neq 1$	?	M	G	-	5	-	1

and is therefore consistent with unity within its uncertainty.

In trap 2 the blue ion has a larger mass, as its free-space cyclotron frequency is lower. It is, therefore, in the metastable state and the other ions are in the ground state. The difference in the frequency between the two polynomials is  $\approx 17$  mHz and the ratio results in

$$R_{\text{trap 2}} - 1 = 115.0(3.5) \cdot 10^{-11} \quad . \quad (7.7)$$

With that discrepancy in the determined frequency ratios of two orders of magnitude, an accidental wrong assignment of the ions' electronic state is unlikely.

### 7.3 Data analysis

For the Xe measurements, the applicability of the cancellation method (see Sec. 5.7.2) was mainly limited by the stabilisation system of the magnet laboratory and the ion lifetime in the trap. In the case of the metastable against the ground state, the fact that the ions are loaded randomly further limits its applicability. Only two configurations of ions in the traps (ground - metastable - ground or metastable - ground - metastable) are usable for the cancellation method. With a production probability of  $\approx 50\%$  of the ion being in the ground or the metastable state, the two configurations appear statistically in 1/3 of the combinations, where an ion identification was possible. Therefore, the

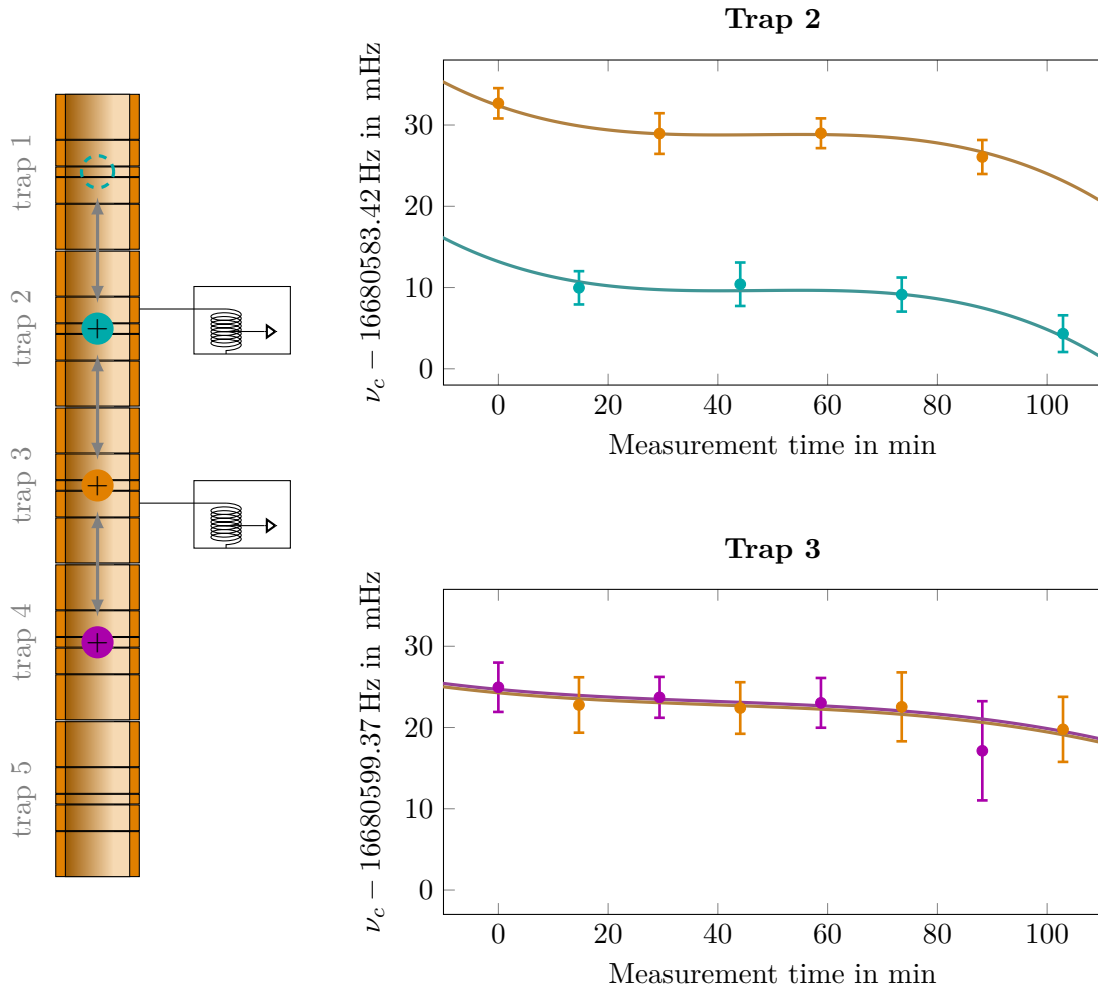


**Figure 7.2:** Identification of the electronic state of the ions. **Left:** Penning traps with the order of loaded ions. **Top:** Determination of the frequency ratio of the two ions in trap 2, identifying the blue ion to be heavier, i.e. in the metastable state, and the orange one to be in the ground state. **Bottom:** In trap 3 the polynomials overlap, indicating that the ions are in the same state, in this case the ground state.

number of data points, which can be analysed with the polynomial method, is higher as all of the ion configurations featuring both electronic states are included (ground - ground - ground or metastable - metastable - metastable are discarded).

Measurement 28 was executed for nearly three complete measurement cycles for ions in the desired order before the uppermost ion was lost after 72 pnp-cycles. The behaviour of the free-space cyclotron frequency during the measurement is shown in Fig. 7.3. The magenta data points correspond to the metastable state, the blue to the

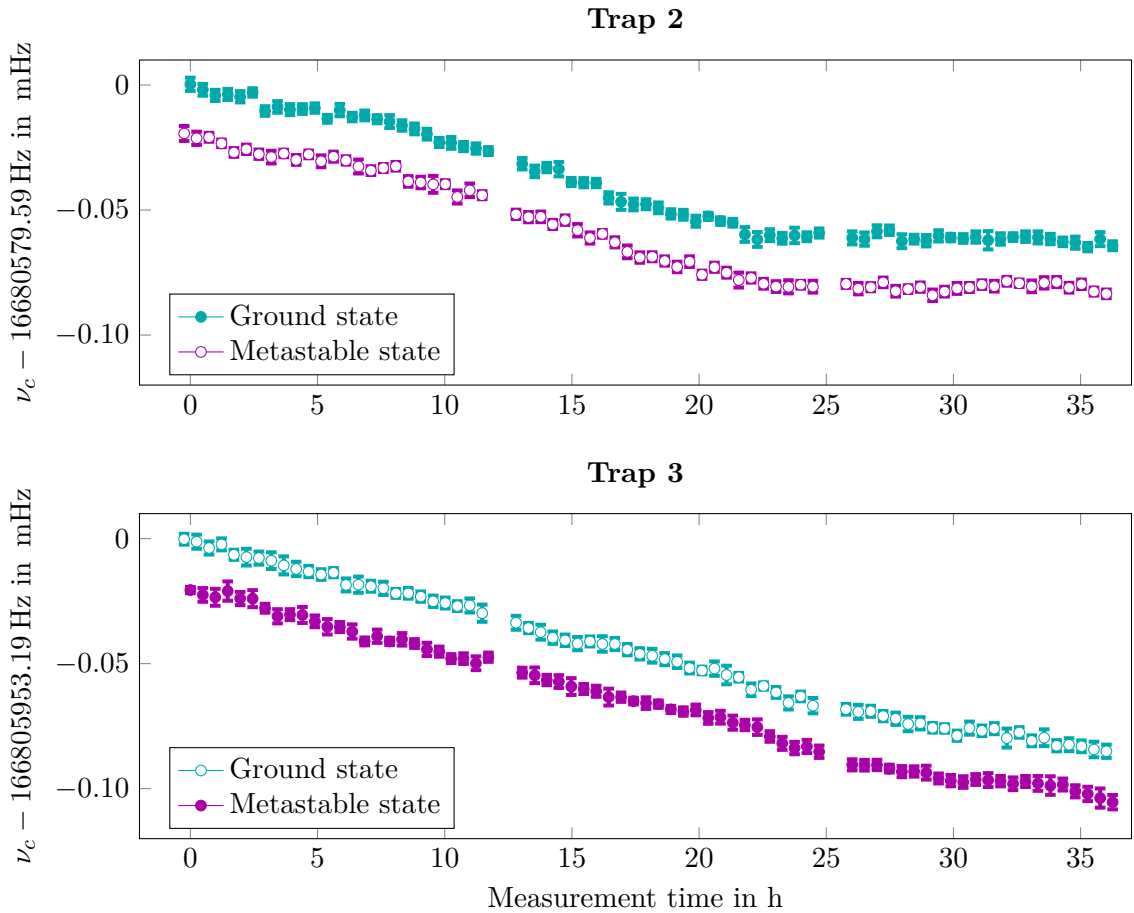


**Figure 7.3:** Free-space cyclotron frequencies in both measurement traps for  $^{187}\text{Re}^{29+}$  ions in measurement 28 recorded over three cycles, see Tab. 7.1. The increase in room temperature during the third cycle after  $\sim 25$  h leads to a different trend in trap 2 for the frequencies. The fourth measurement cycle in trap 3, listed in Tab. 7.1, is not shown since the uppermost ion was lost

ground state. The empty circles and the filled circles indicate frequencies which were determined simultaneously. Compared to Fig. 6.2, the trend in the magnetic field is identical for both traps for the first two cycles (cycles are separated by a gap in the measurement run, at which time an  $N$ -determination measurement was performed). In the third cycle, the temperature in the magnet laboratory, as well as the pressure in the magnet's bore, was increasing, leading to a slightly different trend in trap 2. For a discussion of this effect, see [Kro19].

Due to the sufficiently long lifetime of the ions in the traps, this measurement can be used to compare the cancellation to the polynomial method. In Fig. 7.4 the results of both methods are shown. For the cancellation method, one frequency ratio is determined for each pnp-cycle (top). In the polynomial method (bottom) about five pnp-cycles for

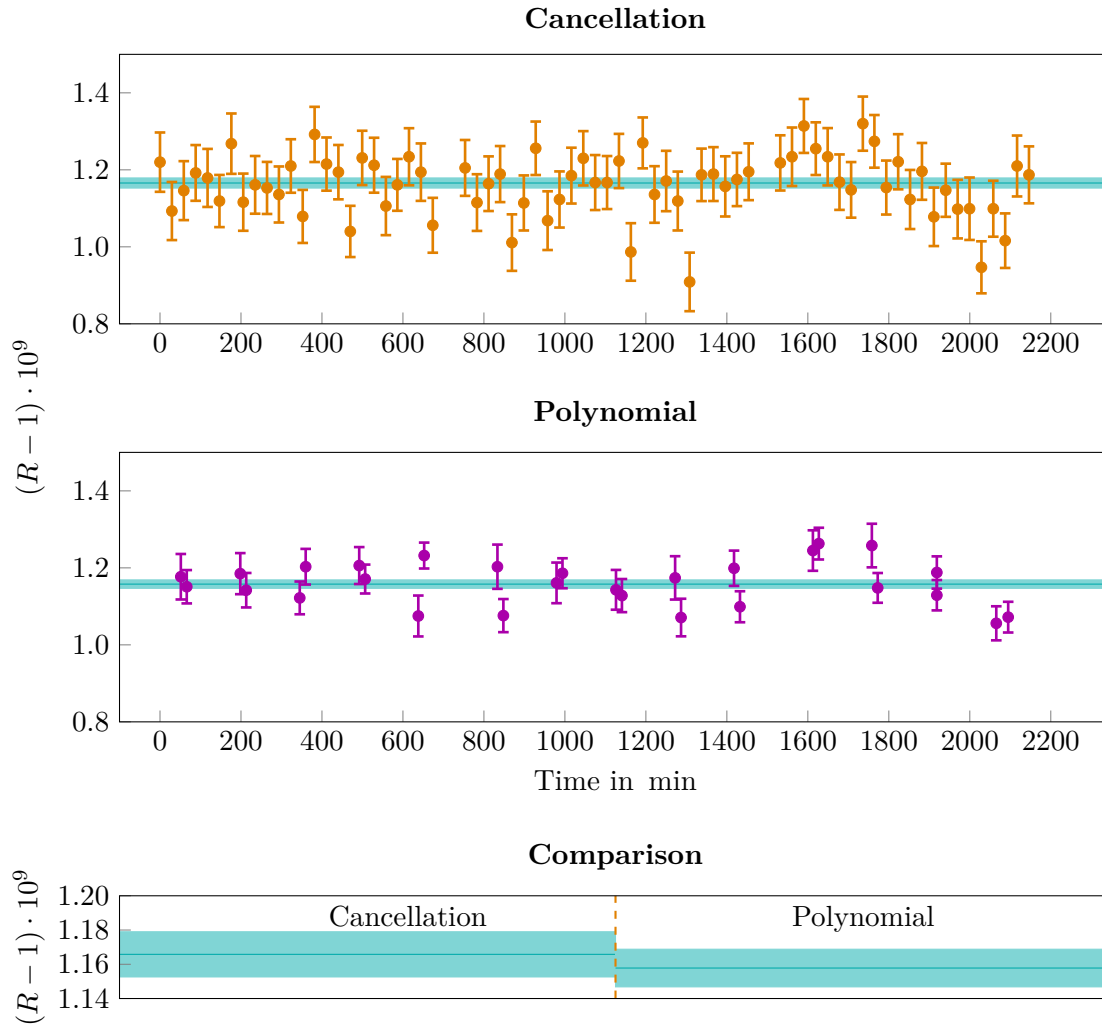


**Figure 7.4:** Comparison of the cancellation (**top**) and polynomial method (**middle**). The uncertainty of each ratio in the cancellation is a factor of  $\sim 2$  larger than those of the polynomial method. **Bottom:** As 5 times more ratios are obtained in the cancellation method compared to the polynomial, both methods lead to similar final uncertainties.

each trap are used for one frequency ratio fit, which results in a factor of five less frequency ratios. The uncertainty of each frequency ratio in the cancellation method is a factor of  $\sim 2$  worse than that for the polynomial method. However, due to the high number of data points, the overall uncertainties are nearly the same:

$$R_{\text{poly}} = 1.000000001158(11) \quad (7.8)$$

$$R_{\text{cancel}} = 1.000000001166(13) \quad (7.9)$$

Both methods agree within  $1\sigma$ , which is shown in the lowest plot.

The effect of the change in magnetic field trend in trap 2 might be mimicked both in the cancellation as well in the polynomial ratios, as the values decrease over the last cycle. In the polynomial plot, the two values for the cyclotron frequency ratio determined at the same time correspond to the two values obtained in trap 2 and trap 3. If the changing magnetic field was the cause for the downward trend, the values for both traps would substantially differ in this region. Since this is not observed, a slowly changing magnetic field does not limit the application of the cancellation method.

For this relatively large number of data points the uncertainty resulting from the cancellation method is still larger than for the polynomial method. While the uncertainty might still be improved in even longer measurements, in the case of  $^{187}\text{Re}^{29+}$  the polynomial method is preferred. It has the advantage of a smaller uncertainty as well as wider applicability to the data measured here, as it does not require a certain order of the ions.

## 7.4 Systematic effects

With the relative mass difference on the order of  $\Delta m/m \approx 10^{-9}$  for the ions in the ground and the metastable state, only a difference in the phase of the modified cyclotron frequency can be measured. Both the axial and the magnetron frequency are determined less precise and are, therefore, identical for both ion states. This leads to the fact that also all voltages and *rf*-fields, whether it be amplitude or frequency, are the same.

As shown in Sec. 2.3, a systematic effect shifts the frequency ratio only by the relative change in the two cyclotron frequencies. In order to change the ratio significantly, one of the two free-space cyclotron frequencies would need to be shifted by  $\Delta\nu_c > 10^{-3}$  Hz with respect to the other frequency. The only effect contributing on this level is a wrong determination of the full number of revolutions  $N$  of the phase. A change of  $\Delta N = \pm 1$  results in a shift of the cyclotron frequency on the order of  $1/t_{\text{acc}} \approx 0.025$  Hz. While the relative shift,  $\Delta\nu_c/\nu_c \approx 1.5 \cdot 10^{-9}$ , is on the same level as the effect of the metastable state, it is larger by  $\approx 4 \cdot 10^{-10}$ . This makes the misinterpretation of a wrong  $N$  as the metastable state impossible. Due to the large discrepancy, a wrong  $N$  would be easily identified and corrected, also eliminating this effect.

The only systematic effect of interest is the one arising from the polynomial fit. Here, measurement 28 was analysed with polynomials of degrees two, three, and four. The differences in the final frequency ratios to are:

$$\begin{aligned} |R_{2\text{nd}} - R_{3\text{rd}}| &= 2.6 \cdot 10^{-12} \quad \text{and} \\ |R_{4\text{th}} - R_{3\text{rd}}| &= 0.6 \cdot 10^{-12} \quad , \end{aligned} \tag{7.10}$$

while all resulted in a statistical uncertainty of the ratio of  $\delta R = 9 \cdot 10^{-12}$ .

Taking the difference between the second and third order polynomial as a systematic uncertainty leads to an overestimation of that uncertainty. The second-order polynomial might just not be sufficient to describe the magnetic field trends. This is evident, as the

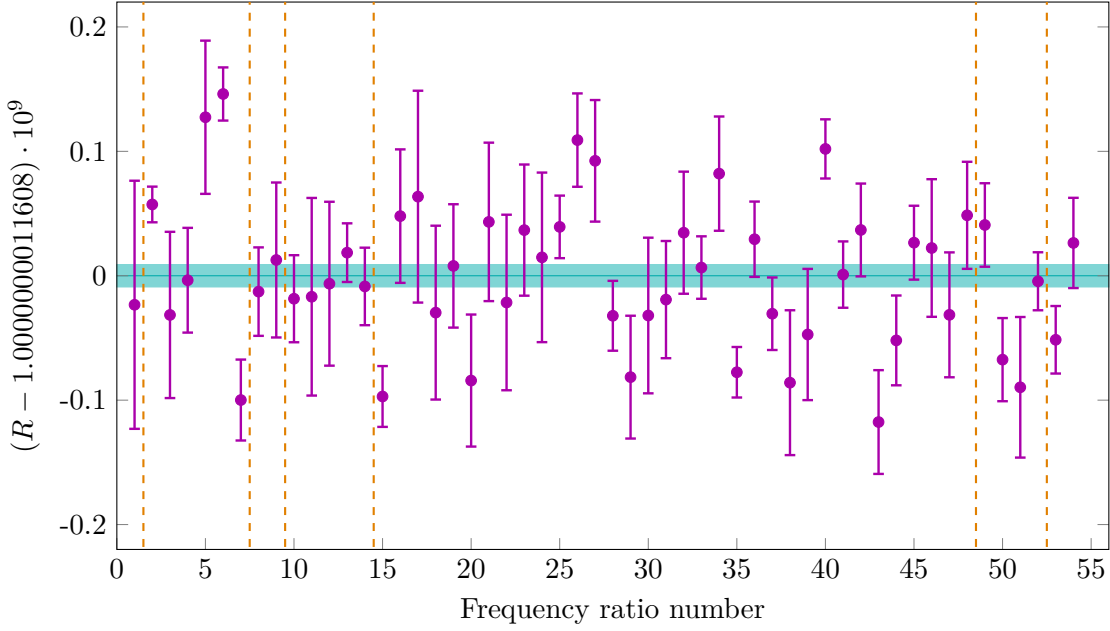


**Figure 7.5:** All cyclotron frequency ratios obtained with the polynomial method of the excited to the ground state in  $^{187}\text{Re}^{29+}$ . The dashed lines divide the different measurement runs listed in Tab. 7.1, except measurement 6 and 10, where no ratio could be calculated due to the short lifetime of the ions in the trap.

difference between the third and the fourth order ratio is a factor of five less and thus both describe the behaviour equally well.

Two of the main systematic shifts for the Xe measurement arose due to the  $B_1$ -term and the image charge shift. Both depend on the mass difference of the two ions. For a relative mass difference of  $10^{-9}$ , both shifts are negligible. The systematic uncertainties can, therefore, be neglected in the measurement of the metastable and the ground state.

## 7.5 Energy of the metastable state

### 7.5.1 Experimental result

In Fig. 7.5, all free-space cyclotron frequency ratios of the metastable state to the ground state determined with the polynomial method are shown. The dashed lines separate the different measurements as listed in Tab. 7.1. No drift or systematic deviation between the measurements is observed. Due to the short ion lifetime, no ratio could be determined from measurements 6 and 10.

An additional statistical uncertainty comes from the two independent analyses performed on the data and is on the order of  $\delta R/R \approx 4 \cdot 10^{-12}$ . The frequency ratio results in:

$$R_{\text{final}}^{\text{Re}} = 1.0000000011608(92) \quad (7.11)$$

As mentioned at the beginning of the chapter, the metastable state was found during the determination of the  $Q$ -value of the  $\beta$ -decay in  $^{187}\text{Re}$  to  $^{187}\text{Os}$ . Os has one proton more, such that  $^{187}\text{Os}^{30+}$  shares the same electronic configuration as  $^{187}\text{Re}^{29+}$ . As a consistency check, the same metastable state was identified in measurements using only  $^{187}\text{Os}^{30+}$  ions. Due to a generally lower production rate of Os ions in the DreEBIT, the statistical uncertainty is a factor 3 less precise than for Re:

$$R_{\text{final}}^{\text{Os}} = 1.0000000011760(270) \quad . \quad (7.12)$$

From these two values, the mass and thereby also the energy difference of the two metastable states can be calculated according to Eq. (5.38). In the calculation of the uncertainty of the mass difference,

$$\delta(\Delta m) = \sqrt{(m_{\text{ground}} \cdot \delta R)^2} \quad , \quad (7.13)$$

the mass uncertainty of the ground state can be neglected. As described in Sec. 5.8, this is suppressed by  $R - 1$  and needs to be known only to a level of  $\delta m/m \approx 10^{-3}$  such that its uncertainty is insignificant. Therefore, it is sufficient to use the literature value of the mass [Wan+17] without any uncertainty for both cases. The mass differences for the metastable states in Re and Os are:

$$\begin{aligned} \Delta E^{\text{Re}} &= 202.2(1.6) \text{ eV} \\ \Delta E^{\text{Os}} &= 207(3) \text{ eV} \quad . \end{aligned} \quad (7.14)$$

The difference in the energies can be explained by the different nuclear charge. As the energy of the electrons in the electric potential of the nucleus roughly scales with  $Z^2$ , the lower energy of the metastable state in Re ( $Z = 75$ ) is explained by the additional proton in Os ( $Z = 76$ ).

### 7.5.2 Comparison with theory

Theoretical predictions of transition energies in HCIs with multiple vacancies in semi-filled shells have to consider not only electronic correlations but also strong relativistic and sizeable QED contributions [Koz+18]. For a comparison of the experimental value, two different theory groups calculated the energy level independently using different approaches and codes.

The first theoretical description employs the multi-configuration Dirac-Fock method (MCDF, see e.g. [IPM89; Ind19]). The second calculation is done with Quanty, a many-body script language (QUANTY, [Hav16]). This program is based on the theory of core-level spectroscopy, which was developed in the field of condensed matter physics. These two results for the energy of the metastable state in  $^{187}\text{Re}^{29+}$  are:

$$\begin{aligned} \Delta E_{\text{QUANTY}} &= 203.95(0.35) \text{ eV} & [\text{BH19}] \\ \Delta E_{\text{MCDF}} &= 202.1(2.7) \text{ eV} & [\text{Ind19}] \quad . \end{aligned} \quad (7.15)$$

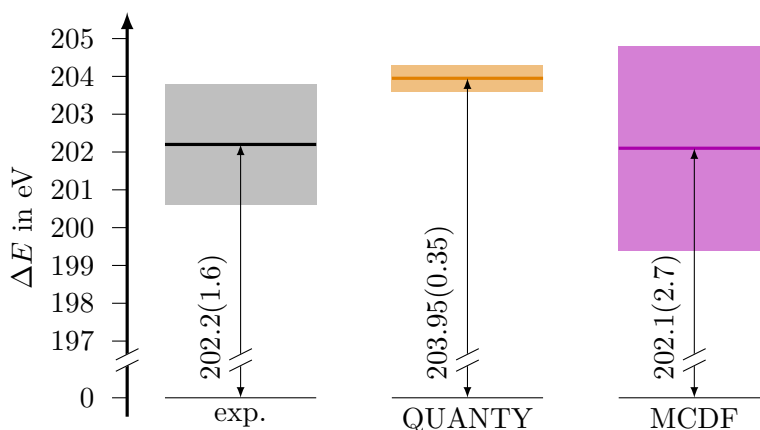


**Figure 7.6:** Comparison of the experimental result to the values obtained by theory for the metastable state in  $^{187}\text{Re}^{29+}$ . The theoretical values are from QUANTY (orange) [BH19] and MCDF calculations (magenta) [Ind19]. All values are in agreement.

A comparison between both calculations and the experimental result is given in Fig. 7.6. All values are in agreement with the experimental value. This identifies the higher mass as an excited state and demonstrates the applicability of PENTATRAP to detect electronic metastable states.

A preliminary calculation of the metastable state in  $^{187}\text{Os}^{30+}$  resulted in  $E_{\text{QUANTY}}^{\text{Os}} = 207.11$  eV [BH19]. Again, this is in agreement with the experimental value,  $\Delta E^{\text{Os}} = 207(3)$  eV.

The (preliminary) theoretical lifetime of the excited state in  $^{187}\text{Re}^{29+}$  is  $\sim 200$  d [Ind19]. No decay of the metastable state in the traps was determined, which would be indicated by a change in the ratio from  $R \approx 1 + 10^{-9}$  to  $R = 1$ . The longest-lived ion in a metastable state was measured for 4 cycles and thereby in the trap for  $\sim 48$  h. This corresponds to an upper limit of the linewidth of  $6 \cdot 10^{-6}$  Hz, which is challenging to characterize with narrow-linewidth spectroscopy lasers [Koz+18]. The measurements presented here are the first direct determination of such metastable states in a HCI. Penning-trap mass spectrometry can, therefore, be used to identify possible clock transitions in highly charged ions with a wavelength  $\lambda < 300$  nm in the future (for details see Chapter 8).



# 8

---

## Summary and Outlook

---

The high-precision Penning-trap mass spectrometer PENTATRAP is now fully functional and commissioned. In the course of this thesis, contributions were made to the redesign of the cryogenic insert as described in [Ris18], to a new detection system, and to an EBIT for the production of highly charged Ho ions. Furthermore, some of the first high-precision measurements including measurements on highly charged Xe and Re ions were performed. The discussed measurements in this thesis illustrate the versatile applications of PENTATRAP:

**Xe masses:** The mass differences of certain Xe isotopes were among the previously most precise known in the mid-heavy regime [Wan+17; HRM13]. The first mass difference measurements with PENTATRAP were, therefore, performed with five stable Xe ions between  $^{126}\text{Xe}^{17+}$  and  $^{134}\text{Xe}^{17+}$ . The results obtained with PENTATRAP agree within  $1\sigma$  with the AME2017. Furthermore, the uncertainty of the mass differences of all measured Xe isotopes could be improved by at least a factor of 4, with the least known mass difference of  $^{126}\text{Xe}$  to  $^{128}\text{Xe}$  even by a factor of 1700.

**Binding energy in Xe ions:** As a second measurement the binding energy of the  $37^{\text{th}}$  electron in  $^{132}\text{Xe}$  was determined by measuring the mass difference of  $^{132}\text{Xe}^{17+}$  and

$^{132}\text{Xe}^{18+}$ . The result of PENTATRAP is in good agreement with theory values:

$$\begin{aligned}\Delta E_{\text{Theo1}}^{\text{prelim.}} &= 432.9 \text{ eV} && [\text{Ind19}] \\ \Delta E_{\text{Theo2}} &= 435.1(3) \text{ eV} && [\text{Har19}] \\ \Delta E_{\text{PENTATRAP}} &= 432.4(1.3)_{\text{stat}}(3.4)_{\text{sys}} \text{ eV} \quad ,\end{aligned}$$

where the uncertainty of the first value is still under investigation, but is currently expected to be about 3 eV [Ind19]. While QED corrections do not play an important role at this low charge state, this proof-of-principle measurement paves the way to perform stringent tests of QED in even higher charged ions in the future.

**Metastable states in Re:** Measurements including  $^{187}\text{Re}^{29+}$  ions were started to determine the  $Q$ -value of the  $\beta$ -decay of Re to Os, see next item. As thereby two different values of the mass difference were determined, separate measurements using only  $^{187}\text{Re}^{29+}$  revealed two ratios, either  $R = 1$  or  $R_{\text{final}}^{\text{Re}} = 1 + 1.1608(92) \cdot 10^{-9}$ . This was attributed to a metastable state in  $^{187}\text{Re}^{29+}$  and allowed the first direct identification of a long-lived electronic state in HCIs by measuring mass differences. A detection of another metastable state in  $^{187}\text{Os}^{30+}$ , which features the same electronic configuration, confirms the measurement.

The energy of the excited state agrees well within its uncertainty to theory calculations:

$$\begin{aligned}\Delta E_{\text{QUANTITY}} &= 203.95(0.35) \text{ eV} && [\text{BH19}] \\ \Delta E_{\text{MCDF}} &= 202.1(2.7) \text{ eV} && [\text{Ind19}] \\ \Delta E_{\text{PENTATRAP}} &= 202.2(1.6) \text{ eV} \quad .\end{aligned}$$

The performed measurements of the metastable states in Re and Os expand the future application of Penning-trap mass spectrometry (PTMS) to also include the determination of electronic excited states and their lifetime.

**$\beta$ -decay in Re:** The measurements of the  $Q$ -value of the  $\beta$ -decay in Re were only briefly mentioned in this thesis as they were paused in favour of continuing the investigations of the metastable state in highly charged Re. Due to this metastable state, two free-space cyclotron frequency ratios of  $^{187}\text{Re}^{29+}$  and  $^{187}\text{Os}^{29+}$  were measured:

$$\begin{aligned}R_{\beta,1} &= 1 + 1.3886(15) \cdot 10^{-8} \\ R_{\beta,2} &= 1 + 1.5024(12) \cdot 10^{-8} \quad ,\end{aligned}$$

where the larger uncertainty of both results comes from a smaller number of measurements compared to the metastable state measurements. For the determination of the  $Q$ -value,

$$Q = m(^{187}\text{Re}^{29+}) (R_{\beta} - 1) + \Delta E_B \quad , \quad (8.1)$$

the binding energy difference  $\Delta E_B$  of the 29 missing electrons in Re and Os needs to be calculated. This calculation is still ongoing and especially its uncertainty is

---

not yet quantified. Assuming the smaller ratio  $R_{\beta,1}$  to correspond to Re in the ground state and with a first preliminary value of  $\Delta E_B = 59.2$  eV [BH19], the  $Q$ -value is determined to:

$$Q_1^{\text{prelim.}} = 2477.4(2.9)_{\text{exp}} \text{ eV} \quad (8.2)$$

with the theoretical uncertainty missing. This  $Q$ -value agrees with the value obtained by PTMS with SHIPTRAP ( $Q = 2490(30)(15)$  eV), but only within  $3\sigma$  with cryogenic microcalorimeters ( $Q = 2466.7(1.6)$  eV) [Nes+14]. At PENTATRAN, further measurements are planned to improve the statistical uncertainty of the  $Q$ -value obtained with PTMS.

The systematic uncertainty of the latter two measurements is vastly reduced as all settings in the measurements are identical. Any other measurement, where the charge-to-mass ratio of the two ions is different by at least  $1 e/u$ , the higher-order magnetic field terms and the image charge effect are limiting the systematic uncertainty.

The higher-order magnetic field terms, especially a spatial gradient  $B_1$ , affect the eigenfrequencies of the ions as different trapping potentials lead to a different position in the trap. These can be overcome in the future using a resonator with a tunable resonance frequency by attaching a high- $Q$  capacitance, as explained in [Wei19].

The second limiting systematic effect is the image charge effect. This can be determined to the required precision by simulations of the Penning traps at PENTATRAN [Sch+19a]. As this shift scales with the mass difference of the ions involved, it is drastically reduced by performing measurements of e.g. the binding energy or the excitation energies of metastable electronic states.

Future improvements of the cryogenic setup include a new trap tower and a cryogenic valve. As explained in Sec. 4.2, the holder structure of the current trap tower is at ground potential. While it is possible to load ions into the traps, the efficiency might be improved when removing this potential barrier. Therefore, a new trap tower is currently set up, which also features more split electrodes to be more flexible when applying  $rf$ -signals to the ion in the trap.

The lifetime of the ions in the trap is currently limited by charge exchange with residual gas atoms. Including a cryogenic valve between the trap and beamline vacuum as described in [Ris18], will allow closing the trap vacuum during the measurements and opening it to the beamline vacuum when new ions need to be loaded. Hereby, an improvement in the vacuum is expected and, thus, also in the storage time of the ions in the traps.

Before implementing these improvements to the experimental setup and also with the limitation of the above mentioned systematic shifts, several measurement ideas can be accomplished by using two ions with nearly identical charge-to-mass ratio:

**$Q$ -value determinations:** In addition to the ongoing investigations of the  $\beta$ -decay in Re also measurements of the  $Q$ -value of the electron capture process in Ho are planned. As the sample size is only on the order of  $10^{14}$  atoms, a new EBIT was set up to efficiently produce ions from such small samples. With the connection

of this EBIT to the PENTATRAP beamline, one of the next planned measurements is the mass difference of Ho and Dy. To that end, preliminary studies of the efficient production of ions have been performed with the HC-EBIT in the context of this thesis. Depending on the chosen charge state, also metastable states will be produced for one or both ions. Theoretical calculations are currently performed [Kön19] to find an optimal charge state, where either no metastable states or only those with a short lifetime are produced. Such calculations would benefit from more experimental data of transitions in HCIs.

**Electronic transitions in ions:** PTMS can be used to identify a vast majority of excited, long-lived states. The applicability is hereby limited by the energy of the excited state, its lifetime and production rate:

**1. Energy:** Assuming the cyclotron frequency ratio of two ions in the trap can be measured with a relative uncertainty of  $5 \cdot 10^{-12}$ , provided enough statistics is collected, the uncertainty of the energy difference is given by  $\delta(\Delta E) = m \cdot 5 \cdot 10^{-12}$  eV. In units of  $\text{eV}/c^2$ , the masses  $m$  of the atoms used in future measurements at PENTATRAP range from  $35 \text{ GeV}/c^2$  ( $^{35}\text{Cl}$ ) to  $235 \text{ GeV}/c^2$  ( $^{235}\text{U}$ ), corresponding to an absolute precision of any energy difference of 0.2 eV to 1.1 eV, respectively. In order to identify the excited state, the transition energy should be at least a factor of 3 larger than the absolute precision.

**2. Lifetime:** The prerequisite for the measurement of any such an excited state is a lifetime comparable to the preparation time of the ions and the run time of the first few pnp-cycles. As the preparation of three ions takes a couple of hours, a lifetime larger than 7 – 10 h would ensure that a decay back to the electronic ground state happens, in most cases, only after the start of the measurement and before the ions are lost due to charge exchange with background gas.

**3. Production rate:** Any measurement with PENTATRAP needs to run for  $\sim 5$  h before a state identification is possible. If the production rate of any excited state is only a few percents, the  $\approx 90$  h measurement time needed to determine the mass ratio to such a high precision as in the case of Re would be accompanied by measurements resulting in unity for  $> 900$  h. Including the ion preparation time and ion losses due to recombination in the traps, such a measurement would take months. Therefore, the production rate needs to be at least about 20% in order to feature reasonable measurement times.

**Nuclear transitions:** The application of PTMS to detect excited states does not distinguish nuclear from electronic excited states. Thus, also nuclear transitions can be identified provided the three requirements mentioned above are fulfilled. The most prominent candidate, the isomeric state in  $^{229}\text{Th}$ , features an excitation energy of 8.28(17) eV [Sei+19]. The mass of  $^{229}\text{Th}$  would lead to an absolute uncertainty of any transition to be determined with PENTATRAP of 1.0 eV, assuming again a relative uncertainty of the frequency ratio of  $5 \cdot 10^{-12}$ . Thereby, the detection of the isomeric state would have been possible to a relative uncertainty of

---

$\approx 12\%$ . On the other hand, the production rate of the isomeric state of only 2% [Wen+16] drastically limits the applicability of PENTATRAP in this case.

**Decay of metastable states:** Another possibility to compare experiment to theory is not just the determination of the energy of a metastable state but also to measure its lifetime. If the lifetime is on the order of 5 – 10 h, it could be estimated by repeated measurements. In such a measurement also the case where all three ions are in the metastable state contributes to the overall statistics. On the other hand, even a rough estimation of the excited state lifetime requires many repeated measurements to collect enough data points. Hereby, a production rate of  $> 50\%$  of the metastable state would be beneficial.

**Test of energy-mass equivalence principle:** The possibility to determine the energy of a very long-lived excited state by determining the mass difference opens up the possibility to also test  $E = mc^2$  in the binding energy of electrons. Similar to the experiments explained in [Rai+05] and Sec. 1.1.1, a comparison of the obtained mass difference of ions in two electronic states to a measurement of the transition energy with XUV lasers [Cin+12] could be performed.

The unique possibility to identify nuclear or electronic excited states with Penning-trap mass spectrometry can lead to contributions with PENTATRAP to a variety of physical cases, ranging from the identification of possible clock transitions for frequency standards or physics beyond the Standard Model of particle physics to providing data for atomic structure calculations. Additionally, the planned  $Q$ -value determination of the electron capture process in Ho will help to improve the upper limit of the electron neutrino mass in the future [Gas+17].



---

## Publications by Rima Schüssler

---

1. **R. X. Schüssler**, M. Door, A. Rischka, H. Bekker, J. R. Crespo López-Urrutia, P. Filianin, S. Eliseev, Y. N. Novikov, S. Sturm, S. Ulmer, and K. Blaum, "Recent Developments at the High-Precision Mass Spectrometer PENTATRAP", *Proceedings of the 12th International Conference on Low Energy Antiproton Physics (LEAP2016)* (2016)

**Note:** cited as [Sch+16].

2. **R. X. Schüssler**, H. Bekker, M. Braß, H. Cakir, J.R. Crespo López-Urrutia, M. Door, P. Filianin, P. Indelicato, Z. Harman, M. Haverkort, W. Huang, C. H. Keitel, C. M. König, K. Kromer, Yu. N. Novikov, A. Rischka, Ch. Schweiger, S. Sturm, S. Ulmer, S. Eliseev and K. Blaum, "Discovery of metastable electronic states by Penning-trap mass spectrometry", *To be published* (2019)

**Note:** Results of [Chapter 7](#)

Further publications:

3. Ch. Schweiger et al., "Production of highly charged ions of rare species by in-trap laser-induced desorption inside an electron beam ion trap", *submitted to Review of Scientific Instruments* (2019)

**Note:** cited as [Sch+19b]

4. A. Rischka et al., "Mass-difference measurements on heavy nuclides with an  $eV/c^2$  accuracy with PENTATRAP", *To be published* (2019)

**Note:** cited as [Ris+19], includes results of [Chapter 6](#)

5. P. Micke et al., "The Heidelberg compact electron beam ion traps", *Review of Scientific Instruments* **89** (2018) 063109

**Note:** cited as [Mic+18]

6. Ch. Böhm et al., "An ultra-stable voltage source for precision Penning-trap experiments", *Nuclear Instruments and Methods in Physics Research Section A* **828** (2016) 125

**Note:** cited as [Böh+16]

7. S. Eliseev et al. "Direct Measurement of the Mass Difference of  $^{163}\text{Ho}$  and  $^{163}\text{Dy}$  Solves the  $Q$ -Value Puzzle for the Neutrino Mass Determination", *Physical Review Letters* **115**, (2015) 062501

**Note:** cited as [Eli+15]

Publications within the ECHo collaboration:

8. L. Gastaldo et al. "The electron capture in  $^{163}\text{Ho}$  experiment – ECHo", *The European Physical Journal Special Topics* **226** (2017) 1623

**Note:** cited as [Gas+17]

9. C. Hassel et al., "Recent Results for the ECHo Experiment", *Journal of Low Temperature Physics* **3-4** (2016) 910

---

## Bibliography

---

- [And62] P. W. Anderson. “Theory of Flux Creep in Hard Superconductors”. *Physical Review Letters* **9** (1962), 309 (cited on page 19).
- [Ara+19] I. Arapoglou et al. “ $g$  Factor of Boronlike Argon  $^{40}\text{Ar}^{13+}$ ”. *Physical Review Letters* **122** (2019), 253001 (cited on page 3).
- [Arn+03] C. Arnaboldi et al. “Bolometric Bounds on the Antineutrino Mass”. *Physical Review Letters* **91** (2003), 161802 (cited on page 5).
- [Ast22] F. W. Aston. “The Atoms of Matter; their Size, Number, and Construction”. *Nature* **110** (1922), 702 (cited on page 1).
- [BDF10] J. C. Berengut, V. A. Dzuba, and V. V. Flambaum. “Enhanced Laboratory Sensitivity to Variation of the Fine-Structure Constant using Highly Charged Ions”. *Physical Review Letters* **105** (2010), 120801 (cited on pages 7, 8).
- [BDF11] J. C. Berengut, V. A. Dzuba, and V. V. Flambaum. “Transitions in Zr, Hf, Ta, W, Re, Hg, Ac, and U ions with high sensitivity to variation of the fine-structure constant”. *Physical Review A* **84** (2011), 054501 (cited on page 8).
- [Bek19] H. Bekker. *Private Communication*. 2019 (cited on pages 113, 115).
- [Ber+02] I. Bergström et al. “SMILETRAP—A Penning trap facility for precision mass measurements using highly charged ions”. *Nuclear Instruments and Methods in Physics Research Section A: Accelerators, Spectrometers, Detectors and Associated Equipment* **487** (2002), 618 (cited on page 2).
- [Ber+12] J. C. Berengut, V. A. Dzuba, V. V. Flambaum, and A. Ong. “Highly charged ions with  $E1$ ,  $M1$ , and  $E2$  transitions within laser range”. *Physical Review A* **86** (2012), 022517 (cited on pages 114, 115).
- [BG82] L. S. Brown and G. Gabrielse. “Precision spectroscopy of a charged particle in an imperfect Penning trap”. *Physical Review A* **25** (1982), 2423 (cited on page 19).
- [BG86] L. S. Brown and G. Gabrielse. “Geonium theory: Physics of a single electron or ion in a Penning trap”. *Review of Modern Physics* **58** (1986), 233 (cited on pages 13, 15, 16, 18, 31).

- [BH19] M. Braß and M. Haverkort. *Private Communication*. 2019 (cited on pages 124, 125, 128, 129).
- [Bla06] K. Blaum. “High-accuracy mass spectrometry with stored ions”. *Physics Reports* **425** (2006), 1 (cited on pages 1, 2, 13).
- [Böh+16] Ch. Böhm et al. “An ultra-stable voltage source for precision Penning-trap experiments”. *Nuclear Instruments and Methods in Physics Research A* **828** (2016), 125 (cited on pages 55, 133).
- [Bre+19] S. M. Brewer et al. “An  $^{27}\text{A}^+$  quantum-logic clock with systematic uncertainty below  $10^{-18}$ ”. *Physical Review Letters* **123** (2019), 033201 (cited on page 7).
- [Bri45] L. Brillouin. “A Theorem of Larmor and Its Importance for Electrons in Magnetic Fields”. *Physical Review* **67** (1945), 260 (cited on page 42).
- [BSO03] P. Beiersdorfer, J. H. Scofield, and A. L. Osterheld. “X-Ray-Line Diagnostic of Magnetic Field Strength for High-Temperature Plasmas”. *Physical Review Letters* **90** (2003), 235003 (cited on page 116).
- [CCS51] E. U. Condon, E. Condon, and G. H. Shortley. *The theory of atomic spectra*. Cambridge University Press, 1951 (cited on page 116).
- [CD18] The NIST Reference on Constants, Units, and Uncertainty. *2018 CODATA Value: Atomic mass unit*. visited 2019-08-20. URL: <https://physics.nist.gov/cgi-bin/cuu/Value?ukg> (cited on page 93).
- [Cin+12] A. Cingöz et al. “Direct frequency comb spectroscopy in the extreme ultraviolet”. *Nature* **482** (2012), 68 (cited on page 131).
- [Cor+89] E. A. Cornell et al. “Single-ion cyclotron resonance measurement of  $M(\text{CO}^+) / M(\text{N}_2^+)$ ”. *Physical Review Letters* **63** (1989), 1674 (cited on pages 33, 57).
- [Cow+56] C. L. Cowan Jr. et al. “Detection of the Free Neutrino: a Confirmation”. *Science* **124** (1956), 103 (cited on page 4).
- [Cre+04] J. R. Crespo López-Urrutia et al. “Progress at the Heidelberg EBIT”. *Journal of Physics: Conference Series* **2** (2004), 42 (cited on page 50).
- [DDF12a] A. Derevianko, V. A. Dzuba, and V. V. Flambaum. “Highly Charged Ions as a Basis of Optical Atomic Clockwork of Exceptional Accuracy”. *Physical Review Letters* **109** (2012), 180801 (cited on page 7).
- [DDF12b] V. A. Dzuba, A. Derevianko, and V. V. Flambaum. “High-precision atomic clocks with highly charged ions: Nuclear-spin-zero  $f^{12}$ -shell ions”. *Physical Review A* **86** (2012), 054501 (cited on page 7).
- [Deh90] H. Dehmelt. “Experiments with an isolated subatomic particle at rest”. *Reviews of Modern Physics* **62** (1990), 525 (cited on page 2).
- [Dil+06] J. Dilling et al. “Mass measurements on highly charged radioactive ions, a new approach to high precision with TITAN”. *International Journal of Mass Spectrometry* **251** (2006), 198 (cited on page 2).

- [DMO71] J. P. Desclaux, D. F. Mayers, and F. O'Brien. "Relativistic atomic wave functions". *Journal of Physics B* **4** (1971), 631 (cited on page 111).
- [Doo15] M. Door. "Erzeugung hochgeladener Chlor- und Siliziumionen für das Pentatrap-Experiment in einer Elektronenstrahlionenquelle unter Anwendung der MIVOC-Methode". Bachelor's thesis. Ruprecht-Karls-Universität Heidelberg, 2015 (cited on page 46).
- [Doo18] M. Door. "New control system and first trap characterization measurements at the high-precision Penning-trap mass spectrometer Pentatrap". Master's thesis. Ruprecht-Karls-Universität Heidelberg, 2018 (cited on pages 56, 58, 68, 107, 110).
- [Dör15] A. Dörr. "PENTATRAP: A novel Penning-trap system for high-precision mass measurements". PhD thesis. Ruprecht-Karls-Universität Heidelberg, 2015 (cited on pages 16, 46, 52).
- [DP14] A. Derevianko and M. Pospelov. "Hunting for topological dark matter with atomic clocks". *Nature Physics* **10** (2014), 933 (cited on page 7).
- [DRE10] DREEBIT GmbH, Dresden. *Instruction manual - Dresden EBIT with Wien Filter*. 2010 (cited on page 39).
- [Ear42] S. Earnshaw. "On the Nature of the Molecular Forces which Regulate the Constitution of the Luminiferous Ether". *Transactions of the Cambridge Philosophical Society* **7** (1842), 97 (cited on page 11).
- [EEN13] S. Eliseev, T. Eronen, and Y. N. Novikov. "Penning-trap mass spectrometry for neutrino physics". *International Journal of Mass Spectrometry* **349-350** (2013), 102 (cited on page 5).
- [Eid+04] S. Eidelman et al. "Review of Particle Physics". *Physics Letters B* **592** (2004), 1 (cited on page 4).
- [Eli+11] S. Eliseev et al. "Octupolar-Excitation Penning-Trap Mass Spectrometry for  $Q$ -Value Measurement of Double-Electron Capture in  $^{164}\text{Er}$ ". *Physical Review Letters* **107** (2011), 152501 (cited on page 2).
- [Eli+13] S. Eliseev et al. "Phase-Imaging Ion-Cyclotron-Resonance Measurements for Short-Lived Nuclides". *Physical Review Letters* **110** (2013), 082501 (cited on page 2).
- [Eli+15] S. Eliseev et al. "Direct Measurement of the Mass Difference of  $^{163}\text{Ho}$  and  $^{163}\text{Dy}$  Solves the  $Q$ -Value Puzzle for the Neutrino Mass Determination". *Physical Review Letters* **115** (2015), 062501 (cited on pages 7, 134).
- [EM95] S. R. Elliott and R. E. Marrs. "A wire probe as an ion source for an electron beam ion trap". *Nuclear Instruments and Methods in Physics Research B* **100** (1995), 529 (cited on page 40).
- [Epp07] S. W. Epp. "Röntgen-Laserspektroskopie hochgeladener Ionen in einer EBIT am Freie-Elektronen-Laser FLASH". PhD thesis. Ruprecht-Karls-Universität Heidelberg, 2007 (cited on page 50).

- [FGV18] V. V. Flambaum, A. J. Geddes, and A. V. Viatkina. “Isotope shift, nonlinearity of King plots, and the search for new particles”. *Physical Review A* **97** (2018), 032510 (cited on page 95).
- [Gab09] G. Gabrielse. “Why Is Sideband Mass Spectrometry Possible with Ions in a Penning Trap?” *Physical Review Letters* **102** (2009), 172501 (cited on pages 13, 20).
- [Gas+17] L. Gastaldo et al. “The electron capture in  $^{163}\text{Ho}$  experiment – ECHo”. *European Physical Journal Special Topics* **226** (2017), 1623 (cited on pages 6, 131, 134).
- [Geo+07] S. George et al. “The Ramsey method in high-precision mass spectrometry with Penning traps: Experimental results”. *International Journal of Mass Spectrometry* **264** (2007), 110 (cited on page 2).
- [GHR89] G. Gabrielse, L. Haarsma, and S. Rolston. “Open-endcap Penning traps for high precision experiments”. *International Journal of Mass Spectrometry and Ion Processes* **88** (1989), 319 (cited on page 16).
- [GKT80] G. Gräff, H. Kalinowsky, and J. Traut. “A direct determination of the proton electron mass ratio”. *Zeitschrift für Physik A* **297** (1980), 35 (cited on page 2).
- [Gon+07] A. J. González Martínez et al. “The Heidelberg EBIT: Present Results and Future Perspectives”. *Journal of Physics: Conference Series* **72** (2007), 012001 (cited on page 50).
- [Gra79] I. P. Grant. “Relativistic atomic structure calculations”. *Computer Physics Communications* **17** (1979), 149 (cited on page 111).
- [Gu08] M. F. Gu. “The flexible atomic code”. *Canadian Journal of Physics* **86** (2008), 675 (cited on page 113).
- [Häf+00] H. Häffner et al. “Testing atomic structure theories with high accuracy mass measurements on highly charged ions”. *Hyperfine Interactions* **127** (2000), 271 (cited on page 112).
- [Häf00] H. Häffner. “Präzisionsmessung des magnetischen Moments des Elektrons in wasserstoffähnlichem Kohlenstoff”. PhD thesis. Johannes Gutenberg-Universität Mainz, 2000 (cited on page 20).
- [Har19] Z. Harman. *Private Communication*. 2019 (cited on pages 111, 128).
- [Hav16] M. W. Haverkort. “Quanta for core level spectroscopy - excitons, resonances and band excitations in time and frequency domain”. *Journal of Physics: Conference Series* **712** (2016), 012001 (cited on page 124).
- [Hei+17] F. Heiße et al. “High-Precision Measurement of the Proton’s Atomic Mass”. *Physical Review Letters* **119** (2017), 033001 (cited on page 2).
- [Hel75] F. R. Helmert. “Über die Berechnung des wahrscheinlichen Fehlers aus einer endlichen Anzahl wahrer Beobachtungsfehler”. *Zeitschrift für Mathematik und Physik* **20** (1875), 300 (cited on page 84).

- [Her58] G. Herrmann. “Optical Theory of Thermal Velocity Effects in Cylindrical Electron Beams”. *Journal of Applied Physics* **29** (1958), 127 (cited on page 42).
- [HJS49] O. Haxel, J. H. D. Jensen, and H. E. Suess. “On the ”Magic Numbers” in Nuclear Structure”. *Physical Review* **75** (1949), 1766 (cited on page 1).
- [Höc16] M. Höcker. “Precision Mass Measurements at THE-Trap and the FSU trap”. PhD thesis. Ruprecht-Karls-Universität Heidelberg, 2016 (cited on page 25).
- [HRM13] M. Höcker, R. Rana, and E. G. Myers. “Atomic masses of  $^{82,83}\text{Kr}$  and  $^{131,134}\text{Xe}$ ”. *Physical Review A* **88** (2013), 052502 (cited on pages 95, 96, 127).
- [Ind19] P. Indelicato. *Private Communication*. 2019 (cited on pages 9, 111, 113, 116, 124, 125, 128).
- [IPM89] P. Indelicato, F. Parente, and R. Marrus. “Effect of hyperfine structure on the  $2\ ^3P_1$  and the  $2\ ^3P_0$  lifetime in heliumlike ions”. *Physical Review A* **40** (1989), 3505 (cited on pages 116, 124).
- [Jen+08] M. Jentschel et al. “Measurement of neutron binding energy of  $^{36}\text{Cl}$  for a determination of  $N_A h$ ”. *2008 Conference on Precision Electromagnetic Measurements Digest*. IEEE. 2008, 632 (cited on page 3).
- [Joh28] J. B. Johnson. “Thermal Agitation of Electricity in Conductors”. *Physical Review* **32** (1928), 97 (cited on page 27).
- [JRR] H. Janka, G. Raffelt, and L. Rudolf. *Brief an die Gruppe der Radioaktiven*. Proc. NEUTRINO ASTROPHYSICS, Ringberg Castle, Tegernsee, 20-24 Oct. 1997, ed. by M. Altmann, W. Hillebrandt, visited 2019-09-30. URL: <https://www.zeuthen.desy.de/~riemanns/UniPVorl/Vorlesungsmaterial/Pauli.pdf> (cited on page 4).
- [Kat11] H. Katori. “Optical lattice clocks and quantum metrology”. *Nature Photonics* **5** (2011), 203 (cited on page 7).
- [Kes+01] E. G. Kessler Jr et al. “The GAMS4 flat crystal facility”. *Nuclear Instruments and Methods in Physics Research A* **457** (2001), 187 (cited on page 3).
- [Ket+14] J. Ketter et al. “First-order perturbative calculation of the frequency-shifts caused by static cylindrically-symmetric electric and magnetic imperfections of a Penning trap”. *International Journal of Mass Spectrometry* **358** (2014), 1 (cited on page 105).
- [Köh15] F. Köhler. “Bound-electron g-factor measurements for the determination of the electron mass and isotope shifts in highly charged ions”. PhD thesis. Ruprecht-Karls-Universität Heidelberg, 2015 (cited on pages 29, 73).
- [Kön19] C. M. König. “To be published”. Master’s thesis. Ruprecht-Karls-Universität Heidelberg, 2019 (cited on page 130).

- [Koz+18] M. G. Kozlov, M. S. Safronova, J. R. Crespo López-Urrutia, and P. O. Schmidt. “Highly charged ions: Optical clocks and applications in fundamental physics”. *Reviews of Modern Physics* **90** (2018), 045005 (cited on pages 124, 125).
- [Kra+] A. Kramida, Y. Ralchenko, J. Reader, and N. team. NIST Atomic Spectra Database (ver. 5.6.1). visited 23.09.2019. URL: <https://physics.nist.gov/cgi-bin/ASD/ie.pl> (cited on pages 111, 114, 115).
- [Kre+08] J. Krempel et al. “Progress on the GAMS-6 double crystal  $\gamma$ -spectrometer”. *2008 Conference on Precision Electromagnetic Measurements Digest*. IEEE, 2008, 634 (cited on page 3).
- [Kre92] M. Kretzschmar. “Single particle motion in a Penning trap: description in the classical canonical formalism”. *Physica Scripta* **46** (1992), 544 (cited on page 16).
- [Kro19] K. Kromer. “Environmentally-induced systematic effects at the high-precision mass spectrometer PENTATRAP”. Master’s thesis. Ruprecht-Karls-Universität Heidelberg, 2019 (cited on pages 49, 100, 120).
- [Lae+03] J. R. de Laeter et al. “Atomic weights of the elements. Review 2000 (IUPAC Technical Report)”. *Pure and Applied chemistry* **75** (2003), 683 (cited on page 97).
- [Lan19] D. Lange. “Untersuchung des Dip-Fit-Algorithmus zur Bestimmung der Axialfrequenz beim Hochpräzisions-Massenspektrometer PENTATRAP”. Bachelor’s thesis. Ruprecht-Karls-Universität Heidelberg, 2019 (cited on pages 76, 88).
- [Lot67] W. Lotz. “An empirical formula for the electron-impact ionization cross-section”. *Zeitschrift für Physik* **206** (1967), 205 (cited on page 42).
- [May48] M. G. Mayer. “On Closed Shells in Nuclei”. *Physical Review* **74** (1948), 235 (cited on page 1).
- [Meh+18] T. E. Mehlstäubler et al. “Atomic clocks for geodesy”. *Reports on Progress in Physics* **81** (2018), 064401 (cited on page 7).
- [Mic+18] P. Micke et al. “The Heidelberg compact electron beam ion traps”. *Review of Scientific Instruments* **89** (2018), 063109 (cited on pages 39, 42, 133).
- [Mil20] J. M. Miller. *Dependence of the input impedance of a three-electrode vacuum tube upon the load in the plate circuit*. Vol. 15. Scientific Papers of the Bureau of Standards, 1920, 351 (cited on page 51).
- [Moo13] A. Mooser. “Der g-Faktor des Protons”. PhD thesis. Johannes Gutenberg-Universität Mainz, 2013 (cited on pages 18, 51).
- [MPG10] J. Magill, G. Pfennig, and J. Galy. *Karlsruher Nuklidkarte/Chart of the Nuclides*. 2010 (cited on page 97).

- 
- [MPS98] P. J. Mohr, G. Plunien, and G. Soff. “QED corrections in heavy atoms”. *Physics Reports* **293** (1998), 227 (cited on page 3).
- [Mye+15] E. G. Myers, A. Wagner, H. Kracke, and B. A. Wesson. “Atomic Masses of Tritium and Helium-3”. *Physical Review Letters* **114** (2015), 013003 (cited on page 2).
- [Nat93] V. Natarajan. “Penning Trap Mass Spectroscopy at 0.1 Ppb”. PhD thesis. Massachusetts Institute of Technology, 1993 (cited on page 28).
- [Nes+14] D. A. Nesterenko et al. “Direct determination of the atomic mass difference of  $^{187}\text{Re}$  and  $^{187}\text{Os}$  for neutrino physics and cosmochronology”. *Physical Review C* **90** (2014), 042501 (cited on pages 5, 129).
- [Nyq28] H. Nyquist. “Thermal Agitation of Electric Charge in Conductors”. *Physical Review* **32** (1928), 110 (cited on page 27).
- [Oli+14] K. A. Olive et al. “Review of particle physics”. *Chinese Physics C* **38** (2014), 090001 (cited on page 4).
- [Pen36] F. M. Penning. “Die Glimmentladung bei niedrigem Druck zwischen koaxialen Zylindern in einem axialen Magnetfeld”. *Physica* **3** (1936), 873 (cited on page 11).
- [PS53] W. Paul and H. Steinwedel. “Notizen: Ein neues Massenspektrometer ohne Magnetfeld”. *Zeitschrift Naturforschung Teil A* **8** (1953), 448 (cited on page 11).
- [QV14] W. Quint and M. Vogel. *Fundamental Physics in Particle Traps*. Springer, 2014 (cited on pages 114, 116).
- [Rai+05] S. Rainville et al. “A direct test of  $E = mc^2$ ”. *Nature* **438** (2005), 1096 (cited on pages 3, 131).
- [Ram39] S. Ramo. “Currents Induced by Electron Motion”. *Proceedings of the IRE* **27** (1939), 584 (cited on page 26).
- [Rep+12] J. Repp et al. “PENTATRAP: a novel cryogenic multi-Penning-trap experiment for high-precision mass measurements on highly charged ions”. *Applied Physics B* **107** (2012), 983 (cited on page 17).
- [Rep12] J. Repp. “The setup of the high-precision Penning trap mass spectrometer PENTATRAP and first production studies of highly charged ions”. PhD thesis. Ruprecht-Karls-Universität Heidelberg, 2012 (cited on pages 46, 54).
- [Ris+19] A. Rischka et al. “Mass-difference measurements on heavy nuclides with an  $\text{eV}/c^2$  accuracy with PENTATRAP”. *To be published* (2019) (cited on pages 96, 133).
- [Ris18] A. Rischka. “The First Direct  $Q_{EC}$  Measurement in  $^{163}\text{Ho}$  and the Development of the High-Precision Mass Spectrometer PENTATRAP for Neutrino Physics”. PhD thesis. Ruprecht-Karls-Universität Heidelberg, 2018 (cited on pages 49, 55, 58, 127, 129).

- [Ros+15] M. Rosenbusch et al. “Probing the  $N = 32$  Shell Closure below the Magic Proton Number  $Z = 20$ : Mass Measurements of the Exotic Isotopes  $^{52,53}\text{K}$ ”. *Physical Review Letters* **114** (2015), 202501 (cited on page 2).
- [Rou+12] C. Roux et al. “The trap design of PENTATRAP”. *Applied Physics B* **107** (2012), 997 (cited on pages 17, 55).
- [Rou12] C. Roux. “High-resolution mass spectrometry: The trap design and detection system of Pentatrap and new  $Q$ -values for neutrino studies”. PhD thesis. Ruprecht-Karls-Universität Heidelberg, 2012 (cited on pages 21, 51, 53, 105).
- [RTP04] S. Rainville, J. K. Thompson, and D. E. Pritchard. “An Ion Balance for Ultra-High-Precision Atomic Mass Measurements”. *Science* **303** (2004), 334 (cited on page 2).
- [San+19] C. Sanner et al. “Optical clock comparison for Lorentz symmetry testing”. *Nature* **567** (2019), 204 (cited on page 7).
- [Sch+16] R. X. Schüssler et al. “Recent Developments at the High-Precision Mass Spectrometer PENTATRAP”. *Proceedings of the 12th International Conference on Low Energy Antiproton Physics (LEAP2016)* (2016) (cited on pages 47, 133).
- [Sch+19a] M. Schuh et al. “Image charge shift in high-precision Penning traps”. *Physical Review A* **100** (2019), 023411 (cited on pages 20, 67, 129).
- [Sch+19b] C. Schweiger et al. “Production of highly charged ions of rare species by in-trap laser ablation in an electron beam ion trap”. *Submitted to Review of Scientific Instruments* (2019) (cited on pages 44, 46, 133).
- [Sch02] P. Schmüser. “Superconductivity in high energy particle accelerators”. *Progress in Particle and Nuclear Physics* **49** (2002), 155 (cited on page 50).
- [Sch15] R. X. Schüssler. “A new Detection System for the high-precision Penning-trap mass spectrometer PENTATRAP”. Master’s thesis. Ruprecht-Karls-Universität Heidelberg, 2015 (cited on page 50).
- [Sch17] C. Schweiger. “Construction and commissioning of a room-temperature electron beam ion trap and development of a wire probe injection system”. Master’s thesis. Ruprecht-Karls-Universität Heidelberg, 2017 (cited on pages 7, 38, 39, 44).
- [Sch19] M. Schuh. “Simulations of the image charge effect in high-precision Penning traps and the new IGISOL ion buncher”. PhD thesis. Ruprecht-Karls-Universität Heidelberg, 2019 (cited on page 105).
- [Sch20] C. Schweiger. “To be published”. PhD thesis. Ruprecht-Karls-Universität Heidelberg, 2020 (cited on pages 40, 45).
- [Sei+19] B. Seiferle et al. “Energy of the  $^{229}\text{Th}$  nuclear clock transition”. *Nature* **573** (2019), 243 (cited on page 130).

- [Sho38] W. Shockley. “Currents to Conductors Induced by a Moving Point Charge”. *Journal of Applied Physics* **9** (1938), 635 (cited on page 26).
- [SI19] Bureau International des Poids et Mesures. *The International System of Units (SI)*. visited 2019-07-31. 2019 (cited on page 21).
- [Str14] S. D. Streubel. “Kontrolle der Umwelteinflüsse auf THe-Trap am Beispiel der Bestimmung des Massenverhältnisses von Kohlenstoff-12 zu Sauerstoff-16”. PhD thesis. Ruprecht-Karls-Universität Heidelberg, 2014 (cited on page 89).
- [Stu+11] S. Sturm et al. “ $g$  Factor of Hydrogenlike  $^{28}\text{Si}^{13+}$ ”. *Physical Review Letters* **107** (2011), 023002 (cited on page 37).
- [Stu08] Student. “The Probable Error of a Mean”. *Biometrika* **6** (1908), 1 (cited on page 84).
- [Stu11] S. Sturm. “The  $g$ -factor of the electron bound in  $^{28}\text{Si}^{13+}$ : The most stringent test of bound-state quantum electrodynamics”. PhD thesis. Johannes Gutenberg-Universität Mainz, 2011 (cited on pages 17, 51, 104).
- [TC88] C. E. Theodosiou and L. J. Curtis. “Accurate calculations of 3p and 3d lifetimes in the Na sequence”. *Physical Review A* **38** (1988), 4435 (cited on page 43).
- [Tho12] J. J. Thomson. “XIX. Further experiments on positive rays”. *The London, Edinburgh, and Dublin Philosophical Magazine and Journal of Science* **24** (1912), 209 (cited on page 1).
- [Ulm+09] S. Ulmer et al. “The quality factor of a superconducting rf resonator in a magnetic field”. *Review of Scientific Instruments* **80** (2009), 123302 (cited on page 50).
- [Ulm+15] S. Ulmer et al. “High-precision comparison of the antiproton-to-proton charge-to-mass ratio”. *Nature* **524** (2015), 196 (cited on page 2).
- [Ulm11] S. Ulmer. “First observation of spin flips with a single proton stored in a cryogenic penning trap”. PhD thesis. Ruprecht-Karls-Universität Heidelberg, 2011 (cited on pages 16, 32, 78).
- [Val06] J. W. F. Valle. “Neutrino physics overview”. *Journal of Physics: Conference Series* **53** (2006), 473 (cited on page 4).
- [Van+12] J. Van Schelt et al. “Mass measurements near the  $r$ -process path using the Canadian Penning Trap mass spectrometer”. *Physical Review C* **85** (2012), 045805 (cited on page 2).
- [Vol+13] A. V. Volotka, D. A. Glazov, G. Plunien, and V. M. Shabaev. “Progress in quantum electrodynamics theory of highly charged ions”. *Annalen der Physik* **525** (2013), 636 (cited on page 3).
- [Wan+17] M. Wang et al. “The AME2016 atomic mass evaluation (II). Tables, graphs and references”. *Chinese Physics C* **41** (2017), 030003 (cited on pages 3, 95, 96, 102, 124, 127).

- [Wei19] A. Weigel. “Detection Electronics Design and First Observation of Bound-Electron Spin Transitions at the ALPHATRAP  $g$ -Factor Experiment”. PhD thesis. Ruprecht-Karls-Universität Heidelberg, 2019 (cited on page 129).
- [Wen+16] L. von der Wense et al. “Direct detection of the  $^{229}\text{Th}$  nuclear clock transition”. *Nature* **533** (2016), 47 (cited on pages 7, 131).
- [Zsc+09] G. Zschornak et al. *DRESDEN ELECTRON BEAM ION SOURCES: LATEST DEVELOPMENTS*. Tech. rep. Technische Universität Dresden and DREEBIT GmbH, 2009 (cited on pages 39, 46).

---

## Acknowledgements

---

Diese Arbeit wäre ohne die Hilfe und Unterstützung vieler Kollegen, meiner Freunde und Familie nicht möglich gewesen.

Zuerst möchte ich mich bei Klaus Blaum bedanken. Lieber Klaus, deine Unterstützung bei einfach allem, deine permanente gute Laune, stetige Erreichbarkeit und dein offenes Ohr, trotz deines vollgepackten Terminkalenders, sind beeindruckend. Vielen Dank für die Freiheiten, die du mir ermöglicht hast, sowohl im Labor, als auch fernab der Penningfallen. Danke für die schönen letzten Jahre in deiner Gruppe und für die Möglichkeit, an diesem großartigen Experiment mitzuwirken!

Vielen Dank an Thomas Pfeifer für die Übernahme der Aufgabe des Zweitgutachters! Und für deine motivierende Art, die mich erstmals ans MPIK gelockt und für die Atomphysik begeistert hat.

Liebes PENTATRAP-Team! Sergey Eliseev, Alexander Rischka, Menno Door, Pavel Filianin, Christoph Schweiger, Kathrin Kromer, Marius Müller, Charlotte König, Daniel Lange und Wenjia Huang: Es hat unglaublichen Spaß gemacht, mit euch allen zusammen zu arbeiten. Jeder Tag im Labor, im Büro, beim Kaffeetrinken, während des Mittagessens oder beim Feierabendbier war gespickt mit tollen Unterhaltungen, interessanten Diskussionen und einer großen Hilfsbereitschaft bei kleinen und großen Problemen. Sergey, vielen Dank für deinen tollen, trockenen Humor und deine ruhige Art, alle Probleme anzugehen. Alex, danke für das Mitschleppen zum Bouldern und die schönen Gespräche dabei über das Experiment, aber auch über alles Mögliche und Unmögliche. Ich habe das Basteln mit dir im Labor sehr genossen! Menno, vielen Dank für deine Rund-um-die-Uhr Hilfs- und Diskussionsbereitschaft, auch weit wegreichend von den alltäglichen Themen des Labors! Christoph, schön, dass du nach meiner Betreuung deiner Masterarbeit bei PENTATRAP geblieben bist und die HC-EBIT super weiterführst. Vielen Dank für deinen Vorrat an Schokolade, unsere geteilte Vorliebe für Spekulatius und deine überschwängliche und ansteckende Begeisterung für viele Themen. Kathrin, es war eine tolle Zeit zusammen mit dir im Büro, da kann kein anderer mithalten. Dein Tatendrang und deine Unternehmungslust sind ebenfalls unschlagbar. Charlotte, danke für die schöne Zeit in Rostock und dein ansteckendes Lachen. Marius und Daniel, vielen

Dank für all die tollen Kaffeepausen und EMBL-Gänge, vorallem während der letzten paar Wochen. Pavel und Wenjia, thanks for your help in the lab and the interesting discussions!

Einen großen Dank auch an die Mitglieder der anderen Penningfallen-Experimente in Heidelberg, Mainz und Genf, vor allem Sven Sturm, Stefan Ulmer, Martin Höcker, Alexander Egl, Tim Sailer, Andreas Weigel, Ioanna Arapoglou, Marc Schuh und Tom Segal für eure Unterstützung, die hilfreichen Diskussionen und die schöne Zeit, sowohl während der Arbeit als auch außerhalb des Instituts. Alex und Tim, vielen Dank für die interessanten und lustigen Gespräche während der Arbeit, beim Sport oder in unserer Lieblingsstadt. Marc, vielen Dank für deine Freundschaft, die Krisensitzungen, die Ike-abesuche, für das Motivieren zum Sport (vor allem das Trampolinspringen), weswegen ich über die Zeit der Doktorarbeit ein ganzes Stück sportlicher geworden bin!

Many thanks to Christoph, Sergey, Menno, Daniel, Ioanna, Wilma, <sup>u</sup>er!u<sup>f</sup>, and Julian for all the work you put into proof-reading larger or smaller parts of this thesis!

Vielen Dank auch an Gabi Weese für alles Organisatorische und die schönen Tage in Singapur. Dankeschön auch an Ralph Zilly für die alltägliche Unterstützung im Labor!

Mein Dank gilt ebenfalls dem MPIK-Konstruktionsbüro unter der Leitung von Frank Müller, vor allem Bettina Mörk und Yannick Steinhauser, für das schnelle Umsetzen aller möglichen Ideen und das Erstellen von tollen Bildern. Vielen Dank an die MPIK-Feinmechanikwerkstatt unter der Leitung von Thorsten Spranz für das schnelle und präzise Fertigen aller Bauteile für das Experiment!

Meiner Familie und meinen Freunden, danke, für den Rückhalt, für euer Verständnis, für eure Geduld, auch wenn ihr mich in letzter Zeit nicht so oft wie sonst gesehen habt! Ursula und Bobby Schüssler, vielen Dank für eure unglaubliche Unterstützung von Anfang an, das Ermöglichen von so vielem und die Hilfe bei jeder noch so kleinen und großen Sache!

Lieber Julian, danke, dass du für mich die letzten Wochen, Monate und Jahre immer da warst, dass du mir Käßspätzle zur Aufmunterung machst und auch meine Serien zum Abschalten mitschaust. Du weißt, bei welcher Gleichung in dieser Arbeit ich immer an dich denken muss und welches Kapitel für dich ist!

**Danke!**